THE UNIVERSITY *of* EDINBURGH

This thesis has been submitted in fulfilment of the requirements for a postgraduate degree (e.g. PhD, MPhil, DClinPsychol) at the University of Edinburgh. Please note the following terms and conditions of use:

- This work is protected by copyright and other intellectual property rights, which are retained by the thesis author, unless otherwise stated.
- A copy can be downloaded for personal non-commercial research or study, without prior permission or charge.
- This thesis cannot be reproduced or quoted extensively from without first obtaining permission in writing from the author.
- The content must not be changed in any way or sold commercially in any format or medium without the formal permission of the author.
- When referring to this work, full bibliographic details including the author, title, awarding institution and date of the thesis must be given.

Massive Galaxies at High Redshift

Henry James Pearce

Institute for Astronomy

School of Physics and Astronomy

University of Edinburgh

Doctor of Philosophy

2011

Abstract

A unique K-band selected high-redshift spectroscopic dataset (UDSz) is exploited to gain further understanding of galaxy evolution at $z > 1$. Acquired as part of an ESO Large Programme, this thesis presents the reduction and analysis of a sample of $\sim$ 450 deep optical spectra of a random 1 in 6 sample of the $K_{AB} < 23$, $z > 1$ galaxy population.

Based on the final reduced dataset, spectrophotometric modelling of the optical spectra and multi-wavelength photometry available for each galaxy is performed using a combination of single and dual component stellar population models. The stellar-mass and age estimates provided by the spectrophotometric modelling are exploited throughout the rest of the thesis to investigate the evolution of massive galaxies at $z > 1$.

Focusing on a K-band bright ($K < 21.5$) sub-sample in the redshift range $1.3 < z < 1.5$ the galaxy size-mass relation has been studied in detailed. In agreement with some previous studies it is found that massive, old, early-type galaxies (ETGs) have characteristic radii a factor $\simeq 1.5 - 3.0$ smaller than their local counterparts at a given stellar-mass. Due to the potential errors in spectrophotometric estimates of the stellar-masses at high redshift velocity dispersion measurements are derived for a sub-sample of massive ETGs at $z > 1.3$ in order to calculate dynamical mass estimates. To date, only a handful of objects at $z > 1.3$ have individual velocity dispersion estimates in the literature. Here the largest single sample (13 objects) of velocity dispersion measurements at high redshift is presented. The results for the sub-sample of objects with dynamical mass estimates confirm the results based on stellar mass estimates that high redshift massive systems are more compact than their local counterparts.

The fraction of K-band bright objects at high redshift that are passively evolving is calculated with specific star-formation rates from the UV rest-frame continuum, [OII] emission and $24\mu m$ data. It is concluded that $\sim 58 \pm 10\%$ of the $K < 21.5$, $1.3 < z < 1.5$ galaxy population is passively evolving. Various photometric techniques for separating star-forming and passively evolving galaxies are assessed by exploiting the accurate spectral types derived for the UDSz spectroscopic sample. Popular high-redshift selection techniques are shown to fail to effectively select complete samples of

passive objects with low levels of contamination. Using detailed information available for the UDSz dataset, various techniques are optimised and then used to estimate the passive fraction from the full UDS photometric catalog. The passive fraction results from the full photometric catalog are found to agree well with the results derived from the UDSz sample.

With the Visible and Infrared Survey Telescope for Astronomy (VISTA) now starting to produce data, the opportunity has been taken to develop high-redshift galaxy population dividers based on the VISTA filters. Using the first data release from the VISTA Deep Extragalactic Observations (VIDEO) survey (VVDS D1 field), the passive fractions of K-band limited samples have been estimated to compare with results derived in the UDS. Within the errors the passive fraction estimates in the UDS and VISTA VVDS D1 field are found to agree reasonably well.

Finally, composite spectra are used to study the evolution of various different galaxy sub-samples as a function of redshift, age, stellar-mass and specific star-formation rate. This work produces an remarkably clean result, showing that the massive, absolute K-band bright, passively evolving ETGs are always the oldest population, with ages close to the age of the Universe at $z \sim 1.4$. In contrast, the late-type, low-mass, star-forming galaxies are always found to be much younger systems. This result strongly supports the downsizing scenario, in which more massive systems complete their stellar-mass assembly before lower-mass counterparts.

Declaration

I declare that this thesis is not substantially the same as any that I have submitted for a degree or diploma or other qualification at any other University. I further state that no part of my thesis has already been or is being concurrently submitted for any such degree, diploma or other qualification.

This thesis is the outcome of my own work except where specifically indicated in the text.

Henry James Pearce
Edinburgh
28 April 2011

This work is dedicated to my parents Peter & Hilary Pearce

Acknowledgements

First and foremost I would like to thank my three amazing supervisors, Dr. Ross "Emotions" McLure, Dr. Michele "The Italian" Cirasuolo and Prof. Jim "The Don" Dunlop. I have learnt so much from them over the last 3-4 years, and much more than just the details of the field. I would like to send out a huge thanks to Trevor "I'm stacked" Back and Paula "Vino" Wilkie for all their help and support. Trevor was there through all the bitching and moaning, and Paula, how would I have filled out a form without you? My parents have always been a great support, and they fully deserve the dedication for this piece of work. I would like to thank Team Vista Hut, who have all contributed to various ideas and debates.

I would like to thank my best mates: Ed, Craney and Tom for all there support. Where would I be without my team, the Squash Lads (Roddick, Volley, Churchill, Pie, C, Noddy, Metcalf, Ahmed, 14" and Crouchy), we had a great time on the court and the dance floor. I would also like to thank my close mates not in Edinburgh who have also given all their support: Sam, Liam, Dwayne, Dan, Jess, Henri, Tash, Briony and Suggers.

I could not have asked for a better house mate, Cheeky Mouse, and I am glad Paul was there as well. The way to a stress free easy life is having a good Landlord, and Paul, Cheeky Mouse and myself had this in our great friend Ryan, and his boss Lou. I would like to thank my great friends Non, Jaz and Lins for being there and housing me for the home straight.

Now for the important ones. Who ever invented houmous, well done. I honestly do not think I could have enjoyed lunch without you. I can not thank the owners and managers of all the bars and clubs on George Street and around the rest of Edinburgh enough. You have supplied me with lash and young beauties for nearly 4 years now.

I would like to thank God for tripping, stubbing his toe and accidently setting off the Big Bang.

When times were hard throughout my PhD (emotionally and financially) Orange Wednesdays stepped up on more than one occasion, they still sting you on the pick 'n' mix though. I would like to thank the CSE and all its staff for giving me a home away from home.

For anyone starting or in the middle of their PhD the greatest piece of advice I can pass on came from Dr. Ross McLure, "Just get it done", which is deeper than you will initially think.

HJP
Royal Observatory, Edinburgh
28th April 2011

Table of Contents

List of Tables

List of Figures

Chapter 1

Introduction

Understanding galaxy formation and evolution is one of the key challenges in extra-galactic astronomy. The ultimate goal is to combine the latest theories and observations to gain a full understanding of how density perturbations in the early Universe evolved into the structures we see in the present day Universe. The goal of this thesis is to exploit a unique spectroscopic data-set to improve our understanding of the assembly and evolution of massive galaxies at redshift $1 < z < 2$.

1.1 Theoretical Framework of Galaxy Evolution

The widely accepted ΛCDM model predicts that the galaxies and large scale structures seen in the Universe today originate from primordial density fluctuations following an inflationary period after the Big Bang. The growth of these fluctuations led to areas of underdensities which became present day voids and overdensities which became the galaxies, groups and clusters of galaxies observed today. This idea was originally put forward by Peebles [1965], who proposed that the expansion of the Universe leads to the cooling of its contents, meaning any large scale perturbations from the overall unifrom mass distribution would grow over time. Dark matter halos were the first structure to form as they are believed to only interact through gravitational forces. These halos played as arenas for the first generation of stars and proto-galaxies. Within the ΛCDM framework, the latest observations constraints suggest that only 4% of the Universe's mass-energy budget is in the form of baryonic (visible) matter; 23% is thought to be in

the form of dark matter (matter that is currently detectable only by its gravitational interactions), and the majority, the remaining 73%, is in the form of dark energy, a still to be understood source of energy believed to be responsible for the increased rate of expansion of the Universe [e.g. Daly and Djorgovski 2003].

1.1.1 Constraining Cosmological Parameters

The isotropy of the early Universe should produce a near perfect blackbody spectrum. The remnants of which should be able to be seen today. This idea was first suggested by Gamow, Alpher and Herman in 1947 and it was first detected by Penzias and Wilson [1965] to be a thermal blackbody spectrum at a temperature of 3.5 ± 1K. The COsmic Background Explorer (COBE) with the Far Infrared Absolute Spectrophotometer (FIRAS) [Mather et al., 1993] went onto measure the temperature of the discovered cosmic microwave background (CMB) thermal spectrum to be 2.726 ± 0.010K [Mather et al., 1994] and further observations improved the result to 2.725 ± 0.002K [Mather et al., 1999].

It was predicted that the primordial density fluctuations would be observable as anisotropies in the CMB [Sachs and Wolfe, 1967]. These anisotropies were first discovered using Differential Microwave Radiometers (DMR) [Smoot et al., 1990] on COBE [Smoot et al., 1992].

The Wilkinson Microwave Anisotropy Probe (WMAP) followed COBE and measured these anisotropies with much higher resolution, sensitivity and accuracy. The position and size of peaks in CMB power spectrum can be used to constrain cosmological parameters. The higher order peaks were not visible with COBE due to its large beam width but the higher resolution of WMAP allowed studies on smaller angular scales. WMAP unveiled the peaks that were being looked for [Larson et al., 2011]. See Figure 1.1. However WMAP data alone is degenerate across the cosmological parameters so additional parameter constraints are required.

Galaxy clustering can be used to constrain cosmological variables through an analogous method. By considering different models of the expanding Universe, cosmological parameters can be estimated from the power spectrum of the distribution of galaxies [e.g. Percival et al. 2001, Cole et al. 2005]. Combining the results from clustering

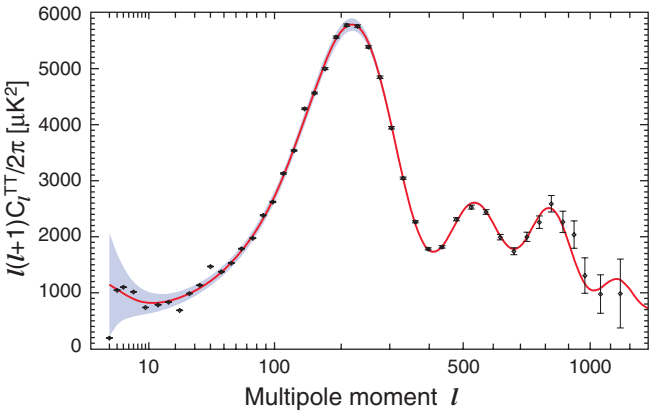

Figure 1.1: The temperature power spectrum from the seven year WMAP results [Larson et al., 2011]. The third acoustic peak and the onset of the Silk damping tail are now well measured by WMAP. The curve is the ΛCDM model best-fit ($\Omega_b h^2 = 0.02270$, $\Omega_c h^2 = 0.1107$, $\Omega_\Lambda = 0.738$, $\tau = 0.086$, $n_s = 0.969$, $\Delta^2_R = 2.38 \times 10^9$ and $A_{SZ} = 0.52$. The gray band represents cosmic variance.

analysis with the knowledge of the CMB power spectrum fluctuations the degeneracy amongst cosmologies can be reduced [Spergel et al., 2003] (see Figure 1.2).

Studying the expansion of the Universe is an effective way to put constraints on cosmological models. Similar to the use of Cepheid variables, the expansion can be traced by observations of supernovae. The processes leading to a type 1a supernova are well understood and the luminosity emitted when one occurs is thought to be well constrained. Therefore these supernovae work as standard candles within the Universe, i.e. a distance can be inferred directly from the observed luminosity of the object. Three of the major supernovae detection projects (past and present) are the Supernova Cosmology Project (SCP) [Perlmutter et al., 1995], the High-z Supernova Search Team [Riess et al., 1997] and Supernova Legacy Survey (SNLS) [Howell et al., 2005]. Kowalski et al. [2008] went on to combine a large collection of supernova datasets to form a "Union" catalog; from this master dataset and in combination with other cosmological measurement estimated the dark energy density to be $\Omega_\Lambda = 0.713^{+0.063}_{-0.068}$.

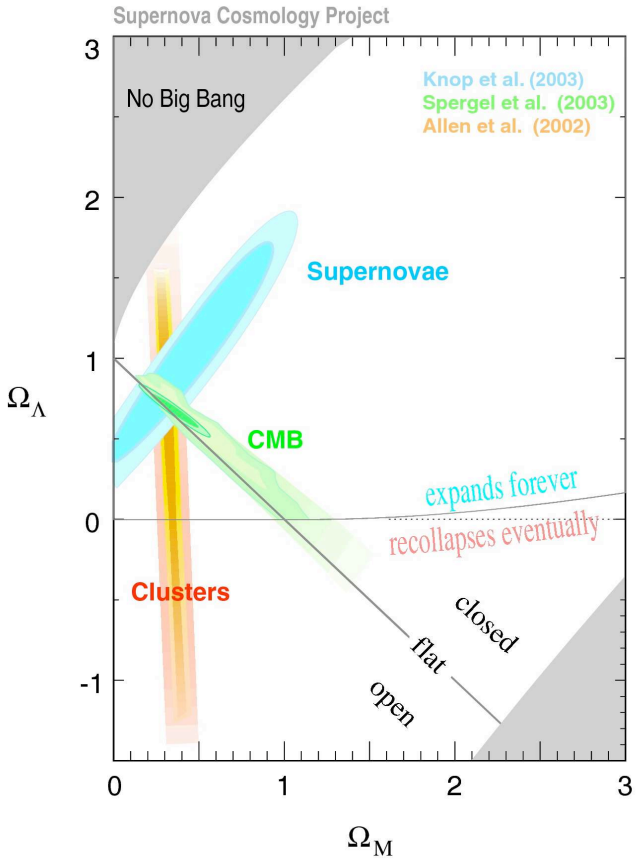

Figure 1.2: Combined constraints to cosmological densities Ω_Λ and Ω_M, using supernovae, CMB and cluster abundance data. The flat Universe with $\Omega_\Lambda + \Omega_M = 1$, is shown with a solid line [Knop et al., 2003].

1.1.2 Semi Analytical Models of Galaxy Evolution

The dark matter halos that form from the primordial mass fluctuations at the start of the Universe are believed to evolve in an hierarchical manner called *hierarchical clustering*. Press and Schechter [1974] presented an analytic theory for how these initial fluctuations would evolve into the mass distribution seen in the Universe today. Assuming a Gaussian distribution of initial density fluctuations, Efstathiou et al. [1988] performed N-body simulation experiments that produced results in good agreement with Press and Schechter [1974]. Bower [1991] extended this work to study how hierarchical clustering would result in groups and clusters of galaxies. Later Kauffmann and White [1993] produced an algorithm that would construct dark matter halo merger

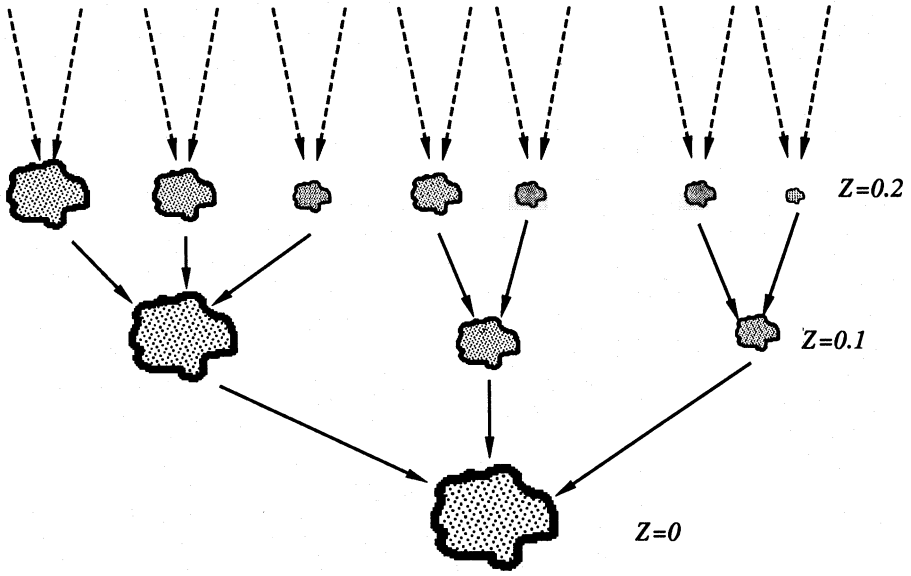

Figure 1.3: A schematic representation of a dark matter halo merger tree from Kauffmann and White [1993].

trees mapping out the mass growth path for condensations of matter in the Universe. See Figure 1.3 for an example of an hierarchical dark matter halo merger tree.

With a basis for how the dark matter structure of the Universe evolved, the next task was to attempt to imprint the baryonic physics of stellar and galaxy formation on top. Early work on this was done by White and Rees [1978] and the first semi-analytical model (SAM) was constructed by White and Frenk [1991]. There are numerous groups using SAMs but the highly active groups working on SAMs are; Durham [e.g. Cole et al. 1994], Munich [e.g. Kauffmann et al. 1993] and Santa Cruz [e.g. Somerville and Primack 1999].

The main ingredients of a SAM are cosmology, dark halos, gas cooling, star formation and feedback. A schematic showing how the main baryonic physical processes are linked is shown in Figure 1.4, taken from a review of the subject by Baugh [2006]. The physics behind all these processes is not fully understood and therefore simple recipes with free parameters are placed into the SAMs to mimic these processes. This leads to SAMs having a vast array of free parameters. Initially these free parameters were tuned to match the large amounts of observational data at $z \sim 0$, such as the luminosity function, the Tully-Fisher relation and the fundamental plane of galaxies. See Figure 1.5 for a

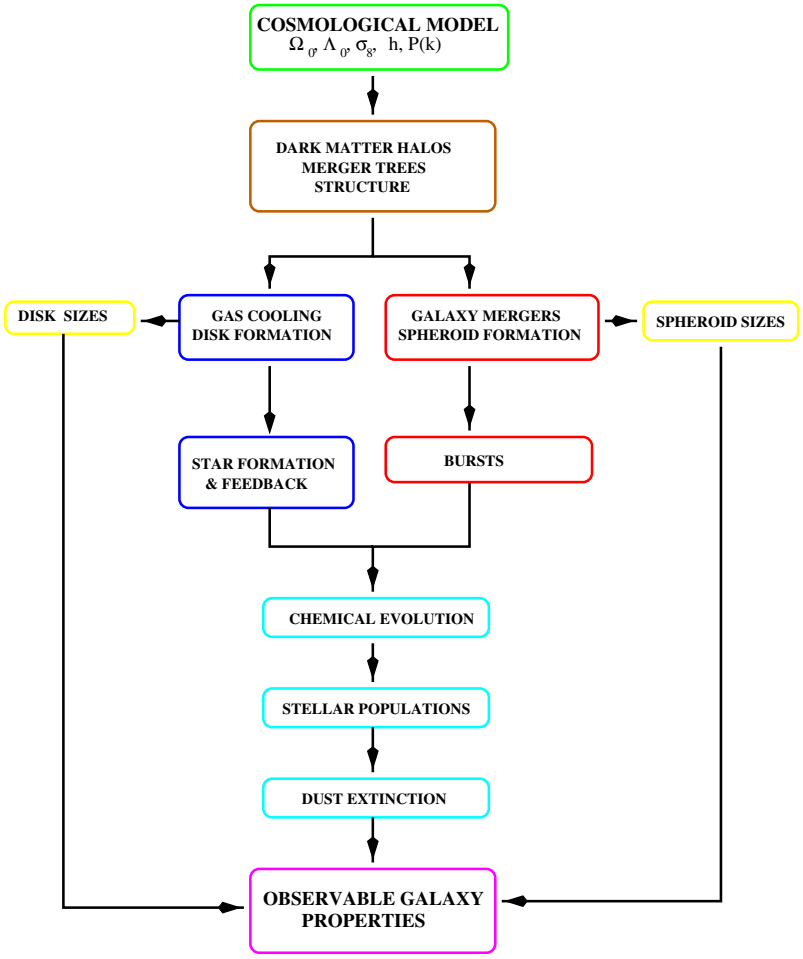

Figure 1.4: A schematic flow chart of the baryonic physical processes that are implemented into semi-analytical models [Baugh, 2006].

schematic of the typical local observations and relation SAMs have their parameters tuned to match [Cole et al., 2000]

Although SAMs are effective at reproducing what is seen in the local Universe, for example Figure 1.6 shows that the Durham model can reproduce the local observed b and K luminosity function [Cole et al., 2000], initially the models had difficulty matching what was seen at higher redshift.

The early SAMs [e.g. Cole et al. 2000 and Somerville et al. 2001] had difficulty matching the number density of massive galaxies discovered at high-redshift by observations with the Submillimetre Common-User Bolometer Array (SCUBA) [Scott et al., 2002], Max-Planck-Millimeter-Bolometer (MAMBO) [Blain et al., 2002] and K-band

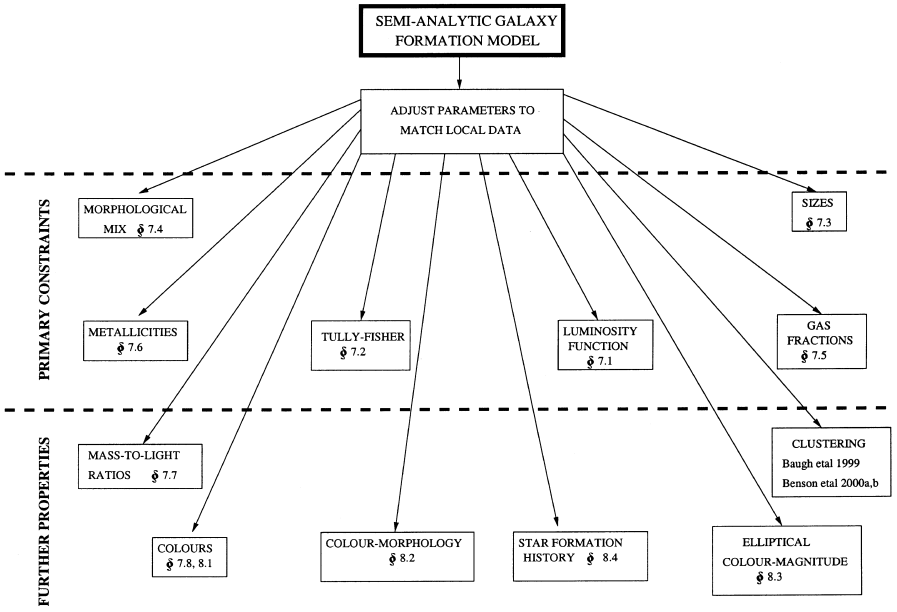

Figure 1.5: A schematic showing the local observations and relations which SAMs have their variables tuned to match [Cole et al., 2000].

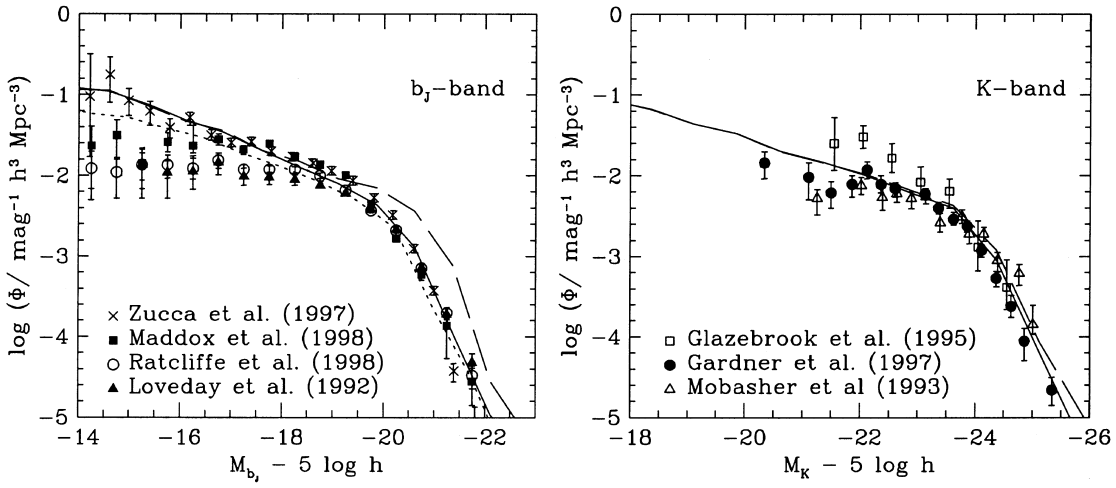

Figure 1.6: Comparison of the b-band (left panel) and K-band (right panel) luminosity function produced by the SAM from Cole et al. [2000] with the observational data available at the time. The solid line in each panel show the model prediction with the inclusion of the effects of dust. The dashed lines are show the model predictions before dust is included.

surveys such as Cimatti et al. [2002b] and Kashikawa et al. [2003]. SCUBA selects high redshift galaxies based on their rest-frame far-IR emission, therefore SCUBA galaxies are dusty galaxies with high star-formation rates that have their UV emission absorbed and re-emitted in the far-IR. SCUBA galaxies may not be massive themselves but due to the extremely high SFR estimated from their far-IR emission (250-2000 $M_{\odot}yr^{-1}$) they are believed to be the progenitors of massive galaxies. Granato et al. [2004] attempted to address this problem with the use of active galactic nuclei (AGN) feedback. Granato et al. [2004] implemented the idea that the radiation drag on the cold gas collapsing into the halo decreases its angular momentum, causing an inflow into a reservoir around the central black hole. Viscous drag then causes the gas to flow from the reservoir into the black hole, increasing its mass and powering the nuclear activity. This increased nuclear activity causes feedback from the black hole which suppresses star-formation, and could help to account for the presence of massive evolved systems at high redshift.

1.2 Constraints on Galaxy Evolution from Optical Studies

Early studies of the global star-formation history of the Universe suggest that the star-formation rate density of the Universe peaked at $z \sim 1$ [Madau et al. 1996, Lilly et al. 1995, Connolly et al. 1997, Madau et al. 1998]. Figure 1.7 shows the original "Madau Plot" of the star-formation rate history of the Universe, based on star-forming galaxies found in the optical bands of the Hubble Deep Field (HDF), which trace the rest frame ultra-violet out past $z \sim 1$.

Optical studies also showed that massive galaxies were rare at high-redshift [Madau et al., 1996], in agreement with the output from contemporary SAMs as they are based on bottom up assembly and the more massive systems should not form until late in the history of the Universe.

However, for the $z > 1$ Universe, optical studies observe the rest-frame ultra-violet. This results in a strong bias against red galaxies, both those that are red from domination of old stellar population and those that are red due to the presence of dust.

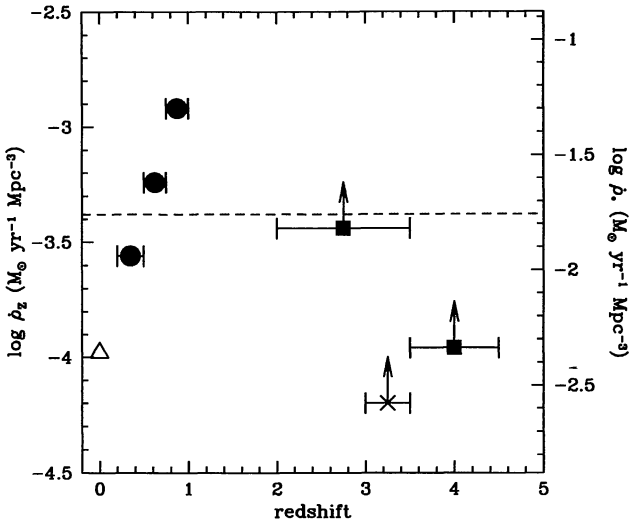

Figure 1.7: The original 'Madau Plot' showing the star-formation rate history of the Universe based on searching for star-forming galaxies in the optical bands of the Hubble Deep Field (HDF) which trace the rest frame ultra-violet out past $z \sim 1$ Madau et al. [1996]

1.3 The Advent of Near-Infrared Studies

The key to improving on the optical studies of the $z > 1$ Universe was to move observations into the near-infrared (NIR), which observe the rest-frame optical at $z > 1$ and are free from bias against red (passively evolving or dust obscured) galaxies. When observing the high-redshift Universe the mass-to-light ratio in the $K(2.2\mu m)$-band has a small range compared to the rest-frame UV and therefore can be used to select galaxies by mass. This makes comparison with galaxy evolution models easier as, fundamentally, models describe galaxies in terms of mass.

The first generation of NIR detectors were developed over 20 years ago [Wynn-Williams and Becklin, 1987]. Elston et al. [1988] took deep K-band imaging of 10 arcmin^2 of the sky and constructed a K vs. $R-K$ colour-magnitude diagram of their observed objects (see Figure 1.8). The $R-K$ colour is of particular interest as the R and K-bands straddle the 4000Å break for galaxies at $z > 1$. At the time, Bright Cluster Galaxies (BCGs), local massive galaxies in the vicinity of cluster centres, were considered the most luminous and reddest galaxies known and everything else was fainter and/or bluer. Consequently, Elston et al. [1988] added lines to their colour-

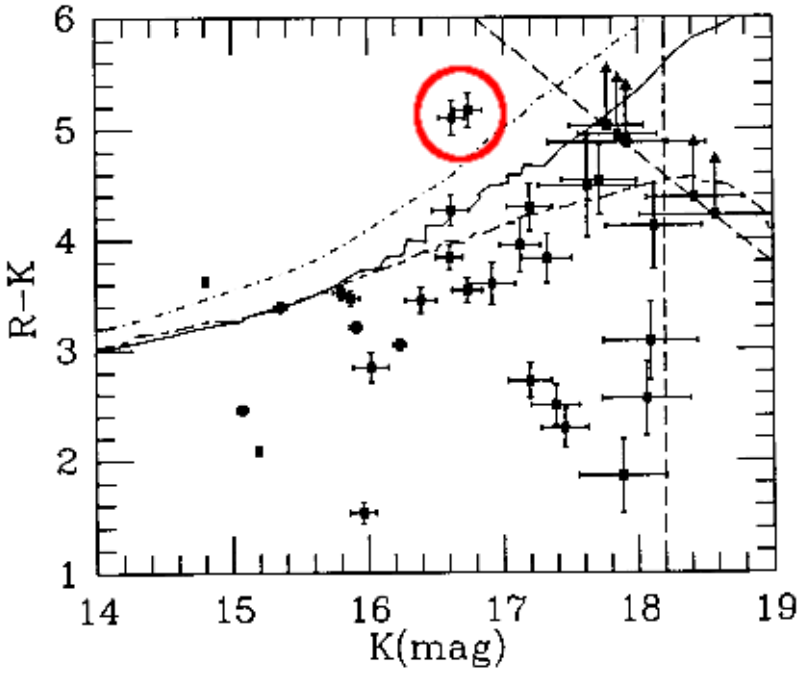

Figure 1.8: A colour magnitude diagram from Elston et al. [1988] showing K vs. $R-K$. The solid and dot-dashed line represent model of a passively evolving Bright Cluster Galaxies (BCG) from Bruzual [1983] and a non-evolving E galaxy derived from IR observations of local ellipticals. The unevenly dashed line represents a Bruzual $\mu = 0.5$ model (μ represents the fraction of the total gas mass that will be in stars after 1 Gyr if dying stars did not return gas to the system, defined as $\mu = 1 - e^{-1/\tau}$, where τ defines the period of star-formation) with ongoing star-formation.

magnitude diagram representing an evolving model of a BCG from Bruzual [1983] and a line representing a non-evolving BCG based on data from nearby galaxies (the solid and dot-dashed curves respectively in Figure 1.8). Using these curves, along with the idea that $R-K$ colours of galaxies out to $z = 1$ are monotonic, the region just below the lines represents the "red envelope", that is, the extreme part of the colour-magnitude diagram that is was believed normal $z \leq 1$ galaxies could populate. Elston et al. [1988] found two galaxies that, due to their extremely red colours, sat outside of this region, and are highlighted by a red circle in Figure 1.8.

Based on their number density, these objects were ruled out as red luminous radio galaxies, as seen by Lilly et al. [1985], as only 1-2 red luminous radio galaxies are expected per deg^2 at $z \approx 1$. Elston et al. [1988] thought they could be a new class of

galaxy representing primeval galaxies at $z > 6$ undergoing a rapid luminous phase of star-formation [Schmidt 1963, Partridge and Peebles 1967]. Elston et al. [1989] acquired $BVRiJHK$ photometric and optical spectroscopic data for these two interesting objects. They concluded that these galaxies were luminous red galaxies at $z = 0.8$. With these, and a third object confirmed to have $K = 17.9$(Vega) and $R - K = 6$(Vega) with a redshift of $z = 1.2 \pm 0.2$ they suggested the existence of a population of extremely luminous galaxies at $z > 0.7$.

Cowie et al. [1990] performed a deep K-band survey on UKIRT and found objects even redder than the two objects found by Elston et al. [1988]. The reddest objects in their sample also had colours redder than extreme M stars and brown dwarfs. These results supported the idea of a high-redshift population of extremely luminous red galaxies, as a system of stars with significant dust is the only object that could be redder than these extremely cool stars.

Djorgovski et al. [1995] performed one of the first studies of galaxy number counts in the K-band using deep Keck observations reaching $K = 24$ over 3 Keck fields of view. They found no turn over in the number counts down to the limits of their data (see Figure 1.9). These early observations instantly showed the power of the NIR to aid astronomical investigations into the high-redshift Universe.

The major drawback with these early studies was the size of the surveys, which were all conducted over a very small area of the sky. However, with the introduction of such instruments as the UKIRT Fast-Track Imager (UFTI) [Roche et al., 2003b] on the UK Infrared Telescope (UKIRT), Ω-Prime [Bizenberger et al., 1998] on the 3.5-m telescope of the Calar Alto Observatory and the Infrared Spectrometer And Array Camera (ISAAC) [Moorwood et al., 1998] on the Very Large Telescope (VLT), larger areas of the sky could be surveyed. This generation was then followed by the most up-to-date NIR instruments such as Wide Field Infrared Camera (WFCAM) [Casali et al., 2007] on UKIRT, Wide-field InfraRed Camera (WIRCam) [Puget et al., 2004] on the Canada France Hawaii Telescope (CFHT) and VISTA InfraRed CAMera (VIRCAM) [Dalton et al., 2006] on VISTA. This generation of NIR cameras can image a significant fractions of a square degree in a single shot, and are currently undertaking major surveys of the high-redshift Universe.

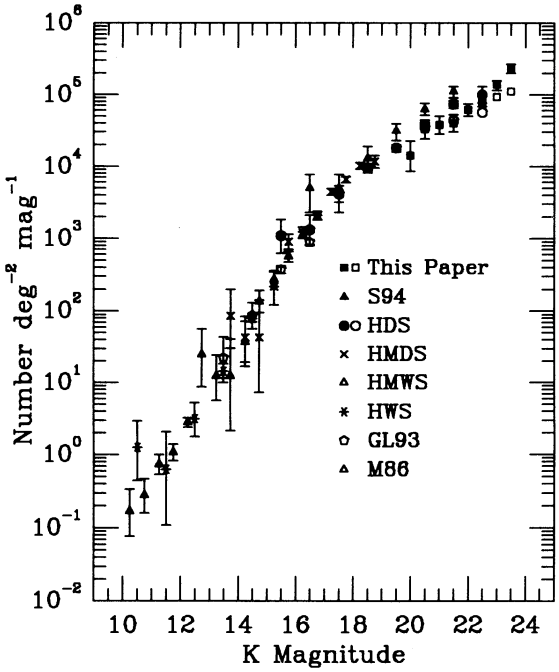

Figure 1.9: Extragalactic number counts in the K-band from Djorgovski et al. [1995]. The K-band magnitudes are in the Vega system. The number counts for the other symbols come from previous K-band surveys based on shallower data. See Figure 2 in Djorgovski et al. [1995] for references for other symbols.

1.4 Results from Early Large Area Near-IR Surveys

The development of large near-IR detectors prompted large near-IR surveys to take place. An early example of large NIR surveys is the Munich Near-IR Cluster Survey (MUNICS), a K-band selected survey over 1 deg^2 that acquired deep J- and K-band imaging [Drory et al., 2001]. With a sample of data from the MUNICS survey, based on the best photometric homogeneity and good seeing, Drory et al. [2004] showed how the number density of K-band selected field galaxies evolves with redshift down to stellar-mass limits of 2×10^{10}, 5×10^{10} and $1 \times 10^{11} h^2 M_{\odot}$ (see Figure 1.10). Drory et al. [2004] found that the more massive galaxies had stronger evolution in number density with decreasing redshift (this is evidence against the idea "downsizing" - see later).

The Great Observatories Origins Deep Survey (GOODS) was a multi-wavelength programme that achieved imaging over a wide range of wave bands in two fields (centred on Hubble Deep Field North (HDF-N) and Chandra Deep Field South (CDFS)) [Fosbury

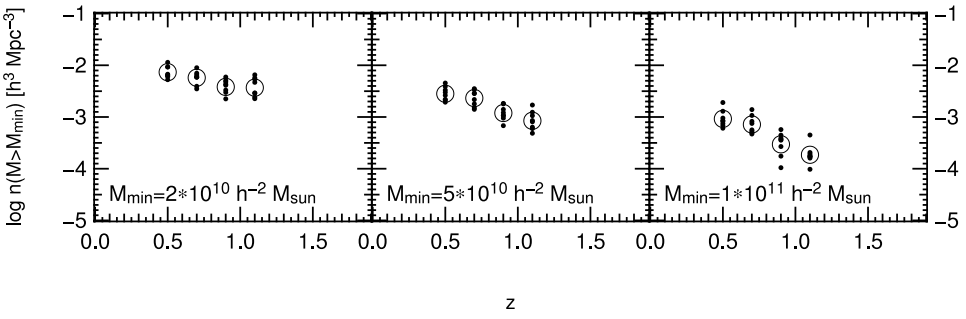

Figure 1.10: Comoving number density of objects having stellar masses exceeding $2 \times 10^{10}h^{-2}M_{\odot}$ (left), $5 \times 10^{10}h^{-2}M_{\odot}$ (middle) and $2 \times 10^{11}h^{-2}M_{\odot}$ (right). The filled circles represent the values measured separately in each survey field and the open circles represent the mean values over the whole survey area [Drory et al., 2004].

et al. 2001,Dickinson et al. 2003]. In particular the GOODS-South survey acquired ultra deep JHK_s data from ISAAC ($M_{AB} \approx 24.25$, 5σ) on the VLT [Retzlaff et al., 2010] over an area on $\sim 150\text{arcmin}^2$.

Using the sample of extremely red galaxies (ERGs) defined by Roche et al. [2003a] from the GOODS-South data, Caputi et al. [2004] estimated the redshift distribution and found the ERGs population to peak in counts at $z \sim 1.5$ (see Figure 1.11).

Similar results were found when Fontana et al. [2006] (using a K- and z-band selected sample of the GOODS-MUSIC (MUltiwavelength Southern Infrared Catalog) dataset) investigated how the galaxy stellar-mass function (GSMF) evolves with redshift (see Figure 1.12). The density of massive galaxies declines slowly up to $z \sim 1.5$ and then rapidly drops off at $z > 2$. There appears also to be differential evolution of the GSMF, where more massive galaxies appear to evolve less than low mass galaxies up to $z \sim 1.5$.

More recently Cirasuolo et al. [2010] investigated the evolution of the near-IR galaxy luminosity function out to $z \sim 4$ using the UKIDSS Ultra Deep Survey (described in detail in Chapter 2) (see Figure 1.13). Cirasuolo et al. [2010] found the evolution of the luminosity function to be best described by a combination of both luminosity and density evolution. This results in a differential evolution of galaxy number density, dependent on galaxy luminosity, with the most luminous galaxies evolving less than the fainter counterparts. This opposed the result found by Drory et al. [2004]. The difference in the results found could be down to the small number statistics of Drory

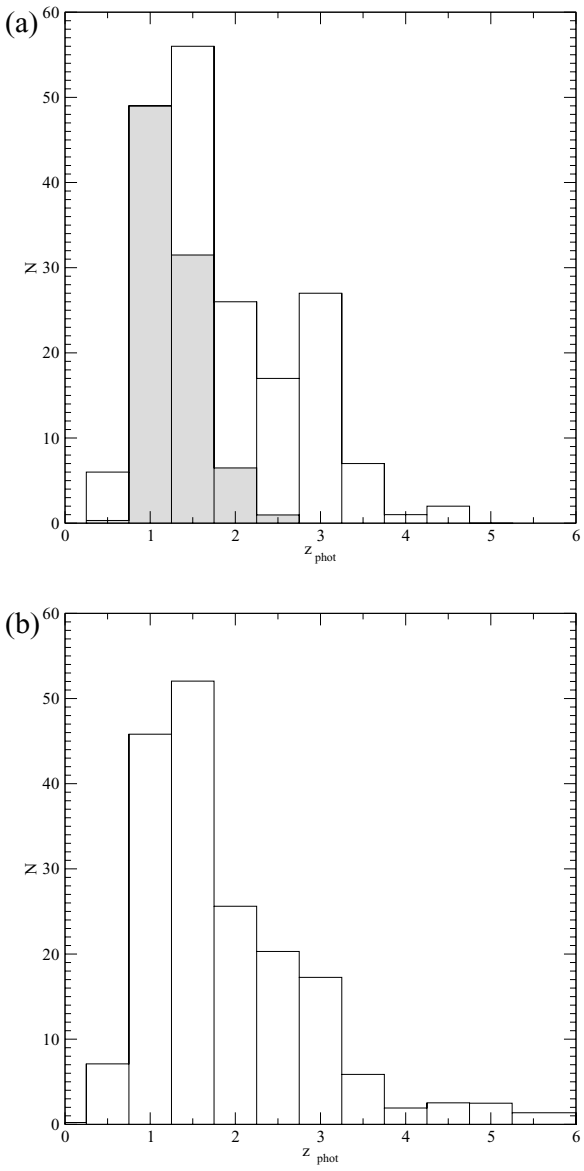

Figure 1.11: The redshift distribution of the extremely red galaxy (ERG) sample from Caputi et al. [2004]. The top panel is based on best fitting photometric redshift only, whereas in the lower panel the probability density distribution of each ERG and small corrections due to the incompleteness of the sample are taken into account. The shaded area in the top panel shows the redshift distribution of ERGs from wider shallower data in the GOODS-South from Moustakas et al. [2004] which has been normalised to match same number of targets in the Caputi et al. [2004] sample in the bin centred on $z_{phot} = 1$.

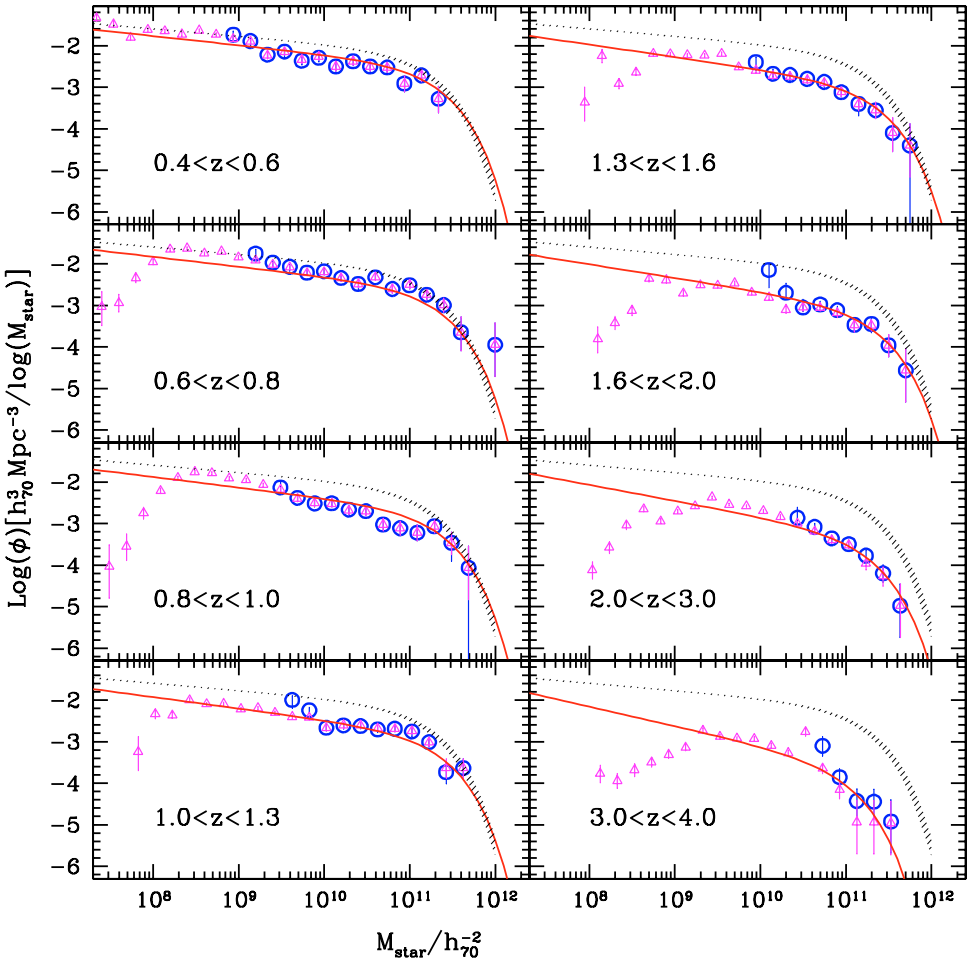

Figure 1.12: Galaxy stellar-mass functions (GSMFs) in the GOODS-MUSIC sample, in different redshift ranges. Big circles represent the GSMFs of the K-selected sample and small triangles show the GSMF of the Z_{850}-selected sample [Fontana et al., 2004]. The dashed region represents the local GSMF of Cole et al. [2001] encompassing its original and the rescaled version that was obtained in Fontana et al. [2004]. The solid line is the evolving fit to the data, computed over the redshift range $0.4 < z < 4$.

et al. [2004] in the high mass high redshift subsample due to rarity of extremely massive systems at high redshift. The high redshift high mass data points most likely contain large errors. There is also likely large errors on the low mass data points at high redshift due to the incompleteness of the Drory et al. [2004] survey at these galaxy masses.

All of these points highlight the effect, coined by Cowie et al. [1996], of *downsizing*. That is, star-formation activity changes as a function of mass with redshift. At high-redshift the massive galaxies dominate the star-formation rate density and this domination migrates down the mass scale with decreasing redshift i.e. the massive galaxies shut off their star-formation first.

1.5 The Nature of Near-IR Selected Galaxies at $z > 1$

As a population of extremely red objects (EROs) at high-redshift was unveiled, various groups started to study the characteristics of these systems. These EROs were spatially extended on the sky, so it was concluded that they were almost definitely galaxies rather than red stars. Roche et al. [2002] investigated the clustering of $z \sim 1$ EROs with a sample of $K < 20$(Vega) galaxies. It was seen that the angular correlation function, $\omega(\theta)$, for EROs is approximately an order of magnitude higher than that of the whole $K < 20$ sample. This was consistent with results from Daddi et al. [2000a] and Firth et al. [2002]. It was believed that this newly discovered population of EROs were either a population of galaxies with old stellar populations and/or with dust reddening [Hu and Ridgway, 1994]. It was also a possibility that they could be described by a population of star-forming galaxies at $z \sim 2.5$ with the bright K-band magnitude attributed to a strong Hα line. However, it was thought unlikely to find a large population of luminous star-forming galaxies existed at $z \sim 2.5$ that had not been previously picked by searches for Lyman-α. More information about the galaxy's SEDs would be required to distinguish between the different interpretations.

Graham and Dey [1996] acquired infrared spectroscopy of and studied in detail HR10, one the reddest EROs discovered by Hu and Ridgway [1994]. Assuming that HR10 was a passively evolving galaxy Hu and Ridgway [1994] estimated it to be an extremely luminous, $\sim 10L^{\star}$, galaxy at $z \sim 2.4$. The infrared spectroscopy acquired by Graham and Dey [1996] showed a high equivalent width emission line at $\lambda = 1.6\mu m$

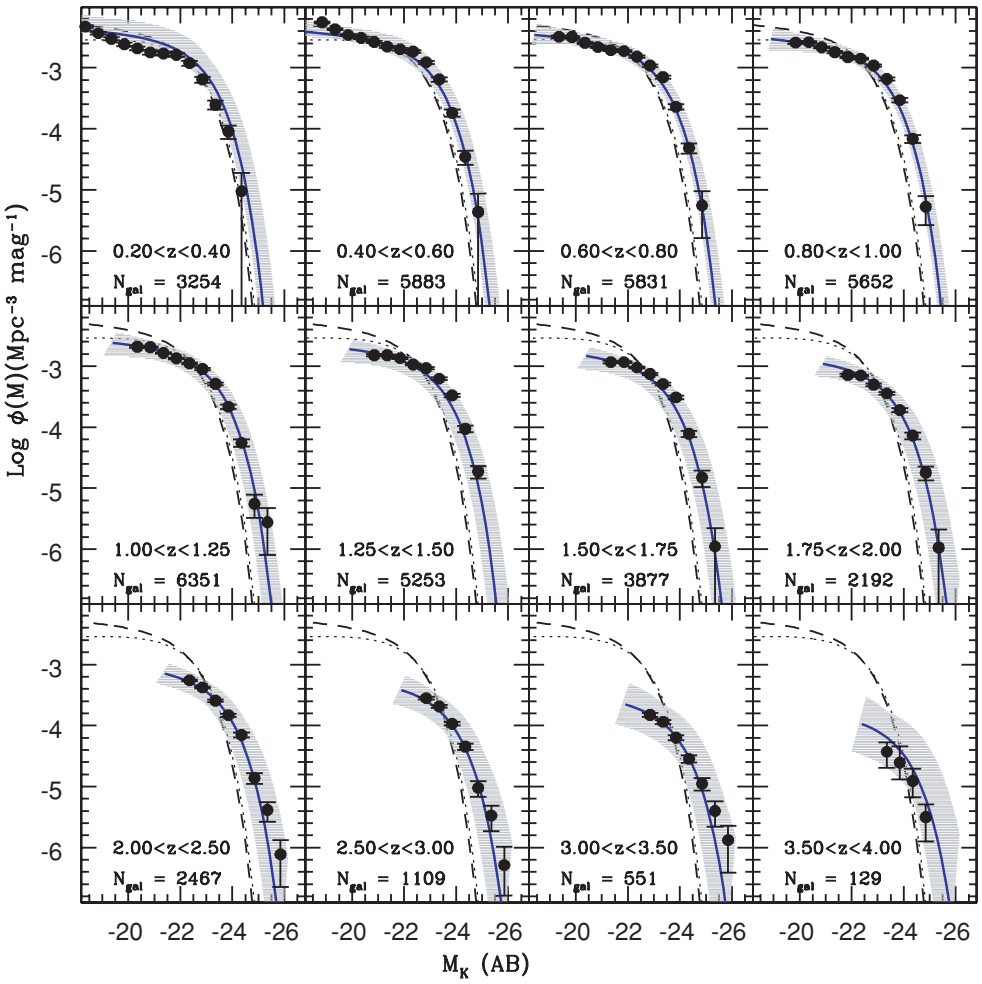

Figure 1.13: Rest-frame K-band luminosity function in 12 redshift bins in the range $0.2 \leq z \leq 4$ [Cirasuolo et al., 2010]. The solid dots represent the luminosity function obtained with the $1/V_{max}$ method for sources in the UDS sample, while the solid line is the best-fitting Schechter function obtained from the likelihood analysis and plotted at the mean redshift of each bin, with the shaded area showing the 1σ uncertainty. In each redshift bin, the faintest point of the luminosity function corresponds to the minimum luminosity for the observed $K \leq 23$ limit, assuming the most conservative k-correction to maximize the level of completeness. For comparison, the dashed and dotted lines are the luminosity function at $z = 0$ obtained by Kochanek et al. [2001] and Cole et al. [2001] respectively.

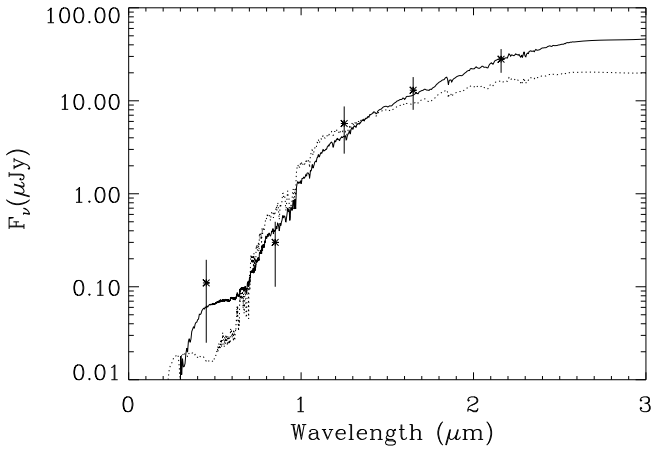

Figure 1.14: The observed (0.4 - 2.2μm) photometry of HR10 with two alternative galaxy SEDs over plotted. The best fit (solid line) is a heavily reddened ($A_v = 1.8$) Sb galaxy template. The dotted line is an unreddened elliptical SED [Graham and Dey, 1996].

which was identified as Hα at $z = 1.44$. At this redshift an unreddened model spectral energy distribution, based on that of nearby galaxies, proved a poor fit to the data because it was unable to reproduce the observed B-band magnitude. An old or reddened elliptical galaxy SED underpredicts the B-band magnitude indicating either a recent episode of star-formation or the presence or an active galactic nucleus (AGN) (see Figure 1.14). Graham and Dey [1996] found the best fitting SED to be a reddened Sb galaxy. When comparing the photometry to the theoretical SEDs of Bruzual and Charlot [1993] they also found that reddening was crucial to get a good fit to the data without seriously changing the initial mass function (IMF). This conclusion of a potential recent episode of star-formation is supported by the galaxy's K-band morphology that is asymmetric and indicates some form of galaxy interaction.

In the same year using the Low Resolution Imaging Spectrograph on Keck, Dunlop et al. [1996] acquired optical spectroscopy of 53W091, one of reddest galaxies from the Leiden-Berkeley Deep Survey (LBDS) [Windhorst et al., 1984]. Combining the optical spectra with deep J- and H-band photometry 53W091 was confirmed to be a red galaxy at $z = 1.552$ from two spectral breaks in the rest-frame UV, 2635Å and 2897Å, and from Mg and Fe absorption features in the same region. The rest-frame UV spectral slope indicated that 53W091 was dominated by an old population of low mass main

sequence stars. Through fits to the stellar atmosphere models of Kurucz [1992] Dunlop et al. [1996] estimated the age of the galaxy to be 3.5Gyrs. This age was consistent with age estimates from fits to various stellar synthesis models. The strength of the UV spectral breaks, which are independent of dust reddening, also indicate an age of >3.5 Gyrs, confirming this to be an observation of a high-redshift red and old galaxy. An age of 3.5 Gyrs is close to the age of the Universe at this redshift in an Einstein-de Sitter cosmology, and puts the formation redshift far higher than that inferred from data on field galaxies [Cowie et al., 1995].

1.5.1 Dusty Starbursts or Passively Evolving?

From the end of the 1990s various research groups focused their time on working towards understanding how the ERO population at high-redshift was divided between passively evolving and dusty starburst galaxies. The first attempts to model dust more realistically than simple foreground extinction was Cimatti et al. [1997], who focused on spheroidal galaxies. Cimatti et al. [1997] constructed three models; one representing a dust disc, one representing the stars being embedded within dust, and one that takes into account the gravitational potentials of stellar objects for a more realistic dust distribution. For a test bed these models were applied to the ERO HR10. It was confirmed that HR10 is a dusty starburst galaxy. Only a model of stars embedded in dust with an extinction of $A_{\rm v} = 1.65$ was found to provide an acceptable fit to the data (see Figure 1.15) supporting the results of Graham and Dey [1996].

This work lead Cimatti et al. [1998] to acquire $850\mu m$ data from the James Clerk Maxwell Telescope (JCMT) and $1250\mu m$ data from the Institut de Radioastronomie Millimetrique (IRAM) for HR10. The object was detected in both bands and synchrotron radiation emission was ruled out as the source of the emission using the constraints from radio observations [Graham and Dey 1996, Jones et al. 1997]. It was concluded that the source of the flux in these bands was from thermal dust emission which corresponds to an inferred star-formation rate (SFR) of $570 - 2250\ M_{\odot}\ {\rm yr}^{-1}$, far larger than local ultra-luminous infrared galaxies (ULIRGs). At the time, this was a surprising result for researchers of global star-formation history (SFH) which, until then, had been investigated via rest-frame ultraviolet (UV) emission. The problem was highlighted by the fact

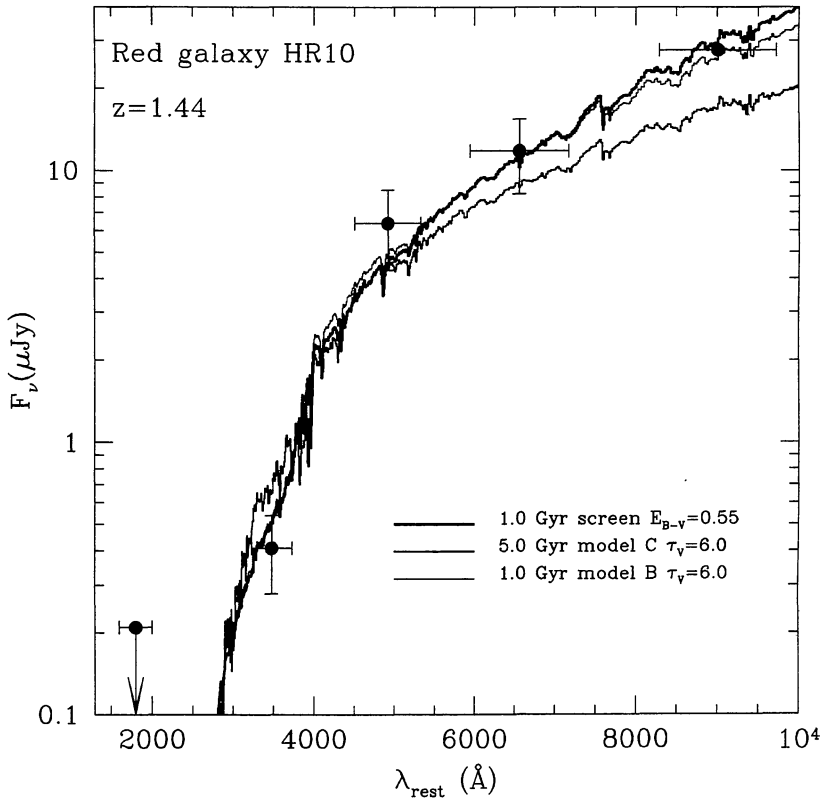

Figure 1.15: The rest-frame UV-optical SED of HR10 (data points from Graham and Dey [1996]). The 3 curves are synthetic stellar spectra extincted by different dust models Cimatti et al. [1997]. Model B represents a spherical dust cloud of constant density encasing the stellar population whereas in Model C the dust density follows the same radial distribution as the stellar population.

the SFR of HR10 derived from the UV is $\sim 1 M_\odot$ yr^{-1}, and from Hα $\sim 80 M_\odot$ yr^{-1}, both of which are at least an order of magnitude below that inferred from the far infrared (FIR). This illustrates the importance of multi-wavelength observations in gaining a full census of the star-formation rate density as a function of redshift. Figure 1.16 is an example of the impact sub-mm observations had on the study into star-formation rate density at high-redshift.

Pozzetti and Mannucci [2000] made the first attempt to use photometric colours to split the high-redshift population of EROs into old quiescent, and dusty star-forming galaxies. Using the fact that old galaxies have a strong 4000Å break, which is shortward of the J-band ($1.2\mu m$) for galaxies at $1 < z < 2$, whereas dusty star-forming galaxies

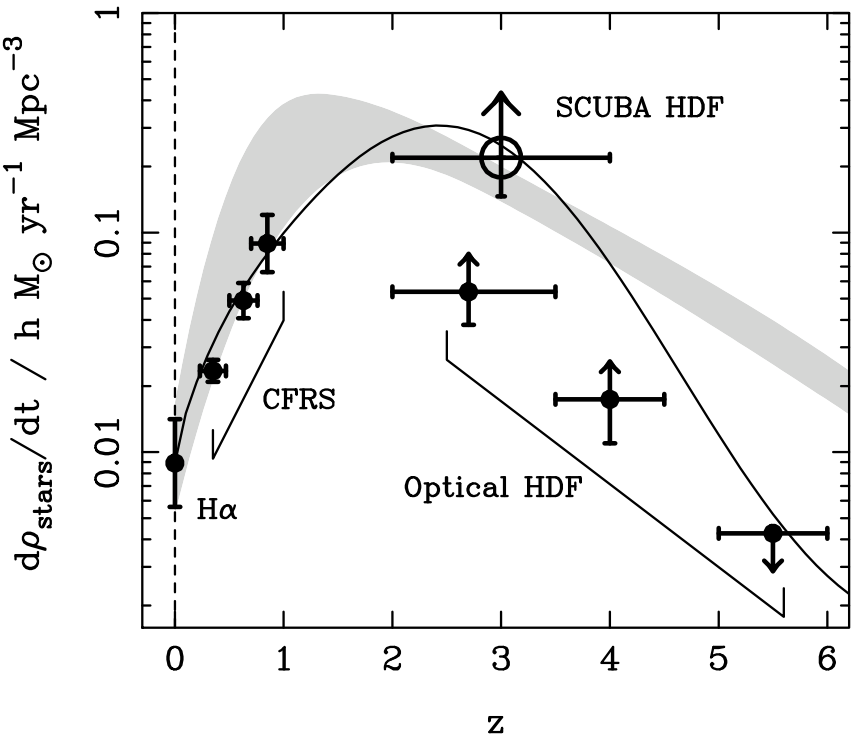

Figure 1.16: The global star-formation history of the universe including the information from SCUBA galaxies [Hughes et al., 1998]. The points labelled CFRS are from the Canada-France Redshift Survey of Lilly et al. [1996], the optical HDF data points are from Madau et al. [1996]. The local data was inferred from local emission-line galaxies from Gallego et al. [1995]. The shaded region shows the prediction (assuming h = 0.65) due to Pei and Fall [1995] who argued using the observed column densities in QSO absorbers, plus the low metallicities in these systems, that the star-formation rate must have peaked between $z = 1$ and $z = 2$. The solid line illustrates what would happen if the star-formation rate tracked the total output of radio-loud AGN [Dunlop, 1998].

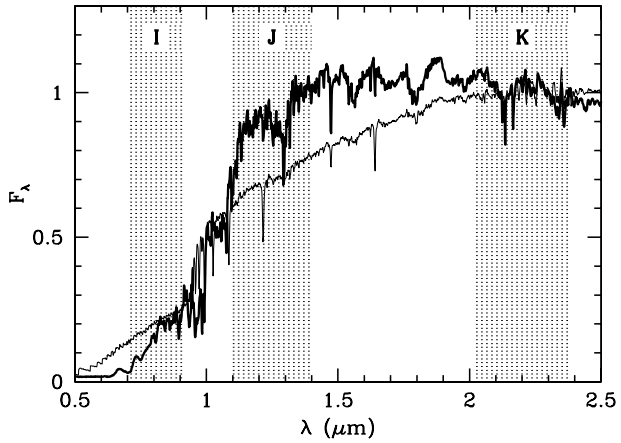

Figure 1.17: Spectra from an old elliptical (thick line) and a dusty starburst (thin line) at $z = 1.5$ [Pozzetti and Mannucci, 2000]. The position of the I, J and K filters are shown. Both spectra have been computed using the Bruzual and Charlot [1993] model (GISSEL 1999). The thick line is a simple stellar population with an age of 15 Gyr, while the thin line shows the spectrum resulting from a constant star formation rate over 1 Gyr when reddened to $E(B-V) = 0.8$ by a screen of dust described by the Small Magellanic Cloud (SMC) law. It is seen that, while the $I - K$ colour selects both types of object, the $J - K$ colour can distinguish between them.

have a smoother drop off in the flux at bluer wavelengths (see Figure 1.17).

Using spectra of local galaxies redshifted out to $z = 1 - 2$ and spectral synthesis models, Pozzetti and Mannucci [2000] divided the $J - K$ vs $i - K$ plane into regions where they expect passively evolving and dusty starburst EROs to be located. This can be seen in Figure 1.18 with passive galaxies defined by $(J-K) > 0.36(I-K)+0.46$ and $I-K > 4$ and dusty starbursts defined as $(J-K) < 0.36(I-K)+0.46$ and $I-K > 4$. Pozzetti and Mannucci [2000] deduced similar criteria for the $J - K$ vs $R - K$ plane with the population divider defined as $(J - K) = 0.34(I - K) + 0.19$ with $R - K > 5.3$ (all photometric magnitudes quoted here use the Vega system).

Using the spectra from the K20 Survey (see Section 1.6.1) and photometry from the GOODS Field, Daddi et al. [2004a] defined another colour-colour plane method (the so-called BzK selection technique) to select starburst and passive galaxies in the redshift interval $1.4 < z < 2.5$. The selection criteria is based on the fact that old galaxies will sit in the top right corner of the BzK colour plot because they have red continuum,

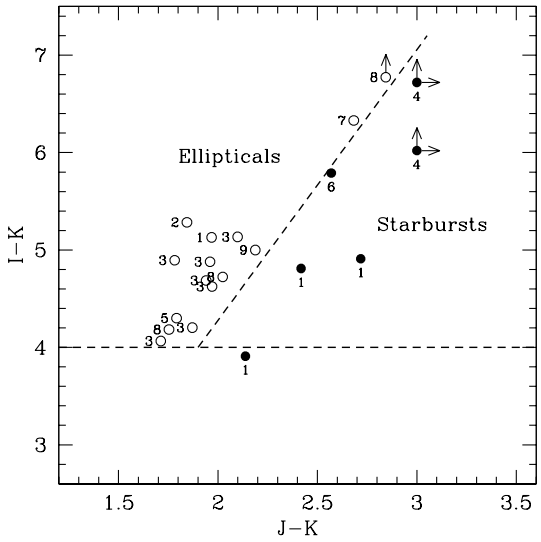

Figure 1.18: The $(J-K)$ versus $(i-K)$ diagram and selection technique to divide passive and star-forming EROs from Pozzetti and Mannucci [2000]. Empty dots are galaxies classified as elliptical, solid dots are dusty starbursts. When necessary, data were transformed into the filter system in use (Cousins I and Bessel & Brett J and K). See Pozzetti and Mannucci [2000] for the references for the numbered data.

due to breaks and absorption features in the rest-frame range 2500-3000Å and a strong 4000Å break, i.e. red colours in the observed $B-z$ and $z-K$ colours. A passive galaxy is defined as $BzK < -0.2$ and $z-K > 2.5$ where $BzK = (z-K)-(B-z)$. All photometric magnitudes here are based on the AB system. The BzK selection criteria are presented in Figure 1.19.

By comparing the multi-wavelength data available for HR10 (a dusty star-burst), LBDS 53W091 and LBDS 53W069 (both old galaxies) Stern et al. [2006] showed that the SEDs are basically indistinguishable using photometry blueward of 10μm in the rest-frame. Moreover, from SED fits Stern et al. [2006] found all 3 galaxies to be massive, $3-6\times10^{11}M_{\odot}$, and a few Gyrs in age. However, HR10, the only dusty starburst of the three, is the only one to be detected in $24\mu m$. Stern et al. [2006] therefore concluded that you need either longer wavelength photometry or deep spectroscopy to distinguish between old passively evolving, and dusty star-forming EROs.

Yan et al. [2004] went on to use Spitzer 24μm data along with R- and K-band imaging in the ELAIS N1 field of the Spitzer First Look Survey (FLS) to put constraints

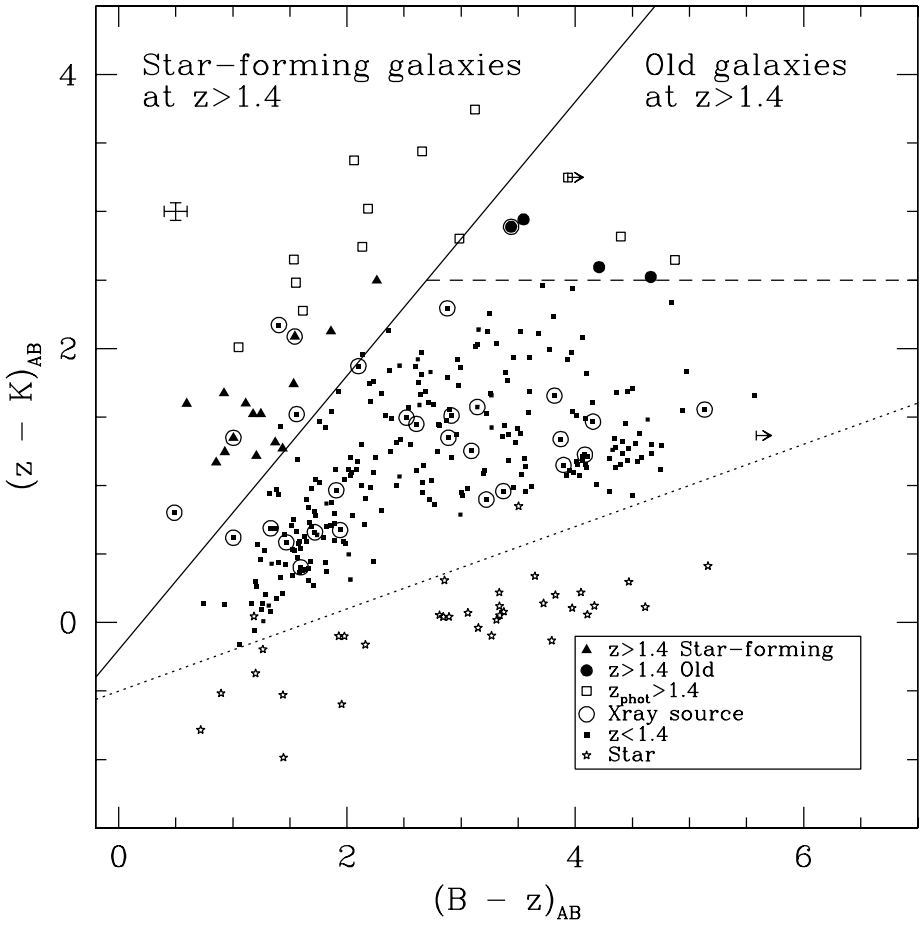

Figure 1.19: Two-colour $(z-K)$ vs. $(B-z)$ diagram for the galaxies in the GOODS area of the K20 survey [Daddi et al., 2004a]. Solid symbols represent galaxies with $z_{spec} > 1.4$, triangles represent galaxies with features typical of young star-forming systems [Daddi et al., 2004b], circles are for galaxies with old stellar populations [Cimatti et al., 2004]. Empty squares are objects with no spectroscopic redshift but $z_{phot} > 1.4$. Sources detected in the X-ray catalogs of Giacconi et al. [2002] and/or Alexander et al. [2003] are circled. Stars show spectroscopically identified galactic objects. The diagonal solid line defines the region $BzK = (z-K)-(B-z) = 0.2$. The horizontal dashed line further defines the region $z - K > 2.5$. The error bar located in the top left part of the diagram shows the median error in the $(z - K)$ and $(B - z)$ colors of objects at $z > 1.4$ (either photometric or spectroscopic). The dotted diagonal defines the region occupied by stars.

on the dusty star-forming to passively evolving galaxy fraction at $z = 1 - 2$. Down to a limit of $K_s < 20.2$(Vega), Yan et al. [2004] found that $50\% \pm 6\%$ of the EROs have 24μm detections. Similar to Cimatti et al. [1998] they also find that a significant fraction of the ERO population are LIRGs or ULIRGs. Using a starburst timescale derived from local LIRGs and ULIRGs, $\sim 10^8$yr, the mass of the 24μm detected sources are in the range $(5 \times 10^9) - (2 \times 10^{10}) M_{\odot}$. Yan et al. [2004] suggest that, within the hierarchical galaxy formation paradigm, these observations explore the massive galaxy population going through a transitional period of merger driven star-formation, with the passive EROs representing the sub-sample that have already completed the transition (an idea first proposed by Kormendy and Sanders [1992]).

With the use of multi-wavelength data and a deep radio map from the Very Large Array (VLA) Smail et al. [2002] investigated the characteristic of EROs at $z \sim 1$. Smail et al. [2002] selected their EROs as galaxies that are brighter than $K = 20.5$(Vega) and have $R - K > 5.3$(Vega), based on the definition from Pozzetti and Mannucci [2000]. This gave Smail et al. [2002] a sample of 68 EROs. They make the point that using the alternative definition from Pozzetti and Mannucci [2000], $I - K > 4$, yields an ERO sample of 99 objects. Twenty-one of the 68 (31%) objects in the ERO sample have detected radio emission above a 3σ limit of 12.6 μJy. The median K-band magnitude of the radio detected and undetected are nearly identical at $K = 19.66 \pm 0.2$ and $K = 19.66 \pm 0.09$ respectively. The brightest ERO in the radio detected sample has a flux of 200μJy, therefore they concluded that the upper limit of the radio luminous AGN within the ERO sample is 2%.

Additionally, Smail et al. [2002] searched for counterparts of their ERO sample in 49.4ks XMM-Newton/EPIC X-ray image. None were found down to an unabsorbed X-ray emission limit of 4×10^{15} ergs s^{-1} cm $^{-2}$ in the 2-10 KeV band. Moreover, using the K-band imaging Smail et al. [2002] morphologically classified 30 galaxies of the ERO sample, 11 of the radio detected subsample and 19 of the radio undetected subsample. The sample was classified simply in to one of three groups; compact/regular, disky/disturbed or too faint to classify. In the radio detected subsample the population split was 0%:82%:18% whereas in the radio undetected subsample the split was 29%:29%:42%. The split for the whole ERO sample is 18%:50%:32%. The radio de-

tected sample have a higher fraction of irregular galaxies and the largest portion of the radio undetected sample are compact. Smail et al. [2002] used the photometric redshift code HYPERZ [Bolzonella et al., 2000] to fit the ERO population, classifying the resulting SED fits as either dusty starburst or evolved. They estimate that 20-45% of the radio undetected sample are dusty starbursts and conclude that $30-60\%$ of the whole ERO sample are dusty starbursts with a median photometric redshift of $z = 1.0 \pm 0.3$. Smail et al. [2002] also concluded that half of the radio detected sources are ULIRGs and >16% of the ERO population brighter than $K > 20.5$ are LIRGs.

All the attempts over the last decade to constrain the ratio of EROs between passive evolving and dusty star-forming galaxies at high-redshift have indicated a ratio of approximately 1:1 for galaxies $z > 1$, depending of sample selection (see Section 5.8 for a selection of these results).

Once the dusty/passive fraction has been determined, it is possible to investigate what contribution EROs make to the cosmic star formation history. This is an important issue as many techniques to select star-forming rely on looking for UV emission which is absorbed in these dusty galaxies.

The separation of the different galaxy populations by different search techniques in a star-formation rate-extinction plane is illustrated in Figure 1.20 from Mannucci et al. [2002]. By assuming that the burst of star-formation in $z > 1$ dusty EROs occurred between $z = 1-1.5$, and using a cosmological parameter suite of $H_0 = 70$ kms^{-2} Mpc^{-1}, $\Omega_m = 0.3$ and $\Omega_\Lambda = 0.7$ Mannucci et al. [2002] roughly estimated the star-formation density of dusty EROs as 0.03 $M_\odot yr^{-1}Mpc^{-3}$. This is similar to that found for Lyman Break galaxies at higher redshift (e.g. Steidel et al. 1999).

1.5.2 The Size-Mass Relation at High-redshift

There is evidence that these massive galaxies at $z > 1$ have different physical properties to their local counterparts. Over the last half decade there has been a significant debate over the size evolution of early-type galaxies (ETGs) since small effective radii at high-redshift were first noted by Daddi et al. [2005b]. Shen et al. [2003] presented the local stellar mass-size relation using the SDSS data and found that radii increased with luminosity and stellar mass for both early and late type galaxies. The local ETGs

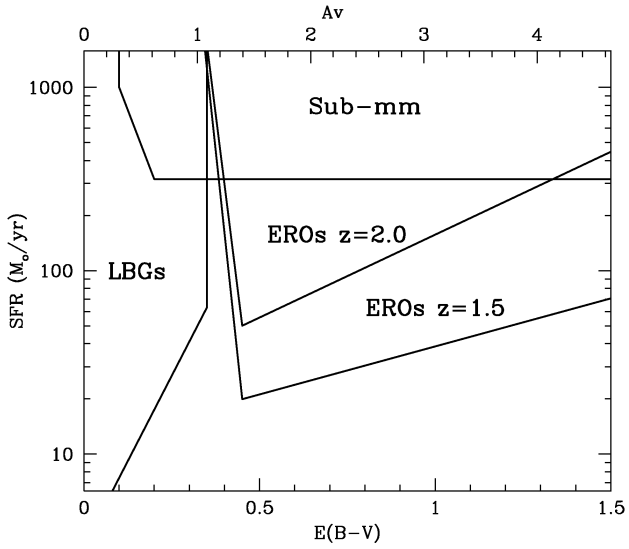

Figure 1.20: A star-formation rate-extinction plane from Mannucci et al. [2002] showing the regions that can selected by various search techniques. Submm studies select galaxies with any extinction but only high star-formation rates. Lyman break galaxies must have $E(B-V) \lesssim 0.3$ but can have any SFR. The ERO technique covers $E(B-V) > 0.3$ and down to $SFR \sim 20 M_{\odot} \mathrm{yr}^{-1}$. The edges are only indicative as they depend on telescope and instrument, the integration time, dust temperature and redshift. These method are based on continuum detections not emission lines.

showed a steeper relation than of the late types, indicating that size was not just a function of mass but that mass assembly history must also play a role (see Figures 1.21 and 1.22).

Figure 1.23 shows how the 10 most massive galaxies in the MUNICS survey from Trujillo et al. [2006a] sit below the local size-mass relation (solid black line). Over the last few years many other studies [e.g. Trujillo et al. 2006a, Trujillo et al. 2006b, Trujillo et al. 2007, Longhetti et al. 2007, McGrath et al. 2008, Buitrago et al. 2008] have also found ETGs at high-redshift to have smaller effective radii than similar mass galaxies in the local Universe. As a consequence, it appears that there must be processes in place that increase the size of ETGs from $z \sim 1.5$ to $z = 0$ without considerably increasing their mass. However, these processes (or possibly just process) are far from being understood.

Some authors believe that the observed effect is due to errors in radii estimation

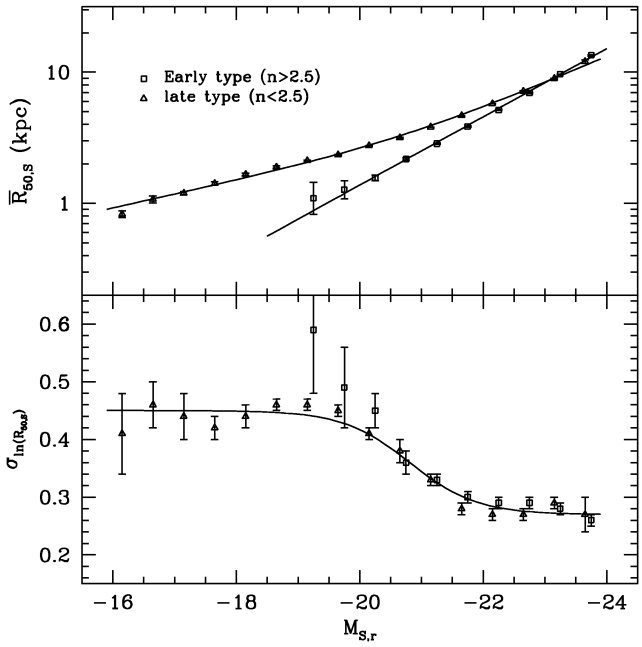

Figure 1.21: The top panel shows the relation between r-band absolute Sérsic magnitude for early- (squares) and late- (triangle) type galaxies in the local SDSS data. Galaxies are classified in relation to their Sérsic index n, $n > 2.5$ for early-types and $n < 2.5$ for late-types. The lower panel shows the scatter on InR for the whole sample as a function of r-band absolute Sérsic magnitude [Shen et al., 2003].

from the possible presence of central nuclear activity that affects the profile fits, or due to a strong morphological K-correction (e.g. Daddi et al. 2005b). Errors could also occur in the stellar-mass estimation at high-redshift which relies upon estimates from photometric fits (e.g. Tonini et al. 2010). It is clear that spectra have an important role to play in confirming if the stellar-mass estimates are inaccurate, with the added possibility of determining a dynamical mass that is not dependent on particular stellar population models. Other authors present astrophysical reasons for the evolution, with ideas ranging from the removal of cold gas from the central regions of the galaxy resulting in a redistributed stellar population [Fan et al., 2008], to the accretion of weakly bound stellar material (minor mergers) [Naab et al., 2009]. The two differing ideas from Fan et al. [2008] and Naab et al. [2009] can be tested with velocity dispersion measurements of high-redshift ellipticals. Both physical processes account for the size evolution, but the evolution of the velocity dispersion for these two scenarios is very different. The

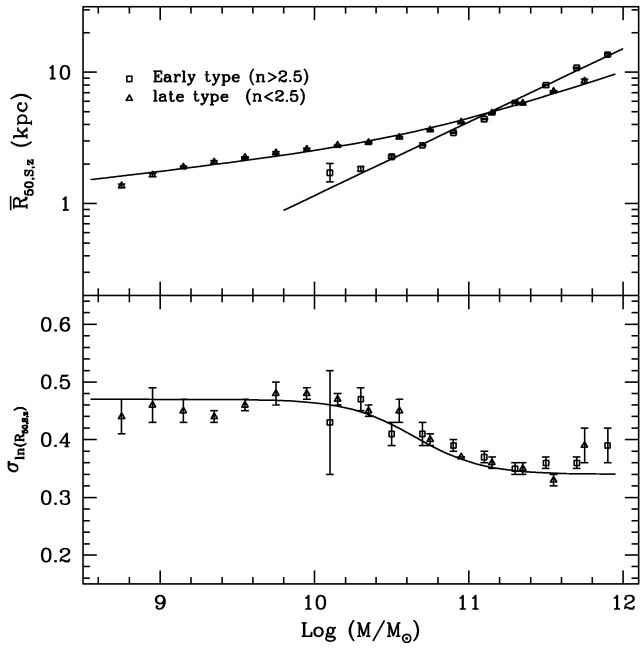

Figure 1.22: The top panel shows the relation between stellar mass for early- (squares) and late- (triangle) type galaxies in the local SDSS data. Galaxies are classified in relation to their Sérsic index n, $n > 2.5$ for Early types and $n < 2.5$ for late types. The lower panel shows the scatter on InR for the whole sample as a function of stellar mass Shen et al. [2003].

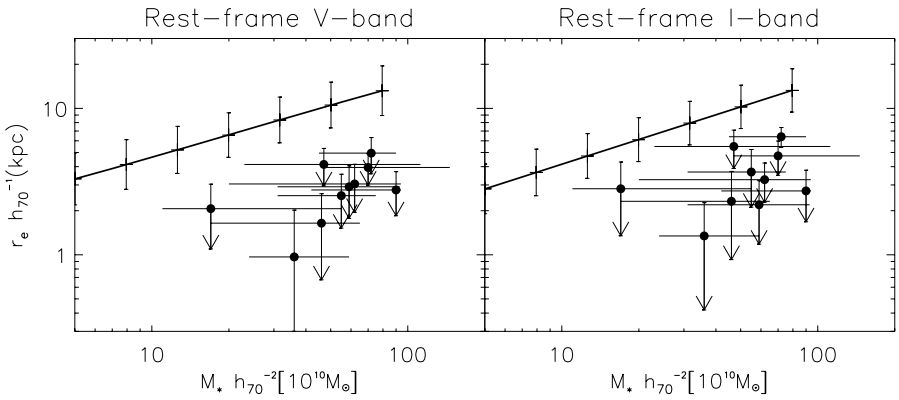

Figure 1.23: The stellar mass-size relation in rest-frame V and I-bands from Trujillo et al. [2006a]. The points with errors bars represent the 10 most massive galaxies in the MUNICS survey and the linear relation is the local relation from SDSS data Shen et al. [2003].

idea of the redistribution of stellar mass from Fan et al. [2008] should see the central velocity dispersion decrease by a factor of ~ 2 compared to equivalent present-day massive galaxies, whereas the minor merging process suggested by Naab et al. [2009] would only show a decrease of at most 20-30% since $z \sim 2$ [Hopkins et al., 2009].

Cappellari et al. [2009] estimated the velocity dispersion for two of the high signal-to-noise individual spectra from the GMASS survey (see Section 1.6.3), and the stack of 13 passive galaxies selected from the GMASS sample [Cimatti et al., 2008]. A near one-to-one between stellar and dynamical mass is found. The velocity dispersion of these galaxies is found to be in agreement with local ETGs.

More recent studies are now finding more normal ETGs, that sit on the local size-mass relation, at high-redshift [Saracco et al. 2009, Mancini et al. 2010] leading to the conclusion that not all high-redshift ETGs undergo dramatic size evolution. Saracco et al. [2009] showed that a sample of 32 ETGs, selected from HST-NICMOS (Near Infrared Camera and Multi-Object Spectrometer) data, could be split into two distinct populations: ETGs with old, evolved stellar populations (oETGs) and ETGs with a younger stellar population (yETGs). It was shown that pure luminosity evolution could map the yETG sample at $z \sim 1.5$ to the local luminosity-size relation from Shen et al. [2003], but the oETGs sit below the local relation. The oETGs follow a relation with the same slope as the local relation but with radii a factor of 2.6 ± 0.5 smaller for an equivalent stellar-masses. Saracco et al. [2009] calculated that if the stellar-masses were overestimated by a factor of two, the radii would still be a factor of 1.7 below the local relation and to bring the galaxies onto the local relation their stellar mass would have to be overestimated by a factor of six, which can not be accounted for by model choice.

After dividing a sample of forty-one $2 < z < 3.5$ galaxies from the FIRES MS 1054 field into passive and star-forming Toft et al. [2007] found that even though both sub-samples have radii smaller than their local mass counterparts, the star-forming galaxies were only, on average, a factor of ~ 2 smaller, whereas the passive subsample were a factor of ~ 5 smaller. This gives evidence for a link between the size of a galaxy and its star-formation activity. Evidence of this had previously been noted by Zirm et al. [2007], who had found $z \sim 2.5$ star-forming galaxies to sit on the local size-mass relation, whereas their quiescent companions sat below it (see Figure 1.24).

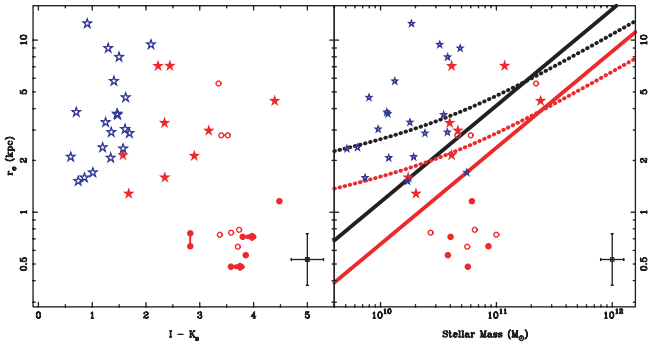

Figure 1.24: Left panel: Half-light radius vs. observed $I - Ks$ color for the star-forming (red stars) and quiescent (filled red circles) distant red galaxies (DRGs), and star-forming lyman break galaxies (LBGs) (blue stars) in the HDF-S. The open red circles are the quiescent $z \sim 1.8$ galaxies from Daddi et al. [2005b]. Two of the passive sources are undetected in I and are therefore shown as lower limits (arrows). The error bar in the bottom right is representative of the fits to the quiescent galaxies. Right panel: Half- light radius vs. stellar mass with the same symbols. The two sets of overplotted lines are the size-mass relationships derived by Shen et al. [2003] for early-type (black solid line) and late-type (black dotted line) galaxies in the local universe and redshifted to $z = 2.5$ using the inferred size-redshift evolution for $M > 3 \times 10^{10} M_{\odot}$ galaxies from Trujillo et al. [2006a] (red lines).

In contrast, Hopkins et al. [2009] argues that the profile fitting that recovers the radii of the high-redshift galaxies could be biased. They show there is a tendency to underestimate the size of massive ETGs at high-redshift due to their large effective radii and Sèric indices. Through simulations, Mancini et al. [2010] showed agreement with these results, and also points out that ETGs are not perfectly Sèrsic.

Mancini et al. [2010] took the 12 K-band brightest and most massive objects from the COSMOS field at $z \geq 1.4$ and found that 9 of them sat on the local size-mass relation. Combining their results with previous work done in the field they find a evolution of $R_e(z = 0)/R_e(z)$ with respect to mass. The most massive object have $R_e(z = 0)/R_e(z) = 1$, and it increases to 2-4 for lower masses, giving further evidence for down-sizing.

Moreover, evidence has recently emerged suggesting that there is also a population of these ultra-compact objects in the local Universe [Valentinuzzi et al., 2010a]. Using the WIde-field Nearby Galaxy-clusters Survey (WINGS)[Fasano et al., 2006] Valentinuzzi

et al. [2010a] found that a significant fraction, 22%, of the mass range $3 \times 10^{10} \leq M_{\star}/M_{\odot} \leq 4 \times 10^{11}$ of the local cluster massive galaxy population are as dense as the the compact high-redshift galaxies mentioned above. Valentinuzzi et al. [2010a] also finds that galaxies with older stellar populations have, on average, a lower effective radius. They conclude when this age factor is taken into account no size evolution is needed from $z = 0 - 2$.

Similarly using the ESO Distant Clusters Survey (EDisCS) Valentinuzzi et al. [2010b] found that 41% of distant cluster galaxies with $M_{\star} \sim 4 \times 10^{10} M_{\odot}$ are superdense galaxies with similar properties to those found in the WINGS survey. They found the median size of cluster galaxies at $z \sim 0.7$ are only 1.18 times smaller than the local median, concluding very modest size evolution over this epoch.

In terms of number density, based on 34 ETGs with $0.9 < z_{spec} < 1.92$ from GOODS-South data, Saracco et al. [2010] found that the population of compact ETGs at high-redshift does not differ from that in the local Universe.

More recently with the use of Keck spectroscopy Newman et al. [2010] investigated the size evolution with respect to the velocity dispersion and dynamical mass of 17 morphologically-selected field spheroidals at $1 < z < 1.6$. Newman et al. [2010] found very little size evolution over the lookback time of ~ 9.5 Gyrs from $z = 0 - 1.6$. For the highest mass galaxies, $\log(M_{dyn}/M_{\odot}) > 11$, they found a required size evolution of ~ 2 and much less evolution for the less massive galaxies. If the massive compact galaxies seen at $z > 2$ [e.g. van Dokkum et al. 2008] are progenitors to these galaxies at $z \sim 1.5$ then very rapid size growth is required.

It is clear that the evolutionary path of ellipticals galaxies from $z \sim 1$ to $z = 0$ is still far from being resolved and is a very interesting area of galaxy evolution research that needs to be tackled if galaxy mass assembly is going to be fully understood.

1.6 Spectroscopic Observations of Near-IR Selected Galaxies at $z > 1$

The early examples of spectroscopy of K-band selected galaxies, discussed in Section 1.5, showed how important spectroscopy was towards gaining a thorough understand-

ing of the entire high-redshift Universe. The first spectroscopic survey of moderate size, down to a magnitude of $K = 20$(Vega) was completed by Cowie et al. [1996]. Cowie et al. [1996] obtained spectra for 393 objects over two Hawaii Deep Survey fields, covering an area of 26 arcmin^2. Through the use of the [OII] emission line and rest-frame UV luminosity (extrapolated from the K-band) they concluded that as you move to higher redshifts, massive galaxies have higher star-formation rates than their lower mass counterparts. This was the first piece of evidence of the downsizing effect discussed in Section 1.4. This differential evolution results in little change of characteristic luminosities of the K- and B-band luminosity functions, $K^\star$ and $B^\star$, from $z = 1$ to $z = 0$.

Cohen et al. [1999a] targeted 195 $K < 20$(Vega) objects over a 14.6 arcmin^2 field. The objects spanned a redshift range of $0.173 < z < 1.44$ with a median redshift of 0.58. The galaxies were split into 4 categories; emission (E), composite (C), absorption (A) and AGN (Q) as defined in Cohen et al. [1999b] (see Figure 1.25 for example of spectra from different classes). Class B is for extreme starburst galaxies but was incorporated into the E category. Cohen et al. [1999b] discovered that members of the same group had very similar SEDs i.e. the emission group (E) had blue UV and IR colours whereas the absorption group (A) had redder colours. This shows why photometric redshifts for samples with high quality photometry work well out to $z = 1$. The "absorption" galaxies were found to be more luminous in the IR than the "emission" galaxies.

Following on from these early spectroscopic studies of K-band selected galaxies, several larger-scale spectroscopic surveys have been conducted over the last decade. In the next three sections these campaigns are discussed.

1.6.1 The K20 Survey

The K20 Survey [Cimatti et al., 2003] was the first large K-band selected spectroscopic survey and was designed to investigate galaxy evolution in the range $0.5 < z < 1.5$. The targets were selected solely using a cut in K-band magnitude, $K < 20$(Vega), without any redshift prerequisites and spectra were obtained with FOcal Reducer and low dispersion Spectrographs 1 and 2 (FORS1 and FORS2) on the Very Large Telescope (VLT) as an ESO Large Programme. The K-Band was used for selection as it selects galaxies by mass up to $z \sim 2$. The $K < 20$(Vega) limit is equivalent to mass limits of

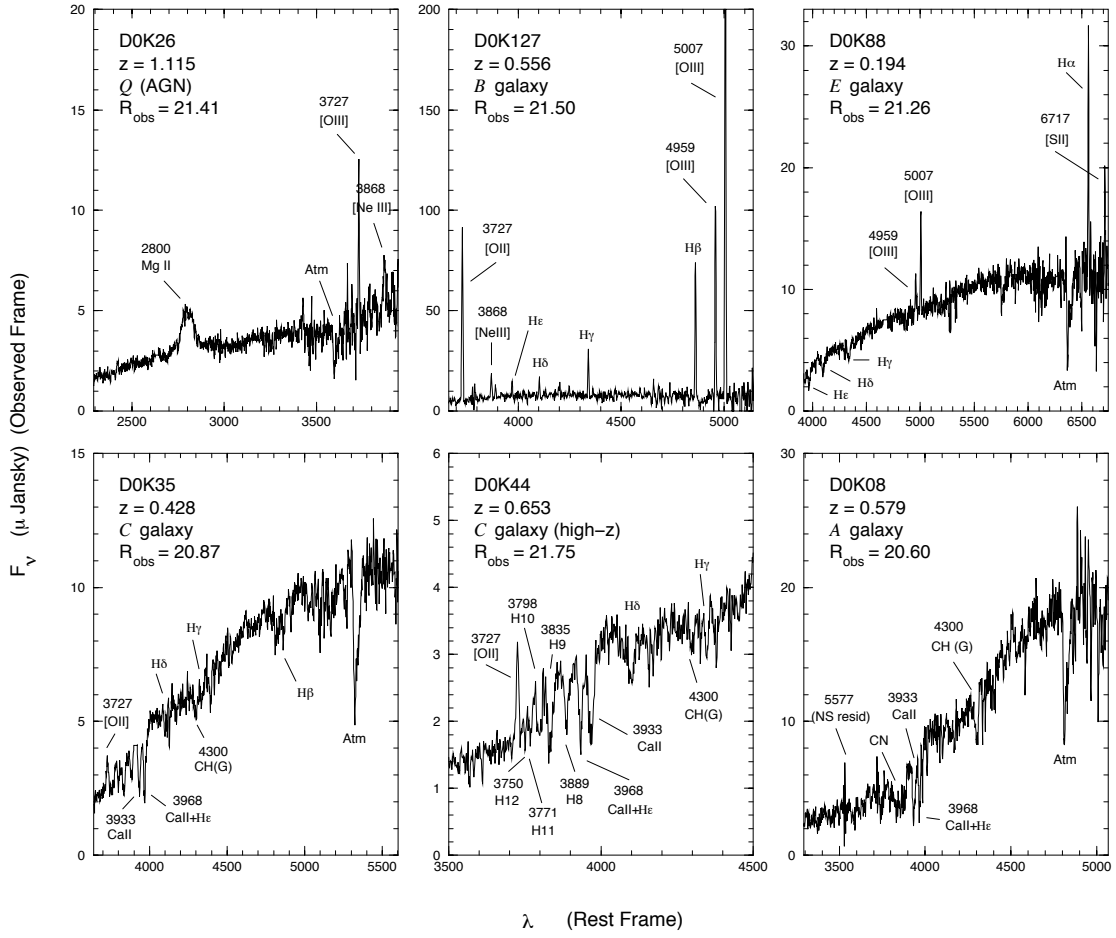

Figure 1.25: Examples of the galaxy classes defined by Cohen et al. [1999b]. E is for emission line galaxies, B is an extreme starburst galaxy, A is an absorption line galaxy, C is a composite galaxy, defined as intermediate between the emission and absorption classes and Q is an AGN. The spectrum of a high-redshift C galaxy is also shown.

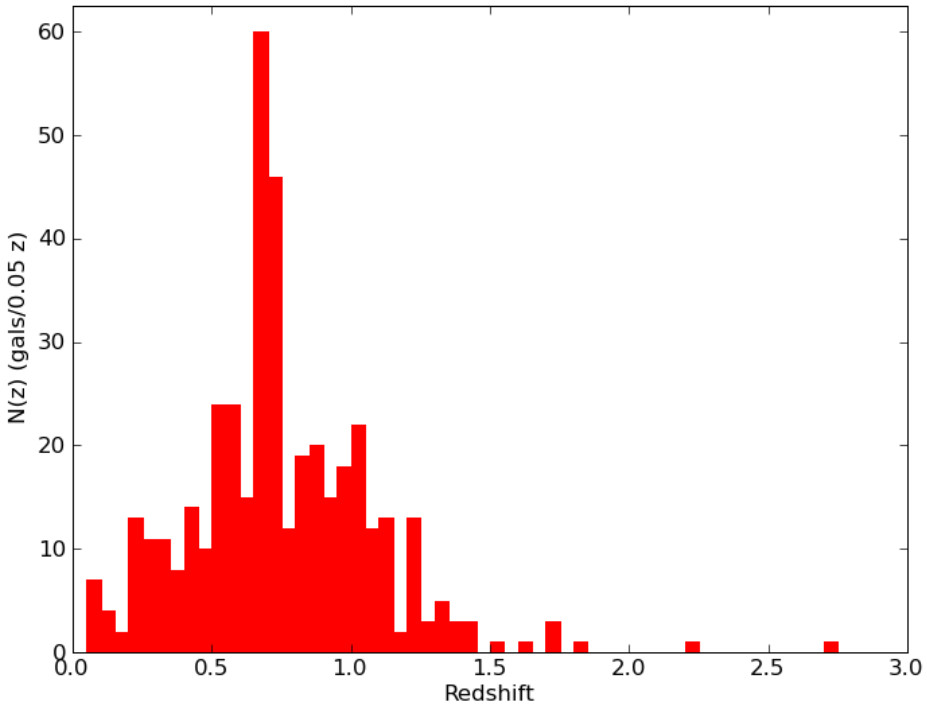

Figure 1.26: The spectroscopic redshift distribution of the K20 survey constructed with data from Cimatti et al. [2003]. The spectroscopic completeness for the complete sample was 87%.

$\simeq 1 \times 10^{10} M_{\odot}$ and $\simeq 4 \times 10^{10} M_{\odot}$ at redshifts $z = 0.5$ and $z = 1.0$ respectively.

The project had two target fields, a sub-field of the Chandra Deep Field South (32.2 arcmin^2) and a field centred on the QSO 0055-269 at $z = 3.6$ (19.8 arcmin^2), giving a total area of 52 arcmin^2. The spectra had integration times between 15 minutes and 8 hours, depending on the brightness of the sources and the survey was conducted on 17 nights over the 2 year period 1999-2000. The simple K-band cut produced 546 objects in the redshift range of $0.05 < z < 2.75$, with a median redshift of $<z> \sim 0.75$, which is below the redshift of the main ERO population. Their spectroscopic completeness was 94%, 92% and 87% at $K < 19.0$, 19.5 and 20.0 respectively. Excluding broad-line AGN and stars the survey obtained 480 spectra with 417 spectroscopic redshifts (see Figure 1.26).

Using data from the K20 survey Cimatti et al. [2002a], examined the ERO popula-

tion at $z \sim 1$. For the $K < 19.2$(Vega) sample Cimatti et al. [2002a] found the surface density of EROs to be 0.88 ± 0.13 arcmin^{-2}, which is a factor of 4 and 10 below that estimate by the hierarchical merging models of Firth et al. [2002] and Smith et al. [2001] respectively. The ratio of old EROs to dusty star-forming EROs was estimated at approximately 1:1. Including errors, Cimatti et al. [2002a] estimated the surface density of old EROs to be $0.27 - 0.55$ arcmin^{-2}, which agrees with the pure luminosity evolution models of Daddi et al. [2000b] which assume $\tau = 0.3$Gyr and a minimum formation redshift of $z_f = 2.2$. Using the [OII] emission line and rest-frame UV continuum, Cimatti et al. [2002a] estimated that dusty star-forming EROs make up $\simeq 20\%$ to the global star-formation rate density of the universe at $z \sim 1$.

Pozzetti et al. [2003] found little evolution in the rest-frame J- and K-band luminosity function out to $z \sim 1.5$ and that red, early-type galaxies dominate the bright end at $z \sim 0.5$ and $z \sim 1.0$. Therefore Cimatti et al. [2002a] indicates that old and massive elliptical galaxies were already in place at $z \sim 1$ and, therefore, they should have formed their stars and assembled their mass at higher redshift. This was in contrast to the hierarchical merging paradigm where massive galaxies do not appear until lower redshifts.

Fontana et al. [2004] used the the K20 survey to study the GSMF as a function of redshift. Fontana et al. [2004] found there to be only small evolution of the GSMF and of the corresponding global stellar mass density out to $z \approx 1$. It was found that the evolution of objects around the local characteristic mass ($\sim 10^{11}$M$_\odot$) was complete by $z \sim 1$. An evolution in the nature of massive galaxies was also observed; at low redshift ($z \lesssim 0.7$) all the massive galaxies are either early-type or early-type with emission galaxies but as redshift increases a larger portion of the massive galaxies are star-forming galaxies.

Moreover, Fontana et al. [2004] found that the $M_\star/L_R$ (where L_R is the rest-frame R-band luminosity) is significantly larger for bright objects at low and intermediate redshift than it is for fainter sources. This implies a short time-scale and/or high formation redshift for the most massive systems and that the lower mass galaxies continue star-formation into later times. This, again, highlights the so-called downsizing effect.

Finally, using both ground based and HST imaging of the K20 survey, Cassata et al.

[2005] and di Serego Alighieri et al. [2005] found some evidence that the distribution of the effective radii of early-type galaxies was shifted to smaller sizes at high-redshift compared to the local distribution.

1.6.2 The Gemini Deep Deep Survey (GDDS)

The Gemini Deep Deep Survey (GDDS) [Abraham et al., 2004] was the next large spectroscopic survey to follow the K20 Survey and was designed to delve further into the redshift range $0.8 < z < 1.8$. The GDDS team selected galaxies using a slightly deeper cut in the K-band, $K < 20.6$(Vega), a colour cut, $I - K > 3.5$(Vega), to ensure the targets were EROs, and a redshift prerequisite of $z_{photo} > 0.8$. This makes the GDDS different from the K20 Survey since as well as a cut in the K-band magnitude it also invokes a photometric colour criteria. The survey was performed over four pointings of the Gemini Multi-Object Spectrograph (GMOS) on Gemini North (centred on SSA22, NOAODW-Cetus, NTT-Deep and LCIR 1511), adding up to over twice the area of the K20 survey. The exposure time between the fields varied from 5 to 25 hrs.

The data were taken between August 2002 and August 2003, and used a mask design algorithm weighted towards selecting targets that had photometry typical of passively evolving luminous red galaxies in the redshift range $0.8 < z < 1.8$. This meant that the GDDS observations sampled one in two galaxies with $22 < I < 24.5$ and $3 < I - K < 5$, but only one in seven of the remaining population ($K < 20.6$, $0.8 < z < 1.8$). The survey had a mean redshift of $<z> \sim 1.2$ and a spectroscopic completeness of 100% for $I < 22$ and 79% for the entire sample. In total the GDDS acquired 225 secure redshifts with 167 in the redshift range $0.8 < z < 2.0$. The redshift distribution for the survey can be seen in Figure 1.27

To put age constraints on the old high-redshift population McCarthy et al. [2004] took the 20 galaxies at $z > 1.3$ that showed signs of an old stellar population from the GDDS and fitted their spectra and B through K photometry to synthetic stellar population models. Each galaxy was best fitted by either an instantaneous burst model or one with a short e-folding time. McCarthy et al. [2004] found the median z, age, z_f and mass of these objects to be 1.49, 1.5 Gyr, 2.5 and $1 \times 10^{11} M_{\odot}$ respectively. The short e-folding times would imply a period of intense star-formation, 300-500 $M_{\odot} yr^{-1}$.

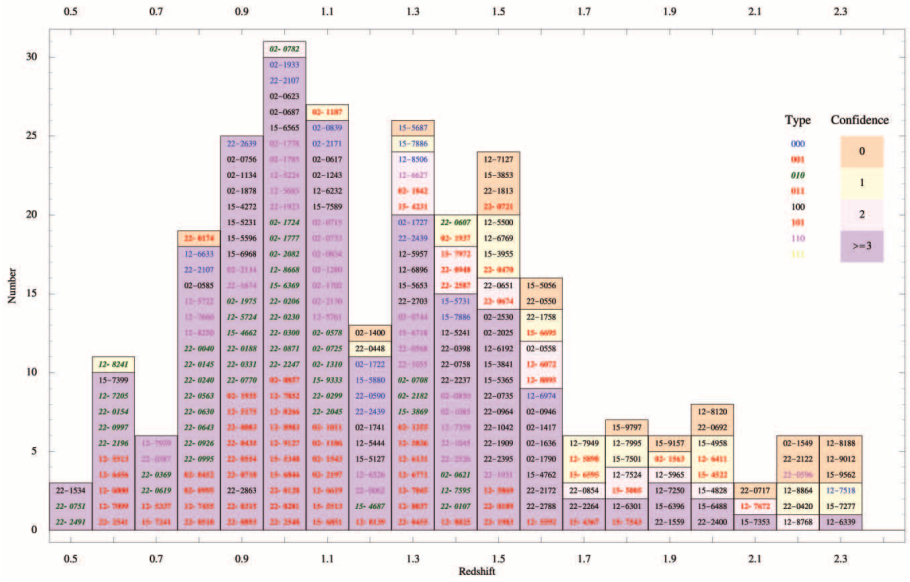

Figure 1.27: The spectroscopic redshift distribution of the Gemini Deep Deep Survey (GDDS). Bar colours indicate confidence in the redshifts, with 0 being the high confidence and a contamination free spectrum and confidence lowering and contamination increase with increasing number. Individual objects are labeled. An explanation of the class system can be found in Section 7.1.1.

From the mass and star-formation rates of these objects it was concluded that they are not related to the Lyman Break Galaxy (LBG) population at $z \sim 3 - 4$.

With the use of fifty-six $0.4 < z < 1.0$ star-forming galaxies Savaglio et al. [2005] detected a 6σ significant correlation between stellar mass and metallicity. The mass-metallicity ($M - Z$) relation is displaced from the $z \sim 0.1$ relation from SDSS data [Tremonti et al., 2004] towards either higher stellar masses or lower metallicities. For a fixed metallicity, galaxies at higher redshift are more massive than their local counterparts. The evolution in the $M - Z$ relation appeared stronger in low mass systems, indicating they were still under construction. Again, this result provided more evidence for the downsizing effect.

The Hδ Lick index gives information about recent star-formation within a galaxy. The Hδ index is only large when the stellar population is dominated by A type stars which only occurs in galaxies of an intermediate age. Using this information, along with the 4000Å break (D4000) as a tracer of a galaxy's age, Le Borgne et al. [2006]

studied the star-formtion history of massive galaxies at $z \sim 1$ using the GDDS sample. Le Borgne et al. [2006] concluded that the $z \sim 1$ galaxies with a small Hδ index and large D4000 experienced their last episode of star-formation at $z \geq 1.8$ and that the majority of their stars were in place before that. Given the large mass of these systems ($> 10^{10.2}$M$_{\odot}$) Le Borgne et al. [2006] implied that these systems must have gone through an intense period of star-formation at $z \geq 2$ matching the result found by McCarthy et al. [2004].

Using the GDDS sample Abraham et al. [2007] found that the fraction of the stellar mass density made up of massive system increased over the redshift range $0.8 < z < 1.7$ and by $z \sim 0.8$ the fraction of the global mass density within massive early-type systems was up to 80%, close to the local value. Abraham et al. [2007] therefore concluded that in this redshift range we are witnessing early-type galaxies becoming the dominant members of the high-mass end of the galaxy population.

1.6.3 The Galaxy Mass Assembly Ultra Deep Spectroscopic Survey (GMASS)

An enhancement of the K20 survey was the Galaxy Mass Assembly Ultra Deep Spectroscopic Survey (GMASS) [Kurk et al., 2009], whose aim was to probe massive galaxies in the range $1 < z < 3$. The field of study was one FORS2 mask in the GOODS South field. The parent GMASS sample, from which the spectroscopic targets were to be selected consisted of 1277 objects detected in the IRAC Spitzer $4.5\mu m$ image with $m_{4.5} < 23.0$(AB). The $4.5\mu m$-band traces the rest frame $1 - 2\mu m$ out to $z \sim 3$, which helps to select by mass more reliably than K-band imaging. The spectroscopic targets were selected from the parent sample with the additional constraints of $z_{phot} > 1.4$, $B < 26(AB)$ and $I < 26(AB)$. This gave 174 targets, which were split into a further 2 samples: blue ($B < 26.5$), to be observed with the 300V grism, and red ($I < 26.0$), to be observed with the 300I grism. The blue sample had exposure time between 12-15 hours while the red sample had exposure times between 15-30 hours. The GMASS team achieved an 85% robust redshift completeness.

Cimatti et al. [2008] extracted a sample of high-redshift passive galaxies using the Mg_{UV} feature [Daddi et al., 2005b] in combination with the rest-frame UV slope. This formed a sample of 13 passive high-redshift galaxies in the redshift range $1.39 < z < 1.99$

with a mean redshift of $z = 1.6$. Cimatti et al. [2008] fitted the 13 galaxies with three different sets of SED models, Bruzual and Charlot [2003], Maraston [2005a] and Charlot & Bruzual 2007 (private communication) (the Maraston [2005a] and Charlot & Bruzual 2007 models include the effect of TP-AGB stars), and found a consistent mean age of the dominant stellar population with all models of ~ 1.5 Gyrs which puts the peak formation redshift at $z \approx 2 - 3$. The mean stellar mass returned by the models was also consistent at $\sim 5 \times 10^{10} M_{\odot}$. Cimatti et al. [2008] made a template passive galaxy spectrum by average combining the 13 galaxies in the sample which equates to a 480hr exposure time composite which can be seen in Figure 1.28. With HST+ACS (Advanced Camera for Surveys) data the majority of the objects in the sample were morphologically classified as ETGs. The majority of the objects were found to have $R_e < 1.5$ kpc and sit below the local size-mass relation making them more compact than the local massive galaxies.

Cassata et al. [2008] studied the stellar mass versus $(U-V)$ rest-frame colour relation for 1021 galaxies in the GMASS sample out to redshift $z > 2$. It is found that the classical bimodality between red and blue galaxies is held out to $z = 2$. The red sequence at all redshifts was found to contain early- and late-type galaxies with the fraction of late-type galaxies increasing with redshift. They witnessed red galaxies with stellar mass $> 1.25 \times 10^{10}$ at $z > 2$, 25% of which are passively evolving with ages > 0.5 Gyrs giving formation epoch of $z > 3$.

1.7 The UKIRT Infrared Deep Sky Surveys (UKIDSS) Ultra Deep Survey (UDS) and UDSz

The latest large spectroscopic survey of K-band selected targets is a follow-up of the Ultra-Deep Survey (UDS), UDSz. The Ultra-Deep Survey (UDS) is part of the UKIRT Infrared Deep Sky Surveys (UKIDSS) being conducted with WFCAM on UKIRT and is the top tier of a wedding cake structure consisting of five surveys. The UDS is the deepest survey of the five and covers an area of 0.8deg^2 (100×100 Mpc at $z = 3$). Observations for the UDS began in September 2005 and the year one data release (DR1) had already reached 5-σ depths of $K_{AB} = 23.5$ and $J_{AB} = 23.7$ making it the

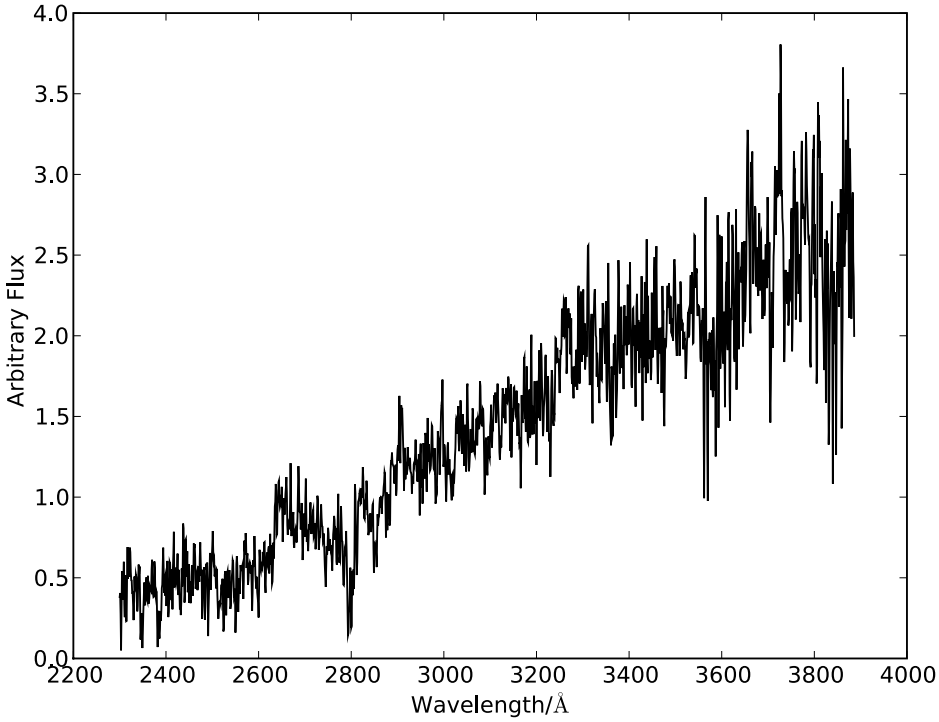

Figure 1.28: A composite passive galaxy spectrum from Cimatti et al. [2008] which was constructed by average combining the spectra of 13 galaxies in the sample, which equated to an exposure time 408 hrs

deepest near-infrared survey over such a large area. The current data release (DR8) reaches 5σ limits of $J = 25.0$, $H = 24.3$ and $K = 24.9$ and is supported by a wide range of multi-wavelength photometric data (see Section 2.1 for full details). This makes it the perfect target field for the next chapter of NIR selected spectroscopic studies. The work in this thesis is centred around the spectroscopic data acquired through the UDSz project. For full details on the UDS and a full description of the UDSz project please see Chapter 2.

Through the thesis a cosmology of $H_0 = 70\text{km}^{-1}\text{Mpc}^{-1}$, $\Omega_m = 0.3$ and $\Omega_\Lambda = 0.7$ is assumed and unless stated magnitudes are in the AB system.

1.8 Summary and Goals of the Thesis

Optical surveys alone were missing large populations of red galaxies at high-redshift; the advent of NIR detectors allowed for new understandings of the processes of galaxy formation and evolution in extra-galactic astronomy. NIR surveys unveiled an entirely new population of high-redshift, red objects, which were found to comprise of passively evolving and dusty star-forming galaxies. These galaxies have been a useful means to test ΛCDM cosmology as well as the accompanying semi-analtyical models of galaxy formation. The detection of massive high-redshift systems from deep K-band surveys has required new theories in galaxy formation and evolution. The physical characteristics of these massive systems have highlighted gaps in the astrophysics of galaxy evolution with massive ETGs appearing to sit below the local size-mass relation at high redshift. To help towards filling in some of the gaps in the understanding of galaxy evolution this thesis will exploit a unique K-band selected spectroscopic data-set. The main goals of the thesis are:

1. Using accurate stellar-mass estimates from spectrophotometric fitting of optical spectra, plus multi-wavelength photometry, to investigate the size-mass relation at $1.3 < z < 1.5$. The relation will be studied as a function of stellar-mass, specific star-formation rate and galaxy spectral type.

2. By utilising high quality spectroscopic data, velocity dispersions will be estimated for the largest single sample of $z > 1.3$ galaxies to date. With radii from deep K-band imaging the dynamical mass of this high redshift sample will be compared to what is observed locally. The dynamical masses will be used as a model independent test of the size-mass relation problem.

3. With rest-frame UV flux measurements, [OII] emission line fluxes, and $24\mu m$ detections, an estimate of the fraction of star-forming to passively evolving galaxies for K-band bright objects at high redshift will be made. Also a passive fraction for the ERO population will be calculated.

4. The known passivity of the spectroscopic sample will be used to test and optimise current photometric selection techniques for dividing the high redshift K-band

selected and ERO populations into passively evolving and star-forming galaxies. The optimised systems along with the latest UDS catalog (DR8) will be used to calculate the passive galaxy fraction for a range of depths in K-band magnitude.

5. Using the filter profiles from the new visible and infrared telescope VISTA and the SEDs of the spectroscopic sample acquired during the fitting process, photometric selection techniques will be developed for different filter sets. The optimised selection techniques well be applied to the first catalog from the new VIDEO survey to give an independent test of the estimated passive fraction.

6. Finally, the galaxy sample will be divided by stellar-mass, absolute K-band magnitude, SSFR and spectral type to study high signal-to-noise composite spectra of these different galaxy populations. These systems will be studied as a function of redshift and age (acquired from spectrophotometric fits). The evolution of spectroscopic features will be investigated as a function of age, stellar mass and specific star-formation rate.

Chapter 2

A Large ESO Spectroscopic Follow-up Programme in the UDS

2.1 The UKIRT Infrared Deep Sky Survey - Ultra Deep Survey

All the data used in this thesis is from the sky region covered by the UKIRT Infrared Deep Sky Survey (UKIDSS Lawrence et al. [2007]) Ultra Deep Survey (UDS). The UDS is the deepest of five UKIDSS surveys that form a wedding cake structure. It is centred on RA=02:17:48, Dec=-05:05:57 (J2000), covers an area of 0.8deg^2 and is the deepest large area near-IR survey to date. The near-IR data used here is from the eighth data release from the project (DR8) which has 5σ depths of $J = 24.9$, $H = 24.3$ and $K = 23.6$ in 2 arcsec-diameter apertures.

2.1.1 Accompanying Photometric Data

The UDS has a vast array of accompanying multi-wavelength data ranging from X-ray to radio. The UDS is covered by the Subaru/XMM-Newton Deep Survey (SXDS), a 1.3deg^2 deep optical survey performed with Suprime-Cam [Miyazaki et al., 2002] on Subaru. The SXDS data-set has provided broad-band photometry in the $BVRi'z'$ bands

with 5σ depths of $B = 27.6$, $V = 27.2$, $R = 27.0$, $i' = 27.0$ and $z' = 26.0$, within a 2 arcsec-diameter aperture.

The UDS also has $850\mu m$ submm data from the Submillimetre Common-User Bolometer Array (SCUBA) as part of the SCUBA Half Degree Extragalactic Survey (SHADES) Mortier et al. [2005],Coppin et al. [2006]. The other key dataset with regard to this thesis is the Spitzer Public Legacy Survey of the UKIDSS Ultra Deep Survey (SpUDS). This project provides deep InfraRed Array Camera (IRAC) images in all four bands ($3.6\mu m$, $4.5\mu m$, $5.8\mu m$ and $8\mu m$) and also Multiband Imaging Photometer for Spitzer (MIPS) $24\mu m$ data.

X-ray data in the UDS was obtained with the XMM-Newton satellite over 400-ks exposures in seven contiguous fields to a depth of approximately a few 10^{-15}ergs $\mathrm{cm}^{-2}\mathrm{s}^{-1}$. There is also deep 1.4 GHz radio data in the UDS from observations with the Very Large Array (VLA) Simpson et al. [2006].

The coverage of all of this data is shown in Figures 2.1 and 2.2. Figure 2.1 shows the data coverage within the UDS of the optical (Subaru), NIR (UKIRT), MidIR (Spitzer) and submillimeter (SCUBA) data. A size comparison between the UDS and similar but smaller area surveys Faint InfraRed Extragalactic Survey (FIRES) [Franx et al., 2000] and GOODS [Fosbury et al. 2001,Dickinson et al. 2003] are also shown. Figure 2.2 shows the X-ray data coverage (blue dotted circles) over the coverage of the NIR data (red square) and optical data (image cross).

2.2 UDSz - UDS Spectroscopic Follow Up

The primary motivation for a spectroscopic follow-up programme to accompany the multi-wavelength data already available in the UDS field was to determine the relationship between environment and galaxy properties at $z > 1$, specifically the emergence of the red-sequence, and to determine the build up of stellar-mass as a function of look-back time in order to directly test galaxy formation models. As already discussed, NIR surveys are ideal for selecting a complete census of massive galaxies at high redshift as they trace the optical light out to $z \sim 2$ which is a more reliable tracer of stellar mass than the rest-frame UV.

The UDS was awarded a Large Programme (hereafter referred to as UDSz) by the

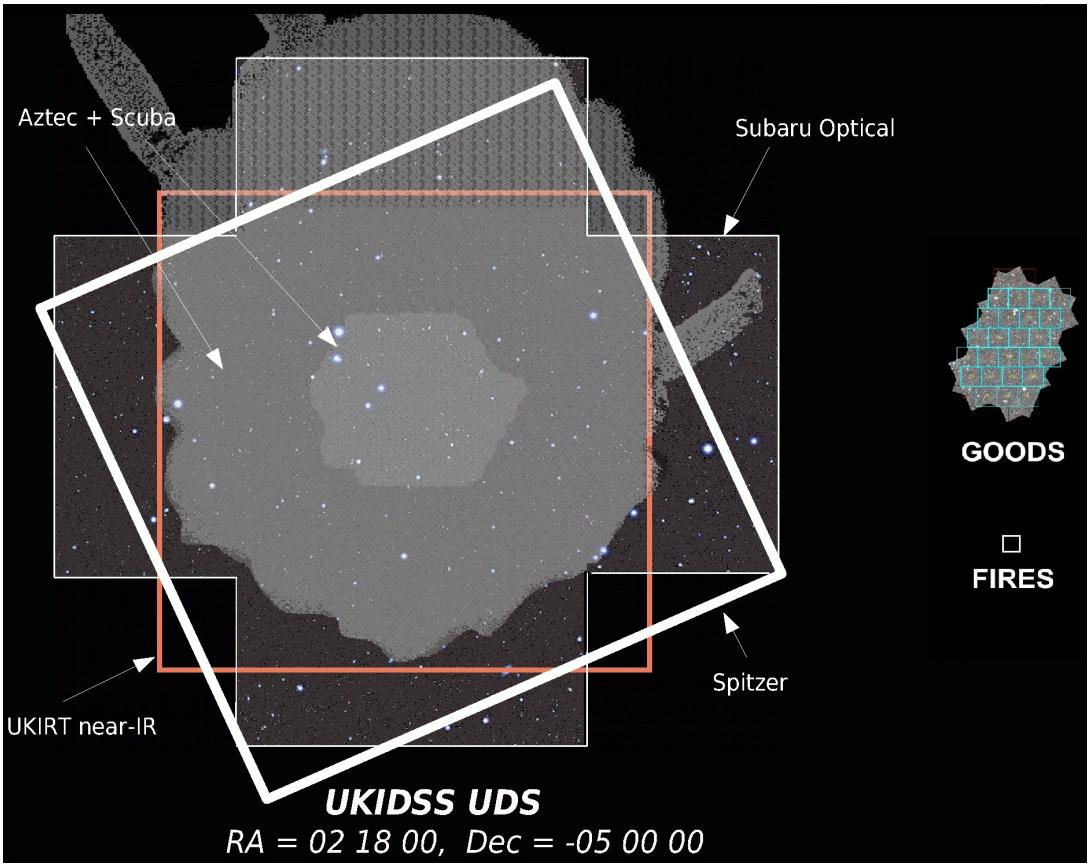

Figure 2.1: Coverage within the UDS of the optical (Subaru), NIR (UKIRT), MidIR (Spitzer) and submillimeter (SCUBA) data. A size comparison between the UDS and similar but smaller area NIR surveys Faint InfraRed Extragalactic Survey (FIRES) [Franx et al., 2000] and GOODS [Fosbury et al. 2001,Dickinson et al. 2003] are also shown.

European Southern Observatory (ESO) to spectroscopically follow up K-band selected targets with the Very Large Telescope (VLT). Omar Almaini from the University of Nottingham was the Principal Investigator (P.I.) for this project with Co Investigators (Co.Is) from Edinburgh, Bologna, Durham, Paris, Bristol, Liverpool John Moores, Imperial, Leiden, Sydney, Leicester and NAOJ. The primary target selection was designed to obtain spectra for a random 1 in 6 sampling of $K < 23$ galaxies at $z_{phot} > 1$ (with a control sample of approximately 500 galaxies with $z_{photo} < 1$, see Figure 2.3 for the photometric redshift distribution for the UDS $K < 23$ sample). The targets were split between the VIsible Multi-Object Spectrograph (VIMOS), for the brighter and bluer targets, and the FOcal Reducer and low dispersion Spectrograph 2 (FORS2) for the

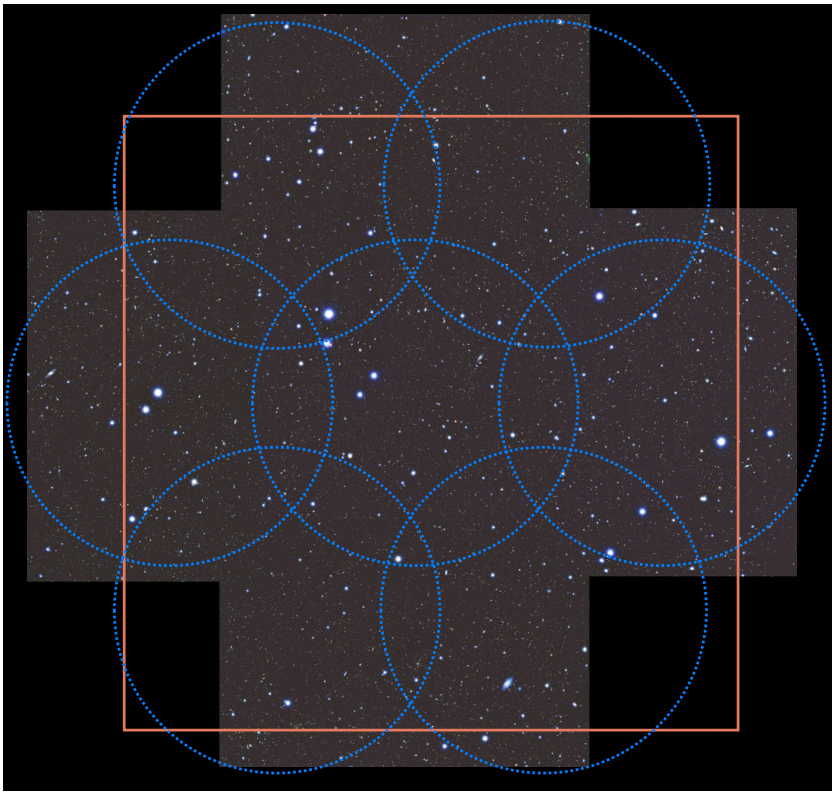

Figure 2.2: X-ray data coverage in the UDS (blue dotted circles) compared the coverage of the NIR data (red square) and optical data (image cross).

fainter, redder sources.

The programme was awarded a total of 235 hours of VLT time with 93 hours used on VIMOS and 142 hours on FORS2. Nine VIMOS fields were used in a 3x3 configuration to cover 90% of the UDS field, see Figure 2.4 (white squares). Targets for the masks were selected at random apart from ensuring that SHADES submillimetre galaxies were selected in the central regions. In total VIMOS observed $\simeq$ 2500 targets. Given the initial K-band selection, the targets that are fainter in the optical are generally very red and were observed using FORS2. Twenty FORS2 masks were used to cover 1/3 of the UDS field, see Figure 2.4 (red squares). Up to the point when this work was concluded 19 out of the original 20 masks had been observed and one additional mask was observed using leftover time that was available within the programme allocation. Based on the data received so far FORS2 has targeted 762 objects in the UDS. This work is based solely on FORS2 targets and so only the observing strategy, data reduction and analysis

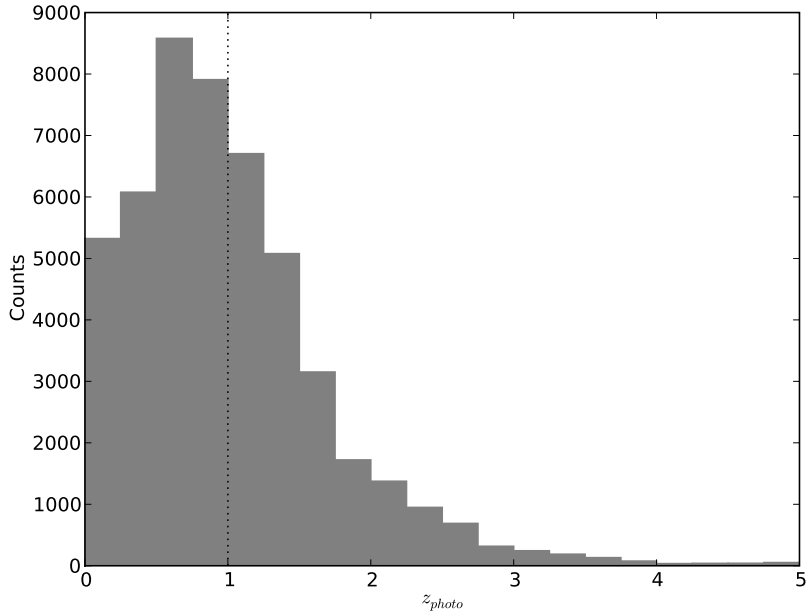

Figure 2.3: The photometric redshift distribution for the UDS $K < 23$ sample. The black dotted line shows the lower limit in photometric redshift for the UDSz sample.

of that data is described here.

2.2.1 FORS2 Mask Design and Observing Strategy

Each FORS2 mask contained approximately 35-40 target galaxies (and several guide stars). The targets were selected to be red but also needed to be bright enough in the optical bands so that a usable spectra could be obtained. As a consequence the following selection criteria were applied: $V > 24.5$ and $i < 24.5$ or $z < 24.0$.

The masks were optimally designed to fit as many 8" x 1" slits as possible. Initially if the most optimal solution still had space left over additional smaller slits were added. However, after reduction of the first few masks was completed, it was realised that the small slits could not be reduced effectively. As a result, for the remaining masks any additional free detector space was used up by enlarging the existing slits to improve sky subtraction. Each pointing had 5 hours of integration time on source, divided up into 6 observing blocks. Each observing block contained 4x745 second exposures in 4 positions (the additional mask contained 2 observing blocks of 4x640 seconds). Multiple observing

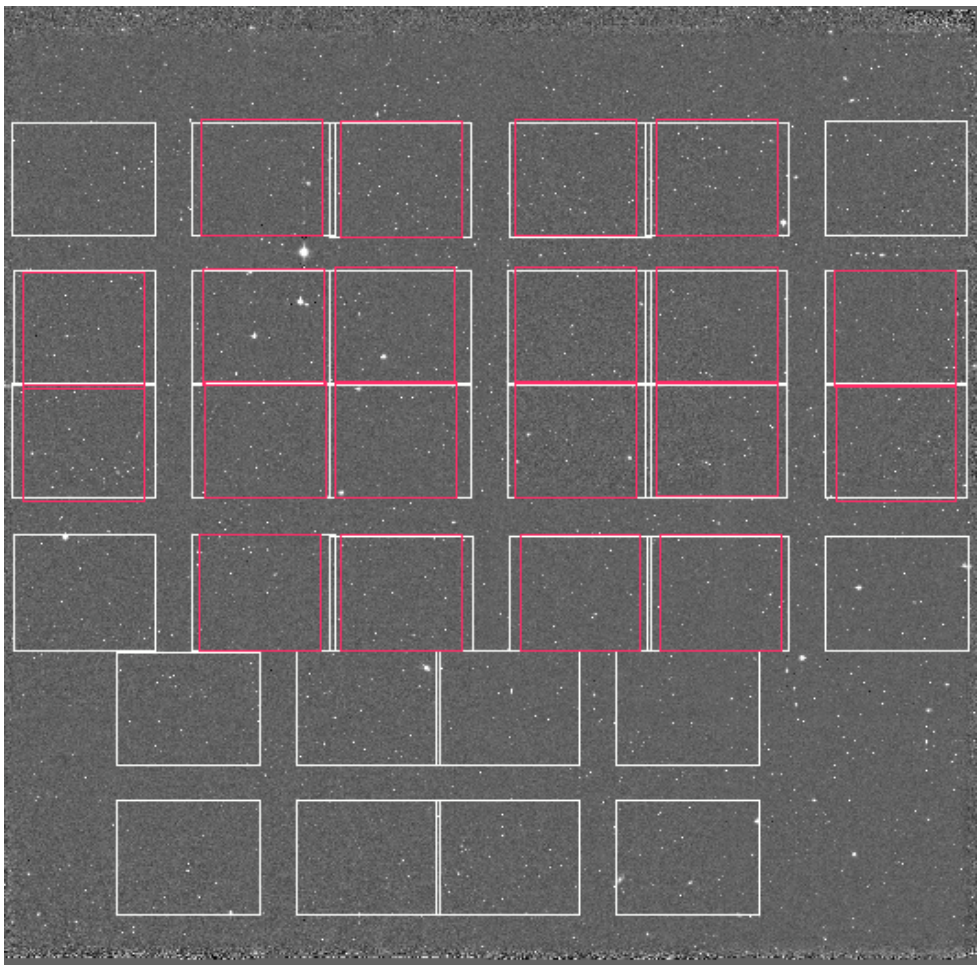

Figure 2.4: VLT spectroscopic mask coverage of the UDS field. VIMOS pointings are shown as white square and FORS2 pointings are shown as red squares.

positions (dithers) were used to avoid exposing a galaxy spectrum for the full exposure time onto a part on the CCD that contains dead and/or hot pixels. In addition, this dither strategy also gave an alternative data reduction option, whereby exposures in different positions can be subtracted from each other to remove the sky signal. This method is used to remove the sky background in near-IR spectra due to the severity of the sky line-emission at those wavelengths. This method was not chosen for our data as it decreases the signal-to-noise of the final sky-subtracted image. This results form the fact that subtracting one exposure away from another will result in the errors on each being added together in quadrature, therefore increasing the noise of the sky-subtracted image.

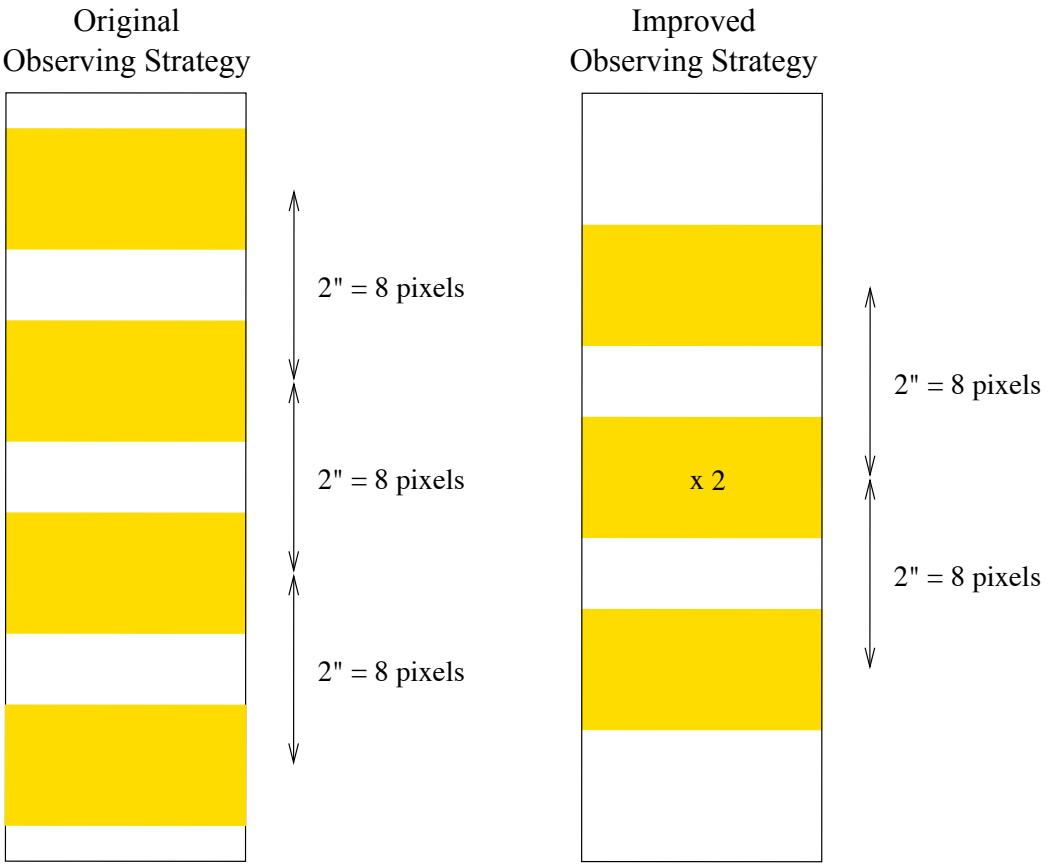

Figure 2.5: Diagram showing the different trace positions for the original (left) and improved (right) observing strategy. The yellow shaded regions show the expected position of the trace of the targets spectrum.

The first mask and a half were observed with a different 4-point dither strategy to the remaining observations. For these masks the four positions started 3" below the centre, then moving up the slit in steps of 2" (see Figure 2.5, left). However this made sky subtraction difficult, see Section 3.2.1. The observing strategy was changed as the sky noise removal was difficult for the upper and lower positions in the original strategy as there were a very small number of pixels at the slit edges to control the sky background fit with, see Section 3.2.1. The improved observing strategy for the remaining masks was to start 2" below centre then do two steps of 2" and then return to the centre for the final position (see Figure 2.5, right). In the next chapter the full details of the data reduction are discussed.

Chapter 3

Reduction of the VLT-FORS2 Spectroscopy

3.1 Explanation of VLT Pipeline and Issues

The FORS reduction pipeline is a subsystem of the VLT Data Flow System (DFS). The pipeline and all the subroutines are public to the user community. The pipeline can be used to automatically process scientific exposures taken with the FORS and FORS2 instruments. The outputs from the pipeline are limited by the quality of the calibration data and the algorithmic implementation of the subroutines. ESO has released two front-end applications through which to run the pipeline; *Esorex* (ESO Recipe Execution Tool) is a front-end that can be run from the command line and *GASGANO* is a Java application version of the pipeline. *GASGANO* is also a Data File Organiser which can be used to systematically view data observed by telescopes which operate in observing blocks.

3.1.1 Reduction of the Calibration Data

The flow chart for the VLT pipeline reduction of the calibration data can be seen in Figure 3.1. All the subroutines in the reduction cascade of the calibration data are combined together in a single recipe called *fors_calib*. This recipe requires the input of 5 raw bias exposures, 5 screen flat exposures, 1 arc lamp exposure, a grism table and a line catalog (MASTER_LINECAT). The grism table is a file that contains the

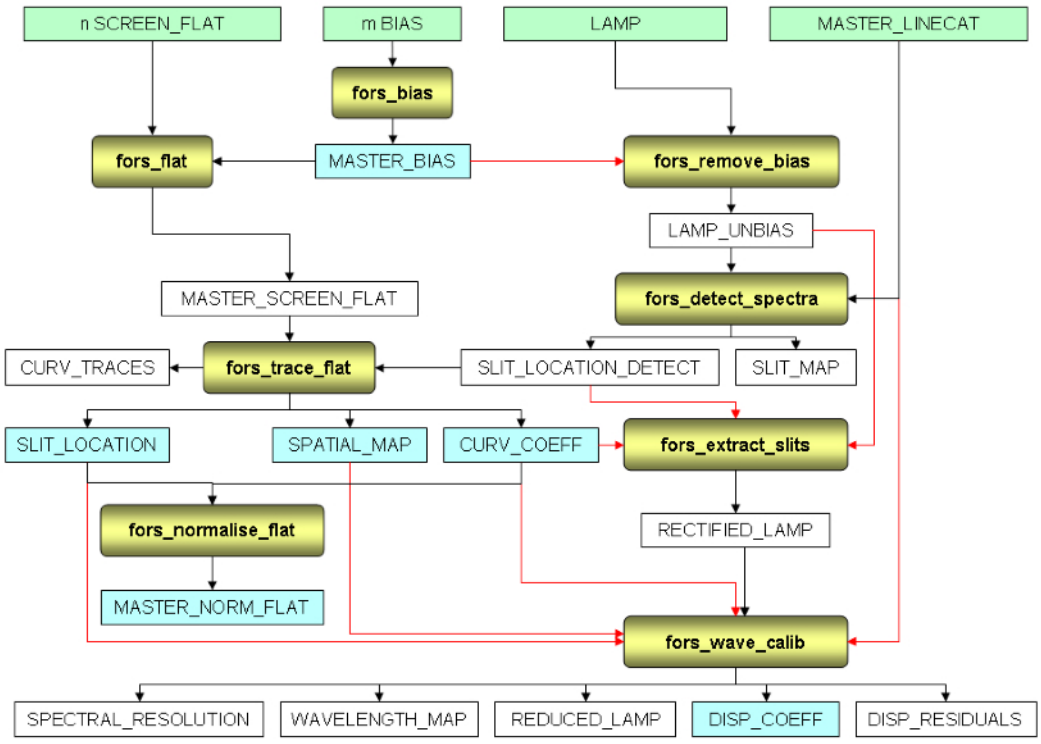

Figure 3.1: A cascade explaining the reduction of FORS2 calibration data. The recipe combining all these subroutines is called *fors_calib*.

configuration parameters controlling the extraction of the spectra for the particular grism that was used during the observations. The line catalog is a list of spectral lines and their corresponding wavelengths, in Ångstroms, for the arc lamp used.

Firstly *fors_bias* creates a MASTER_BIAS by making a median stack of the 5 bias frames. The value of the MASTER_BIAS at each pixel is the median of the 5 corresponding pixels from the 5 raw frames. The minimum and maximum pixel values at each position are, by default, removed when a mean instead of median stack is used. The 5 raw screen flat exposures and MASTER_BIAS are then used to make a MASTER_SCREEN_FLAT using *fors_flat*. Each of the raw flat-field exposures are bias subtracted and are then averaged to create a MASTER_SCREEN_FLAT.

Next, using a bias-subtracted raw arc lamp exposure, the MASTER_SCREEN_FLAT and the MASTER_LINECAT, the slit spectra are detected (*fors_detect_spectra*) and traced (*fors_trace_flat*) on the MASTER_SCREEN_FLAT and a preliminary wavelength

calibration is found. The important outputs are CURV_TRACES, which gives the position of the top and bottom of each slit in 10 pixel steps across the CCD chip, and SLIT_LOCATION which gives the position of the top and bottom of each slit at the central wavelength position on both the CCD image and the rectified (corrected for any curvature in the spectra) image of the arc lamp exposure. The CURV_TRACES output is produced by fitting a polynomial to the detected slit edges. An additional output that will be used later is the SPATIAL_MAP, a map of spatial positions on the CCD. In this map each pixel has the value of its distance from the top edge of is corresponding slit.

Finally a MASTER_NORM_FLAT is created by dividing the MASTER_SCREEN_FLAT by a smoothed version of itself using *fors_normalise_flat*. The smoothed version is created by box smoothing the image with a box of 10 pixel radius in the spatial and dispersion directions. Then using the SLIT_LOCATION, the MASTER_NORM_FLAT, the SPATIAL_MAP, the CURV_COEFF (a table containing the coefficients from the polynomial fitting to the slit edges which produced CURV_TRACES), and the rectified arc lamp exposure (*fors_extract_slits*) the final wavelength calibration is calculated, from the spatially rectiÞed arc lamp frame and is stored in DISP_COEFF (*fors_wave_calib*).

3.1.2 Reduction of the Scientific Data

The reduction cascade for the processing of the scientific data can be seen in Figure 3.2. Due to the faintness of the observed galaxies, the individual science exposures contained very low levels of flux from the targets. In this case the pipeline was unable to detect and trace the spectrum for a large fraction of the targets. Therefore this led to issues with the sky-subtraction, as an object's signal could be used in the sky fit and would result in a bad fit and, potentially, the flux of the target being subtracted away. Also this gave problems with the spectral extraction itself, which obviously could be seriously inaccurate if the spectrum of the object cannot be detected correctly. Therefore the VLT pipeline's reduction of scientific data had to be optimised, as can be seen in Figure 3.3, where the areas shaded grey are replaced with purposely written scripts. In Figure 3.4, reductions of three example slits are presented; the far left reduction of each of the examples is achieved solely with the VLT pipeline, the far right is our optimised

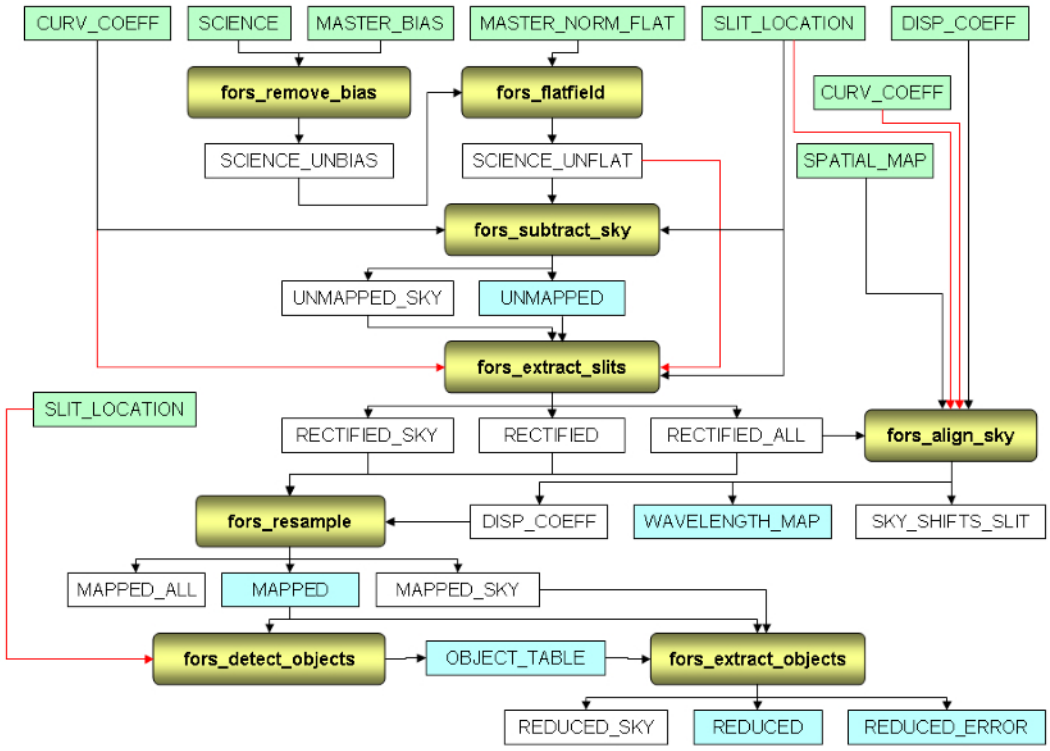

Figure 3.2: A cascade explaining the reduction of FORS2 scientific exposures. The recipe combining all the subroutines is *fors_science*.

reduction. As can be seen the reduction from the VLT pipeline leaves sky residuals in all the sky line positions, even in the areas with only weak sky emission. Along the whole of the spectrum in the wavelength direction there appear to be higher sky residuals above the object's spectrum than below. Also, towards the red end, the sky noise removal completely fails. The optimised reduction leaves only small residuals on the strongest sky lines and the residuals are uniform across the slit, both in the spatial direction and as function of wavelength.

The subroutines of the original VLT pipeline that are used are briefly described here, while in the next section a detailed description of the subroutines optimised during this thesis will be given. *fors_remove_bias* uses the MASTER_BIAS to bias subtract all the raw science frames. The result from this is then divided by the MASTER_NORM_FLAT by *fors_flatfield* to give a bias-subtracted flat-fielded science exposure. Sky background subtraction is performed next, which has been optimised and is described in Section

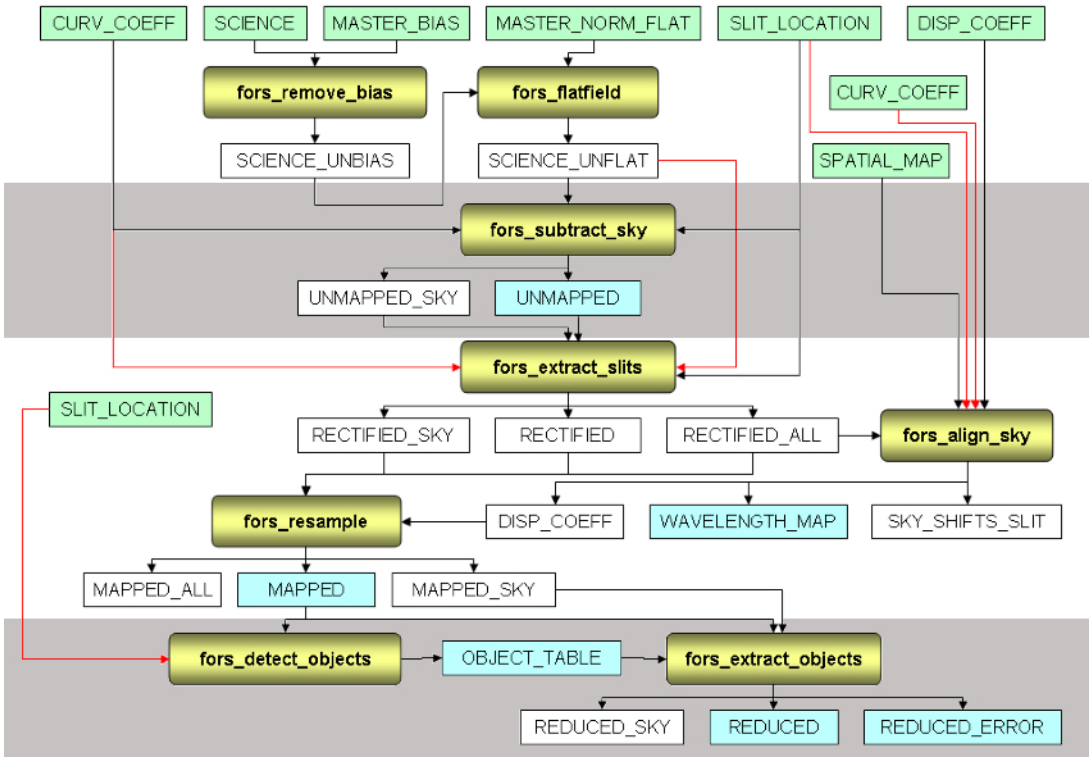

Figure 3.3: A reduction cascade for *fors_science*. The grey shaded areas contain the subroutines that failed for targets in the sample and were replaced with purposely written scripts.

3.2.1. *fors_extract_slits* then uses the information for the location and trace of the slit found during the reduction of the calibration data, CURV_COEFF, SLIT_LOCATION and the sky subtracted science data and produces rectified science and sky images with any curvature along the slits removed. This is then fed into *fors_align_sky* along with SLIT_LOCATION, SPATIAL_MAP, CURV_COEFF and DISP_COEFF and the rectified slits are used to see if any adjustments are needed to the wavelength calibration found during the reduction of the calibration data. *fors_resample* uses all of this to align the slits by wavelength. The final result is a bias-subtracted, flat-fielded, sky-subtracted, rectified and wavelength-calibrated multi-object CCD image. Using scripts created during this thesis, and the SLIT_LOCATION output from the *fors_calib* recipe, all of the slit spectra are cut out of the individual exposures. These individual exposure slits were then stacked as described in Section 3.2.2 and the 1D and error spectrum were extracted as described in Section 3.2.3.

3.2 Optimising the VLT Pipeline for the UDSz Data

3.2.1 Sky Subtraction

As the CCD contains multiple object spectra, the easiest way to perform the detection of the single spectra was to use the knowledge of slit location obtained from calibration and information of the expected position of the object along the slit. For the latter, as described in the previous chapter, the observations were constructed such that each observing block was built up of 4 exposures; the first being positioned 2 arcseconds below the centre on the slit, the second in the centre of the slit, the third 2 arcseconds above the centre and the fourth position returned to the centre of the slit. This information is summarised in Table 3.1 and presented in Figure 2.5.

At the same time the location of the slit is found as described above; *fors_calib* gives an output, CURV_TRACES, which details the location of the top and the bottom of each slit every 10 pixels along the length of the CCD. A python script was written to cut out each of these 10-pixel segments and save them to disk. The *background* package from PyRAF (a command language for running IRAF based on Python) was used to subtract the sky noise from each segment. Working on a column-by-column basis, *background* fits a polynomial to the allocated pixels in each column and subtracts this fit from the entire column of pixels. Within *background* one can set the order of the polynomial, the pixel range to use in the fitting process and any thresholds by which pixels should be rejected from the fitting sample. When fitting the sky background the sample of pixels to be used in the fit was set to exclude the region containing the spectrum of the target using the knowledge of its expected location. A two-iteration 2σ clip of the pixel values in the fitting sample in each column was performed to remove any cosmic rays or bad pixels from the fitting sample. It was found that a second-order polynomial was required to deal with all the sky lines along the spectra. Zeroth- and first-order polynomials were tried as the lowest order acceptable fit possible is desired to reduce the number variables in the fitting process. The zeroth-order fit results in a bimodality in the residuals in the sky lines, implying that there is at least a gradient in the skylines (see Figure 3.4, second reduction from the left in each example). The first-order fit provided a good sky subtraction for all of the skylines $\lesssim 9300$Å, but left

bad residuals for the majority of the skylines at the red end of the spectrum (see Figure 3.4, second reduction from the right in each example). Each segment was then returned to the CCD image for rectification and sky line alignment.

3.2.2 Stacking of Individual Science Exposures

The stacking of the 24 individual exposures was performed using the *imcombine* task in PyRAF. This package allows one to combine FITS images in a variety of ways. The images can simply be added using the summing feature or can be combined via an average or median stack. When summing the frames, the package works on a pixel-by-pixel basis and sums all the values from a certain pixel position in each exposure. For average(median) stacks the average(median) is calculated for the corresponding pixel position respectively. Pixel rejection parameters can also be included in the form of sigma clips, the removal of a certain number of the highest and lowest valued pixels or give a straight lower and/or upper threshold value. The images can be offset before stacking by a designated number of pixels in the x and y directions.

The stacking method adopted was to use an average stack, with a 2σ clip, with offsets to take into account the different observing positions within the observing strategy. The pixel scale on the FORS2 chips is 0.25" per pixel so, for a single block of observations, the offsets required in the spatial direction can be seen in Table 3.1 and are depicted in Figure 3.5. The top and bottom 8 pixels of the stack were removed as they only contained the sky residuals from a single exposure and were not going to be used in the extraction of the 1D object or error spectrum (Figure 3.5). The final stack was then divided by the exposure time of an individual exposure (745s).

Throughout the testing it was seen that bad rows of pixels in the FORS2 detector could heavily affect the final stack, and so, for each target, four stacks were made; one stacking all the exposures together, one removing the bottom, one removing the middle and one removing the top position. The full stack was used unless a position needed to be removed due to artifacts in the CCD image. Along with a bad stack being made due to bad rows of pixels and artifacts on the detector the SLIT_LOCATION output file can be slightly inaccurate and when cutting the slits out of the individual science exposures part of the gap between the slits can be included, resulting in horizontal rows of zero

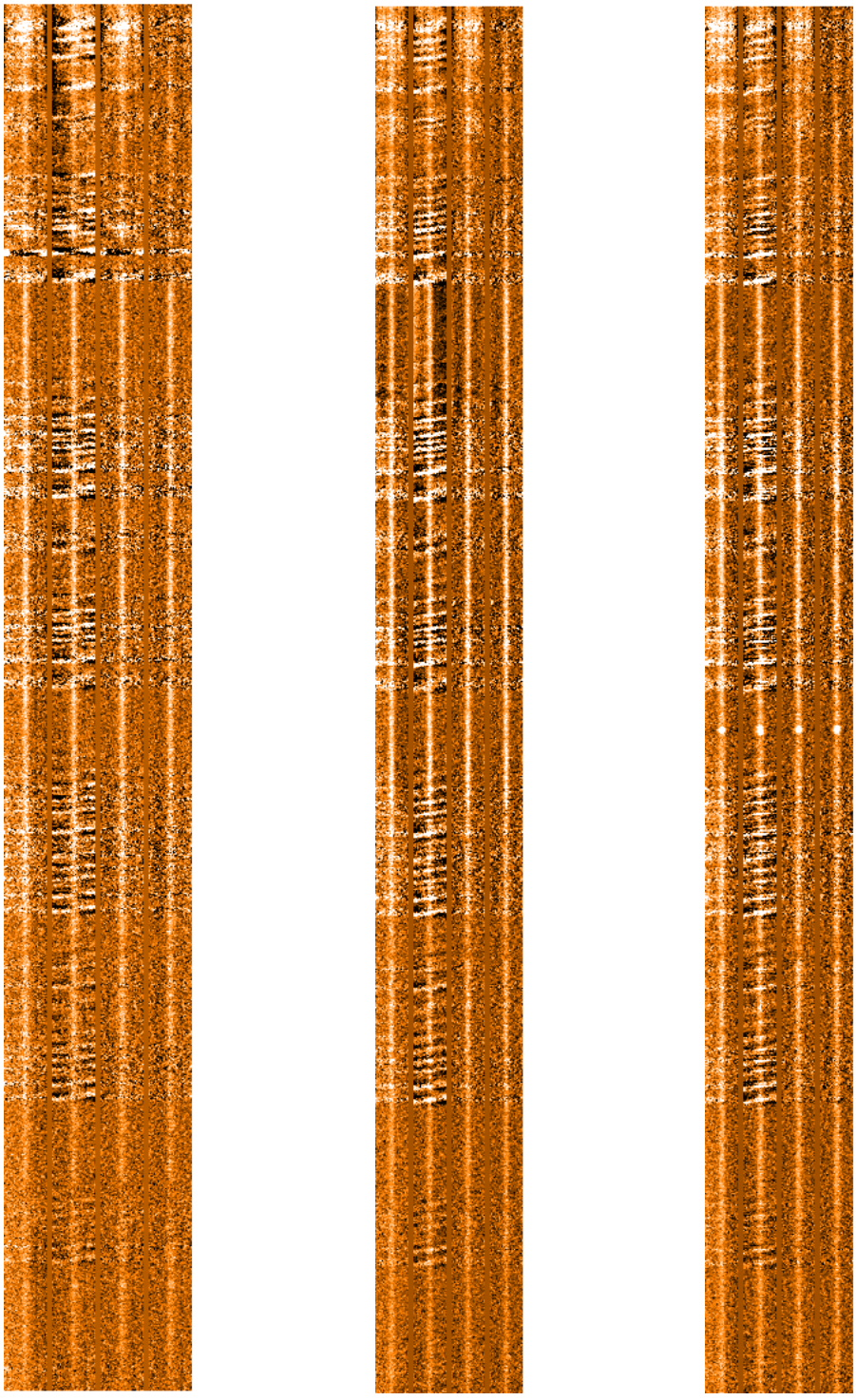

Figure 3.4: The final two-dimensional stacks for four different reductions for three example objects. For each object the far-left reduction was made using the original VLT pipeline, second from the left is a reduction from the optimised pipeline with a zeroth-order sky fit, second from the right is a reduction from the optimised pipeline with a first-order sky fit and the far right is a reduction from the optimised pipeline with a second-order sky fit, the method used for final reduction of the data.

Table 3.1: The offsets for the exposures in a single observing block. The offsets are the same for all 6 observing blocks.

Observation	Spectral Position	Offset in pixels
1	2" below centre	-8
2	Centre of slit	0
3	2" above centre	+8
4	Centre of slit	0

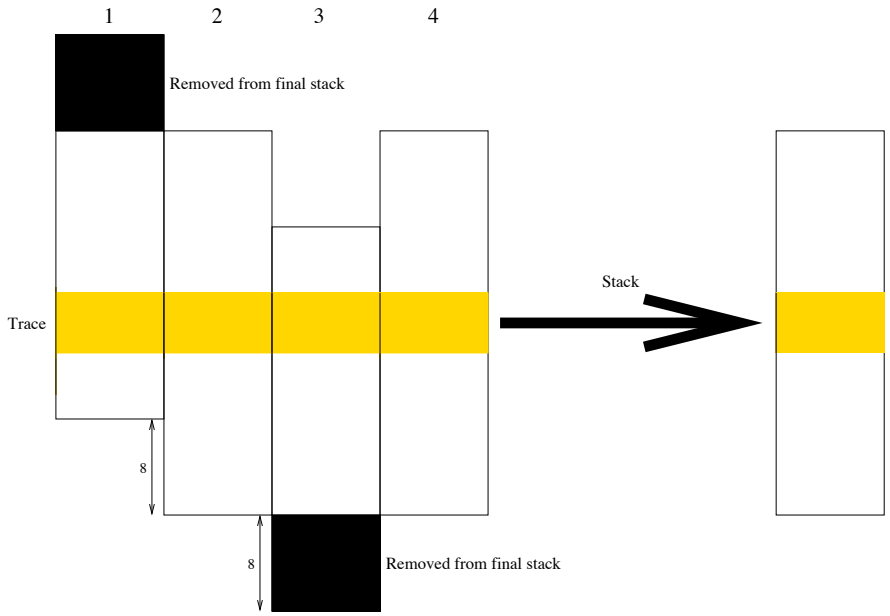

Figure 3.5: Diagram showing how the 4 exposures from a single observing block are stacked together accounting for the offsets resulting from the observing strategy.

counts. These slits have to be manually recut and stacked.

3.2.3 Extraction and Cleaning of the 1D Spectra

The PyRAF package *apall* offers a good tool for the extraction of the 1D galaxy spectra. However, due to the faintness of the target sources, two of the stages of the extraction process with *apall* (defining location of the aperture spatially on the two dimensional spectrum and tracing the flux along the spectrum) had to been done interactively and this was not realistic due to the number of spectra to be analysed. Therefore a python code was developed that would automatically simultaneously extract the object spectra and its corresponding error spectrum.

The VLT pipeline provides an effective rectification of the spectra, so after inspection of a random sample of spectra, it was concluded that the flux could be considered to be dispersed horizontally along the two-dimensional spectrum. To find the trace the two-dimensional spectrum of each object was binned up using an 11-pixel box in the dispersion direction. The script then scanned along the 2D spectrum trying to locate the trace. By construction of the stack (described above) the trace is expected in the middle of the stack (see Figure 3.5). For each column in the binned-up 2D spectrum the middle 5 or 6 pixels were tested to find which one contains the centre of the trace. If the stack contained an odd number of rows the middle 5 (centre and ± 2 pixels) was used and if the stack contains an even number of rows the central 6 pixels was used, see Figure 3.2.3.

At each of these 5 or 6 central pixels for each column (in the binned spectrum) the surrounding 5 pixels are summed and the value recorded. The summing of 5 pixels was chosen since inspection of a collection of final 2D spectra showed that the targets signal never spanned more than 5 pixels spatially. This works as an estimation of the target flux if the current central pixel was the trace.

For each column the pixel value which produced the largest flux value was recorded as the trace. Once a trace was estimated for each column in the binned 2D spectrum the mode of these trace values was taken to be the trace for target flux. The expected trace value (the middle row of the 2D spectrum) and the trace estimate from the above method were both recorded in an extraction log file.

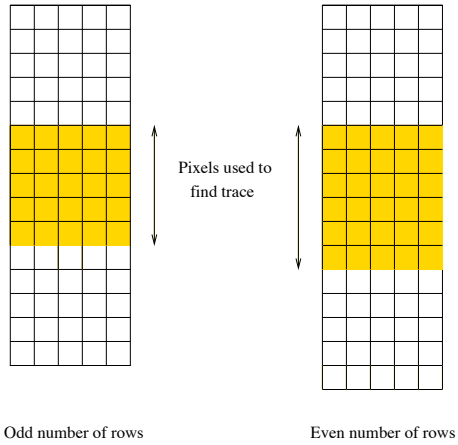

Figure 3.6: Diagram showing 5 columns of a stack that contains an odd(left) and even(right) number of rows. The pixels shaded yellow are the pixels that were examined when searching for the trace.

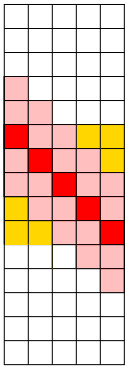

Figure 3.7: Diagram showing the pixels that were summed to find the trace of an object's stacked spectrum. The pink pixels show the pixels that were summed when the corresponding red pixel is trialled as the trace.

Table 3.2: The range of allowed and default weight values for the extraction pixels.

Pixel	Weight Range	Default Weight
+2	0.05-0.15	0.1
+1	0.10-0.30	0.2
Trace	0.20-0.40	0.3
+1	0.10-0.30	0.2
+2	0.05-0.15	0.1

To achieve an optimal extraction of the flux a weighted extraction of the 5 pixels surrounding the trace pixel was needed. In each column the flux was spatially distributed approximately as a Gaussian. The distribution of the Gaussian was investigated as a function of wavelength. From a collection of test objects it was concluded that the weights were constant as a function of wavelength (see Figure 3.8 for an example). Therefore, a single weight for each of the 5 extraction pixels was needed. This was found by moving along the (original unbinned) 2D object spectrum and for each column recording the fraction of the total flux that was contained in each of the 5 extraction pixels. The weight for each of the 5 pixels was then found by a least-squares-fit of a constant function to the set of values for each pixel (see Figure 3.8). Since a lot of the spectra contained low levels of signal-to-noise per pixel this fit was sometimes hard to find correctly so a range of weights for each pixel were defined and if the estimate fell outside of this then a default value was adopted. The ranges and default values can be found in Table 3.2. The estimated weights were recorded in the extraction log file.

Once the trace and the optimal extraction weights was established, a 1D spectrum of the object was extracted using the original 2D spectrum, and at every column a weighted extraction flux recorded as the weighted mean of the pixels around the trace, i.e.

$$f_{col} = \frac{\sum_{i=1}^{5} f_i w_i}{\sum_{i=1}^{5} w_i}, \tag{3.1}$$

where f_{col} is the extracted flux for an individual column of pixels, f_i is the flux in one of the individual extraction pixels and w_i is its corresponding weight.

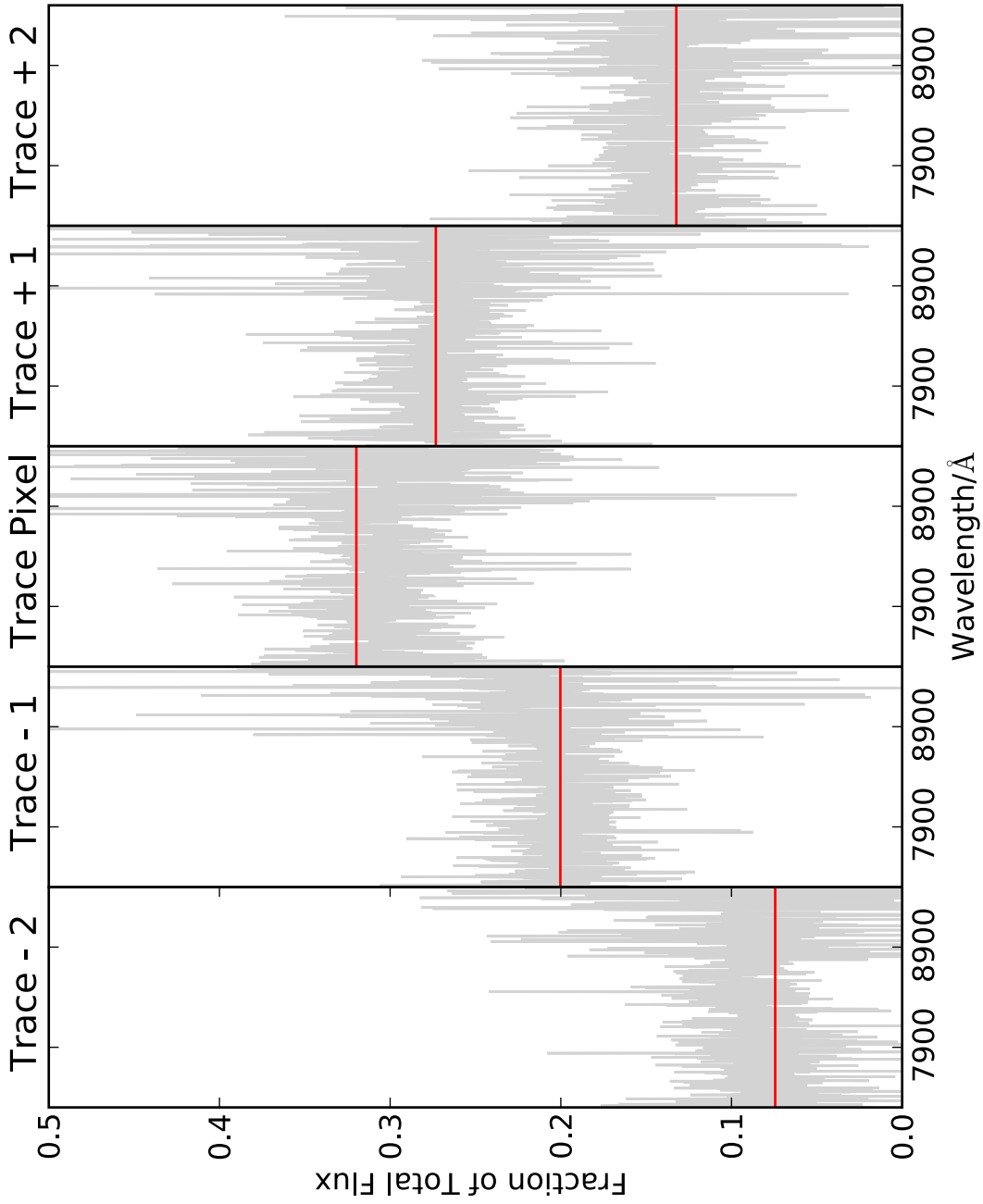

Figure 3.8: Example of how the fraction of flux in each of the extraction pixels varied as function of wavelength. The five panels show the fraction of flux in each pixel as a function of wavelength. The red line is the best fitting constant function.

Flux calibration of the extracted spectra

The extracted one-dimensional flux and error spectra are then corrected for the average airmass value of the nights during which the mask was observed, using:

$$f_{airmass-corrected,\lambda} = f_{observed,\lambda} \times 10^{0.4AC_\lambda}, \tag{3.2}$$

where $f_{airmass-corrected,\lambda}$ is the airmass-corrected flux at a given λ, $f_{observed,\lambda}$ is the extracted flux at a given λ, A is the average airmass and C_λ is the value of the extinction correction function at a given λ. The atmospheric extinction curve used can be seen in Figure A.1

The sensitivity of the CCD then needed to be considered and corrected for. This was done by using the sensitivity function of the CCD. The sensitivity function was found by using the observation of a standard star that was observed on the same nights as the mask considered, to make sure it was observed in similar conditions to the science data. Due to the brightness of the standard star, *fors_calib* and *fors_science* can be used in their complete form. As with our optimised pipeline *fors_science* normalises the exposure time to 1 second. Once a fully reduced 2D spectrum of the standard star was obtained, its spectrum was extracted in the same way as for the objects. The PyRAF packages *standard* and *sensfunc* were used to compare the observed with the expected spectrum, and hence produce a sensitivity function. The *standard* package requires the extracted 1D spectrum of the standard star, the airmass at the time of observation, an atmospheric extinction file and the expected spectrum of the standard star. Examples of an extracted standard star spectrum and its corresponding expected spectrum are shown in Figure 3.9. The expected stellar spectrum file needs to be in the form of an ascii table with 3 columns; column 1 is wavelength, column 2 is magnitude(AB) and column 3 is the band-width (see Table A.1 for an example standard star calibration file). The PyRAF *standard* package generates an output table that is made up of 4 columns; column 1 is wavelength (same as the standard star calibration file), column 2 is the flux of the star in the corresponding band-pass, column 3 is the band-width (same as the standard star calibration file) and column 4 contains the number of counts from the extracted spectrum in the corresponding band-pass. The first line of the file

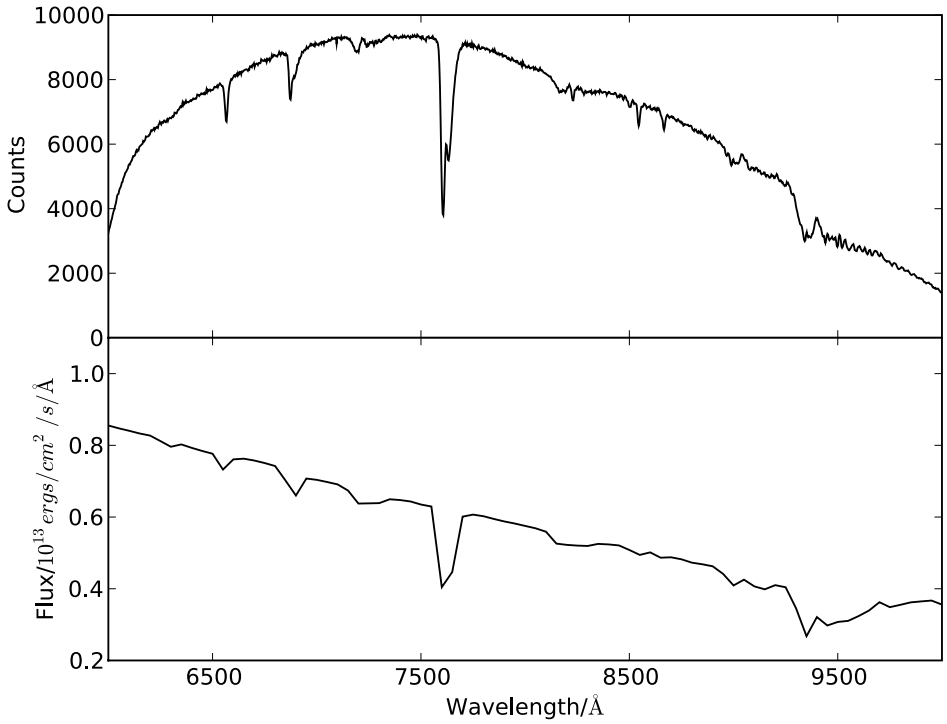

Figure 3.9: The top panel shows the unflux-calibrated spectrum of a standard star. The bottom panel shows a flux-calibrated spectrum of the same star.

contains a line of additional information; the input extracted spectrum file name, the aperture number, the length of the spectrum, the exposure time, the airmass and the wavelength range (for an example of output file see Table A.2).

The PyRAF *sensfunc* package then uses the information generated by the *standard* package and an atmospheric extinction file to produce a sensitivity function for the CCD. For each point in the output table a calibration factor is calculated by,

$$C = 2.5 \log (O/TBF) + AE, \tag{3.3}$$

where O is the observed counts in a given bandpass, T is the exposure time of the observation, B is the band-width, F is the flux per Angstrom at the bandpass for the standard star, A is the airmass of the observation, and E is the extinction at a given bandpass. Once *sensfunc* has calculated all these points the sensitivity function is

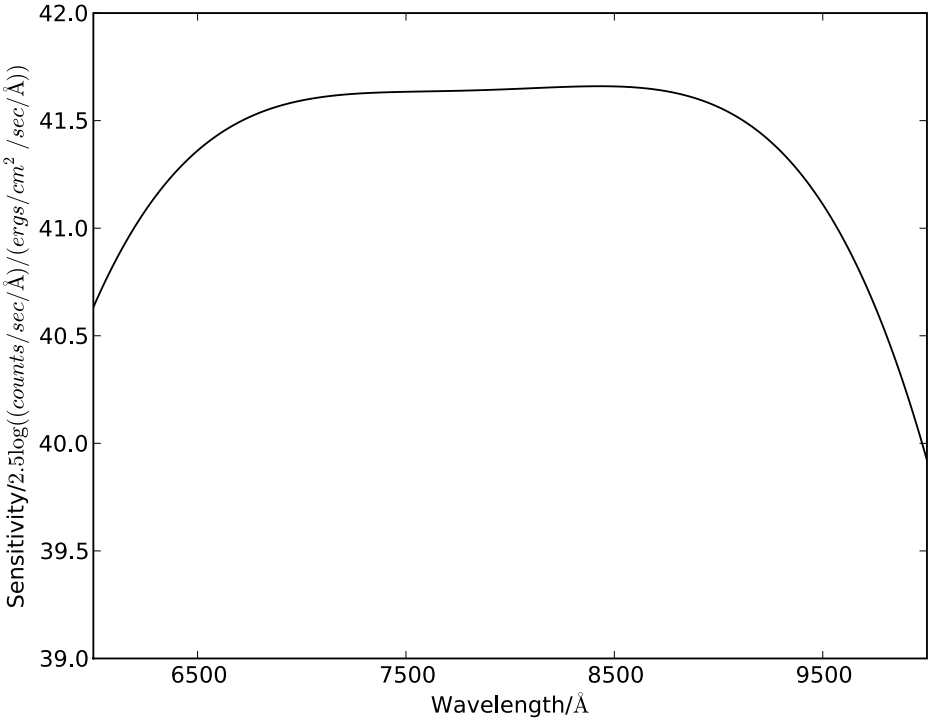

Figure 3.10: Derived sensitivity function for the standard star shown in Figure 3.9

found by fitting a polynomial curve, which is done interactively, changing the function and order, while *sensfunc* is operating. The resulting sensitivity function is in units of $2.5 \log \frac{\text{counts/sec/Å}}{\text{ergs/cm}^2\text{/sec/Å}}$ (see Figure 3.10 for the sensitivity function of the standard star).

This sensitivity function is then used to correct the extracted airmass-corrected spectrum using,

$$f_{sens-corrected,\lambda} = f_{airmass-corrected,\lambda} \times 10^{-0.4 S_\lambda}, \tag{3.4}$$

where $f_{sens-corrected,\lambda}$ is the CCD sensitivity corrected flux at a given λ, $f_{airmass-corrected,\lambda}$ is the extracted flux at a given λ, and S_λ is the value of the sensitivity function at a given λ.

Correcting for atmospheric telluric features

The spectrum then needed to be corrected for telluric contamination which originates from molecules in the Earth's atmosphere. This was also done using the observation of the standard star. The 1D spectrum of the standard star is meant to approximate to a blackbody spectrum and the position of the telluric features in the optical are known. A high-order polynomial was fitted to the spectrum of the standard star excluding the regions containing the telluric features. In the optical the telluric features occur at $6532 - 6591$Å, $6841 - 6936$Å and $7568 - 7700$Å. Known regions of bad skylines were excluded from the fitting because these are dealt with during the sky-subtraction; in the optical range particular bad skylines appear redward of 9275Å. For an example of an extraction of a standard star from one of the masks and the fitting polynomial see the top panel of Figure 3.11. The spectrum of the standard star was then divided by the high-order polynomial fit with the resulting function being very close to unity except in the telluric regions which are lower. To ensure that only the telluric regions were corrected, all the values outside this region were forced to be exactly equal to one (see the bottom panel of Figure 3.11 for example of telluric correction function). To correct the object's 1D spectrum for the telluric features it was simply divided by the telluric function.

Correcting the spectral normalisation to match photometry

The airmass, sensitivity and telluric-corrected spectrum was then normalised to match the objects photometry in a 3" diameter catalog. The spectral shape was left unchanged and the spectrum simply had its overall normalisation changed by a factor equal to the difference between the integral of the flux in the spectrum over the i-band filter and the flux in the observed i-band magnitude. Integrating the spectrum over the i-band filter was done in (λ, f_λ) space using,

$$F = \frac{\int f_\lambda R_\lambda}{\int R_\lambda / \lambda^2} d\lambda, \tag{3.5}$$

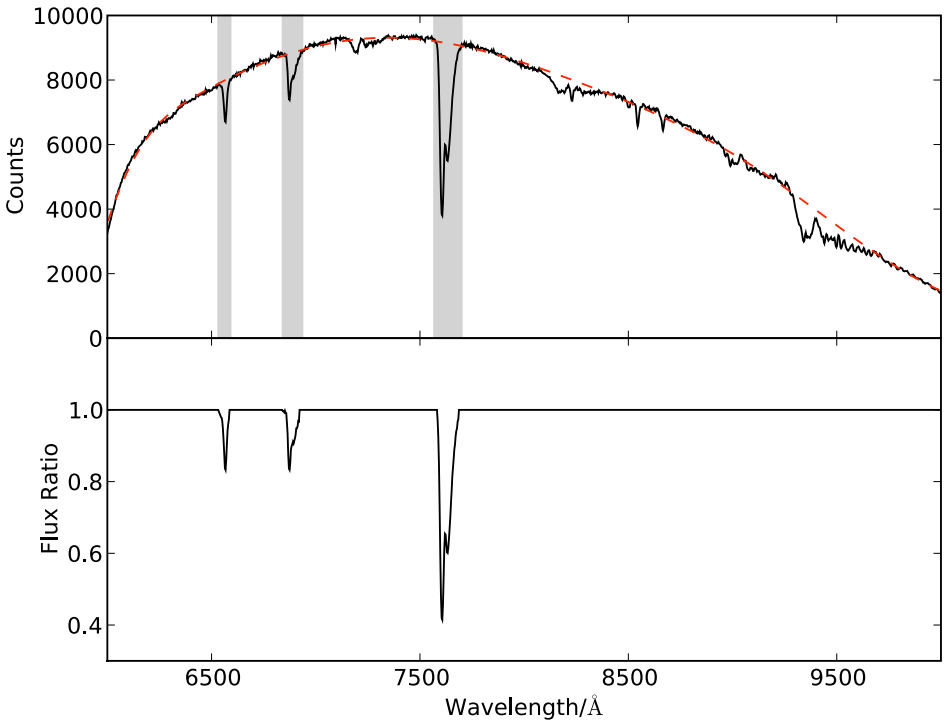

Figure 3.11: Top panel shows an extraction of a standard star from one of the masks. The black line is the spectral extraction, the dashed red line is the high order polynomial fit and the shaded grey regions are known areas with telluric features. The bottom panel shows an example of a final telluric correction function.

where F if the flux over the i-band in the spectrum, f_λ is the flux in the spectrum and R_λ is the filter profile for the i-band. This was then converted to a magnitude using,

$$m = -2.5 \log (F) \tag{3.6}$$

and,

$$C = 10^{\frac{m-M}{2.5}}, \tag{3.7}$$

where m is the i-band magnitude in the spectrum and M is the photometric i-band magnitude.

Only the i-band was used, as opposed to the R, i and z bands, since this was the only band fully spanned by all the spectra. If a slit is not located centrally in the dispersion axis on the CCD, part of the wavelength coverage is lost at either of the ends

of the spectrum.

This 1D spectrum and R, i and z photometry was then plotted and saved as a postscript file for inspection before any further reduction was carried out. Each plot was visually inspected to check that the spectrum looked sensible and that the spectrum had been properly normalised to the photometry.

For the production of each object's error spectrum the information of the trace and extraction pixel weights from the extraction of the objects spectrum was used along with the information of the exposures used in the final stack (accounting for any re-stacks due to bad pixels and/or inaccuracies in the SLIT_LOCATION output file) and the corresponding offsets. For each column in the dispersion direction and each of the extraction pixels the values from all of the exposures used in the final stack were recorded. These were normalised to the exposure time of a single science frame (745s). The result was an "error-stack" which had 5 rows and the same number of columns as the final science stack where each pixel has a value equal to,

$$p_{i,j} = stddev(stack\_pixels)/\sqrt{no.\ of\ stack\_pixels}, \tag{3.8}$$

where $p_{i,j}$ is the j^{th} pixel in the i^{th} column, *stddev* means standard deviation and *stack_pixels* is the set of all the values that went into that position in the final stack.

From the "error-stack" the objects error spectrum can be extracted. A weighted extraction was obtained using Equation 3.9, which is the same as for the object spectrum except the error values are added in quadrature.

$$\sigma_{col} = \frac{\sqrt{\sum_{i=1}^{5} \sigma_i^2 w_i^2}}{\sum_{i=1}^{5} w_i} \tag{3.9}$$

The extracted error spectrum was then corrected for airmass extinction, CCD sensitivity and telluric features in the same way as the object spectrum.

Each spectrum was put through a minor cleaning procedure which consisted of plotting the one-dimensional spectra using the *splot* package in PyRAF and removing any unrealistic pixel spikes or troughs which could not be accounted for by the error spectrum.

Finally as the spectra had been oversampled by a factor of two the 1D and error

Table 3.3: The flag classification system for spectroscopic redshift estimation for the UDSz galaxy spectra

Flag	Description
A	Secure redshift with multiple spectral feature and good template match
B	Confident redshift estimate with single feature and/or good template match
C	Uncertain redshift, but best estimate is provided
D	No redshift estimate obtained

spectrum for each object was binned up using a 2-pixel bin. The final output for each object was a FITS file with three extensions; the final 2D stack, 1D and error spectrum, and a text file of both the 1D and error spectrum.

3.3 Redshift Estimation

An estimation of the spectroscopic redshift for each object was found by initially fitting each object with three composites from the K20 Survey representing early-, intermediate- and late-type galaxies [Mignoli et al., 2005]. The best-fit template provided an estimate of the redshift and spectral type. An independent estimate of the redshift was provided by inspection of each object performed by Dr. R. J. McLure. For the spectra that resulted in a science grade redshift (A or B - see later), $\sim 70\%$ of the total extracted spectra, the majority, $\sim 90\%$, had excellent redshift agreement ($\Delta z \sim 0.001$) from the two estimates. It was the lower signal-to-noise and featureless spectra where the differences occurred, and where further discussion was required. Armed with these two independent estimates, a final visual estimation of each source was undertaken by Dr. R. J. McLure, Dr. M. Cirasuolo, Prof. J. S. Dunlop and myself yielding a final redshift estimate and a classification flag for each object. The classification flag was categorised as given in Table 3.3 with Flag A being the most secure redshift and Flag D indicating that no estimate could be made.

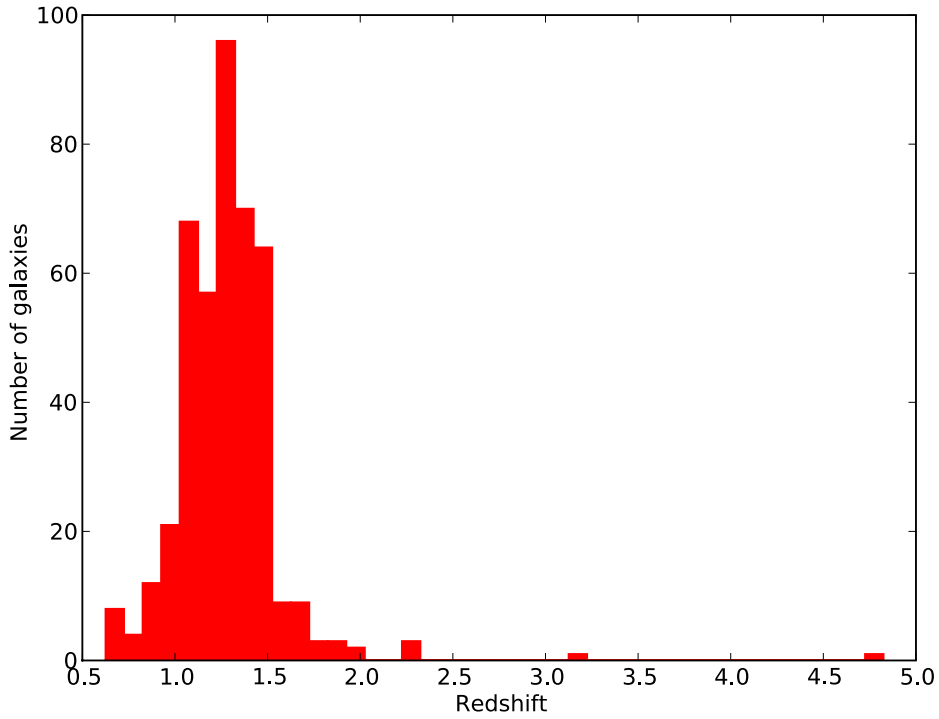

Figure 3.12: The spectroscopic redshift distribution of the galaxies with scientific grade redshifts (Flag A or B) from the K-band selected follow up programme in the UDS, UDSz.

3.4 Reduction and Redshift Statistics

On the masks that were reduced and used for science purposes in this thesis there was a total of 762 targets consisting of 718 K-band selected targets, and 44 additional sources such as Lyman Break Galaxies (LBGs) and SCUBA sources. From this target sample 654 (91%) 1D spectra were successfully extracted, of which 641 were normalised to match their i-band photometry. Of the 13 that were not normalised, 9 had no i-band photometry and 4 had such low levels of flux in their spectra that the integrated flux over the spectrum under the i-band filter was negative. From the sample of extracted and normalised spectra 443 (69%) have science grade (Flag A or B) redshifts, 12 of which were stars. The redshift distribution of the sample is shown in Figure 3.12. The whole sample has a median redshift of $z = 1.283$.

Chapter 4

Data Analysis Techniques

In addition to producing an accurate redshift, the spectra can also be used to derive physical properties of the observed galaxies. The various techniques used to analyse the optical spectra and multi-wavelength photometric data of each galaxy will be discussed here. Descriptions are provided of how physical characteristics such as stellar mass, dynamical mass, age and star formation rates are calculated along with how measurements of spectral features are made. The method for calculating velocity dispersions of elliptical galaxies will discussed in detail and the construction of composite spectra and photometry of samples of galaxies will be described.

4.1 Spectrophotometric Fits to Optical Spectra and Multi-Wavelength Photometry

4.1.1 Galaxy Evolution Models

Armed with the optical spectra and the multi-wavelength photometry for each galaxy it is possible to derive accurate estimates of the ages and stellar masses of the targets. As galaxies are complex systems made up of potentially several stellar sub-systems from different generations of star-fomration, it is necessary to invoke models with a variety of star-formation histories to obtain good fits to the data. Here we adopt the latest Charlot & Bruzual 2007 models (Stephane Charlot, private communication, hereafter CB07), which include the effects of thermally pulsating asymptotic giant branch (TP-AGB)

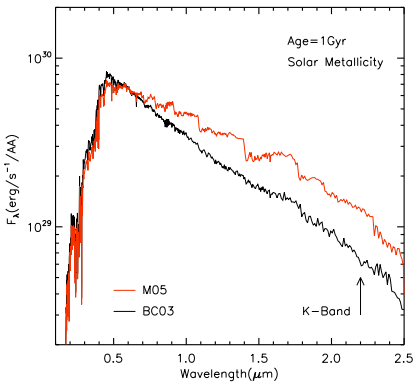

Figure 4.1: A simple stellar population spectral energy distribution from Maraston [2005b] (red line) compared with the equivalent predictions from Bruzual and Charlot [2003] (black line). The plot refers to a 1 Gyr old population with solar metallicity.

stars. These stars have maximum fuel consumption at ages $0.3 \leq t \leq 2$ Gyrs and at this time can have a large effect on the NIR region [Maraston, 2005b], see Figure 4.1 for an example of the difference in SED shape with and without the inclusion of TP-AGB stars. There is a vigorous debate over which of the currently available evolutionary synthesis models provide the best fits to the data, or indeed, whether any of the current generation of models can accurately reproduce high quality galaxy spectra. For example Carter et al. [2009] have shown that the models of Bruzual & Charlot can reproduce the broadband UV to NIR photometry in present day ellipticals but that the models of Maraston [2005b] can not (for sensible physical parameters). This provides some confidence that we can proceed to use the models of Bruzual & Charlot to fit the optical to IRAC photometry for $z \sim 1$ galaxies in the present study. On the other hand, it is well known [e.g. Tojeiro et al. 2010] that all models struggle to provide formally acceptable fits for high signal-to-noise galaxy spectra, even allowing for quite complex SFHs. The extent to which this reflexes inadequacies in the detailed modelling or remaining systematics in the data is unclear.

Each galaxy is fit with so-called "τ models" and two component burst models (TCM). The τ models use an exponentially decaying star-formation rate (SFR), SFR $\propto \exp(-t/\tau)$, where t is the time since formation began and τ is the e-folding time, a variable determining the duration of star-formation. Large values of τ, up to 10 Gyrs,

were allowed, which approximate a constant star-formation rate. The parameter space for these models therefore consists of four variables; the τ value, the metallicity of the system, the age of the system and the level of dust attenuation which was applied assuming the Calzetti et al. [2000] law.

The TCM models are made up of two sequential bursts (simple stellar populations) to represent a scenario in which the galaxy forms the majority of its stars at an early stage but has undergone a more recent episode of star-formation. These models are included to prevent objects where the stellar population is dominated by old stars but have had a recent minor starburst that contributes significantly to the rest-frame UV flux being incorrectly classified as younger star-forming galaxies. This is important for the sample studied in this thesis as it is from the red end of the full sample that made up the VLT Large Programme.

The TCM models were constructed by normalising the flux of the younger stellar component to match that of the older population at a rest-frame wavelength of 5000Å. The flux of the two stellar populations were then combined in a fashion that the two populations account for different fractions of the total galaxy mass. The contributing mass fraction of the younger population could vary between 0 and 1, with a finer grid of values at low mass fractions as it is expected that the red galaxies will contain only of a small population of younger stars.

Only a small mass fraction of a younger stellar population is needed to significantly affect the rest-frame UV luminosity of a galaxy mass-dominated by an old stellar population. For an illustration of this see Figure 4.2 where the black line is the SED of a 2 Gyr-old SSP. The red, blue and grey lines show the resulting SED when 0.1%, 0.2% and 0.5% of the total galaxy mass is from a 10Myr-old stellar population. As you can see from Figure 4.2, even with a mass fraction of only 0.1% the starburst still completely dominates the rest-frame UV. However, the end of the rest-frame optical and into the rest-frame NIR the old population is by far the most dominate component in terms of light.

The parameter space for these models consists of 6 variables; metallicity of the old stellar component, age of the old stellar components, metallicity of the young stellar component, age of the young stellar components, the mass fraction of the younger stellar

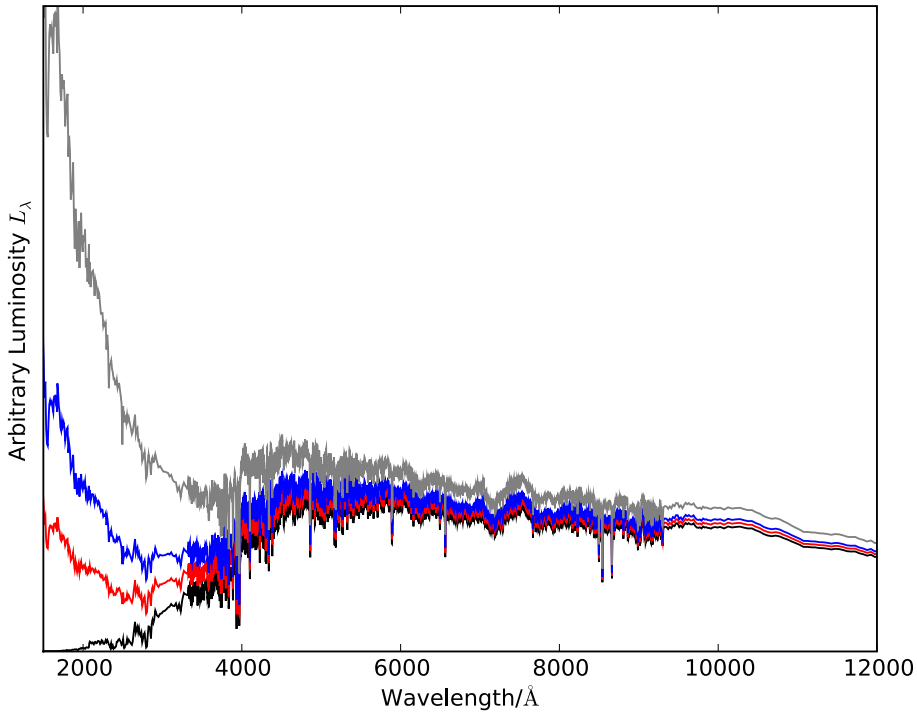

Figure 4.2: The black line is the SED of a 2 Gyr-old SSP. The red, blue and grey lines show the resulting SED when 0.1, 0.2 and 0.5% of the total galaxy mass is from a 10 Myr-old stellar population.

component and dust reddening (A_v) that was applied using the Calzetti et al. [2000] law.

For all star-formation histories (SFHs) the age of the spectral energy distribution (SED) was never allowed to exceed the age of the Universe at each object's redshift. For the TCM models the age of the young stellar components was never allowed to exceed that of the old component.

4.1.2 Model Fitting Process

For the fitting process each model was redshifted to the galaxy's redshift and the target spectra were binned up to match the resolution of the models in the fitting region. The models were then simultaneously fit to the observed optical spectra and $BVJHK$ and IRAC 3.6 & 4.5μm photometry in the observed frame. The region of the spectra used

during the fitting was 6200-9600Å. This was due to the increased severity of the skylines beyond 9600Å and the increased susceptibility to errors in the flux calibration at the extreme ends of the spectra. The photometric broad-band magnitudes were converted to a flux, f_λ, and a model flux for each band was calculated by integrating the model over the filter profiles. The *Riz* optical bands are not used as this region of the galaxy's SED is covered by the optical spectra. The best fit model was found by reducing χ^2,

$$\chi^2 = \sum_i \frac{(d_i - nm_i)^2}{\sigma_i^2}, \tag{4.1}$$

where d_i is the value of the data spectra at point i, m_i is the value of the model spectra at point i, σ_i is the error on the data at point i (which comes from the galaxy's error spectrum) and n is overall normalisation between the data and model.

The normalisation was calculated by solving,

$$\frac{d\chi^2}{dn} = 0, \tag{4.2}$$

i.e. finding the minimum χ^2 with respect to the normalisation. This gives the following analytic formula for the normalisation factor,

$$n = \frac{\sum_i \frac{d_i m_i}{\sigma_i^2}}{\sum_i \frac{m_i^2}{\sigma_i^2}} \tag{4.3}$$

We know that each spectra contains a small number of points that are not physically correct nor accounted for by the error spectrum. Also the galaxy spectra contain emission lines which the models do not. To remove this unusable information from the spectra each galaxy went through the fitting process twice. On the second run spectral points which produced a $\chi^2 > 9$, a point that is a 3σ outlier, on the first fitting were removed from the fitting process. This process is justified because the stellar population synthesis models are known not to produce the detailed features seen in the real data [Tojeiro et al., 2010]. As a consequence, as the signal-to-noise of the data improves the mismatch between data and models tends to an increasingly large χ^2 and models which are incorrectly dominated by small features. Therefore as the signal-to-noise increases the number of spectral points which have an individual $\chi^2 > 9$ increases, see Figures

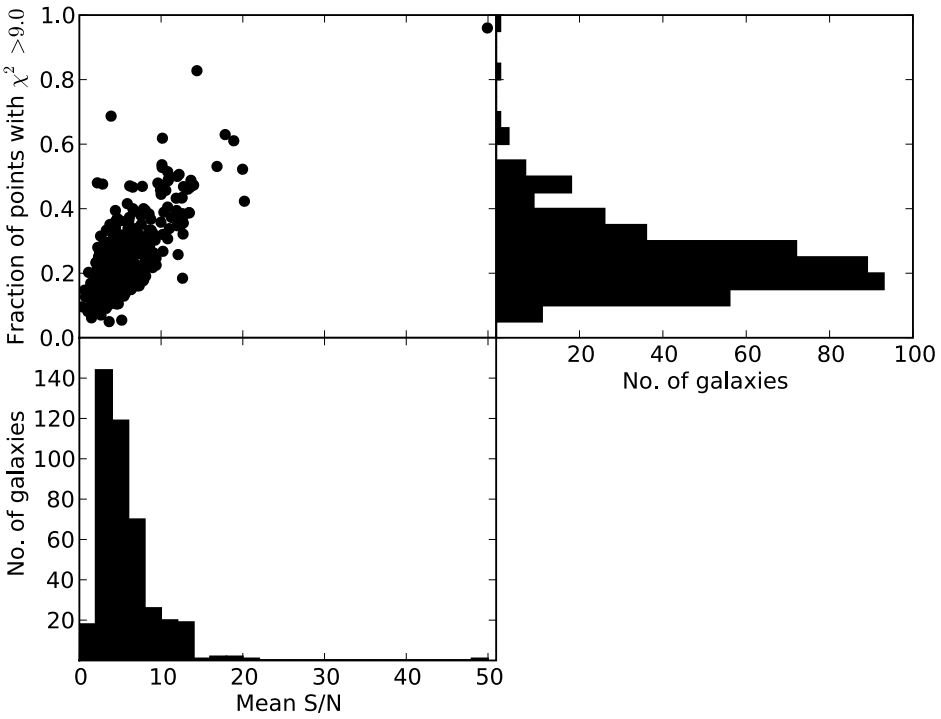

Figure 4.3: The top left plot shows signal-to-noise versus the fraction of points that have $\chi^2 > 9$ for the (first run) fits to the τ models. Signal-to-noise is measured as the mean signal-to-noise per pixel in the range 6200-9600Å, the region used during the fitting process. The lower histogram shows the spread of signal-to-noise throughout the sample and the right-hand histogram shows the spread of the fraction points that have $\chi^2 > 9$.

4.3 and 4.4 for this trend from fits to the spectra with τ and TCM models respectively.

In Figures 4.3 and 4.4 you can see that the fraction of points removed due to having a $\chi^2 > 9$ scales with signal-to-noise. Signal-to-noise is measured as the mean signal-to-noise per pixel in the range 6200-9600Å, the region used during the fitting process. The lower histogram in each figure shows the spread of signal-to-noise throughout the sample and the right histogram shows the spread of the fraction points that have $\chi^2 > 9$.

As shown simply rejecting points based on a cut in χ^2 would result in rejecting large portions of the spectra for the high signal-to-noise objects so a limit on the number of points that can be rejected is required. To estimate this, for the fits to the τ and TCM models, we took all the galaxies within one median absolute deviation of the median

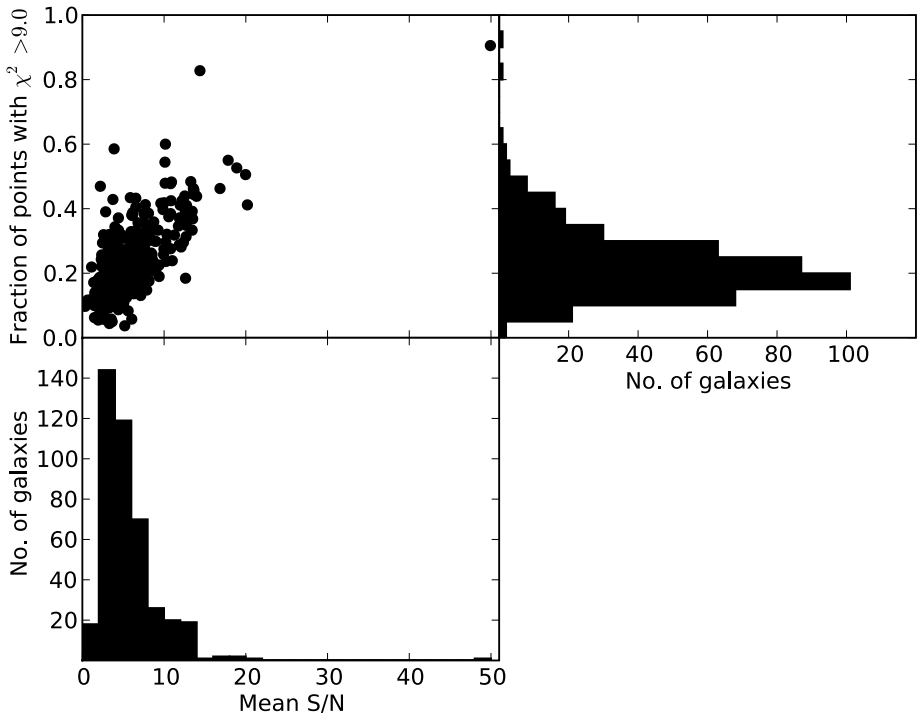

Figure 4.4: The top left plot shows signal-to-nosie versus the fraction of points that have $\chi^2 > 9$ for the (first run) fits to the TCM models. Signal-to-noise is measured as the mean signal-to-noise per pixel in the range 6200-9600Å, the region used during the fitting process. The lower histogram shows the spread of signal-to-noise throughout the sample and the right-hand histogram shows the spread of the fraction points that have $\chi^2 > 9$.

signal-to-noise and then took the mean fraction of points with $\chi^2 > 9$ of this subsample. This was 21.8% and 20.4% for the fits to the τ and TCM models respectively. Therefore we set a maximum limit of 22% of the points that could be rejected. For the galaxies that had more than 22% of their points producing $\chi^2 > 9$, the points to be rejected were the points producing the largest χ^2s.

4.2 Star-formation Rate Indicators

One of the main goals of this thesis is to accurately establish the fraction of truly passive galaxies at $z > 1$, as such it is clearly important to determine the levels of on-going star-

formation in each member of the sample. One measure is model dependent and comes from the best fitting τ-models. In this section I briefly review the empirical methods

4.2.1 Estimates from [OII] emission

Nebular emission associated with star-forming regions can be used as a direct trace of the young massive stellar population [Kennicutt, 1998]. The most reliable emission line used in SFR estimation is Hα as it should scale directly with the fluxes of the embedded stars. However, unfortunately, for the redshifts studied here ($z > 1$), the Hα line is redshifted out of optical spectra. Higher order Balmer lines are also potential SFR indicators when Hα is not available, but are not ideal candidates because they are weaker than Hα and are more affected by dust attenuation [Kennicutt, 1998]. The strongest line blueward of Hα, in normal (non-AGN) galaxies, is the [OII]3726,3729 doublet. It is not as good a tracer of star-formation as Hα because it is sensitive to metallicity, density and the ionisation state of the gas. However, using Hα [Kennicutt, 1998] and Hβ [Gallagher et al., 1989], the [OII] luminosity can be calibrated as a SFR indicator.

For the galaxies in our sample the star-formation rate has been estimated from the continuum subtracted flux of the [OII] emission line in the optical spectra, which is then converted into a luminosity, and then a star-formation rate using the relation from Kennicutt [1998],

$$\mathrm{SFR}(M_{\odot} yr^{-1}) = (1.4 \pm 0.4) \times 10^{-41} L_{[OII]}\ (ergs\ s^{-1}). \tag{4.4}$$

The errors on the amount of flux in the [OII] emission line were calculated using the error spectrum for each object. The typical error on the [OII] flux is comparable to the scatter on the relation between the luminosity of [OII] and the SFR.

4.2.2 Estimates from the rest-frame UV flux

It would be helpful to observe a region of a galaxy's SED that scales linearly with SFR. The rest-frame UV ($\sim 1000-3000$Å) provides this since in a galaxy that is forming stars the UV continuum emission is dominated by O and B type stars with mass $> 10 M_{\odot}$.

For the redshift range of the galaxies in our sample the B-band observes the rest-frame UV region used in the star-formation rate estimated by Madau et al. [1998], i.e. 1500-2800Å(it is only the ∼5% at the extreme high redshift end where the majority of the rest-frame region observed by the B-band is <1500Å). Therefore for all the galaxies in our sample we can use the relation from Madau et al. [1998],

$$SFR(M_{\odot}yr^{-1}) = 3.04 \times 10^{-8-0.4M_{UV}} \tag{4.5}$$

where M_{UV} is the absolute UV magnitude,

$$M_{UV} = m_B - 25.0 - 5\log(D_L) + 2.5\log(1+z), \tag{4.6}$$

where m_B is the apparent B-band magnitude, D_L is the luminosity distance in Mpc, 25.0 is the zero point and z is the galaxy's redshift. The constant in Equation 4.5 has been corrected for a Chabrier IMF.

A SFR estimated from the UV is effected by dust which must be corrected for. This can be approached in two ways, either the UV flux can be corrected using the A_v recovered from the best-fitting model, or the UV SFR can be left uncorrected and added to a SFR estimated from the far-infrared (FIR), if available, as this is the region of the SED where the UV photons are remitted after being absorbed by the dust.

4.2.3 Estimates from 24μm flux

If a galaxy contains dust the UV photons emitted by the massive O and B type stars can be absorbed by the dust. Therefore a galaxy can appear quiescent in rest-frame UV and optical wavelengths. However in this case the UV photons get re-emitted in the FIR with the peak of this emission at $\sim 100\mu m$. Therefore with an estimation of the total infrared luminosity you can calculate a star-formation rate. Ideally one would like to therefore have a measure of the full bolometric as determined from observation in the FIR ($100 - 500\mu m$). However, Elbaz et al. [2010] have shown that, at least out to $z \sim 1.5$, $24\mu m$ observations provide a, perhaps surprisingly, good estimate of SFR.

For the objects that have detections in the MIPS $24\mu m$ data a SFR can therefore be estimated. To do this we have used the conversion from rest-frame $8\mu m$ to total

infrared luminosity from Bavouzet et al. [2008],

$$L_{IR}/L_{\odot} = 377.9 \times (\nu L_{\nu}/L_{\odot})^{0.83}_{8\mu m} \pm 37\%, \tag{4.7}$$

and the conversion from total infrared luminosity to SFR from Kennicutt [1998],

$$SFR(M_{\odot} yr^{-1}) = 4.5 \times 10^{-44} L_{IR}. \tag{4.8}$$

The rest-frame $8\mu m$ luminosity conversion was chosen as this would involve the smallest K-correction as $< 24/(1+z) > \approx 10.5\mu m$ for our sample of galaxies. To acquire a rest-frame $8\mu m$ luminosity from a $24/(1+z)\mu m$ luminosity a model is required to calculate a K-correction. We used the model from Lagache et al. [2003] assuming a starburst galaxy with $L = 10^{11} L_{\odot}$. The model was normalised to match the $24/(1+z)\mu m$ luminosity by integrating the model over the $24\mu m$ MIPS filter. The rest-frame $8\mu m$ luminosity was then recovered from the model by integrating over the IRAC $8\mu m$ filter.

4.3 Measurement of Spectral Features

Given the availability of high signal-to-noise spectra it is important to extract as much information from the galaxy spectra as possible. Consequently, a code was written to measure the 4000Å break (D4000, Bruzual [1983]), the equivalent width of the [OII] emission line (EW[OII]), a UV spectral slope index (CI) and the Balmer break [Kriek et al., 2006].

D4000 and the Balmer break are both defined as,

$$\text{Break strength} = \frac{(\lambda_2 - \lambda_1) \int_{\lambda_1}^{\lambda_2} F_{\nu} d\lambda}{(\lambda_4 - \lambda_3) \int_{\lambda_3}^{\lambda_4} F_{\nu} d\lambda}, \tag{4.9}$$

where (λ_1, λ_2, λ_3, λ_4) = (3750Å, 3950Å, 4050Å, 4250Å) for D4000 and (λ_1, λ_2, λ_3, λ_4) = (3500Å, 3650Å, 3800Å, 3950Å) for the Balmer break.

The equivalent width of the [OII] emission was calculated as,

$$EW[OII] = \int_{3713}^{3741} \frac{F_{\lambda} - F_c}{F_c} d\lambda, \tag{4.10}$$

where F_λ is the flux in the [OII] emission line and F_c is the continuum flux line underneath the emission line. Estimating the continuum beneath the line was done by linearly interpolating between the mean flux in a pass-band either side of the line. The pass-bands were defined as 3653-3713Å and 3741-3801Å.

It was decided to define the CI such that it covered as near to a featureless part of the rest-frame UV spectrum as possible. CI is defined as,

$$CI = -2.5 \log \left(\frac{F_{\nu,1}}{F_{\nu,2}} \right) \tag{4.11}$$

where $F_{\nu,1}$ is the mean flux in the wavelength region 2925-3200Å and $F_{\nu,2}$ is the mean flux in the wavelength region 3400-3700Å (3555-3630Å is excluded as this contains the FeI 3585 feature). This is similar to a colour index defined by Cimatti et al. [2008] which used the regions 2700-3100Å and 3100-3500Å. The colour index here is better as it is was designed to avoid spectral features in the rest-frame UV. The colour index from Cimatti et al. [2008] covers the Mg_{UV} feature [Daddi et al., 2005b], which is an age and metallicity indicator, and also an unknown feature at $\sim$ 3235Å. The colour index defined in Equation 4.11 estimates the slope of the UV continuum without any contamination. Figure 4.5 shows the regions used to define the colour indices from Cimatti et al. [2008] and Equation 4.11 in the upper and lower panels respectively. The regions are shown as shaded grey areas enclosed by dashed black lines. The red dotted lines highlight features in the rest-frame UV spectrum.

4.4 Velocity Dispersion Estimation

In elliptical or pressure supported galaxies the motion of the stars within the galaxies produce a velocity dispersion that is present in the stellar spectral features within the galaxy spectrum. It is assumed that the broadening of absorption features within the galaxy spectra are the convolution of the stellar absorption features and the velocity dispersion of the galaxy. Therefore with reference to a standard stellar spectra this velocity dispersion can be estimated from the galaxy spectra.

For a spectrum of given dispersion the velocity resolution, $R = \lambda/\delta\lambda$, is better with increasing wavelength i.e. the red end. Therefore the Ca IR Triplet 8498, 8542 & 8662

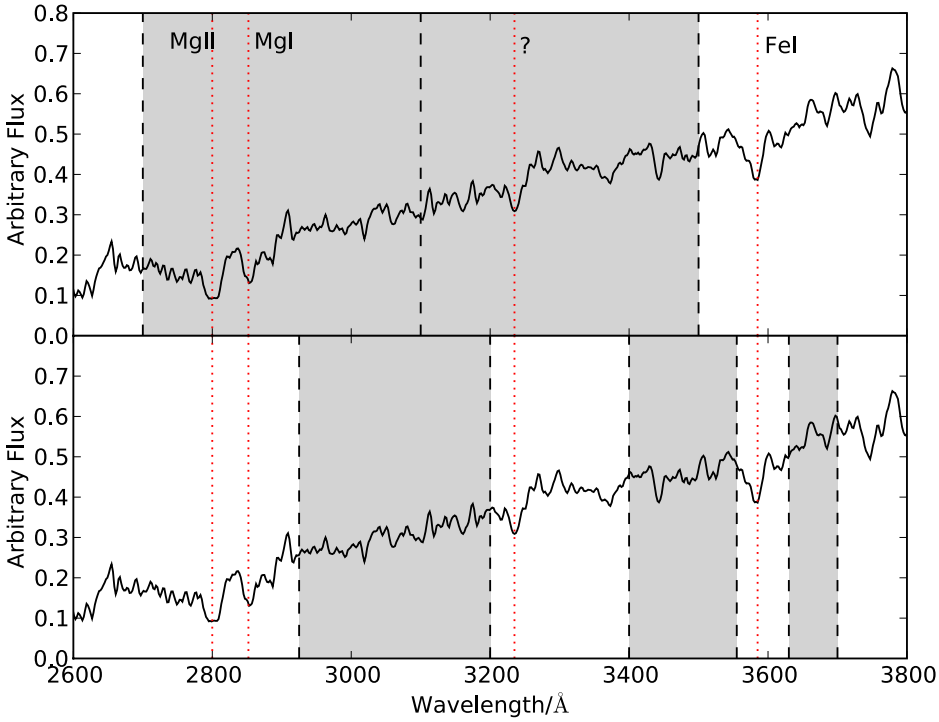

Figure 4.5: The upper panel shows the regions used in the colour index definition from Cimatti et al. [2008] and the lower panel is for the index defined in Equation 4.11. The regions are shown as shaded grey areas enclosed by dashed black lines. The red dotted lines highlight features in the rest-frame UV spectrum.

(e.g. Dressler 1984) and the CO absorption line at $2.29\mu m$ (e.g. Silge and Gebhardt 2003) are features commonly using for estimation of galaxy velocity dispersion. However, for high redshift galaxies these features are redshifted into the NIR, which contains a lot of strong sky emission that can heavily contaminate the feature.

For high-redshift galaxies the only features with the potential of being used for velocity dispersion estimates in optical spectra are MgII, MgI (together forming the Mg_{UV} feature), the Balmer lines and Ca H & K. The Balmer line-widths are mainly due to processes within the stars (for example the $H\delta$ line may be dominated by rotation and pressure broadening of A stars [Wolf and Sheinis, 2008] rather than influenced by their motion within the galaxy. The galaxies in our sample are red so the highest signal-to-noise features will come from the red end of the spectra. The Ca H & K features

have a 40% higher velocity resolution than the Mg_{UV} feature. Therefore for all objects with $z \leq 1.5$ the Ca H & K absorption lines are the best candidates to use for the velocity dispersion estimates. Many authors in the past have avoided using the Ca H & K absorption features due to the features being placed next to the 4000Å break which causes issues removing the continuum accurately. Also Ca H & K are intrinsically broad and therefore are not suited for recovering small velocity dispersions [Dressler, 1984]. However, based on our stellar-mass estimates the galaxies in our sample are massive, so reasonably high velocity dispersions are expected. Ca H & K are strong features and therefore have the benefit of being usable in lower signal-to-noise spectra [Dressler, 1979].

4.4.1 Fitting Convolved Stellar Spectra to Galaxy Spectra

The velocity dispersions were estimated by fitting each galaxy spectra with stellar spectra convolved with a range of Gaussian distributions (assumed to represent the velocity dispersion of the galaxy). Since a sample of stellar spectra containing high signal-to-noise Ca H & K features was required, the 215 stellar spectra from the STELIB Stellar Library Le Borgne et al. [2003] that contain the Ca H & K features were chosen.

Attempting to fit the continuum across the the 4000Å break (i.e. a discontinuity in the continuum) will often lead to the strengths of Ca H & K being wrongly estimated. Depending on the flux levels blueward and redward of the 4000Å break, and the strength of the break itself, the strength of the Ca H & K features can be underestimated or overestimated by either fitting through or over the features. See Figure 4.6 for an example.

Choosing a fitting region of 3915-3985Å for the Ca H & K features the above issues can be avoided by estimating the continuum using small pass-bands either side and assuming, since the fitting region only spans a small wavelength range, that the continuum through the fitting region can be estimated by a linear function.

Therefore using the mean flux in the two pass bands either side of the Ca H & K features, 3900-3915Å and 3985-4000Å, a linear flux was constructed across the features as an estimate of the continuum. This function is then divided through the spectrum and error spectrum of the galaxy. This same procedure is applied to the stellar spectra,

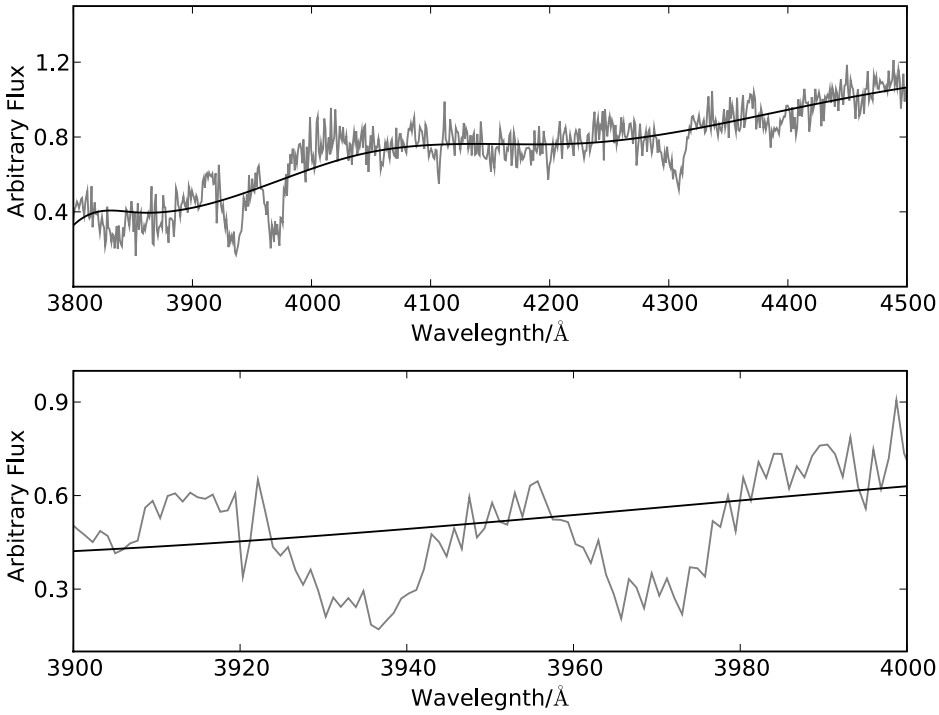

Figure 4.6: Example of a bad continuum fit through the Ca H & K features due to fitting the continuum over too wide a wavelength range.

see Figure 4.7 for an example. The top panel shows the stellar spectra plotted in black with the continuum fit in red and the grey shaded regions are the regions used to define the slope. The lower panel shows the continuum divided spectrum, the grey region shows the spectral range that will be used in the fitting process and the red dotted line shows a relative flux level of 1.

A direct fitting method between the continuum divided Gaussian broadened stellar and galaxy spectra was used to estimate the velocity dispersion of the target galaxies. This method was chosen over Fourier methods (e.g. Sargent et al. 1977), which have the advantage of simplifying the convolution stage of the calculation, as errors are more easily incorporating in the fitting process. The best velocity dispersion estimate was found by reducing the χ^2 between the data and the Gaussian convolved star.

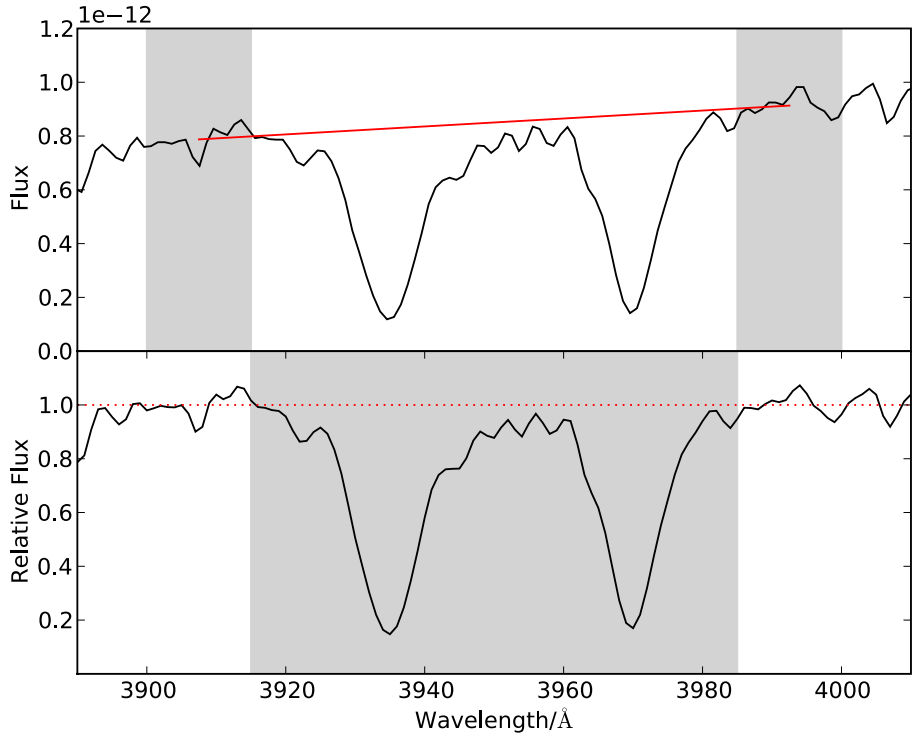

Figure 4.7: Plot showing an example of the continuum fit across the Ca H & K features in a stellar spectra from the STELIB Library. The top panel shows the stellar spectra plotted in black with the continuum fit in red. The grey shaded regions are the regions used to define the slope. The lower panel shows the continuum divided spectrum. The grey region shows the spectral range used in the velocity dispersion fitting process. The red dotted line shows a relative flux level of 1.

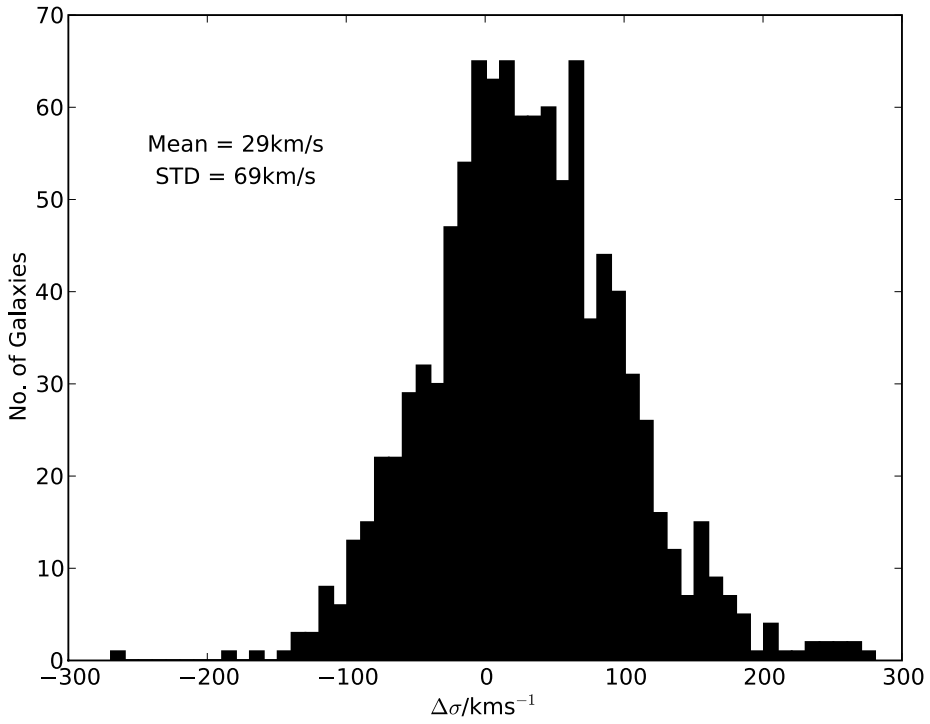

Figure 4.8: Distribution of $\Delta\sigma$ for the SDSS galaxy sample for the test using the SDSS templates at full resolution (1Å per pixel).

4.4.2 Testing the Method on SDSS Data

To test the velocity dispersion estimation method a sample of ∼1000 SDSS high signal-to-noise spectra were used to see if the results obtained by the SDSS team [Bernardi, 2007] could be reproduced. Using the method described above various tests were run, initially an attempt was made to reproduce the SDSS velocity dispersions by fitting the Ca H & K region using the SDSS stellar templates at their high resolution of 1Å per pixel. Let $\Delta\sigma$ be the difference in the velocity dispersion estimates of the SDSS and the estimations made here. The distribution $\Delta\sigma$ for this initial test can be seen in Figure 4.8.

The test was repeated but with the SDSS stellar templates replaced with the stellar spectra from the STELIB stellar library. See Figure 4.9 for the distribution of $\Delta\sigma$ from this test, it is nearly identical to the distribution recovered from the test using the SDSS

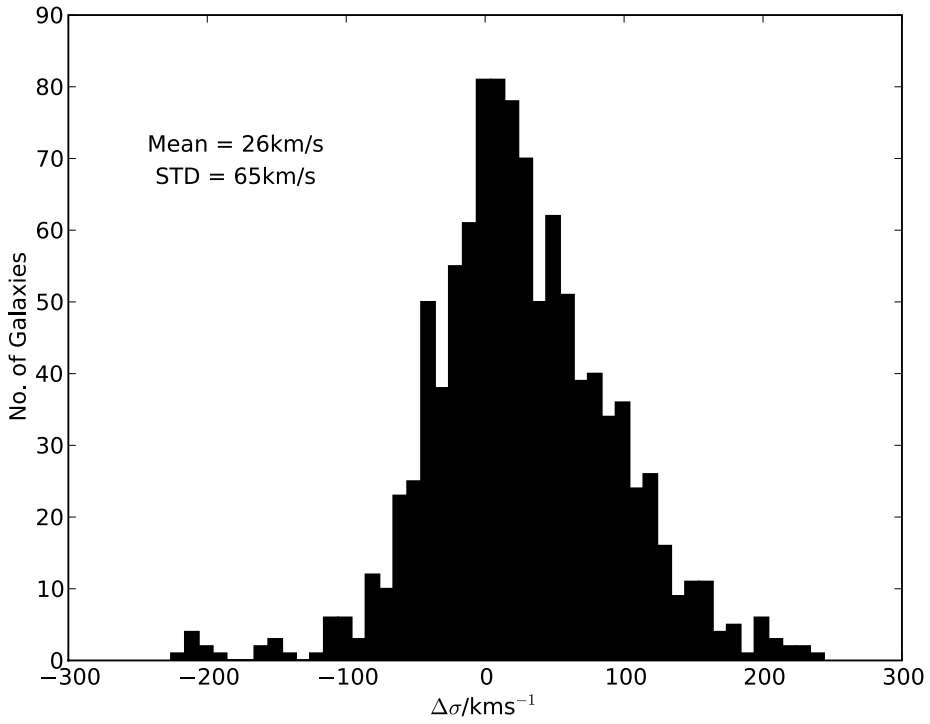

Figure 4.9: Distribution of $\Delta\sigma$ for the SDSS galaxies for the test using the STELIB Library templates at full resolution (1Å per pixel).

templates indicating, that choice of template does not play an important role.

Next the SDSS galaxy spectra were binned up to 2.6Å, so they matched the resolution of the galaxy spectra in the sample studied here. The stellar spectra were rebroadened to include an initial broadening with a Gaussian of $\sigma \sim 1.8$ to account for the difference in resolution introduced between the galaxy and stellar spectra. Figure 4.10 shows the distribution of $\Delta\sigma$ for the velocity dispersion recovered using the SDSS templates after degrading the resolution of both the test galaxy spectra and the templates.

As before this test was then repeated with the STELIB stellar library. This final test is the method that would be used on the galaxy sample studied here. The $\Delta\sigma$ distribution for the velocity dispersions recovered for the final test and can be seen in Figure 4.11.

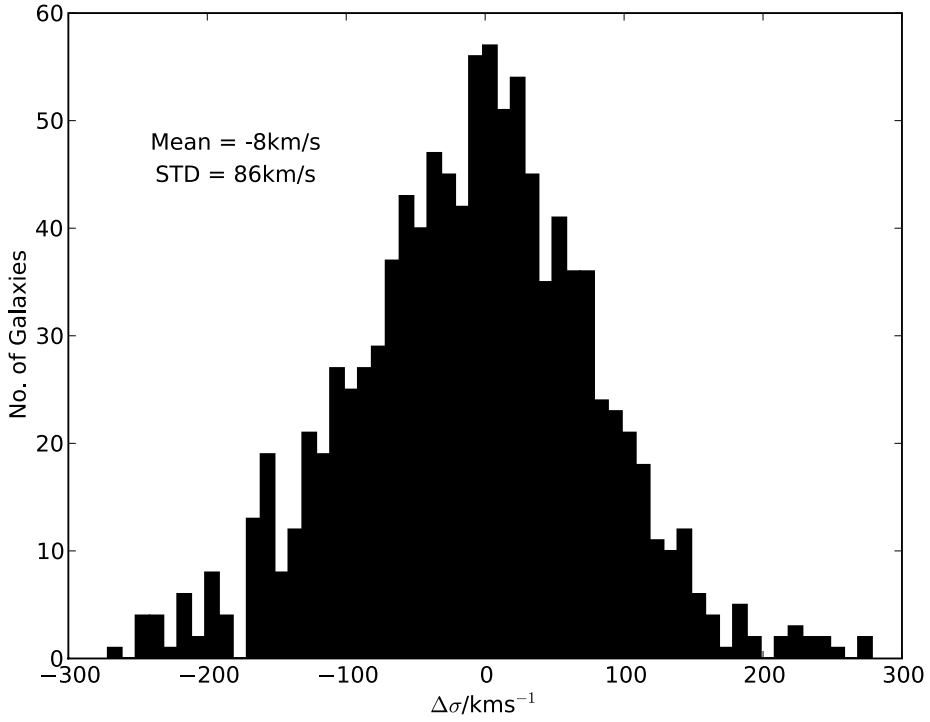

Figure 4.10: Distribution of $\Delta\sigma$ for the SDSS galaxies for the test using the SDSS templates after the resolution of both spectra and templates were degraded to 2.6Å per pixel.

From Figure 4.11 is can be concluded that the method used here can be used to estimate the velocity dispersions of elliptical galaxies, with a typical accuracy of $\pm 76 \mathrm{kms}^{-1}$ which is consistent with our typical error of 45 if it is also assumed similar errors actually apply to the SDSS values. We thus conclude that our estimated uncertainties in velocity dispersion are reasonable.

4.5 Composite Construction

To improve signal-to-noise and get a measurement of the typical spectral properties of a galaxy sample, a powerful technique is to produce so-called composite spectra composed of stacks of spectra grouped by redshift, type, stellar mass etc. This technique is exploited in Chapter 7, and the methods adopted are outlined here.

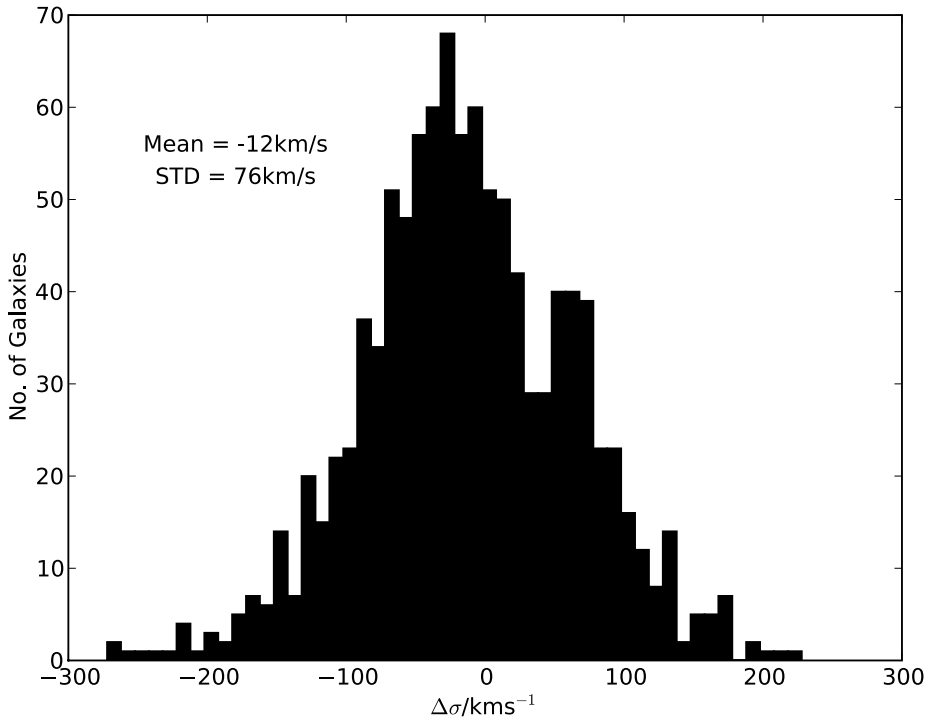

Figure 4.11: Distribution of $\Delta\sigma$ for the SDSS galaxies for the test using the STELIB Library templates after the resolution of both spectra and templates were degraded to 2.6Å per pixel.

4.5.1 Spectral Composites

To stack spectra a common wavelength region is require so that each spectra can be correctly normalised. If the spectra are not normalised to each other the final composite will be biased towards the brighter objects in the sample which could obviously bias the final characteristics of the composite. For example the brighter objects in the sample could be more massive or have higher star-formation rates depending on what rest-frame wavelengths are covered by the optical spectra. There could also be second order biases from this, for example if you bias towards the more massive galaxies you could also be biasing towards older galaxies.

Given the range of redshifts spanned by our sample there is not a common overlap region which can be used to normalise all galaxies. Therefore we decided to make all composite spectra in redshifts bins that will contain a common overlap region between

Table 4.1: Definitions of redshift bins used for combining galaxy spectra.

Bin	Lookback times (Gyr)	Redshifts
1	6.25-7.75	0.691-1.009
2	7.75-8.25	1.009-1.138
3	8.25-8.75	1.138-1.291
4	8.75-9.25	1.291-1.472
5	9.25-10.75	1.472-2.294

all the galaxies in that bin. The science results from the composite spectra will come from the redshift bin stacks but for presentation purposes composites from the full redshift range are desirable. To produce composites spanning the full redshift space of our sample we then combined the redshift bin composites. This is not ideal but we believe it is better than the alternative of using a "master galaxy spectrum", around the median redshift, that has overlapping regions with all the other spectra in the sample and normalising all other spectra to that as in Abraham et al. [2004]. This will give a SED shape bias to the final composite. For example if your "master galaxy spectrum" is a red object then the lower redshift objects in your sample will be normalised to the red, brighter end of the spectrum and the higher redshift objects to the fainter blue end of the spectrum.

We defined redshift bins to cover equal periods of lookback in the epoch spanned by the majority of our spectra, these are shown in Table 4.1. For each galaxy sample the composite was constructed with the following procedure. Initially each galaxy spectra was de-redshifted to the rest-frame. The normalisation region was defined as the maximum spectral wavelength overlap between the spectra in the sample. Each galaxy was then normalised over this range. A master wavelength grid was then constructed spanning the full range of the spectra included in the composite, with a pixel bin size taken to be to the rest-frame pixel bin size of the galaxy with the median redshift in the sample. A flux for each master pixel bin was then calculated as the weighted median of all the pixels (and sub pixels) from the galaxies that have flux covering that pixel. The error spectrum for each composite was produced by calculating the standard error on all the points that made up a pixel bin on the final composite and times it by 1.253 to

get the standard error on the median.

This process was then mimicked when stacking together the composites of the different redshift bins.

4.5.2 Photometric Composite

To maximise the information from each galaxy their photometry were also combined to give information shortward and longward of the optical spectra.

Each galaxy's photometry is converted to a flux, f_λ, and normalised by the same factor as the galaxy's optical spectrum was in the creation of the spectral composite. Each photometric point was taken to be a boxcar function with a width such that the function had the same area as the original filter transmission with the height of that at the effective wavelength, see Figure 4.12 for an example of this for the H-band, where the grey line shows the true filter profile for the H-band and the red boxcar function shows the approximation.

Due to the fact that within a given redshift bin the span of redshifts is small an average band measurement was created for each photometric band by taking the median of all the fluxes for a band. The band width was taken to be the boxcar filter for that band from the galaxy with the median redshift.

The analysis techniques described above have been used throughout this thesis to determine the physical characteristics of the spectroscopic K-band selected sample within the UDS. The stellar mass and radii estimates are used to investigate the size-mass relation at high-redshift and the velocity dispersion estimates present to opportunity to determine dynamical masses and investigate this relation with model independent galaxy mass estimates. The stellar mass estimates along with the SFR estimates are used to derive specific star-formation rates (SSFRs) which are then used to divide the galaxy sample into passively evolving and actively star-forming subsamples. The construction of composites is used to study the average properties and evolution of various galaxy subsamples.

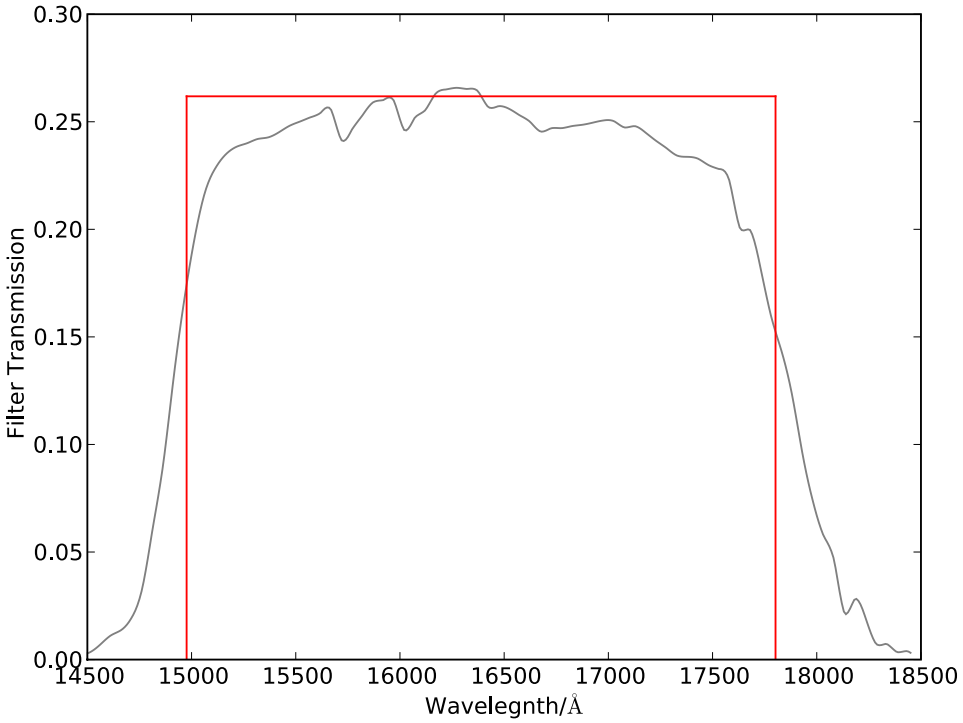

Figure 4.12: The grey line shows the true filter profile for the H-band and the red boxcar function shows the approximation used when constructing the photometric composite.

Chapter 5

Massive Galaxies at $1.3 \lesssim z \lesssim 1.5$

Massive galaxies at high-redshift are very important when constraining galaxy evolution models as until recently they were theoretically predicted to only form at $z \leq 1$ through hierarchical clustering. Understanding these systems is going to play a crucial role in developing theories to describe the Universe we observe. Accurate measurements of their physical characteristics is required to gain this understanding. Here a unique spectroscopic sample of high redshift K-band bright targets have been studied. Stellar and dynamical-masses are used to investigate the high-redshift size-mass relation which is far from being fully understood. Dynamical masses have been derived from the largest single sample of velocity dispersions measurements at $z > 1.3$. Finally, specific star-formation rates are calculated in order to estimate the passive fraction of the K-band bright population at high-redshift. The redshift range $1.3 \lesssim z \lesssim 1.5$ was chosen as it gave the largest sample of galaxies at the highest redshifts while still including key features with the wavelength range covered by the FORS2 spectra (e.g. Mg_{UV}, the [OII] emission line and the 4000Å break.)

5.1 The Galaxy Sample

In order to extend spectral studies of massive galaxies at high-redshift into new territory a sample was compiled of all the high-redshift objects, $1.3 \lesssim z_{spec} \lesssim 1.5$, that are bright in the K-band, with $K_{total} \leq 21.5$. This produced a sample of 82 high-redshift objects (see Table 5.1 for the spectroscopic redshifts, K-band magnitudes and the $R-K$ colours)

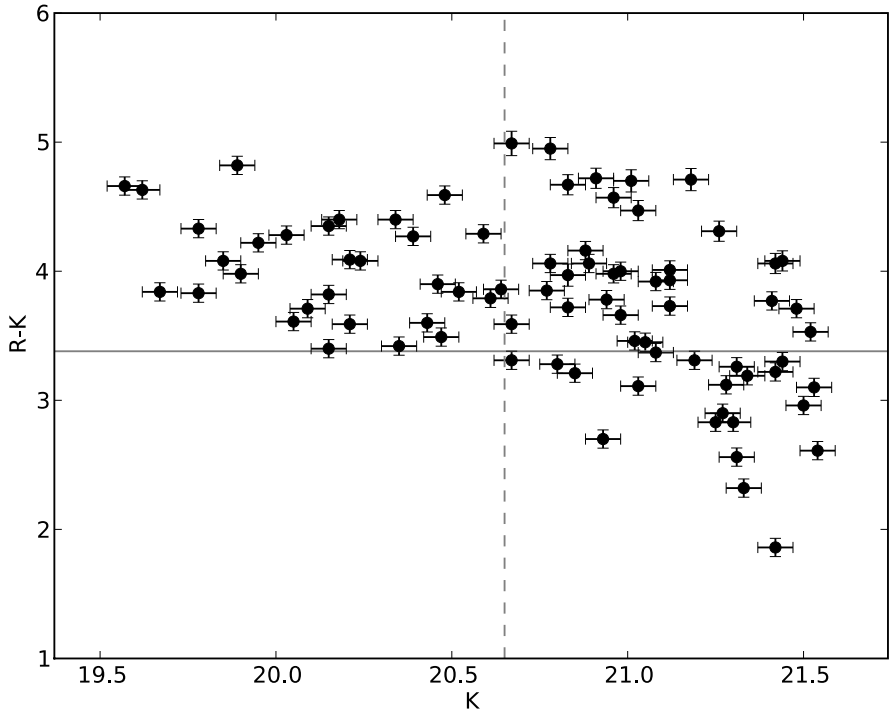

Figure 5.1: $K-(R-K)$ colour magnitude diagram for the galaxies in our sample. The solid grey line shows $R-K=3.38$, which is equivalent to a $(R-K)_{Vega}=5$ and the vertical grey dashed line is a magnitude cut of $K=20.65$ which separates a pure ERO sample from a mixed sample.

with a mean redshift of $<z>=1.41$, hereafter referred to as the K-Bright sample. One of the FORS2 masks potentially contains a structure at $z\sim1.32$ for which 4 of the members made it into the our sample, removing this structure does not change the mean redshift. Figure 5.1 shows K vs. $R-K$ plot for the galaxy sample, where the solid grey line shows $R-K=3.38$, which is equivalent to $(R-K)_{Vega}=5$, the standard definition for an extremely red object (ERO). Overall, $61/82$ ($\sim75\%$) of our sample are EROs and have $R-K>3.38$. Notably splitting the sample by K-band magnitude at $K<20.65$ (the vertical grey dashed line in Figure 5.1) produces two sub-samples with 100% and 60% EROs respectively

Table 5.1: Basic properties of the K-Bright sample. Column 1 lists the IDs, columns 2 & 3 lists the RA and DEC (J2000) respectively, column 4 lists the spectroscopic redshift (typically accuracy of ±0.002), column 5 lists the K-band magnitude (in a 3" aperture) and column 6 lists the $R-K$ colours.

ID	RA	DEC	z_{spec}	K	R-K
69422	02:18:43	-04:51:17	1.296	20.15	3.40
80073	02:18:08	-04:45:02	1.299	20.18	4.40
76779	02:17:36	-04:46:57	1.303	21.52	3.53
80464	02:18:35	-04:44:49	1.304	21.48	3.71
65948	02:17:27	-04:53:19	1.305	20.64	3.86
63940	02:16:46	-04:54:28	1.311	21.44	4.08
53901	02:19:15	-05:00:13	1.313	19.85	4.08
32058	02:18:47	-05:12:57	1.315	20.93	2.70
58266	02:19:19	-04:57:47	1.316	20.09	3.71
42643	02:19:12	-05:06:44	1.319	19.78	3.83
79330	02:17:19	-04:45:22	1.320	21.19	3.31
46450	02:19:09	-05:04:37	1.320	20.83	3.72
29501	02:18:46	-05:14:28	1.320	21.03	3.11
77399	02:17:05	-04:46:32	1.321	20.03	4.28
46091	02:19:09	-05:04:49	1.321	20.34	4.40
50618	02:19:12	-05:02:09	1.321	20.43	3.60
65792	02:19:14	-04:53:23	1.322	21.05	3.45
79998	02:17:20	-04:45:07	1.323	20.98	3.66
50326	02:17:37	-05:02:22	1.325	21.08	3.92
77581	02:18:02	-04:46:27	1.326	21.08	3.37
53783	02:17:59	-05:00:20	1.329	21.42	3.22
73006	02:16:55	-04:49:10	1.331	20.67	3.31
60493	02:19:20	-04:56:25	1.332	19.67	3.84
75483	02:16:58	-04:47:43	1.372	20.15	3.82
78289	02:18:05	-04:46:03	1.380	21.33	2.32
73717	02:17:22	-04:48:46	1.380	21.30	2.83
42941	02:17:38	-05:06:37	1.394	21.03	4.47
77327	02:18:03	-04:46:36	1.399	20.52	3.84
79158	02:17:59	-04:45:30	1.399	19.90	3.98

Table 5.1: - continued

ID	RA	DEC	z_{spec}	K	R-K
49095	02:18:47	-05:03:04	1.401	20.61	3.79
79274	02:17:06	-04:45:30	1.401	21.27	2.90
45629	02:19:10	-05:05:08	1.401	21.42	4.06
61110	02:18:33	-04:56:04	1.402	20.83	3.97
56208	02:16:24	-04:58:59	1.402	20.67	3.59
54647	02:18:50	-04:59:51	1.405	20.96	4.57
63911	02:16:18	-04:54:27	1.405	20.24	4.08
57918	02:18:34	-04:58:00	1.407	20.77	3.85
56439	02:17:23	-04:58:48	1.408	19.62	4.63
45372	02:18:32	-05:05:15	1.408	20.21	4.09
44194	02:19:25	-05:05:52	1.408	20.05	3.61
59320	02:16:07	-04:57:07	1.409	19.78	4.33
32227	02:16:59	-05:12:51	1.410	20.91	4.72
54522	02:17:32	-04:59:55	1.410	21.18	4.71
49961	02:17:37	-05:02:33	1.411	20.48	4.59
63237	02:18:08	-04:54:51	1.412	20.98	4.00
46492	02:18:39	-05:04:34	1.414	20.47	3.49
52436	02:17:36	-05:01:07	1.421	20.46	3.90
63675	02:16:52	-04:54:37	1.429	21.12	4.01
29788	02:16:59	-05:14:20	1.435	21.41	3.77
81348	02:17:03	-04:44:21	1.435	21.50	2.96
62125	02:17:19	-04:55:27	1.441	19.57	4.66
53841	02:17:02	-05:00:18	1.444	20.78	4.95
46886	02:17:06	-05:04:23	1.451	21.28	3.12
78217	02:17:22	-04:46:03	1.456	20.59	4.29
47359	02:18:42	-05:03:58	1.456	20.21	3.59
48550	02:18:06	-05:03:26	1.456	20.88	4.16
32476	02:17:59	-05:12:43	1.458	21.53	3.10
73600	02:17:06	-04:48:50	1.458	21.26	4.31
19851	02:18:07	-05:20:33	1.458	20.80	3.28
58689	02:17:19	-04:57:34	1.459	21.12	3.93
64357	02:17:17	-04:54:13	1.460	21.31	3.26

Table 5.1: - continued

ID	RA	DEC	z_{spec}	K	R-K
79138	02:17:21	-04:45:32	1.461	20.85	3.21
78923	02:17:21	-04:45:41	1.462	20.89	4.06
44334	02:17:25	-05:05:49	1.467	19.95	4.22
62775	02:16:49	-04:55:06	1.467	21.01	4.70
66424	02:17:01	-04:53:03	1.467	20.83	4.67
71384	02:17:26	-04:50:08	1.477	19.89	4.82
72088	02:17:19	-04:49:46	1.477	21.34	3.19
72815	02:17:30	-04:49:18	1.477	21.31	2.56
30838	02:16:58	-05:13:38	1.477	21.54	2.61
60843	02:18:40	-04:56:14	1.478	21.25	2.83
53230	02:18:51	-05:00:36	1.478	20.35	3.42
70067	02:17:24	-04:50:56	1.478	20.96	3.98
56151	02:18:44	-04:59:01	1.483	20.78	4.06
52354	02:16:53	-05:01:11	1.483	21.42	1.86
48451	02:19:14	-05:03:25	1.485	20.15	4.35
29201	02:17:20	-05:14:41	1.485	21.44	3.30
43168	02:18:34	-05:06:28	1.491	21.12	3.73
47774	02:18:30	-05:03:50	1.497	20.94	3.78
50229	02:18:38	-05:02:24	1.498	21.02	3.46
54253	02:16:23	-05:00:02	1.502	20.39	4.27
61727	02:18:02	-04:55:44	1.505	20.67	4.99

Table 5.2: Table describing the parameter space of the τ and two component burst (TCM) stellar population models used to fit the K-Bright sample. Large values of τ are allowed to approximate constant star-formation. In the TCM models the age of the young stellar component is not allowed to exceed that of the old component. The age of the τ model and of the old stellar component in the TCM models is not allowed to exceed that of the age of the Universe at a given redshift.

Model Type	Parameters
τ	τ: $0.1, 0.3, 0.5, 1, 3, 5, 10$Gyr
	Metallicity: $0.2, 0.4, 1, 2.5 Z_{\odot}$
	Age: 0.001Gyr - Age of Universe
TCM	Met. of old pop: $0.2, 1 Z_{\odot}$
	Age of old pop: 0.5Gyr - Age of Universe
	Met. of young pop: $0.2, 1, 2.5 Z_{\odot}$
	Age of young pop: $0.01 - 0.5$Gyr
	Flux fraction of young pop: $0.0 - 1.0$

5.2 Spectrophotometric Fits to the Targets

Using the spectrophotometric fitting process described in Section 4.1 and the parameter space described in Table 5.2 each galaxy was fitted to a model grid of up to $\sim 5 \times 10^5$ models per object, depending on the galaxy's redshift. The best-fitting parameters for each galaxy for the τ and TCM models can be seen in Tables 5.3 and 5.4 respectively, and four example spectrophotometric fits are shown in Figure 5.2. In Figure 5.2 the optical galaxy spectra are plotted in black, the error spectra are green, the photometry is in red and the best-fitting models are plotted in grey. The left panel of each row shows the full fit and the right panel shows a close up of the fitting region containing the optical spectra. For presentation purposes the optical spectra have been smoothed by a 5 pixel boxcar.

5.2.1 Galaxy Stellar-Mass Estimates

A stellar-mass estimate can be acquired from the best-fitting model from the spectrophotometric fitting process. Two mass estimates are available for each galaxy, one

Table 5.3: The best-fitting parameters for each galaxy from the spectrophotometric fits with exponentially decaying star-formation rate models (τ models). Column 1 is the object's ID, column 2 in the τ of the model, column 3 is the metallicity relative to solar, column 4 is the model age, column 5 is the ratio of age to τ, column 6 is the required amount of reddening via the Calzetti Law [Calzetti et al., 2000] and column 7 is the stellar-mass of the best-fitting model. Uncertainty in the mass is derived by marginalising over all τs, metallicities, ages and A_vs for the single component models. The uncertainty is relatively small because the redshift is accurately determined and here we are only considering τ models.

ID	τ (Gyr)	Met. ($Z/Z_\odot$)	Age (Gyr)	Age/τ	Av	$M_\star$ ($10^{11}\mathrm{M}_\odot$)
69422	0.3	0.4	2.30	7.7	0.3	$1.31^{+0.10}_{-0.10}$
80073	0.3	2.5	2.20	7.3	0.2	$1.22^{+0.12}_{-0.05}$
76779	0.3	0.2	1.61	5.4	0.4	$0.14^{+0.04}_{-0.02}$
80464	0.3	0.4	1.61	5.4	0.4	$0.19^{+0.02}_{-0.02}$
65948	0.3	0.2	2.10	7.0	0.6	$0.56^{+0.05}_{-0.07}$
63940	0.3	1.0	2.30	7.7	0.1	$0.32^{+0.01}_{-0.03}$
53901	0.5	1.0	3.50	7.0	0.2	$2.18^{+0.29}_{-0.87}$
32058	0.3	0.2	1.70	5.7	0.0	$0.28^{+0.03}_{-0.01}$
58266	1.0	0.2	4.25	4.3	0.6	$1.37^{+0.20}_{-0.03}$
42643	0.5	0.2	4.00	8.0	0.5	$2.62^{+0.03}_{-0.23}$
79330	0.3	2.5	0.64	2.1	1.5	$0.31^{+0.19}_{-0.02}$
29501	1.0	0.2	3.25	3.3	0.6	$0.44^{+0.10}_{-0.17}$
46450	0.3	0.2	2.20	7.3	0.5	$0.64^{+0.05}_{-0.05}$
77399	0.3	2.5	1.80	6.0	0.4	$1.15^{+0.54}_{-0.14}$
46091	0.3	0.2	3.25	10.8	0.6	$1.23^{+0.44}_{-0.12}$
50618	0.5	2.5	3.00	6.0	0.0	$1.27^{+0.06}_{-0.25}$
65792	0.5	2.5	2.60	5.2	0.0	$0.57^{+0.09}_{-0.20}$
79998	0.3	0.4	2.00	6.7	0.1	$0.34^{+0.08}_{-0.04}$
50326	0.5	0.2	4.25	8.5	0.1	$0.56^{+0.04}_{-0.03}$
77581	0.3	0.4	1.80	6.0	0.0	$0.26^{+0.10}_{-0.00}$
53783	0.3	0.2	1.80	6.0	0.1	$0.22^{+0.03}_{-0.01}$
73006	0.3	0.2	1.14	3.8	0.8	$0.39^{+0.06}_{-0.03}$
60493	0.3	2.5	2.10	7.0	0.0	$2.12^{+0.05}_{-0.22}$
75483	0.3	0.4	2.20	7.3	0.2	$1.21^{+0.10}_{-0.16}$
78289	0.3	1.0	1.14	3.8	0.0	$0.20^{+0.03}_{-0.04}$
73717	0.3	0.2	0.01	0.0	3.0	$0.11^{+3.57}_{-0.01}$
42941	0.3	1.0	1.68	5.6	0.9	$0.55^{+0.08}_{-0.05}$

Table 5.3: - continued

ID	τ (Gyr)	Met. ($Z/Z_\odot$)	Age (Gyr)	Age/τ	Av	$M_\star$ (10^{11}M$_\odot$)
77327	0.3	1.0	2.10	7.0	0.0	$0.85^{+0.04}_{-0.08}$
79158	0.3	1.0	1.90	6.3	0.4	$1.82^{+0.21}_{-0.06}$
49095	0.5	0.2	3.00	6.0	0.2	$0.70^{+0.11}_{-0.23}$
79274	0.5	1.0	1.90	3.8	0.1	$0.29^{+0.04}_{-0.01}$
45629	0.3	0.2	2.60	8.7	0.4	$0.45^{+0.04}_{-0.02}$
61110	0.3	0.2	4.25	14.2	0.2	$1.02^{+0.05}_{-0.13}$
56208	0.3	0.2	2.10	7.0	0.2	$0.64^{+0.03}_{-0.06}$
54647	0.5	0.2	4.00	8.0	0.4	$0.87^{+0.03}_{-0.11}$
63911	0.3	1.0	2.10	7.0	0.0	$1.01^{+0.00}_{-0.13}$
54647	0.5	0.2	4.00	8.0	0.4	$0.85^{+0.04}_{-0.11}$
57918	0.5	0.2	4.00	8.0	0.1	$0.94^{+0.08}_{-0.05}$
56439	0.3	0.4	2.30	7.7	0.7	$3.02^{+0.24}_{-0.19}$
45372	0.3	2.5	2.10	7.0	0.0	$1.43^{+0.11}_{-0.16}$
44194	0.5	1.0	2.60	5.2	0.2	$1.39^{+0.07}_{-0.19}$
54522	0.3	1.0	2.10	7.0	0.4	$0.51^{+0.07}_{-0.04}$
59320	0.3	1.0	1.80	6.0	0.4	$1.52^{+0.23}_{-0.20}$
32227	0.5	1.0	2.20	4.4	1.25	$0.86^{+0.09}_{-0.09}$
54522	0.5	0.2	3.25	6.5	0.8	$0.65^{+0.14}_{-0.24}$
49961	0.3	1.0	2.00	6.7	0.4	$0.96^{+0.14}_{-0.04}$
63237	0.3	0.4	1.80	6.0	0.3	$0.35^{+0.05}_{-0.01}$
46492	0.3	0.2	1.70	5.7	0.3	$0.52^{+0.01}_{-0.01}$
52436	0.3	0.2	1.90	6.3	0.6	$0.92^{+0.03}_{-0.09}$
63675	0.3	1.0	0.72	2.4	2.0	$0.58^{+0.16}_{-0.08}$
81348	0.5	1.0	2.30	4.6	0.0	$0.31^{+0.05}_{-0.12}$
29788	0.3	1.0	1.80	6.0	0.2	$0.34^{+0.05}_{-0.05}$
62125	0.5	0.2	4.25	8.5	0.5	$4.22^{+0.66}_{-0.20}$
53841	0.3	0.4	1.61	5.4	1.25	$0.69^{+0.04}_{-0.15}$
46886	0.5	1.0	2.00	4.0	0.1	$0.33^{+0.01}_{-0.01}$
78217	0.3	0.4	2.00	6.7	0.3	$0.70^{+0.02}_{-0.12}$
48550	0.3	1.0	1.61	5.4	0.5	$0.54^{+0.08}_{-0.02}$
47359	0.3	1.0	2.00	6.7	0.0	$1.35^{+0.14}_{-0.14}$

Table 5.3: - continued

ID	τ (Gyr)	Met. ($Z/Z_\odot$)	Age (Gyr)	Age/τ	Av	$M_\star$ (10^{11}M$_\odot$)
32476	0.5	1.0	2.10	4.2	0.1	$0.30^{+0.01}_{-0.01}$
73600	0.3	1.0	2.10	7.0	0.1	$0.45^{+0.07}_{-0.02}$
19851	0.3	1.0	1.43	4.8	0.3	$0.50^{+0.30}_{-0.06}$
58689	0.3	1.0	1.80	6.0	0.2	$0.45^{+0.19}_{-0.06}$
64357	0.3	1.0	1.61	5.4	0.0	$0.32^{+0.18}_{-0.08}$
79138	0.3	1.0	1.61	5.4	0.0	$0.53^{+0.06}_{-0.10}$
78923	0.3	1.0	2.30	7.7	0.0	$0.82^{+0.07}_{-0.07}$
44334	0.3	1.0	2.10	7.0	0.1	$1.49^{+0.07}_{-0.20}$
62775	0.3	0.4	1.70	5.7	0.9	$0.50^{+0.16}_{-0.01}$
66424	0.5	1.0	3.25	6.5	0.4	$1.05^{+0.15}_{-0.29}$
71384	0.5	1.0	3.75	7.5	0.0	$2.73^{+0.42}_{-0.38}$
72088	0.3	1.0	1.43	4.8	0.1	$0.29^{+0.27}_{-0.07}$
72815	0.3	1.0	0.64	2.1	1.0	$0.30^{+0.01}_{-0.03}$
30838	0.3	0.4	0.45	1.5	1.25	$0.17^{+6.92}_{-0.01}$
70067	0.3	1.0	2.10	7.0	0.0	$0.63^{+0.4}_{-0.06}$
60843	0.3	1.0	1.43	4.8	0.0	$0.37^{+0.03}_{-0.01}$
53230	0.5	1.0	2.60	5.2	0.0	$1.23^{+0.17}_{-0.51}$
56151	0.3	0.4	2.40	8.0	0.0	$0.80^{+0.06}_{-0.06}$
52354	0.3	0.2	0.90	3.0	0.0	$0.16^{+0.02}_{-0.01}$
29201	0.3	0.4	1.43	4.8	0.2	$0.22^{+0.13}_{-0.02}$
48451	0.5	1.0	2.75	5.5	0.6	$2.19^{+0.33}_{-0.74}$
43168	0.3	1.0	1.70	5.7	0.1	$0.43^{+0.05}_{-0.01}$
47774	0.3	1.0	1.70	5.7	0.0	$0.50^{+0.10}_{-0.14}$
50229	0.3	1.0	1.80	6.0	0.0	$0.59^{+0.31}_{-0.07}$
54253	0.5	1.0	3.50	7.0	0.0	$1.73^{+0.26}_{-0.34}$
61727	0.3	0.2	2.75	9.2	0.5	$0.98^{+0.24}_{-0.19}$

Table 5.4: The best-fitting parameters for each galaxy from the spectrophotometric fits with the two component burst models (TCM models). Column 1 is the ID of the object, column 2 is the metallicity of the older stellar population, column 3 is the age estimate of the old stellar population, column 4 is the metallicity of the younger stellar population, column 5 is the age estimate of the younger stellar population, column 6 is the required amount of reddening via the Calzetti Law [Calzetti et al., 2000], column 7 is the stellar-mass of the best-fitting model and column 8 is the fraction of mass that resides in the younger stellar component. Uncertainty in the mass is derived by marginalising over all metallicities, ages, A_vs and young component mass fractions for the two component models. The uncertainty is relatively small because the redshift is accurately determined and here we are only considering the TCM models.

ID	Old Pop. Met. ($Z/Z_\odot$)	Old Pop. Age (Gyr)	Young Pop. Met. ($Z/Z_\odot$)	Young Pop. Age (Gyr)	Av	$M_\star$ ($10^{11}\mathrm{M}_\odot$)	Mass Fraction
69422	0.2	4.50	1.0	0.51	0.3	$1.83^{+0.27}_{-0.07}$	0.050
80073	1.0	4.50	1.0	0.36	0.2	$1.94^{+0.11}_{-0.09}$	0.010
76779	1.0	1.28	0.2	0.36	0.1	$0.13^{+0.10}_{-0.00}$	0.100
80464	1.0	0.72	0.2	0.01	0.8	$0.23^{+0.03}_{-0.03}$	0.002
65948	0.2	1.61	2.5	0.14	0.5	$0.45^{+0.07}_{-0.01}$	0.005
63940	0.2	4.50	2.5	0.29	0.4	$0.52^{+0.03}_{-0.16}$	0.020
53901	1.0	4.25	0.2	0.07	0.2	$3.15^{+0.18}_{-0.54}$	0.001
32058	0.2	1.02	2.5	0.29	0.1	$0.20^{+0.05}_{-0.02}$	0.400
58266	0.2	4.50	2.5	0.10	0.7	$1.75^{+0.26}_{-0.11}$	0.020
42643	1.0	2.30	0.2	0.29	0.3	$2.17^{+1.16}_{-0.33}$	0.010
79330	1.0	1.28	2.5	0.10	0.5	$0.21^{+0.11}_{-0.03}$	0.100
29501	1.0	2.30	0.2	0.10	0.4	$0.56^{+0.04}_{-0.18}$	0.020
46450	0.2	3.50	2.5	0.51	0.2	$0.53^{+0.05}_{-0.07}$	0.200
77399	0.2	4.50	0.2	0.20	0.9	$2.11^{+0.31}_{-1.02}$	0.020
46091	0.2	3.50	2.5	0.51	0.7	$1.30^{+0.22}_{-0.23}$	0.100
50618	1.0	2.50	0.2	0.03	0.1	$1.05^{+0.48}_{-0.10}$	0.001
65792	1.0	2.75	0.2	0.03	0.0	$0.63^{+0.31}_{-0.04}$	0.001

Table 5.4: - continued

ID	Old Pop. Met. ($Z/Z_\odot$)	Old Pop. Age (Gyr)	Young Pop. Met. ($Z/Z_\odot$)	Young Pop. Age (Gyr)	Av	$M_\star$ ($10^{11}\mathrm{M}_\odot$)	Mass Fraction
79998	1.0	2.50	0.2	0.51	0.1	$0.58^{+0.27}_{-0.11}$	0.050
50326	0.2	3.75	1.0	0.14	0.1	$0.56^{+0.11}_{-0.08}$	0.001
77581	0.2	4.50	0.2	0.29	0.1	$0.63^{+0.07}_{-0.26}$	0.020
53783	0.2	4.50	1.0	0.36	0.2	$0.45^{+0.07}_{-0.08}$	0.100
73006	0.2	4.50	0.2	0.36	0.6	$0.61^{+0.29}_{-0.38}$	0.200
60493	1.0	4.50	2.5	0.29	0.1	$3.57^{+0.51}_{-0.89}$	0.020
75483	1.0	1.80	0.2	0.36	0.0	$1.08^{+0.13}_{-0.12}$	0.020
78289	0.2	4.50	2.5	0.10	0.1	$0.45^{+0.07}_{-0.09}$	0.050
73717	0.2	2.30	2.5	0.10	0.1	$0.28^{+0.05}_{-0.02}$	0.050
42941	1.0	0.90	0.2	0.01	1.25	$0.58^{+0.72}_{-0.05}$	0.001
77327	0.2	4.25	2.5	0.36	0.2	$1.25^{+0.04}_{-0.05}$	0.050
79158	1.0	3.75	2.5	0.36	0.2	$2.82^{+0.21}_{-0.37}$	0.050
49095	0.2	3.75	0.2	0.10	0.3	$1.13^{+0.30}_{-0.28}$	0.005
79274	1.0	1.61	0.2	0.07	0.1	$0.33^{+0.37}_{-0.09}$	0.020
45629	1.0	0.90	2.5	0.51	0.5	$0.30^{+0.16}_{-0.05}$	0.300
61110	0.2	4.25	2.5	0.51	0.2	$0.91^{+0.14}_{-0.04}$	0.050
56208	1.0	4.25	1.0	0.51	0.0	$1.14^{+0.16}_{-0.14}$	0.100
54647	0.2	4.25	2.5	0.29	0.5	$1.04^{+0.00}_{-0.22}$	0.020
63911	1.0	2.75	2.5	0.36	0.0	$1.35^{+0.46}_{-0.08}$	0.050
54647	0.2	4.25	0.2	0.29	0.4	$0.96^{+0.13}_{-0.15}$	0.005
57918	0.2	4.25	2.5	0.36	0.0	$0.89^{+0.17}_{-0.09}$	0.020
56439	0.2	4.25	1.0	0.51	0.8	$4.66^{+0.70}_{-0.62}$	0.050

Table 5.4: - continued

ID	Old Pop. Met. ($Z/Z_\odot$)	Old Pop. Age (Gyr)	Young Pop. Met. ($Z/Z_\odot$)	Young Pop. Age (Gyr)	Av	$M_\star$ (10^{11}M$_\odot$)	Mass Fraction
45372	1.0	2.00	2.5	0.29	0.1	$1.06^{+0.32}_{-0.09}$	0.050
44194	1.0	3.00	2.5	0.10	0.1	$1.76^{+0.10}_{-0.29}$	0.010
54522	0.2	4.25	2.5	0.36	0.8	$0.80^{+0.05}_{-0.08}$	0.100
59320	1.0	2.00	1.0	0.07	0.4	$2.07^{+0.44}_{-0.46}$	0.005
32227	1.0	1.28	0.2	0.01	0.9	$0.49^{+0.38}_{-0.06}$	0.001
54522	1.0	4.25	2.5	0.36	0.5	$0.91^{+0.05}_{-0.24}$	0.050
49961	1.0	3.75	1.0	0.36	0.2	$1.62^{+0.16}_{-0.09}$	0.020
63237	1.0	1.80	2.5	0.05	0.3	$0.59^{+0.03}_{-0.06}$	0.005
46492	0.2	4.25	2.5	0.14	0.6	$1.33^{+0.20}_{-0.62}$	0.050
52436	1.0	4.25	1.0	0.51	0.5	$1.47^{+0.22}_{-0.40}$	0.200
63675	1.0	2.00	2.5	0.07	1.25	$0.76^{+0.47}_{-0.23}$	0.05
81348	1.0	1.61	0.2	0.01	0.0	$0.32^{+0.05}_{-0.02}$	0.001
29788	1.0	3.00	1.0	0.36	0.1	$0.51^{+0.20}_{-0.21}$	0.050
62125	0.2	4.25	0.2	0.20	0.5	$4.74^{+0.00}_{-0.87}$	0.001
53841	1.0	3.75	0.2	0.29	0.9	$1.56^{+0.36}_{-0.87}$	0.020
46886	1.0	2.50	2.5	0.07	0.1	$0.49^{+0.10}_{-0.15}$	0.020
78217	0.2	4.25	2.5	0.14	0.3	$1.27^{+0.06}_{-0.24}$	0.010
48550	1.0	1.61	1.0	0.03	0.4	$0.65^{+0.18}_{-0.03}$	0.002
47359	1.0	1.80	0.2	0.07	0.0	$1.51^{+0.08}_{-0.24}$	0.002
32476	1.0	2.50	1.0	0.10	0.1	$0.45^{+0.23}_{-0.08}$	0.020
73600	1.0	1.61	2.5	0.14	0.2	$0.45^{+0.08}_{-0.05}$	0.010
19851	1.0	0.72	0.2	0.05	0.7	$0.54^{+0.76}_{-0.02}$	0.020
58689	1.0	3.75	2.5	0.36	0.4	$0.66^{+0.11}_{-0.28}$	0.200

Table 5.4: - continued

ID	Old Pop. Met. ($Z/Z_\odot$)	Old Pop. Age (Gyr)	Young Pop. Met. ($Z/Z_\odot$)	Young Pop. Age (Gyr)	Av	$M_\star$ ($10^{11}\mathrm{M}_\odot$)	Mass Fraction
64357	1.0	1.61	2.5	0.14	0.1	$0.36^{+0.03}_{-0.08}$	0.050
79138	1.0	1.02	1.0	0.01	0.0	$0.45^{+0.27}_{-0.01}$	0.001
78923	1.0	2.00	2.5	0.51	0.0	$0.59^{+0.09}_{-0.04}$	0.200
44334	1.0	2.00	1.0	0.20	0.1	$1.63^{+0.28}_{-0.13}$	0.010
62775	1.0	0.90	1.0	0.10	1.5	$0.74^{+0.34}_{-0.11}$	0.050
66424	1.0	3.00	0.2	0.05	0.4	$1.23^{+0.39}_{-0.31}$	0.001
71384	1.0	3.75	0.2	0.14	0.0	$3.32^{+0.35}_{-0.15}$	0.001
72088	1.0	1.02	0.2	0.03	0.2	$0.32^{+0.21}_{-0.04}$	0.005
72815	0.2	1.28	2.5	0.10	0.4	$0.14^{+0.48}_{-0.00}$	0.400
30838	0.2	3.50	0.2	0.07	1.0	$0.47^{+0.01}_{-0.24}$	0.100
70067	1.0	2.50	0.2	0.05	0.0	$0.96^{+0.08}_{-0.10}$	0.001
60843	1.0	1.02	2.5	0.10	0.0	$0.30^{+0.03}_{-0.03}$	0.050
53230	0.2	4.25	0.2	0.03	0.0	$1.59^{+0.07}_{-0.64}$	0.001
56151	1.0	1.02	0.2	0.36	0.1	$0.57^{+0.01}_{-0.07}$	0.005
52354	0.2	0.90	1.0	0.05	0.2	$0.20^{+0.37}_{-0.05}$	0.100
29201	1.0	0.90	2.5	0.05	0.4	$0.31^{+0.01}_{-0.05}$	0.020
48451	1.0	4.00	2.5	0.20	0.4	$2.69^{+0.40}_{-0.66}$	0.020
43168	1.0	2.00	0.2	0.36	0.1	$0.53^{+0.05}_{-0.08}$	0.050
47774	0.2	4.00	0.2	0.05	0.0	$0.89^{+0.12}_{-0.32}$	0.002
50229	1.0	1.61	2.5	0.03	0.0	$0.64^{+0.08}_{-0.00}$	0.002
54253	1.0	2.75	0.2	0.07	0.0	$1.60^{+0.24}_{-0.14}$	0.001
61727	1.0	1.28	0.2	0.36	0.0	$0.41^{+0.07}_{-0.01}$	0.005

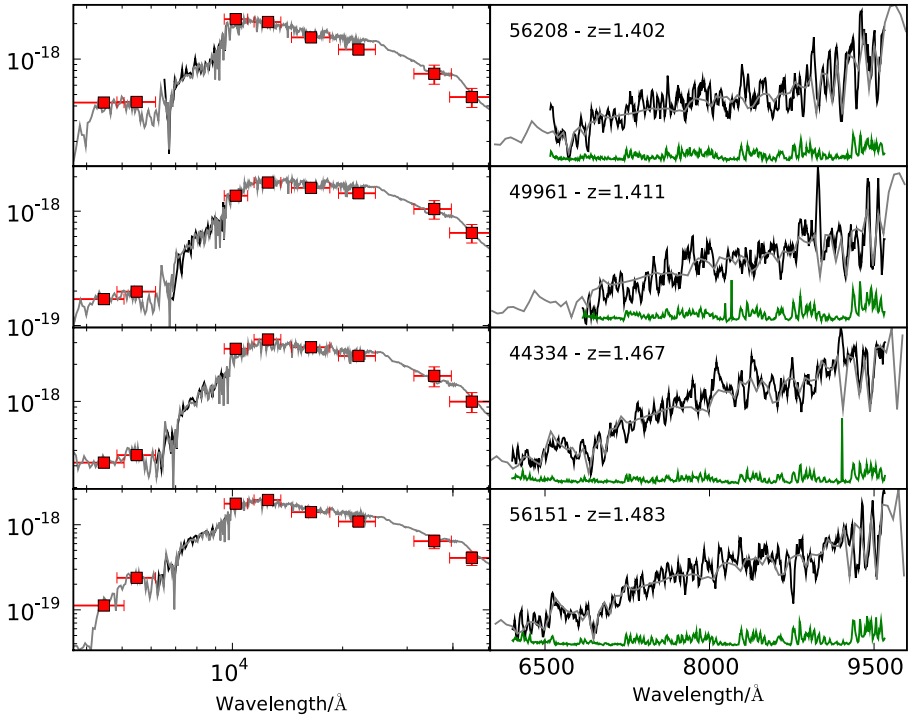

Figure 5.2: Plots illustrating the spectrophotometric fitting process for four example objects from the K-Bright sample. The left-hand panel shows the combined fit to the spectrum and photometry, while the right-hand panels are a zoom in showing the model fit through the spectrum in detail. The optical spectrum is in black, the error spectrum is in green, the photometry is in red and the best-fitting model is in grey. For presentation purposes the optical spectra has been smoothed by a 5 pixel boxcar.

from the fit to the stellar synthesis models with exponentially decaying star-formation, τ models, and one from the two component models, TCM models. The galaxy mass can be directly recovered from the fits as all the models are normalised to be $1M_{\odot}$ and the CB07 models provide a table of effective M/L ratio as a function of population age.

The errors on the mass are found by correcting all the χ^2 such that the best-fitting model has a χ^2 equal to the degrees of freedom (DOF). The plus and minus errors on the mass are calculated from the smallest and largest masses of the models that have a corrected $\chi^2 \leq DOF + 1.0$ (marginalising over all the parameters). This method was adopted because, as discussed previously, the models are unable to accurately reproduce the optical spectra in detail (see Section 4.1). Therefore, apart from the galaxies with low signal-to-noise, it is unlikely a statistically acceptable fit would be found. The fits with the TCM and τ models had median reduced $\chi^2 s$ of 2.7 and 2.8 respectively. The uncertainty on the mass estimates is relatively small because the redshift is accurately determined and here we are only considering the TCM models.

The distribution of the masses recovered from these two sets of models can be seen in Figure 5.3, where the masses recovered from the τ models are presented in the upper panel and the masses recovered from the fits with the TCM models can be seen in the lower panel. The median mass recovered from the fits to the τ models was $5.9 \pm 1.0 \times 10^{10} M_{\odot}$ where for the TCM models it is $6.6 \pm 1.3 \times 10^{10} M_{\odot}$. It is noteworthy that both estimates are in reasonable agreement, and both confirm (as expected) that $K < 21.5$ galaxies at $z > 1$ are massive systems.

For the majority of the galaxies in the sample the stellar-masses estimated from the two different sets of models are consistent to within a factor of 2. This can be seen in Figure 5.4, the grey solid line shows the one-to-to relation and the the dashed lines enclose a region where the masses vary by up to a factor of two. It is noticeable that the majority of the galaxies sit above the one-to-one relation indicating that the fits to the TCM models often recover larger mass estimates than fits to the τ models. This is to be expected as the TCM models can be thought to estimate the maximal mass of the galaxy since, when using two bursts, the old component is free to fully satisfy fitting the mass dominated part of the spectra while the young component can be used to fit any residual and/or recent star-formation without compromising the fit to the NIR bands.

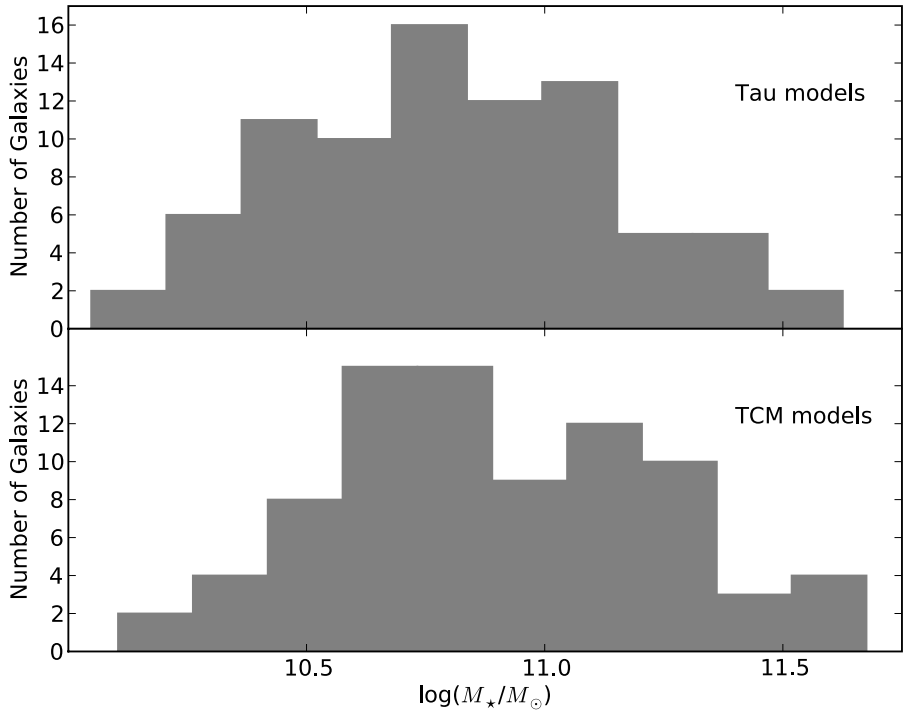

Figure 5.3: Histograms of the distribution of stellar-masses from the spectrophotometric fits with the τ (upper panel) and TCM (lower panel) models.

Given that the stellar-mass estimates from both models are comparable, to avoid constantly quoting two stellar-mass estimates, the stellar-mass estimates from the TCM models are adopted from now on. None of the proceeding science results are affected by this decision.

5.2.2 Galaxy Ages from the Two Component Models

Direct estimates of the galaxy ages can be extracted from the TCM model fits. Of particular interest within this context is the age of the old (mass-dominant) component, which can provide interesting information on the mass assembly epoch of these galaxies. The median age of the galaxies in this study is 2.75 ± 0.2 Gyrs at $<z>= 1.41$ which implies that these galaxies are already old at high-redshift. Figure 5.5 is a redshift versus age plot for the galaxies in the sample, in which the grey solid line shows the

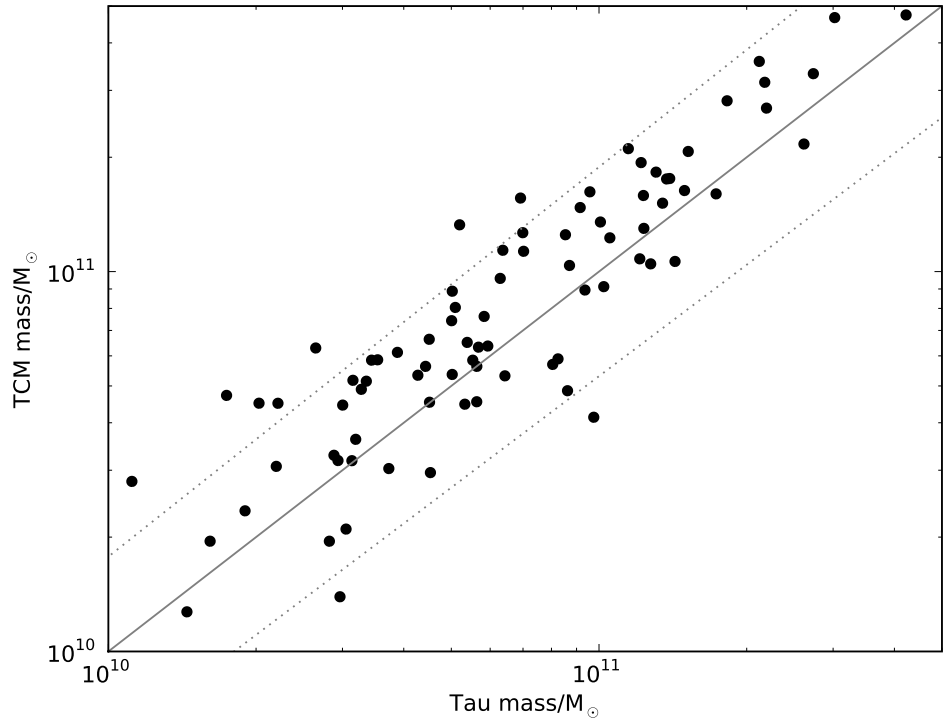

Figure 5.4: A comparison of the masses recovered from the spectrophotometric fits with the τ and TCM models. The grey solid line shows the one-to-to relation and the dashed lines enclose a region where the masses vary by up to a factor of two.

age of the Universe and the grey dashed lines show 25%, 50%, and 75% of the age of the Universe at each redshift. From the sample $34/82 \approx 41.5\%$ have ages greater than 75% the age of the Universe at their redshift. It is also noticeable that $25/82 \approx 30.5\%$ of the sample have ages that are over 90% that of the Universe.

The median age of the young population in the best-fitting models is 0.14 Gyrs. The fitting suggests that $\approx 68\%$ (56/82) of the sample have had an episode of star-formation in the last 300Myrs. However, the fits to the TCM models also show that typically the young stellar population make up only 2% of the systems mass.

Splitting the galaxy sample by mass shows that the most massive systems are the also the oldest in the Universe. Figure 5.6 is a reproduction of Figure 5.5 but with galaxies colour coded depending on their estimated stellar mass. The blue and red dots represent galaxies with stellar-masses less than and greater than $10^{11} M_{\odot}$ respectively.

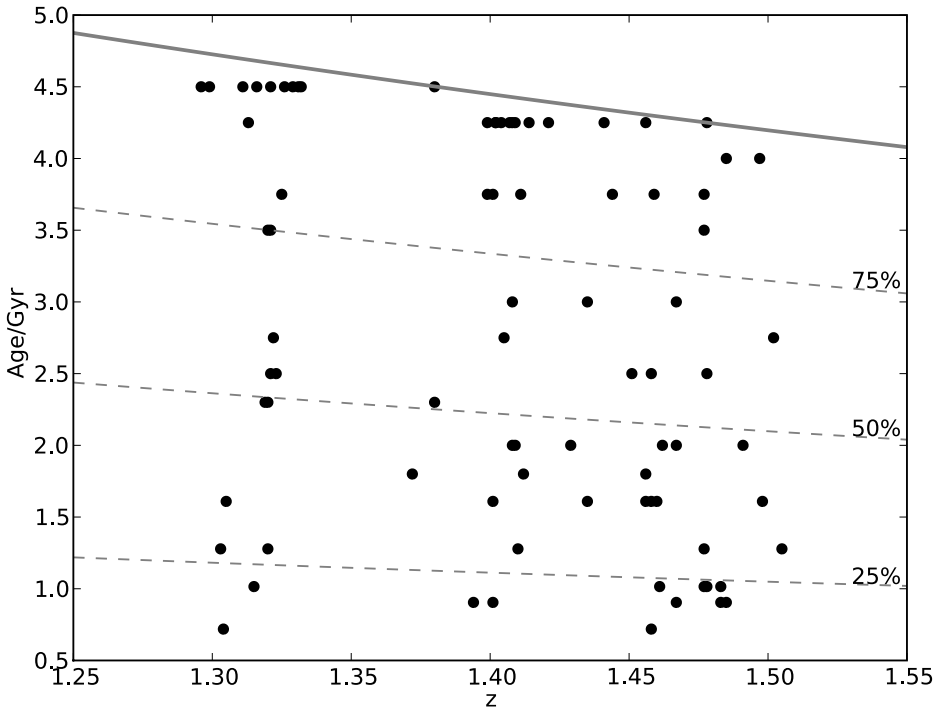

Figure 5.5: Redshift versus age plot for the galaxies in our sample. The grey solid line shows the age of the Universe at each redshift. The grey dashed lines show 25%, 50% and 75% of the age of the Universe at each redshift. The area above the solid grey line was forbidden within the fitting process.

The galaxies with stellar-masses less than $10^{11} M_{\odot}$ have a median age that is 40% of the age of the Universe, whereas the more massive systems have a median age that is 90% the age of the Universe.

5.3 Galaxy Radii

The galaxy radii were estimated from the deep K-band imaging available in the UDS as the near-IR (NIR) bands are good for size estimations at high-redshift since they trace the rest-frame optical light of the galaxies which is a better tracer of the stellar-mass distribution than the rest-frame UV.

The galaxy radii were supplied by Dr Emma Curtis-Lake. The radii were calculated

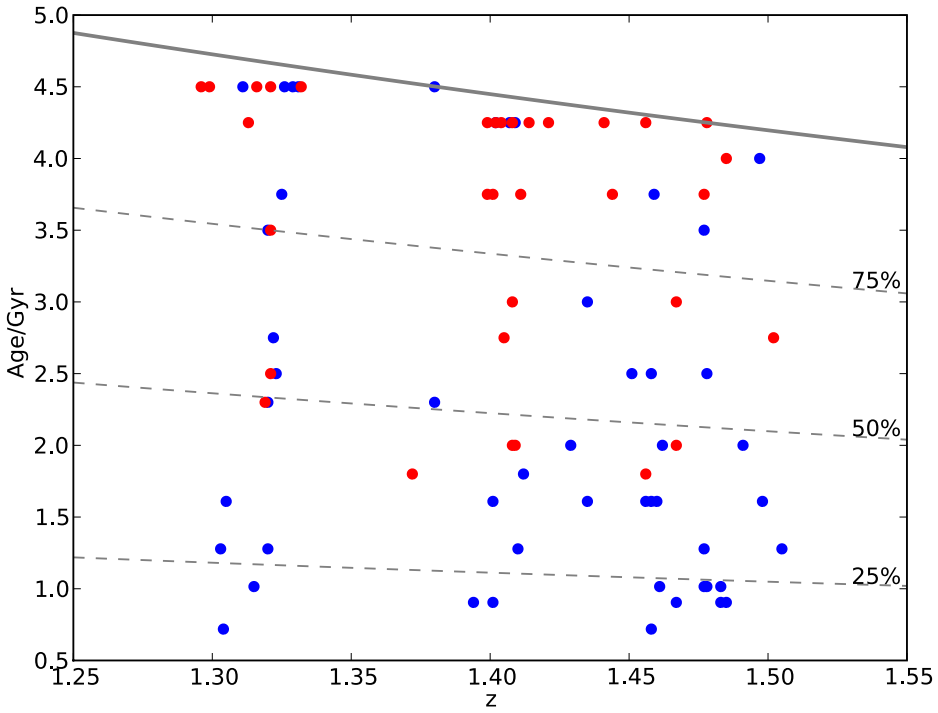

Figure 5.6: Redshift versus age plot for the galaxies in our sample. The grey solid line shows the age of the Universe at each redshift. The grey dashed lines show 25%, 50% and 75% of the age of the Universe at each redshift. The blue and red dots represent galaxies with stellar-masses less than and greater than $10^{11} M_{\odot}$ respectively. The area above the solid grey line was forbidden within the fitting process.

using a modified version of GALAPAGOS [Barden et al 2009] and GALFIT [Peng et al., 2002]. GALAPAGOS is a wrapper script for GALFIT that runs source extraction (SExtractor, Bertin and Arnouts 1996) and fits single Sèrsic profiles to each object in the image, taking initial parameters from the SExtractor catalogue. The advantage of GALAPAGOS to using GALFIT alone is that it has an algorithm for background estimation and it will fit to any nearby objects that could influence the fit. For each object it produces a tile of the image and masks any other objects in the image using the SExtractor segmentation map.

Here the code was run on regions of the K-band image with the object of interest in the centre and it was adapted to introduce a loop over R_e, Sérsic index and background

to estimate accurate errors on these parameters from contours of constant $\Delta\chi^2$. Each of the parameters was kept constant and the overall normalisation of the profile minimised to minimise the χ^2 value at each point in the grid. To ensure that the background was not used to compensate for other features in the profile at different Sèrsic indices (for example at small Sèrsic index, a very small radius can be fitted to a disk galaxy with prominent bulge if the background is allowed to compensate for the disk brightness), all of the background pixels in a limited area around the object that contributed to a clipped histogram of the background counts (determined by 3-sigma clipping) and not masked as contributing to another object in the segmentation image, were included in the calculation of χ^2. The histogram of background counts is quite flat at the peak in the UDS K-band image and it is within this peak that the background is varied within the grid. The resulting 3D contours showed that the derived Sérsic index and R_e correlate with the background, even in this small range of allowed background values. Including the loop over the background value increases the size of the confidence contours significantly and as such gives a much better representation of the true errors involved in the fitting.

5.4 The Size Stellar-mass Relation at High-Redshift

Recently high-redshift surveys have unveiled what appears to be a mysterious result: massive galaxies at high-redshift appear much more compact than would be expected at low-redshift. Several authors have found high-redshift ETGs to be a factor 4 smaller than their low-redshift counterparts making them almost two orders of magnitudes denser. A compilation of the size-mass relation data for the various samples in the literature can be seen in Figure 5.7. The grey line is the local relation from the SDSS data Shen et al. [2003] with the typical dispersion on the radii shown with the grey dotted lines. The median redshift of the local sample is $z \approx 0.1$. The different symbols correspond to other studies of the size-mass relation performed at moderate to high-redshift. The grey filled squares are 7 passively evolving ETGs from the Hubble Ultra Deep Field (UDF) with spectroscopic redshifts in the range $1.4 \leq z \leq 2.5$ from Daddi et al. [2005b] and the filled green squares are 9 massive ETGs at $z \sim 1.5$ from Longhetti et al. [2007] with stellar-masses from Longhetti et al. [2005]. For the full list of symbols

see the caption of Figure 5.7. As far as one can tell all authors have defined galaxy size via the half-light radius and, to as far as possible ensure further consistency all the stellar-masses from different studies and the local relation have been corrected to a Chabrier initial mass function (IMF) Chabrier [2003] using the conversions in Cimatti et al. [2008]. It is clear that the majority of the galaxies, over the whole mass range, sit below the local relation.

Even though "early-type galaxy" samples are compared to the early-type galaxy relation from Shen et al. [2003] different authors have different selection methods for creating their ETG samples. The local relation from Shen et al. [2003], that all samples are compared to, is based on the morphology of the galaxy such that the Séric index is $n > 2.5$. None of the studies plotted on Figure 5.7 follow this selection technique exactly. Daddi et al. [2005b], Longhetti et al. [2007], di Serego Alighieri et al. [2005], Cimatti et al. [2008] and part of the Rettura et al. [2006] sample were classified as ETGs based on the galaxy spectra indicating they were evolved systems. McGrath et al. [2008] and Mancini et al. [2010] used morphologies along with spectral or SED shapes to define their sample while part of the Rettura et al. [2006] sample was simply made from a colour cut.

The size-mass relation for the K-Bright sample can be seen in Figure 5.8. Again, the grey line is the local relation from the SDSS data Shen et al. [2003] with the dispersion on the radii shown by the grey dotted lines. From the K-Bright sample 13/82 galaxies sit above the local relation with an mean stellar-mass of $\sim 0.4 \times 10^{11} M_{\odot}$, 30/82 galaxies sit within the errors of the local relation with an mean stellar-mass of $\sim 0.9 \times 10^{11} M_{\odot}$ and 39/82 galaxies sit below the local relation with an mean stellar-mass of $\sim 1.4 \times 10^{11} M_{\odot}$. Therefore we see a trend with mass, with the lower mass objects sitting on (or above) the local relation and the higher mass objects sitting below the relation. The sample spans fully across the local relation but, as the sample is far from complete at $< 4 \times 10^{10} M_{\odot}$, it is difficult to draw solid conclusion regarding the lower mass objects. Previous studies have little to no objects with stellar-masses $< 4 \times 10^{10} M_{\odot}$ so this region still represents unknown territory in terms of the high-redshift size-mass relation.

Figure 5.9 shows the same information as Figure 5.8 but the objects have been grouped into five stellar-mass bins, $< 5 \times 10^{10} M_{\odot}$, $5 - 7.5 \times 10^{10} M_{\odot}$, $7.5 \times 10^{10} - 1 \times$

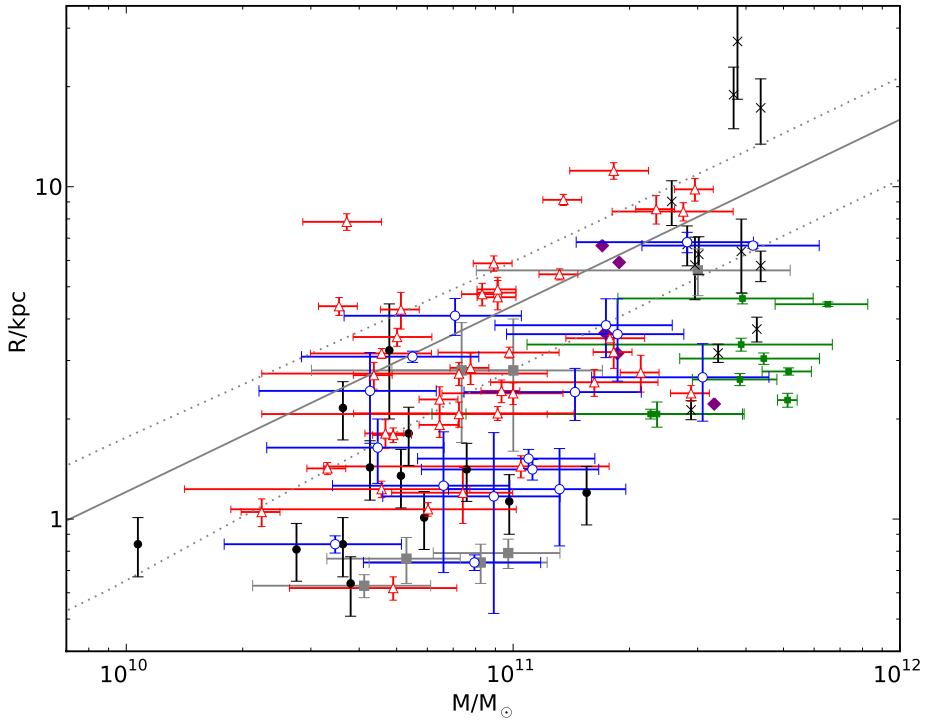

Figure 5.7: Stellar-mass versus radii plot for high-redshift galaxies. The grey line is the local relation from the SDSS data [Shen et al., 2003] with the dispersion on the radii shown by the grey dotted lines.. The grey filled squares are 7 passively evolving ETGs from the Hubble Ultra Deep Field (UDF) with spectroscopic redshifts in the range $1.4 \leq z \leq 2.5$ from Daddi et al. [2005b]. The filled green squares are 9 massive ETGs at $z \sim 1.5$ from Longhetti et al. [2007] with stellar-masses from Longhetti et al. [2005]. The purple diamonds are 5 (excluding the merger) passively evolving luminous red galaxies at $z \sim 1.5$ from McGrath et al. [2008]. The black crosses are 12 ultra-massive passively evolving ETGs with $z_{photo} > 1.4$ from the COSMOS field from Mancini et al. [2010]. The filled black circles are 13 old and passive ETGs from the GMASS survey from Cimatti et al. [2008]. The open blue circles are 17 passive ETGs at $z \sim 1$ in the K20 survey from di Serego Alighieri et al. [2005]. The open red triangles are 40 ETGs at $z \sim 1$ from Rettura et al. [2006] with stellar-masses from Fontana et al. [2004]. The 8 from the K20 survey have been left out as they are in the sample from di Serego Alighieri et al. [2005]. All the stellar-masses from different studies and the local relation have been corrected to a Chabrier initial mass function (IMF) Chabrier [2003] using the conversions in Cimatti et al. [2008].

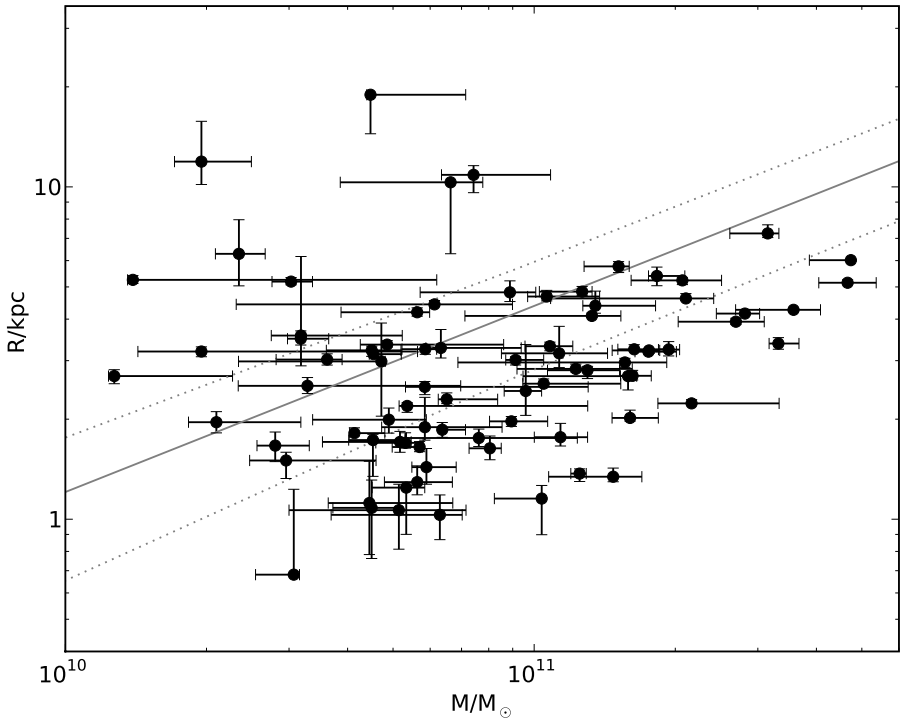

Figure 5.8: Stellar mass versus radii plot for the K-Bright sample. The grey line is the local relation from the SDSS data [Shen et al., 2003] with the dispersion on the radii shown by the grey dotted lines. See text for discussion.

$10^{11}M_\odot$, $1-2\times10^{11}M_\odot$ and $>2\times10^{11}M_\odot$. There appears to be a trend with mass but this most likely appears due to a switch is galaxy population with mass. The lower mass galaxies are probably dominated by late-type galaxies and higher mass galaxies being dominated early-type galaxies. The fives bins have an average ratio of galaxy radii to local equivalent $\langle R(z)/R(0)\rangle$ of 1.84, 0.96, 0.67, 0.63, 0.59 respectively. This could indicate that the galaxies fall away from the local at high-redshift with increasing mass. But within the errors all the mass bins could follow the local relation but lowered by a factor of ~ 1.6.

5.4.1 Dividing the Sample by Age

It has been suggested by Saracco et al. [2009] that splitting the sample by age can split the population into normal and compact ETGs. The sample was divided into two

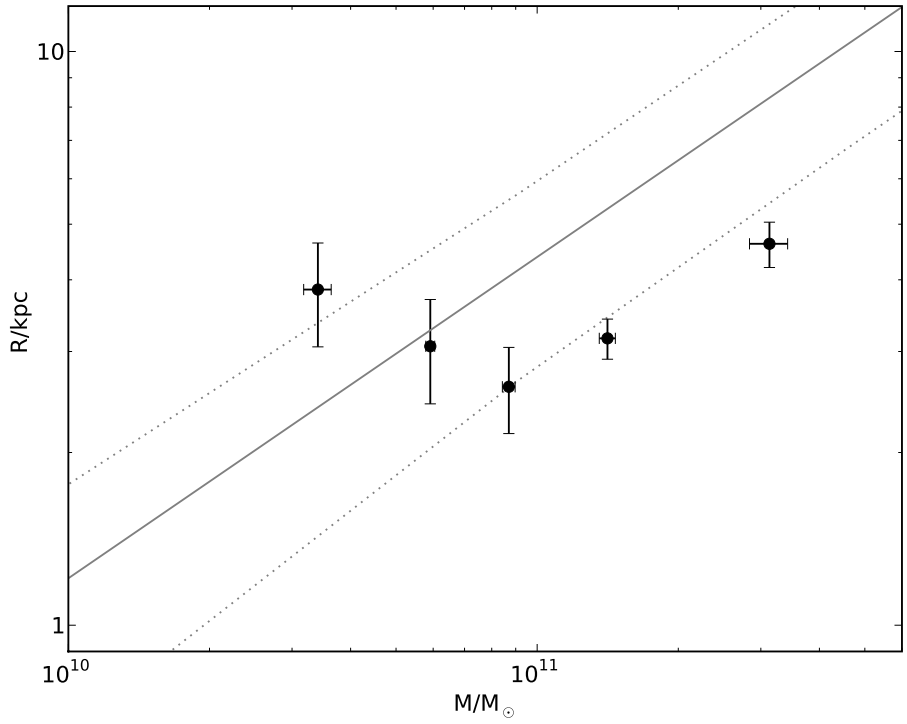

Figure 5.9: Stellar mass versus radii plot for the sample. The black dots represent mass bins of $< 5\times10^{10}M_\odot$, $5-7.5\times10^{10}M_\odot$, $7.5\times10^{10}-1\times10^{11}M_\odot$, $1-2\times10^{11}M_\odot$ and $> 2\times10^{11}M_\odot$. The grey lines are as in Figure 5.8

populations, galaxies with an age younger and older that half the age of the Universe at their respective redshift. Splitting by a fractional age of the Universe was chosen as using a particular age to divide the population, as was done by Saracco et al. [2009], has redshift implications attached to it. Dividing by a fractional age selects all the old and young galaxy at each redshift. A repeat of Figure 5.8 but with our sample divided by age can be seen in Figure 5.10. The blue symbols are the galaxies with an age less than half the age of the Universe for their redshift and the red symbols are galaxies with ages older than half the age of the Universe for their redshift. The younger population has a mean mass of $\sim 0.6\times10^{11}M_\odot$ and has an average ratio of galaxy radii to local mass equivalent of $\langle R(z)/R(0)\rangle = 1.56$. Whereas the older population has a mean mass of $\sim 1.4\times10^{11}M_\odot$ and has an average ratio of galaxy radii to local mass equivalent of $\langle R(z)/R(0)\rangle = 0.69$.

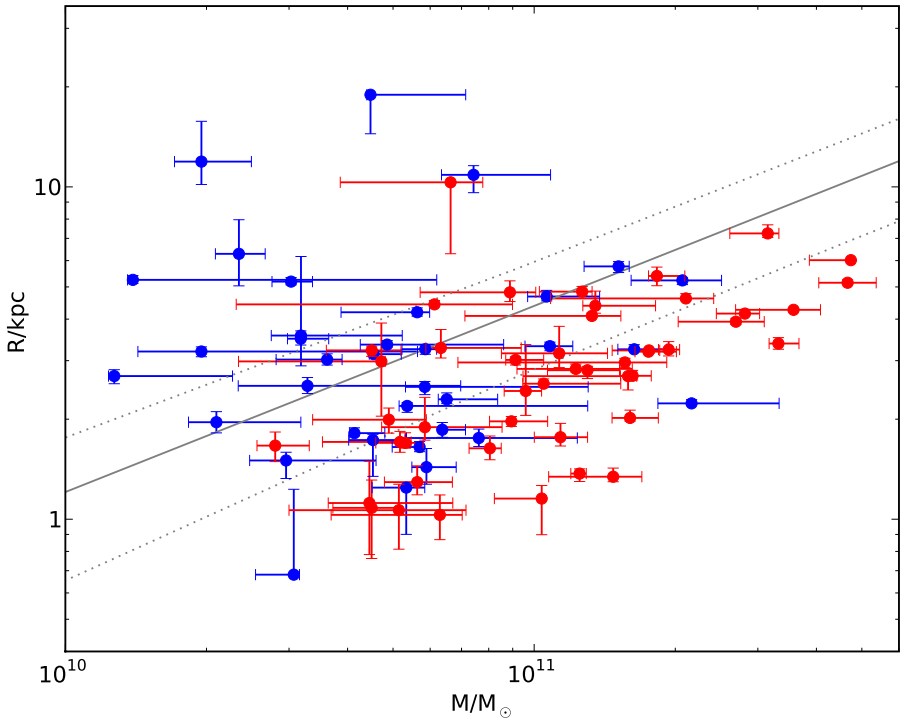

Figure 5.10: Stellar mass versus radii plot for the sample. The blue symbols are the galaxies with an age less than half the age of the Universe for their redshift and the red symbol are galaxies with ages older than half the age of the Universe for their redshift. The grey lines are as in Figure 5.8

This result is reasonably robust since the mass estimate have been made using a Chabrier IMF and the use of a Salpeter IMF would increase the stellar masses by a factor of ~ 2. Moreover, the stellar population models adopted here account for the possible effects of TP-AGB stars which, if removed, would also increase the stellar-mass. Since the radii have been estimated from low-resolution ground based imaging, if anything, they could be overestimates. All these potential sources of errors do therefore not change the results that it appears older high-redshift massive systems sit below the local size-mas relation.

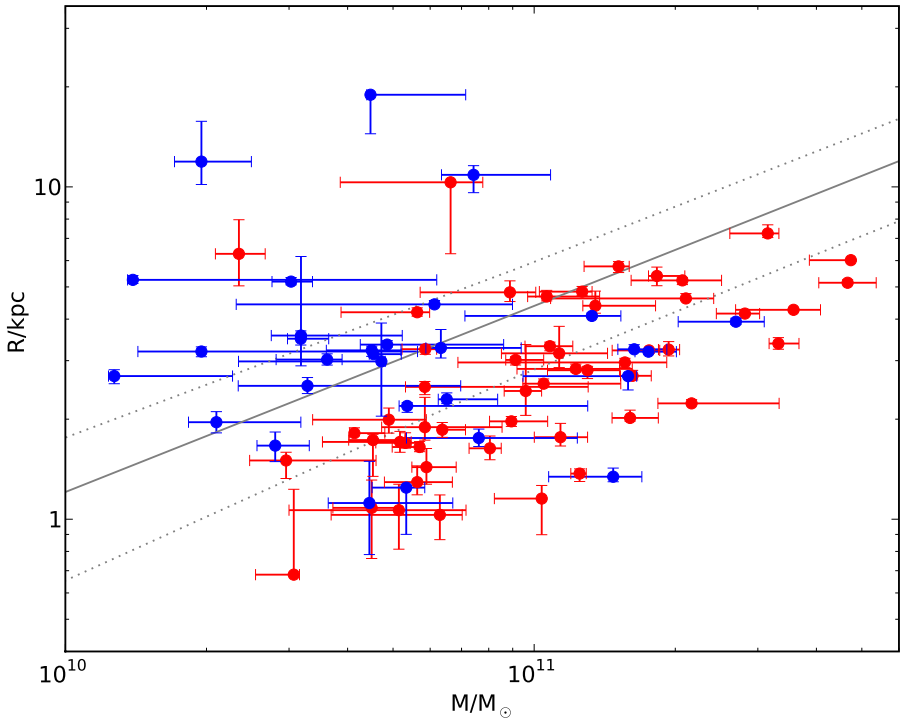

Figure 5.11: Stellar mass versus radii plot for the K-Bright sample. The blue symbols are the star-forming galaxies in the sample and the red symbol are passively evolving galaxies. The grey lines are as in Figure 5.8.

5.4.2 Dividing the Sample by Passivity

To follow on from the idea of dividing the sample by age, the sample was split based on whether or not the galaxies are star-forming or passively evolving. A full explanation of the classification process is described in Section 5.8. Figure 5.11 shows the size-mass relation when the galaxy sample is split according to their passivity, with star-forming galaxies are plotted in blue and passive galaxies in red. This division in the sample gives very similar results to dividing the sample by age. Star-forming and passive galaxies have an average ratio of galaxy radii to local mass equivalent of $\langle R(z)/R(0)\rangle = 1.61$ and $\langle R(z)/R(0)\rangle = 0.74$ respectively. The error considerations from dividing the sample by age holds for this result.

5.4.3 Dividing the Sample by Spectral Type

It is clear that there is a differential deviation from the local size-mass relation with various galaxy characteristics. As the local relation is based on early-type galaxies it would be beneficial to compare just the ETGs in the sample to the local relation (Shen et al. 2003 also supplies a size-mass relation for late-type galaxies but the number of late-type galaxies in this sample is too small to investigate). A scheme to classify galaxies as either early-, intermediate or late-type is discussed and provided in Section 7.1.1. Of the 82 galaxies in this sample they are split 35:11:36 into early-, intermediate- and late-type galaxies respectively. The size-mass relation for just early-type galaxies is shown in Figure 5.12.

Studying just the early-type galaxies has removed a large fraction of the lower mass galaxies. Approximately 70% of the early-type galaxies in the sample sit below the local. It appear they still follow the form of the local relation but sit a factor of ~ 1.5 below.

5.5 Velocity Dispersion Estimates

In Section 5.6 the analysis of the size-mass relation is extended by calculating dynamical masses which rely on accurate velocity disperison estimate. Good signal-to-noise is required to obtain accurate estimates of the velocity dispersion so galaxies were selected from the UDSz sample based on them having $\mathrm{SNR}_{CaHK} \geq 7.5$, where SNR_{CaHK} is equal to the median signal to noise per pixel in the fitting region 3915 - 3985Å. This cut was obtained from fitting all the galaxies in the UDSz with $z > 1.2$ and investigating down to which signal-to-noise threshold a velocity dispersion estimate could be constrained. This signal-to-noise cut (and removing bluer galaxies with weak Ca H & K features) produced a sub-sample 13 galaxies. The fits for this sub-sample can be seen in Figure 5.13, where the thick green line is the spectrum of the galaxy, the black line is the best-fitting convolved stellar spectrum and the thin grey line is the error spectrum for each galaxy. As the velocity dispersion estimate for each of the 13 galaxies was found by fitting a range of templates, the errors on the velocity dispersions were found by marginalising over all over parameters to calculate the best χ^2 for each velocity

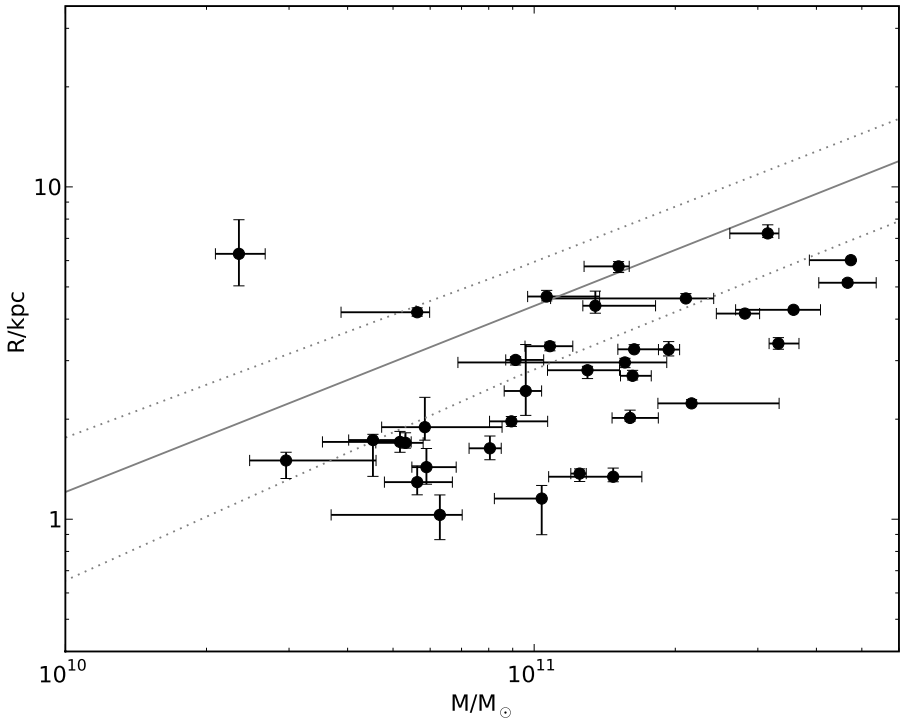

Figure 5.12: Stellar mass versus radii plot for the early-type galaxies in the K-Bright sample. The grey lines are as in Figure 5.8

dispersion, normalising all the χ^2 values such that the best-fitting templates has a reduced χ^2 value of 1 and then obtaining the range of velocity dispersions that have a $\Delta\chi^2 = 1$ from the global minimum χ^2.

The velocity dispersions and errors for the 13-object sub-sample can be found in Table 5.5. The final value of each targets velocity dispersion has been aperture corrected using Equation 5.1, Jorgensen et al. [1995], where σ_{ap} is the measured velocity dispersion in km/s, R_{eff} is the effective radius in kpc and $R_{ap}(z)$ is half the width of our FORS2 slit in kpc at the distance of the galaxy.

$$\sigma_{eff} = \sigma_{ap}\left(\frac{R_{eff}}{R_{ap}(z)}\right)^{-0.04} \tag{5.1}$$

Note that this aperture correction typically amounts to a correction of $\sim 1.5\%$.

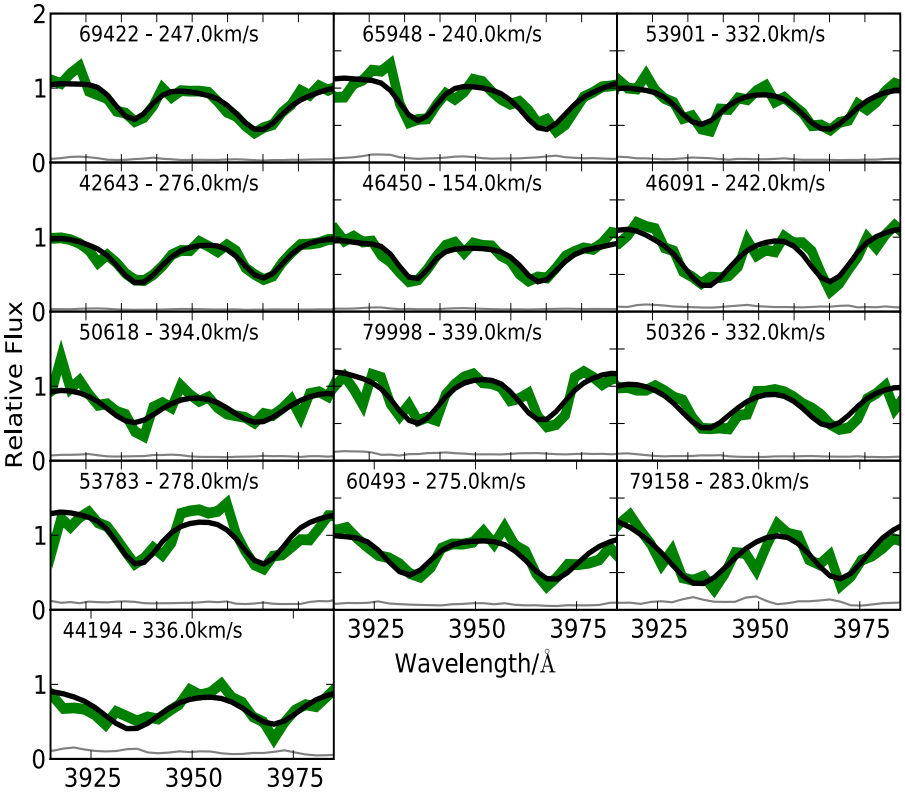

Figure 5.13: Velocity dispersion fits to our 13 galaxies with $\mathrm{SNR}_{CaHK} \geq 7.5$, where SNR_{CaHK} is the median signal to noise per pixel in the fitting region 3915 - 3985Å. The thick green line is the spectrum of the galaxy and the black line is the best-fitting convolved stellar spectrum. The thin grey line is the error spectrum for each galaxy.

Table 5.5: Table showing the velocity dispersion and dynamical mass estimates for the high signal-to-noise targets in the sample.

ID	z	σ (km/s)	Radius (kpc)	M_{dyn} ($10^{11} M_{\odot}$)	$M_{\star}$ ($10^{11} M_{\odot}$)
69422	1.296	$247.0^{+32.0}_{-34.0}$	$5.39^{+0.34}_{-0.35}$	$3.88^{+1.02}_{-1.09}$	$1.83^{+0.27}_{-0.07}$
65948	1.305	$240.0^{+50.0}_{-53.0}$	$3.14^{+0.06}_{-0.05}$	$2.12^{+0.88}_{-0.93}$	$0.45^{+0.07}_{-0.01}$
53901	1.313	$332.0^{+37.0}_{-77.0}$	$7.24^{+0.45}_{-0.21}$	$9.36^{+2.18}_{-4.37}$	$3.15^{+0.18}_{-0.54}$
42643	1.319	$276.0^{+25.0}_{-21.0}$	$2.23^{+0.06}_{-0.0}$	$2.00^{+0.36}_{-0.30}$	$2.17^{+1.16}_{-0.33}$
46450	1.320	$154.0^{+47.0}_{-57.0}$	$1.70^{+0.12}_{-0.06}$	$0.48^{+0.29}_{-0.35}$	$0.53^{+0.05}_{-0.07}$
46091	1.321	$242.0^{+59.0}_{-69.0}$	$2.81^{+0.08}_{-0.16}$	$1.93^{+0.94}_{-1.11}$	$1.3^{+0.22}_{-0.23}$
50618	1.321	$394.0^{+68.0}_{-129.0}$	$2.56^{+0.09}_{-0.05}$	$4.66^{+1.62}_{-3.04}$	$1.05^{+0.48}_{-0.10}$
79998	1.323	$339.0^{+65.0}_{-56.0}$	$1.89^{+0.43}_{-0.16}$	$2.55^{+1.14}_{-0.87}$	$0.58^{+0.27}_{-0.11}$
50326	1.325	$332.0^{+60.0}_{-68.0}$	$1.29^{+0.15}_{-0.11}$	$1.68^{+0.64}_{-0.70}$	$0.56^{+0.11}_{-0.08}$
53783	1.329	$278.0^{+64.0}_{-63.0}$	$1.08^{+0.23}_{-0.32}$	$0.98^{+0.50}_{-0.53}$	$0.45^{+0.07}_{-0.08}$
60493	1.332	$275.0^{+46.0}_{-46.0}$	$4.27^{+0.04}_{-0.05}$	$3.79^{+1.27}_{-1.27}$	$3.57^{+0.51}_{-0.89}$
79158	1.399	$283.0^{+54.0}_{-63.0}$	$4.16^{+0.02}_{-0.05}$	$3.92^{+1.49}_{-1.74}$	$2.82^{+0.21}_{-0.37}$
44194	1.408	$336.0^{+82.0}_{-66.0}$	$3.22^{+0.01}_{-0.07}$	$4.26^{+2.08}_{-1.67}$	$1.76^{+0.10}_{-0.29}$

5.6 Dynamical Mass Estimates

To investigate concerns of stellar-mass estimates affecting the high-redshift size-mass relation, the velocity dispersion estimates were used to calculate dynamical mass estimate which are a model indepedent method of acquire a mass estimate for the galaxy. To calculate dynamical masses Equation 5.2 was used, where σ is the velocity dispersion in km/s, R_e is the effective radius in kpc, G is the gravitational constant and C is a constant such that $\log(C/G) = 6.07$, C/G has units of $M_{\odot} km^{-1} s\ kpc^{-1}$. This is the commonly used relation for local ellipticals [Jorgensen et al., 1996] and has also been used at high-redshift [van Dokkum and Stanford, 2003].

$$M_{dyn} = \frac{C\sigma^2 R_e}{G} \tag{5.2}$$

5.6.1 Comparing Dynamical Mass and Stellar-Mass

Figure 5.14 shows the relation between stellar and dynamical mass for several samples of high-redshift galaxies. The open blue circles are 17 galaxies from di Serego Alighieri et al. [2005] from the K20 survey with 15 in the redshift range $0.88 \leq z \leq 1.3$ and 2 at $z \sim 0.67$. The open green triangles are 40 ETGs at $z \sim 1$ from Rettura et al. [2006]. Rettura et al. [2006] acquired the velocity dispersions from the literature with 36 from van der Wel et al. [2005] and 4 from Holden et al. [2005]. The 8 galaxies from Rettura et al. [2006] taken from the K20 survey have been left out as they are in the sample from di Serego Alighieri et al. [2005]. The two open black triangles are the two early-type galaxies at $z \sim 1.4$ from Cappellari et al. [2009] from the GMASS survey. The galaxies from this work are shown as the large filled red circles and the black dotted line shows the one-to-one relation. All the stellar-masses from different studies have been corrected to a Chabrier initial mass function [Chabrier, 2003] using the conversions in Cimatti et al. [2008].

Of the sub-sample with velocity dispersion estimates, 11/13 of our galaxies sit above the one-to-one relation and on average, the dynamical mass is ~ 2.45 times that of the stellar population. Considering all of the samples together the more massive galaxies tend to have a larger dynamical masses relative to their stellar-mass whereas this relation is reversed for the lower mass part of the sample.

5.6.2 The Size-Dynamical Mass Relation at High-Redshift

The size against dynamical mass plot can be seen in Figure 5.15, the symbols are as in Figure 5.14 with the addition of ~ 57000 SDSS galaxies (grey dots). The SDSS sample was chosen to be galaxies at $z < 0.1$. The radii plotted here are the radii containing 50% of the Petrosian flux [Petrosian, 1976] in the z-band. The z-band was chosen as this samples the same rest-frame part of the galaxy's SED as the K-band samples for the galaxies in the K-Bright sample. The dynamical masses were calculated using the same method as used on our own galaxies, described in Section 5.6.

The 13 targets studied here all sit on or below the compact edge of the local size-dynamical mass locus, with approximately half sitting below the locus. This adds more support to the idea that massive galaxies at high-redshift are more compact than their

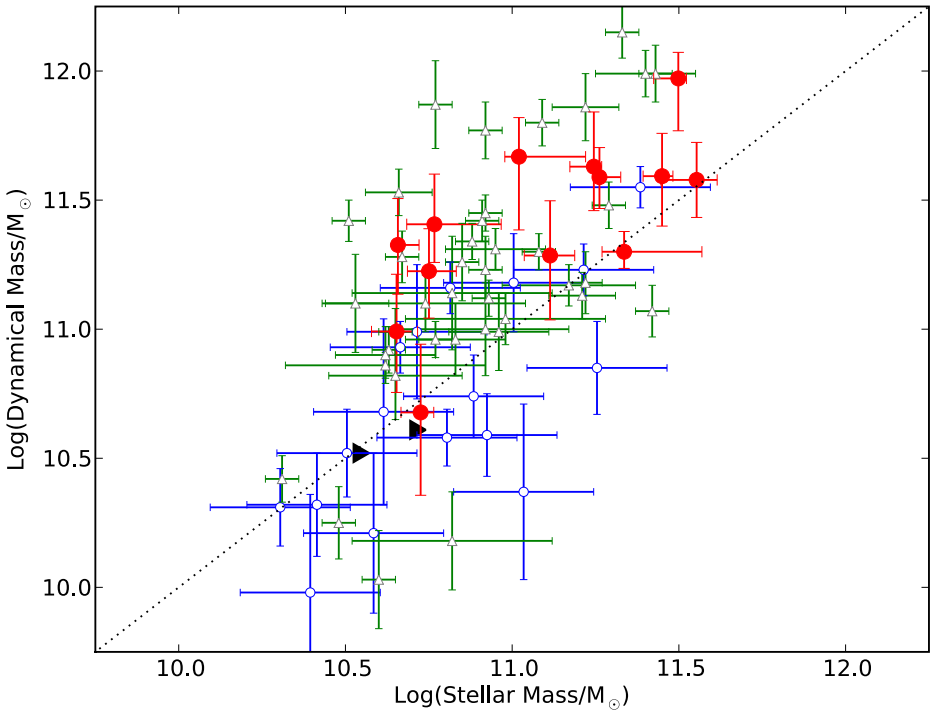

Figure 5.14: Stellar masses versus dynamical mass. The open blue circles are 17 galaxies from di Serego Alighieri et al. [2005] from the K20 survey with 15 in the redshift range $0.88 \leq z \leq 1.3$ and 2 at $z \sim 0.67$. The open green triangles are 40 ETGs at $z \sim 1$ from Rettura et al. [2006]. Rettura et al. [2006] acquired the velocity dispersions from the literature with 36 from van der Wel et al. [2005] and 4 from Holden et al. [2005]. The 8 Rettura et al. [2006] uses from the K20 survey have been left out as they are in the sample from di Serego Alighieri et al. [2005]. The two open black triangles are the two early-type galaxies at $z \sim 1.4$ from Cappellari et al. [2009] from the GMASS survey. The galaxies from this work are shown as the large filled red circles and the black dotted line shows the one-to-one relation.

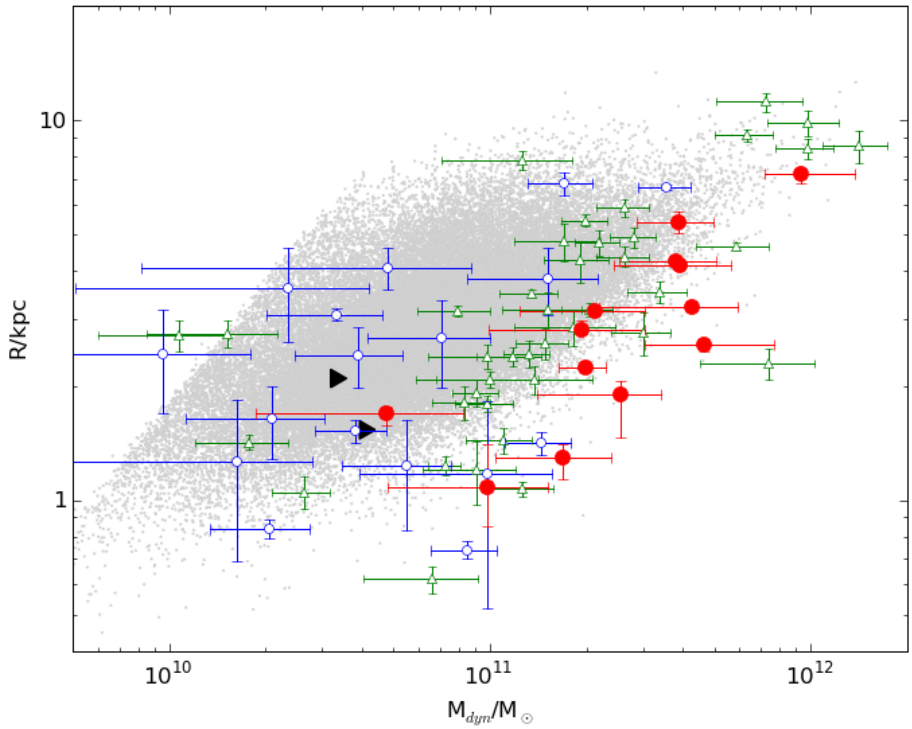

Figure 5.15: Dynamical mass versus size plot for high-redshift galaxies. The open blue circles are 17 galaxies from di Serego Alighieri et al. [2005] from the K20 survey with 15 in the redshift range $0.88 \leq z \leq 1.3$ and 2 at $z \sim 0.67$. The open grey triangles are 40 ETGs at $z \sim 1$ from Rettura et al. [2006]. Rettura et al. [2006] acquired the velocity dispersions from the literature with 36 from van der Wel et al. [2005] and 4 from Holden et al. [2005]. As with the stellar-mass versus dynamical mass plot we have left out the 8 galaxies Rettura et al. [2006] uses from the K20 survey as they are in the sample from di Serego Alighieri et al. [2005]. The two open black triangles are the two early-type galaxies at $z \sim 1.4$ from Cappellari et al. [2009] from the GMASS survey. The galaxies from this work are shown as the large filled red circles.

local counterparts.

5.7 Specific Star-formation Rates

In order to investigate the fraction of truly passive galaxies in the sample it necessary to calculate star-formation rates (SFR) for each galaxy. Using the various star-formation indicators and SFR estimators described in Section 4.2 we have calculated three independent estimates of the SFR for the galaxies in our sample, one from the rest-frame UV corrected using the A_v from the best-fitting model, one from the [OII] emission line flux and one from a $24\mu m$ flux where there is a detection. The results can be see in Table 5.6. The mass stated here is the stellar-mass estimate from the fits to the TCM models, see Section 5.2.1. The UV star-formation rates have been corrected for reddening using the A_v recovered from the spectrophotometric fits to the TCM models. The flux from the [OII] emission line has been corrected for an $A_v = 1.0$ [Kennicutt, 1998]. This correction was adopted because as the conversion from $L_{[OII]}$ to a SFR estimate is calibrated against $H\alpha$ the extinction at $H\alpha$ needs to be applied and an average extinction of 1 magnitude is found my several authors [e.g. Kennicutt 1983 and Niklas et al. 1997]. A reason for not correcting the SFR by the extinction value found during the fitting is that there are good reasons to expect the extinction correction for the [OII] emission line is not necessarily the same as derived for the UV continuum. All the $24\mu m$ fluxes used here were supplied by Dr. Karina Caputi.

5.8 The Passive Fraction of Galaxies at $1.3 \leq z \leq 1.5$

From Fontana et al. [2009] the definition of a "passive" galaxy can be defined as a galaxy with specific star-formation rate (SSFR), $\dot{M}/M_\star < (t(z))^{-1}$, where $t(z)$ is the age of the universe at redshift z. This is based on the idea that if a galaxy's mass is it's star-formation history averaged over the age of the Universe, i.e. $M_\star = \langle \dot{M} \rangle_{past} \times t(z)$, and a passive galaxy can be thought of as one where $\dot{M} < \langle \dot{M} \rangle_{past}$ then this implies $\dot{M}/M_\star < (t(z))^{-1}$.

For our objects the specific star-formation rate (SSFR) is based on the highest star-formation rate from the three different estimates and the stellar-mass estimate is from

Table 5.6: Table showing estimates of star-formation rate from different indicators

ID	z	SFR_{UV} $(M \odot yr^{-1})$	$\mathrm{SFR}_{[OII]}$ $(M \odot yr^{-1})$	$\mathrm{SFR}_{24\mu m}$ $(M \odot yr^{-1})$	$M_\star$ $(10^{11} M\odot)$	SSFR $(10^{-10} yr^{-1})$	1/t(z) $(10^{-10} yr^{-1})$
69422	1.296	2.90 ± 0.24	0.75 ± 0.47	-	$1.83^{+0.00}_{-0.07}$	$0.16^{+0.03}_{-0.01}$	2.11
80073	1.299	0.44 ± 0.04	< 0.48	-	$1.94^{+0.0}_{-0.09}$	$0.02^{+0.00}_{-0.00}$	2.11
76779	1.303	0.48 ± 0.04	4.66 ± 1.42	-	$0.13^{+0.00}_{-0.00}$	$3.66^{+3.09}_{-1.12}$	2.12
80464	1.304	2.50 ± 0.21	2.34 ± 0.89	-	$0.23^{+0.00}_{-0.03}$	$1.07^{+0.17}_{-0.15}$	2.12
65948	1.305	0.74 ± 0.11	3.79 ± 1.14	118.36 ± 47.86	$0.45^{+0.0}_{-0.01}$	$26.05^{+11.2}_{-10.55}$	2.12
63940	1.311	0.29 ± 0.07	< 0.66	-	$0.52^{+0.00}_{-0.16}$	$0.06^{+0.01}_{-0.02}$	2.13
53901	1.313	1.04 ± 0.09	< 0.69	26.97 ± 12.59	$3.15^{+0.0}_{-0.54}$	$0.86^{+0.4}_{-0.43}$	2.13
32058	1.315	1.39 ± 0.11	8.66 ± 2.94	-	$0.2^{+0.00}_{-0.02}$	$4.44^{+1.95}_{-1.60}$	2.14
58266	1.316	4.55 ± 0.37	19.50 ± 5.83	248.94 ± 97.18	$1.75^{+0.00}_{-0.11}$	$14.2^{+5.92}_{-5.62}$	2.14
42643	1.319	2.08 ± 0.17	6.71 ± 2.02	-	$2.17^{+1.00}_{-0.33}$	$0.31^{+0.19}_{-0.10}$	2.14
79330	1.320	2.80 ± 0.23	15.84 ± 4.64	116.94 ± 48.9	$0.21^{+0.00}_{-0.03}$	$55.7^{+36.91}_{-24.36}$	2.14
29501	1.320	2.47 ± 0.2	5.85 ± 2.06	-	$0.56^{+0.00}_{-0.18}$	$1.04^{+0.37}_{-0.49}$	2.14
46450	1.320	0.58 ± 0.05	1.66 ± 0.65	-	$0.53^{+0.00}_{-0.07}$	$0.31^{+0.12}_{-0.13}$	2.14
77399	1.321	5.02 ± 0.41	2.56 ± 1.66	-	$2.11^{+0.00}_{-1.02}$	$0.24^{+0.04}_{-0.12}$	2.14
50618	1.321	1.62 ± 0.13	15.31 ± 4.45	-	$1.05^{+0.00}_{-0.10}$	$1.46^{+0.08}_{-0.45}$	2.14
46091	1.321	0.63 ± 0.15	< 1.66	-	$1.3^{+0.00}_{-0.23}$	$0.05^{+0.01}_{-0.01}$	2.14
65792	1.322	1.00 ± 0.08	16.97 ± 5.03	110.37 ± 61.48	$0.63^{+0.00}_{-0.04}$	$17.45^{+12.88}_{-9.8}$	2.14
79998	1.323	0.65 ± 0.05	4.15 ± 1.55	-	$0.58^{+0.00}_{-0.11}$	$0.71^{+0.42}_{-0.03}$	2.15
50326	1.325	0.18 ± 0.05	< 1.35	-	$0.56^{+0.00}_{-0.08}$	$0.03^{+0.01}_{-0.01}$	2.15

Table 5.6: - continued

ID	z	SFR_{UV} $(M \odot yr^{-1})$	$\mathrm{SFR}_{[OII]}$ $(M \odot yr^{-1})$	$\mathrm{SFR}_{24\mu m}$ $(M \odot yr^{-1})$	$M_\star$ $(10^{11} M\odot)$	SSFR $(10^{-10} yr^{-1})$	1/t(z) $(10^{-10} yr^{-1})$
77581	1.326	0.92 ± 0.08	< 0.78	-	$0.63^{+0.00}_{-0.26}$	$0.15^{+0.02}_{-0.06}$	2.15
53783	1.329	0.96 ± 0.08	6.58 ± 2.03	-	$0.45^{+0.00}_{-0.08}$	$1.46^{+0.5}_{-0.52}$	2.15
73006	1.331	5.06 ± 0.42	11.18 ± 3.58	83.35 ± 34.85	$0.61^{+0.0}_{-0.38}$	$13.6^{+8.53}_{-10.20}$	2.16
60493	1.332	1.79 ± 0.15	8.38 ± 2.96	-	$3.57^{+1.00}_{-0.89}$	$0.23^{+0.09}_{-0.1}$	2.16
75483	1.372	0.89 ± 0.07	5.35 ± 1.74	-	$1.08^{+0.00}_{-0.12}$	$0.5^{+0.17}_{-0.17}$	2.21
78289	1.380	3.43 ± 0.28	34.42 ± 9.90	-	$0.45^{+0.00}_{-0.09}$	$7.64^{+2.5}_{-2.68}$	2.22
73717	1.380	1.52 ± 0.13	17.32 ± 5.05	105.51 ± 43.89	$0.28^{+0.00}_{-0.02}$	$37.64^{+17.09}_{-15.99}$	2.22
42941	1.394	2.91 ± 0.53	7.96 ± 2.45	-	$0.58^{+1.00}_{-0.05}$	$1.36^{+1.73}_{-0.44}$	2.24
79158	1.399	1.6 ± 0.13	8.37 ± 2.66	-	$2.82^{+0.00}_{-0.37}$	$0.3^{+0.10}_{-0.10}$	2.25
77327	1.399	0.92 ± 0.08	< 0.98	-	$1.25^{+0.0}_{-0.05}$	$0.07^{+0.01}_{-0.01}$	2.25
79274	1.401	2.38 ± 0.2	15.38 ± 4.50	-	$0.33^{+0.00}_{-0.09}$	$4.68^{+5.43}_{-1.92}$	2.25
49095	1.401	1.59 ± 0.13	11.54 ± 3.42	-	$1.13^{+0.00}_{-0.28}$	$1.02^{+0.41}_{-0.39}$	2.25
45629	1.401	0.45 ± 0.10	1.08 ± 0.74	-	$0.3^{+0.00}_{-0.05}$	$0.36^{+0.32}_{-0.26}$	2.25
56208	1.402	0.99 ± 0.08	8.59 ± 2.63	-	$1.14^{+0.00}_{-0.14}$	$0.75^{+0.26}_{-0.25}$	2.25
61110	1.402	0.46 ± 0.27	6.8 ± 2.16	-	$0.91^{+0.0}_{-0.04}$	$0.74^{+0.26}_{-0.24}$	2.25
54647	1.404	0.49 ± 0.12	4.95 ± 1.73	-	$1.04^{+0.0}_{-0.22}$	$0.48^{+0.17}_{-0.19}$	2.25
63911	1.405	0.64 ± 0.05	< 4.75	-	$1.35^{+0.00}_{-0.08}$	$0.05^{+0.02}_{-0.0}$	2.25
57918	1.407	0.26 ± 0.06	< 1.10	-	$0.89^{+0.00}_{-0.09}$	$0.03^{+0.01}_{-0.01}$	2.26
44194	1.408	2.4 ± 0.2	10.91 ± 3.21	31.49 ± 16.78	$1.76^{+0.0}_{-0.29}$	$1.79^{+0.96}_{-1.0}$	2.26
56439	1.408	2.28 ± 0.19	15.56 ± 4.63	-	$4.66^{+1.00}_{-0.62}$	$0.33^{+0.11}_{-0.11}$	2.26
45372	1.408	0.94 ± 0.08	8.71 ± 3.82	-	$1.06^{+0.00}_{-0.09}$	$0.82^{+0.43}_{-0.37}$	2.26

Table 5.6: - continued

ID	z	SFR_{UV} $(M \odot yr^{-1})$	$SFR_{[OII]}$ $(M \odot yr^{-1})$	$SFR_{24\mu m}$ $(M \odot yr^{-1})$	$M_\star$ $(10^{11} M\odot)$	SSFR $(10^{-10} yr^{-1})$	1/t(z) $(10^{-10} yr^{-1})$
59320	1.409	2.87 ± 0.24	10.49 ± 4.26	-	$2.07^{+0.00}_{-0.46}$	$0.51^{+0.23}_{-0.23}$	2.26
54522	1.409	0.81 ± 0.20	< 0.91	-	$0.8^{+0.00}_{-0.08}$	$0.10^{+0.03}_{-0.03}$	2.26
32227	1.410	2.55 ± 0.29	4.05 ± 1.56	169.04 ± 69.46	$0.49^{+0.00}_{-0.06}$	$34.8^{+30.44}_{-14.93}$	2.26
49961	1.411	0.61 ± 0.06	6.94 ± 2.14	-	$1.62^{+0.0}_{-0.09}$	$0.43^{+0.14}_{-0.13}$	2.26
63237	1.412	0.86 ± 0.09	1.79 ± 0.94	-	$0.59^{+0.0}_{-0.06}$	$0.31^{+0.16}_{-0.16}$	2.26
46492	1.414	4.87 ± 0.40	10.00 ± 3.03	134.45 ± 55.35	$1.33^{+0.00}_{-0.62}$	$10.13^{+4.45}_{-6.28}$	2.27
52436	1.421	2.64 ± 0.22	5.43 ± 1.8	273.02 ± 108.6	$1.47^{+0.0}_{-0.4}$	$18.52^{+7.88}_{-8.92}$	2.28
63675	1.429	6.86 ± 0.56	3.23 ± 1.05	139.08 ± 57.45	$0.76^{+0.00}_{-0.23}$	$18.25^{+13.64}_{-9.31}$	2.29
81348	1.435	1.27 ± 0.1	5.86 ± 1.85	41.99 ± 18.91	$0.32^{+0.00}_{-0.02}$	$13.21^{+6.26}_{-6.01}$	2.29
29788	1.435	0.43 ± 0.06	2.84 ± 0.93	-	$0.51^{+0.00}_{-0.21}$	$0.55^{+0.28}_{-0.29}$	2.29
62125	1.441	1.05 ± 0.12	< 1.78	-	$4.74^{+0.0}_{-0.87}$	$0.02^{+0.00}_{-0.00}$	2.3
53841	1.444	1.40 ± 0.25	2.09 ± 0.74	-	$1.56^{+0.00}_{-0.87}$	$0.13^{+0.06}_{-0.09}$	2.31
46886	1.451	1.71 ± 0.14	3.15 ± 0.99	-	$0.49^{+0.00}_{-0.15}$	$0.64^{+0.24}_{-0.28}$	2.32
47359	1.456	1.59 ± 0.13	< 2.25	-	$1.51^{+0.00}_{-0.24}$	$0.1^{+0.01}_{-0.02}$	2.32
48550	1.456	1.34 ± 0.11	15.15 ± 4.88	84.46 ± 36.99	$0.65^{+0.0}_{-0.03}$	$12.97^{+6.77}_{-5.71}$	2.32
78217	1.456	0.94 ± 0.08	10.37 ± 3.02	-	$1.27^{+0.0}_{-0.24}$	$0.82^{+0.24}_{-0.28}$	2.32
19851	1.458	6.28 ± 0.52	14.58 ± 4.69	116.7 ± 49.96	$0.54^{+1.0}_{-0.02}$	$21.77^{+32.44}_{-9.36}$	2.33
32476	1.458	1.48 ± 0.12	18.73 ± 5.37	-	$0.45^{+0.0}_{-0.08}$	$4.21^{+2.45}_{-1.43}$	2.33
73600	1.458	0.32 ± 0.06	< 0.31	-	$0.45^{+0.00}_{-0.05}$	$0.07^{+0.02}_{-0.02}$	2.33
58689	1.459	1.32 ± 0.11	6.94 ± 2.05	-	$0.66^{+0.0}_{-0.28}$	$1.05^{+0.36}_{-0.54}$	2.33
64357	1.460	1.39 ± 0.11	8.05 ± 2.36	71.73 ± 32.84	$0.36^{+0.00}_{-0.08}$	$19.83^{+9.20}_{-10.09}$	2.33

Table 5.6: - continued

ID	z	SFR_{UV} $(M \odot yr^{-1})$	$\mathrm{SFR}_{[OII]}$ $(M \odot yr^{-1})$	$\mathrm{SFR}_{24\mu m}$ $(M \odot yr^{-1})$	$M_\star$ $(10^{11} M\odot)$	SSFR $(10^{-10} yr^{-1})$	1/t(z) $(10^{-10} yr^{-1})$
79138	1.461	1.72 ± 0.14	34.04 ± 9.79	142.63 ± 58.41	$0.45^{+0.00}_{-0.01}$	$31.87^{+23.05}_{-13.06}$	2.33
78923	1.462	0.30 ± 0.04	1.37 ± 0.64	-	$0.59^{+0.00}_{-0.04}$	$0.23^{+0.11}_{-0.11}$	2.33
62775	1.467	5.37 ± 0.88	5.66 ± 1.76	42.98 ± 19.09	$0.74^{+0.00}_{-0.11}$	$5.79^{+3.7}_{-2.71}$	2.34
44334	1.467	1.00 ± 0.08	7.00 ± 2.75	113.22 ± 46.94	$1.63^{+0.00}_{-0.13}$	$6.93^{+3.11}_{-2.92}$	2.34
66424	1.467	0.61 ± 0.08	10.58 ± 3.07	-	$1.23^{+0.00}_{-0.31}$	$0.86^{+0.37}_{-0.33}$	2.34
30838	1.477	16.0 ± 1.32	73.08 ± 20.9	-	$0.47^{+0.00}_{-0.24}$	$15.48^{+4.44}_{-8.97}$	2.35
72815	1.477	6.05 ± 0.50	32.76 ± 9.43	117.04 ± 55.33	$0.14^{+0.0}_{-0.00}$	$84.01^{+292.45}_{-39.78}$	2.35
72088	1.477	2.11 ± 0.17	11.71 ± 3.41	-	$0.32^{+0.00}_{-0.04}$	$3.68^{+2.6}_{-1.18}$	2.35
71384	1.477	0.48 ± 0.04	7.76 ± 2.33	-	$3.32^{+0.00}_{-0.15}$	$0.23^{+0.07}_{-0.07}$	2.35
53230	1.478	2.23 ± 0.18	55.93 ± 16.05	-	$1.59^{+0.00}_{-0.64}$	$3.53^{+1.02}_{-1.74}$	2.35
60843	1.478	1.72 ± 0.14	32.27 ± 9.29	134.3 ± 55.67	$0.30^{+0.00}_{-0.03}$	$44.32^{+19.02}_{-18.8}$	2.35
70067	1.478	0.57 ± 0.06	3.19 ± 1.18	-	$0.96^{+0.00}_{-0.10}$	$0.33^{+0.13}_{-0.13}$	2.35
52354	1.483	8.32 ± 0.68	57.27 ± 16.39	122.36 ± 46.39	$0.20^{+0.0}_{-0.05}$	$62.72^{+120.95}_{-29.12}$	2.36
56151	1.483	0.36 ± 0.08	4.04 ± 1.22	-	$0.57^{+0.0}_{-0.07}$	$0.71^{+0.22}_{-0.23}$	2.36
48451	1.485	2.24 ± 0.18	8.21 ± 2.54	180.55 ± 71.95	$2.69^{+0.00}_{-0.66}$	$6.7^{+2.85}_{-3.14}$	2.36
29201	1.485	2.08 ± 0.17	2.72 ± 0.87	-	$0.31^{+0.00}_{-0.05}$	$0.89^{+0.29}_{-0.32}$	2.36
43168	1.491	0.90 ± 0.07	13.06 ± 3.89	-	$0.53^{+0.00}_{-0.08}$	$2.45^{+0.77}_{-0.82}$	2.37
47774	1.497	1.17 ± 0.1	20.98 ± 6.76	-	$0.89^{+0.00}_{-0.32}$	$2.36^{+0.83}_{-1.14}$	2.38
50229	1.498	1.25 ± 0.1	< 3.16	-	$0.64^{+0.00}_{-0.00}$	$0.2^{+0.03}_{-0.02}$	2.38
54253	1.502	0.73 ± 0.06	< 5.24	-	$1.6^{+0.00}_{-0.14}$	$0.05^{+0.01}_{-0.01}$	2.39
61727	1.505	0.16 ± 0.05	< 1.46	-	$0.41^{+0.00}_{-0.01}$	$0.04^{+0.01}_{-0.01}$	2.39

the spectrophotometric fits to the TCM models. We have a total of 52/82 confirmed passive objects. To convert this to a passive galaxy fraction for the $K \leq 21.5$ and $1.3 \leq z \leq 1.5$ universe we need to look at the rest of the UDS sample using photometric redshifts.

Taking UDS DR8 and making cuts of $K \leq 21.5$ and $1.3 \leq z_{photo} \leq 1.5$ gives 1249 galaxies. Considering the criteria which were applied when constructing the masks for observation ($V > 24.5$ and $i < 24.5$ or $z < 24.0$, see Section 2.2) of these 1249 galaxies, 761 passed the criteria (observable) and the remaining 488 failed the criteria (unobservable). Assuming that the fraction of passive galaxies we found in the spectroscopic sample studied here can be extrapolated to the entire "observable" sample implies from the "observable" Universe we have $(52/82) \times 761 \approx 483$ passive galaxies and $(30/82) \times 761 \approx 278$ actively star-forming galaxies. The passive fraction of the "unobservable" Universe was found by estimating the fraction of star-forming galaxies.

Of the 30 star-forming galaxies in the sample there were 21 galaxies with $24\mu m$ detections and 18 that had star-formation rates estimates from [OII] high enough with respect to their stellar-mass to be classified as star-forming. Therefore there were 9 galaxies that were identified as star-forming from the presence of an [OII] emission line with no detection in $24\mu m$. If the star-formation estimated from the UV was high enough for the galaxy to be classed as star-forming the [OII] and/or $24\mu m$ estimates were always higher. There were 23 galaxies in the sample that had a $24\mu m$ detection, therefore there were two galaxies with a $24\mu m$ detection that had sufficient mass that they were classified as passive evolving.

The $24\mu m$ catalog was crossed matched with UDS DR8 objects that had a K-band detection. It was found that 200 galaxies of the "unobservable" sample ($K < 21.5$, $1.3 \leq z_{photo} \leq 1.5$ and $V < 24.5$) had $24\mu m$ detections. Therefore $(21/23) \times 200 \approx 183$ of these galaxies were expected to be forming enough stars to be classified as actively star-forming. Using the relation found in the sample it is expected that an additional $(9/21) \times 183 \approx 78$ objects could be found as star-forming, the fraction with [OII] but no $24\mu m$ detection. Therefore it is estimated that 257/488 of the "unobservable" sample is star-forming. So the estimate of the passive fraction of the $K < 21.5$ and $1.3 \leq z_{photo} \leq 1.5$ Universe is $(483 + 227)/1249 \approx 57 \pm 10\%$. It should be noted that the

number of objects in the "unobservable" sample that could be classified as star-forming solely from [OII] emission could be higher as the "unobservable" sample is bluer, this would reduce the passive fraction.

Cutting the sample at $K < 20.65$, i.e. to select a pure ERO population (see Figure 5.1) gives 30 objects, 23 of which are passive. Following the same procedure as above the passive fraction for the $K < 20.65$ and $1.3 \leq z_{photo} \leq 1.5$ is $\approx 75 \pm 19\%$. Many authors calculate the passive fraction of a K-band bright sample but with an ERO colour cut included. Applying an $R-K > 3.38$ colour cut to the K-Bright sample used here and repeating the analysis above gives a passive fraction of $\sim 78 \pm 33\%$.

Considering the most massive galaxies ($M_\star > 7 \times 10^{10} M_\odot$) in the K-Bright sample the passive fraction is $32/40 = 80 \pm 19\%$. This is consistent with the fraction found from the ERO subsample. This can be understood from the stellar-mass versus R-K relation for the sample (Figure 5.16) which shows all galaxies with $M_\star > 7 \times 10^{10} M_\odot$ are EROs.

5.8.1 Comparison with Results in the Literature

From spectral classification Cimatti et al. [2002a] put constraints of $33 - 67\%$ on the passive fraction of EROs, $K_{Vega} < 19.2$ and $(R-K)_{Vega} > 5$.

Using radio data along with $RizJHK$ photometry of EROs, $K_{Vega} < 20.5$ and $(R-K)_{Vega} > 5.3$, Smail et al. [2002] estimated a passive fraction of $40\% \pm 15\%$

Using stellar population synthesis models, restricted to those representing dusty star-forming and old stellar populations, and $BVRizJHK$ photometry, Miyazaki et al. [2003] classified 247 EROs, $K < 22.1$ and $R - K > 3.35$. They found 143 to be old passive galaxies, giving a passive fraction of 58%

Fontanot and Monaco [2010] used the MORGANA semi-analytical model [Monaco et al., 2007] to study EROs, $(R-K)_{Vega} > 5$. Using the definition of a passive galaxy from Brinchmann et al. [2004], i.e. SSFR $\leq 10^{-11} yr^{-1}$, Fontanot and Monaco [2010] found that for $K_{Vega} < 22$ and $(R-K)_{Vega} > 5$ the passive fraction was 32%. At $K_{Vega} < 20.3$ and $(R-K)_{Vega} > 5$ their predicted passive fraction increases to 38% and it increases further to 47% for a $K_{Vega} < 19.2$ and $(R-K)_{Vega} > 5$. They also predict a passive fraction of 44% for a $K_{Vega} < 20.3$ and $(R-K)_{Vega} > 5.3$

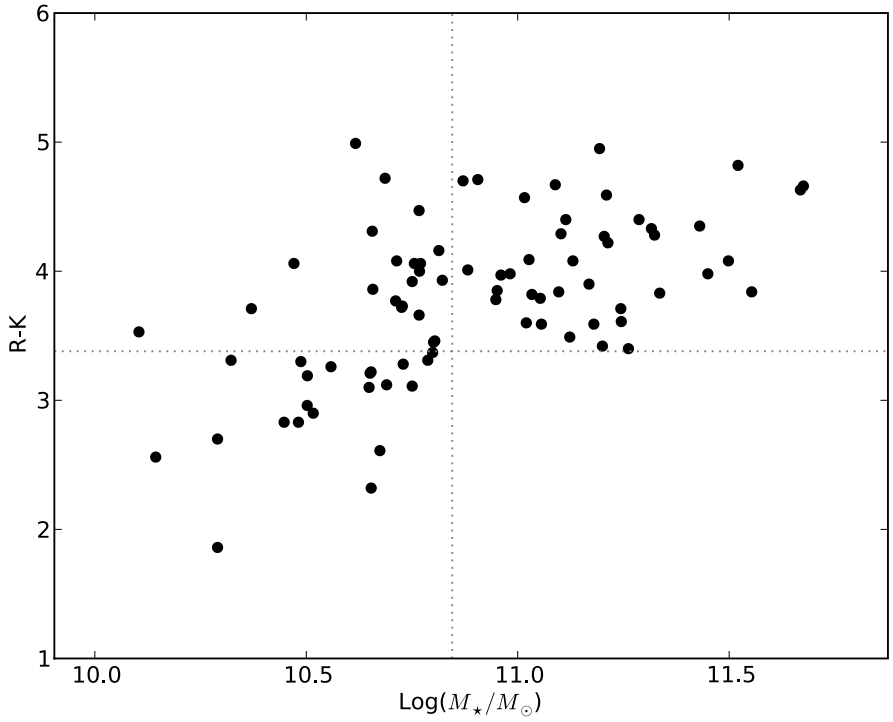

Figure 5.16: stellar mass versus R-K colour for the K-Bright sample. The vertical grey dotted line corresponds to a stellar-mass of $7 \times 10^{10} M_\odot$ and the horizontal grey dotted line represents the colour cut for ERO selection, $R - K > 3.38$.

The passive fraction estimate found here for the $K < 21.5$ sample here is consistent with the results found by Miyazaki et al. [2003]. Even though there is no colour constraint on the sample studied here it has a brighter cut in K-band depth than Miyazaki et al. [2003] and $\approx 75\%$ of our sample are EROs anyway. The $K < 21.5$ passive galaxy fraction estimate also sits within the range of values estimated by Cimatti et al. [2002a]. The fraction estimated by Smail et al. [2002] is significantly lower than the one found here, which is probably due to the fainter cut in K-band magnitude. The theoretical predictions made by Fontanot and Monaco [2010] sit below what is observed here and by the other authors.

The passive fraction recovered for galaxies with $K < 20.65$ ($\approx 75\%$) is very high, but even though this criteria selects a purely ERO sample it is selecting only the very brightest EROs. Therefore these are potentially the most massive EROs which could

explain the large passive fraction. The passive fraction recovered for the full $K < 21.5$, $R - K > 3.38$ appear large but when considering the large errors agree with the result of the bright sample from Cimatti et al. [2002a]. Also the lower fraction from Smail et al. [2002] and Miyazaki et al. [2003] originate from fainter samples.

Fontana et al. [2009] investigated the evolution of the passive fraction of sample that are mass complete above $7 \times 10^{10} M_{\odot}$. For the redshift range studied here Fontana et al. [2009] recovers a passive fraction of $\sim 50 - 60\%$. The values recovered here for the $M_{\star} > 7 \times 10^{10} M_{\odot}$ sample are large but agree within in the the errors and for $K < 21.5$ sample the mass completeness is only $\sim 1 \times 10^{11}$ and therefore the results here is based on an incomplete sample.

5.9 Summary & Conclusions

The optical spectra and multi-wavelength photometry of a large sample of high-redshift K-band bright sources has been exploited to recover accurate measurements of their physical characteristics. Age and accurate stellar-mass estimate were recovered from spectrophotometric fits to the galaxies data. A wide range of star-formation histories were used, with so called τ models, burst models and double burst models all fit to the galaxy's optical spectra and photometry. There is a positive relation between mass and age with the more massive systems also being the older systems, in agreement with the general downsizing scenario for massive galaxy assembly.

Investigating the size-mass relation shows a differential trend with stellar mass. The lower-mass systems sit on the local relation, whereas the systems of large stellar-mass tend to sit below the relation that is seen locally. Following the work of Saracco et al. [2009] the sample was split into young and old galaxies in relation to whether they were older or younger than 50% of the age of the Universe at their redshift. The young systems span the local size-mass relation as opposed to the older systems which sit, on average, a factor ~ 1.5 below the relation. A very similar result was found when the sample was split by passivity, with the more passive objects sitting below the relation, and spectral type, with ETGs also consistently sitting below the relation.

The velocity dispersions estimated here were used to calculate the dynamical masses as these are model independent mass estimates and therefore a solid test for the high-

redshift size-mass relation. Comparing the resulting dynamical masses to ones acquired from velocity dispersions estimates from the SDSS it is shown (Figure 5.15) that all 13 objects sit towards or below the lower edge of the local size-dynamical mass relation indicating that these objects really are compact.

The fact that the massive galaxies studied here sit below the local size-mass relation, in agreement with many other authors [e.g. Trujillo et al. 2006a, Trujillo et al. 2006b, Trujillo et al. 2007, Longhetti et al. 2007, McGrath et al. 2008, Buitrago et al. 2008], leads to two potential scenarios.

One option is that size evolution of the massive systems at high-redshift is required to join the local size-mass relation. There are several theories to explain this evolution which include the redistribution of stellar-mass due to mass ejection from quasar feedback [Fan et al., 2008], the dry merger hypothesis where dense cores are created at high-redshift through a gas rich merger and then dry mergers between then and the present increase the effective radii [Khochfar and Silk, 2006] and also size-evolution has been considered a result of the accretion of mass via minor mergers [Naab et al., 2009].

Another option is that compact galaxies are present in the local Universe and that normal sized galaxies are present at high-redshift but, due to selection effects, both populations have been missed. Recently Taylor et al. [2010] went is search of compact galaxies in the local Universe. It was shown, especially at low redshift $z \leq 0.05$, that SDSS selection effects would miss bright and compact objects to avoid saturation and cross-talk in the spectrograph. Taylor et al. [2010] found 63 galaxies to sit a factor of 2 or more below the local relation from Shen et al. [2003] and have higher than average velocity dispersions. Moreover, Mancini et al. [2010] found that 9 of the K-band brightest and most massive objects from the COSMOS field at $z \geq 1.4$ sat on the local size-mass relation. In this scenario no size evolution is required between high-redshift and the present day and that complete samples at low- and high-redshift have not yet been acquired.

Saracco et al. [2011] found similar results to this study, that at $z \sim 1.5$ normal and compact ETGs coexist. Saracco et al. [2011] found that dissipative merging at high redshfit can produce compact remnants and a large fraction of the stellar mass is produced concurrently with the merging. Nipoti et al. [2009] investigated whether dry

merging could account for the size evolution witnessed in ETGs from high redshift to the present day. Considering both major- and minor-merger hierarchies, Nipoti et al. [2009] conÞrm that dry mergers bring compact ETGs closer to the local relation, but they can not match the factor of ~ 5 seen in van Dokkum et al. [2008]. Nipoti et al. [2009] finds a growth factor from dry mergers from $z = 2.3$ to the present day of ~ 1.9. This growth factor is consistent with the results found here and other studies at $z \sim 1.5$, of $\sim 1.5-2$. So not including the extreme results of van Dokkum et al. [2008] and expect minor size evolution over the $\sim$ 3Gyrs period between $z \sim 1.5-2.3$ dry mergers appear to be a plausible mechanism for size evolution of ETGs from high redshift to the local Universe.

With the use of SSFRs the passive fraction for the K-band bright Universe was estimated at $58 \pm 10\%$. This is consistent with several other studies in the literature such as Cimatti et al. [2002a] and Miyazaki et al. [2003]. Although most of the studies in the literature have been of purely ERO samples as opposed to simply a cut in K-band magnitude, the consistency of the result derived here is unsurprising given that $75 \pm 19\%$ for the K-Bright sample are EROs. When cutting the sample at $K < 20.65$ to get a pure EROs sample the passive fraction recovered ($\approx 75\%$) is very high, but even though this criteria selects a purely ERO sample it is selecting only the very brightest EROs.

The passive fractions recovered from the ERO ($K < 21.5$, $R - K < 3.38$) and high mass ($M_\star > 7 \times 10^{10} M_\odot$) samples are $78 \pm 33\%$ an $80 \pm 19\%$ respectively are both large but carry large errors which bring them in agreement with other studies. The $K < 21.5$ sample is only mass complete down to $\sim 1 \times 10^{11}$ which could be another source for the difference and cosmic variance could also play a role in the difference of these results from that of other authors.

Recent theoretical studies have only looked at the passive fraction of the ERO population at high redshift. Studying the ERO, $(R - K)_{Vega} > 5$, samples at varying cuts in K-band magnitude Fontanot and Monaco [2010] found passive fractions of 32%, 38% and 47% for $K_{Vega} < 22$, 20.3 and 19.2 samples. These results sit a factor ~ 2 below the passive fraction calculated for our bright ($K < 21.5$), ERO ($R - K > 3.38$) sample and even below our result for simply the K-Bright sample (just $K < 21.5$). Therefore it

would appear that theoretical SAM studies are still not yet producing enough passive galaxies at high redshift.

To calculate the passive galaxy fraction for a complete unbiased K-band selected sample at high redshift optimised photometric techniques are required.

Chapter 6

Separating Galaxy Populations at High-Redshift

There are several techniques that use broad-band colours to separate K-band selected galaxy populations at high-redshift [e.g. Pozzetti and Mannucci 2000, Daddi et al. 2004a, Williams et al. 2009]. Such techniques are extremely useful for extracting particular galaxy populations from large photometric data-sets with limited spectroscopic coverage. These techniques are calibrated using the understanding and knowledge of SEDs of particular galaxy types. The large spectroscopic sample used in this thesis presents a unique opportunity to assess and potentially improve these techniques using the information obtained from the optical spectra and accompanying data.

6.1 Examining Photometric Division of Galaxy Populations at High-Redshift

Using the knowledge of the passivity of the UDSz sample from UV flux, the [OII] emission line and $24\mu m$ data we investigate the effectiveness of current techniques that use photometric colours to separate passive and star-forming galaxy populations at high redshift. We will investigate and optimise the BzK diagram from Daddi et al. [2004a] which uses the $B-z$ and $z-K$ colours to separate the $1.4 < z < 2.5$ galaxy population into quiescent and star-forming systems, the $(J-K)$ v $(i-K)$ diagram that divides the $1 < z < 2$ ERO population into passive and dusty star-forming from Pozzetti and

Mannucci [2000] and then a relatively new technique from Williams et al. [2009] that uses the rest-frame $(V - J)$ and $(U - V)$ colours to select passive and star-forming galaxies from $z = 0$ to $z = 2$.

6.1.1 The BzK Diagram

The BzK diagram [Daddi et al., 2004a] is used to select passive and star-forming galaxies at $1.4 < z < 2.5$. The original population dividers, as defined by Daddi et al. [2004a], are shown in Figure 1.19. Daddi et al. [2004a] calibrated the technique using data from the K20 survey (see Section 1.6.1) and therefore it is calibrated for galaxies with $K < 20$(Vega). This was possible due to the high spectroscopic completeness of the $K20$ survey. The BzK was an empirical diagram that was justified by SSPs afterwards. The selection criteria is based on the fact that old galaxies will sit in the top right corner on the BzK colour plot because they have red continuum, due to breaks and absorption features in the rest-frame range 2500-3000Å and a strong 4000Å break, i.e. red colours in the observed $B-z$ and $z-K$ bands. In contrast, an actively star-forming galaxy is defined to be one with $BzK \geq -0.2$, where $BzK = (z - K) - (B - z)$, as this area will be filled with systems that have blue UV rest-frame colours but can be allowed a range of optical-NIR colours to allow for dusty objects. A passive galaxy is defined as $BzK < -0.2$ and $z - K > 2.5$. This scheme was devised with the Bessel B-band, F850LP z-band from HST+ACS, and the VLT+ISAAC K-band filters.

Although widely employed [e.g. Daddi et al. [2005a], Takagi et al. [2008], McCracken et al. [2010]] recent work from Karim et al. [2011] has shown (see Figure 6.1) that for $z < 1.8$ the BzK selectcion technique starts to miss a substantial fraction of the passive population, and by $z \sim 1.5$ it is a poor method for selecting passive galaxies.

This work provided motivation to use our spectroscopic redshifts and knowledge of the passivity of our sample to improve the BzK selection technique. Figure 6.2 shows the BzK selection technique applied to our sample with different limiting K-band magnitudes. The top, middle and bottom panels are for the $K < 21.0$, 22.0 and 23.0 samples respectively. The red circles and blue triangles are known passive and star-forming galaxies at $1.4 < z < 2.5$ respectively based on the definition in Section 5.8 and the black crosses are galaxies with $z_{spec} < 1.4$. The grey dotted line

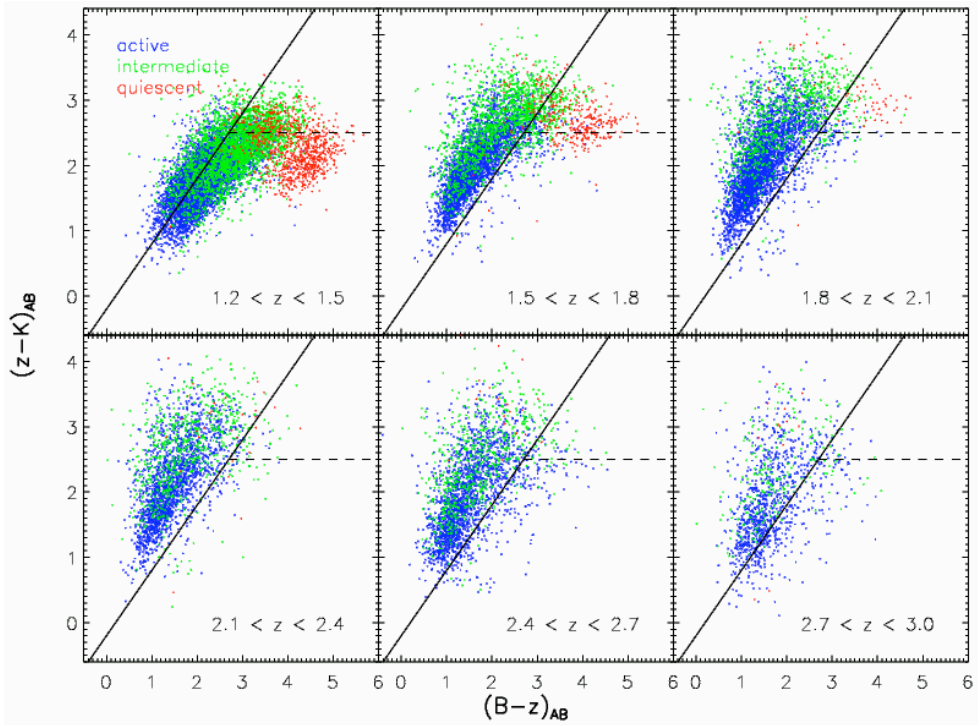

Figure 6.1: BzK diagram in various redshift bins from Karim et al. [2011]. The colour coding refers to our choice of the $(NUV - r^{+})_{temp}$ colour threshold in order to predefine systems with high (blue), intermediate (green) and negligible (red) star formation activity.

shows the population divisions defined by Daddi et al. [2004a], described above, and the solid grey lines show these division corrected to the filters used in the UDS by Hartley et al. [2008]. Based on the spectroscopic sample it is immediately apparent that the corrections devised by Hartley et al. [2008] worsen the identification of passive galaxies.

Assessment of the BzK Diagram

For the $K < 21.0$ sample there are 40 galaxies at $1.4 < z < 2.5$ and 92 at $z < 1.4$. Of the 40 high-redshift galaxies, 28 are passive and 12 are star-forming galaxies. The original BzK diagram (with UDS filter corrections) correctly selects $1/28$ ($\sim 4\%$) of the confirmed passive sample, with $3(\sim 11\%)$ selected to be star-forming and the rest as low-redshift targets. A large fraction of the confirmed star-forming galaxies ($8/12 \approx 67\%$) are selected as star-forming with the remainder selected as low-redshift galaxies. Of the 92 low-redshift galaxies 100% were correctly selected.

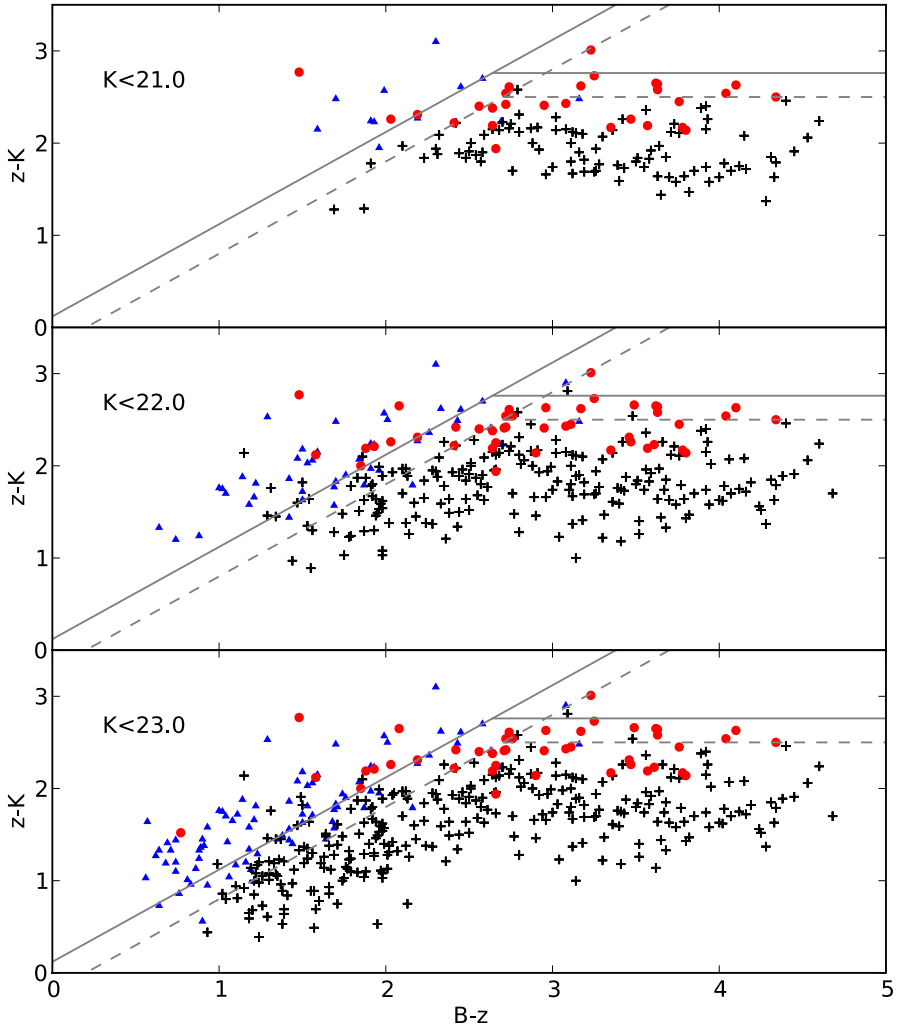

Figure 6.2: The BzK diagram for the spectroscopic sample. The top, middle and bottom panels are for the $K < 21.0$, 22.0 and 23.0 samples respectively. The red circles and blue triangles are known passive and star-forming galaxies at $1.4 < z < 2.5$ respectively, based of the definition in Section 5.8 and the black crosses are galaxies with $z_{spec} < 1.4$. The grey dotted lines shows the population divisions defined by Daddi et al. [2004a] and the solid grey lines show these division corrected to the filters used in the UDS by Hartley et al. [2008].

For the $K < 22.0$ sample there are 88 galaxies at $1.4 < z < 2.5$ and 203 at $z < 1.4$. Of the 88 high-redshift galaxies, 43 are passive and 45 are star-forming galaxies. The original BzK diagram (with UDS filter corrections) correctly selects 1/43 ($\sim 2\%$) of the confirmed passive sample, with 8($\sim 19\%$) selected to be star-forming and the rest as low-redshift targets. Over two-thirds ($31/45 \approx 69\%$) of the confirmed star-forming galaxies are selected as star-forming with 1($\sim 2\%$) selected to be passive and the remainder selected as low-redshift galaxies. Of the 203 low-redshift targets 196/203 ($\sim 97\%$) were correctly selected with one galaxy misidentified as a passive galaxy and six misidentified as high-redshift star-forming galaxies.

For the $K < 23.0$ sample there are 129 galaxies at $1.4 < z < 2.5$ and 287 at $z < 1.4$. Of the 129 high-redshift galaxies, 44 are passive and 85 are star-forming galaxies. The original BzK diagram (with UDS filter corrections) correctly selects 1/44 ($\sim 2\%$) of the confirmed passive sample, with 9($\sim 20\%$) selected to be star-forming and the rest as low-redshift targets. Approximately 65% (55/85) of the confirmed star-forming galaxies are selected as star-forming with 1($\sim 1\%$) selected to be passive and the remainder selected as low-redshift galaxies. Of the 287 low-redshift targets 278/287 ($\sim 97\%$) were correctly selected with one misidentified as a high-redshift passive galaxy and eight misidentified as high-redshift star-forming galaxies.

Considering contamination within the selection boxes; of all the galaxies selected to be high-redshift passive galaxies 1/1(100%), 1/3($\sim 33\%$) and 1/3($\sim 33\%$) for the $K <$ 21.0, 22.0 and 23.0 sample respectively are actually passive. Of all the galaxies selected to be high-redshift star-forming galaxies 8/11($\sim 73\%$), 31/45($\sim 69\%$), 55/72($\sim 76\%$) are star-forming galaxies. All of this is summarised in Table 6.1, where each column shows how the different galaxy populations are is distributed on the BzK diagram.

These results demonstrate that the population dividers defined in BzK space are far from perfect. However, visual inspection shows that it should be possible to dramatically improve the selection criteria.

Optimising the BzK Diagram

From Figure 6.2 it is clear that the dividers defined by Daddi et al. [2004a] have the correct slopes but just need translating to become optimal. This was done using the

Table 6.1: The distribution of known galaxy populations on the BzK diagram. Columns 2, 3 and 4 shows how the known passive, star-forming and low-redshift targets are distributed.

	Passive	Star-forming	Low-redshift
$K < 21.0$(totals)	28	12	92
p-BzK	1	0	0
sf-BzK	3	8	0
low-z-BzK	24	4	92
$K < 22.0$(totals)	43	45	203
p-BzK	1	1	1
sf-BzK	8	31	6
low-z-BzK	34	13	196
$K < 23.0$(totals)	44	85	287
p-BzK	1	1	1
sf-BzK	9	55	8
low-z-BzK	29	13	278

following method. Consider two populations that can be divided by a relation of two properties, here the properties are photometric colours. Two indices are defined, the C index, which is produced by multiplying together the fractions of correctly selected galaxies from the two populations and the I index, which is the number of incorrectly selected galaxies divided by the total number of galaxies selected in each region multiplied together i.e. a contamination factor. The best population divider was found by maximising the $C - I$ index i.e. the line that selects the most galaxies of one population correctly with the minimum contamination.

This method has been applied to the three samples studied above and the resulting optimal population dividers are shown in Figure 6.3 as solid grey lines. The symbols are as in Figure 6.2 and the top, middle and bottom panels are again for the $K < 21.0$, 22.0 and 23.0 samples respectively. The original dividing lines defined by Daddi et al. [2004a] were (corrected for the UDS filters) $BzK < 0.12$ and $z - K > 2.76$ where $BzK = (z - K) - (B - z)$. In contrast optimal dividers calculated for the $K < 21.0$,

22.0 and 23.0 samples are:

$$BzK < -0.12, z - K > 2.16 \quad \text{for} \quad K < 21.0 \tag{6.1}$$

$$BzK < -0.09, z - K > 2.13 \quad \text{for} \quad K < 22.0 \tag{6.2}$$

$$BzK < -0.09, z - K > 2.13 \quad \text{for} \quad K < 23.0 \tag{6.3}$$

For the $K < 21.0$ sample the optimised BzK diagram correctly selects 23/28 ($\sim$ 82%) of the confirmed passive sample, with 3(12.5%) selected to be star-forming and the rest as low-redshift targets. The number of confirmed star-forming galaxies to be selected as star-forming has increased to 10/12 ($\sim$ 83%) with the remainder selected as high-redshift passive galaxies. Of the 92 low-redshift targets 76/92 ($\sim$ 83%) were correctly selected while 16($\sim$ 17%) were misidentified as high-redshift passive galaxies.

For the $K < 22.0$ sample the optimised BzK diagram correctly selects 33/43 ($\sim$ 77%) of the confirmed passive sample, with 9($\sim$ 21%) selected to be star-forming and the remainder as a low-redshift targets. A very large fraction (39/45 $\approx$ 87%) of the comfirmed star-forming galaxies are selected as star-forming with 4($\sim$ 9%) selected to be passive and the remainder selected as low-redshift galaxies. Of the 203 low-redshift targets 161/203 ($\sim$ 79%) were correctly selected while 29 were misidentified as high-redshift passive galaxies and 13 as high-redshift star-forming galaxies.

For the $K < 23.0$ sample there are 129 galaxies at $1.4 < z < 2.5$ and 287 at $z < 1.4$. Of the 129 high-redshift galaxies 44 are passive and 85 are star-forming galaxies. The optimised BzK diagram correctly selects 33/44 (75%) of the confirmed passive sample, with 10($\sim$ 23%) selected to be star-forming and the remainder as a low-redshift target. Nearly all (76/85 $\approx$ 89%) of the confirmed star-forming galaxies are selected as star-forming with 4($\sim$ 5%) selected to be passive and the remainder selected as low-redshift galaxies. Of the 287 low-redshift targets 238/287 ($\sim$ 83%) were correctly selected while 29 were misidentified as high-redshift passive galaxies and 20 as high-redshift star-forming galaxies.

Considering contamination within the optimised selection boxes of all the objects selected to be high-redshift passive galaxies 23/41(56%), 32/65($\sim$ 49%) and 33/66(50%)

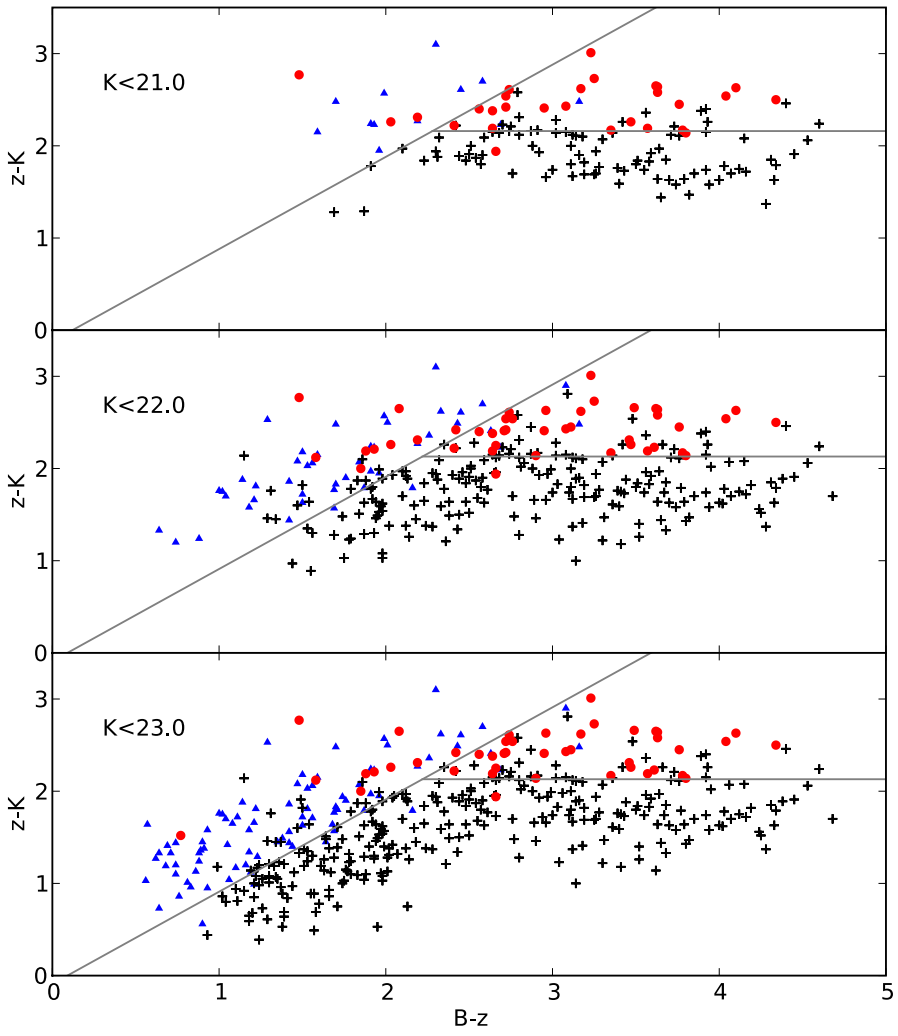

Figure 6.3: Optimised BzK diagram. The symbols are as in Figure 6.2, the top, middle and bottom panels are for the $K < 21.0$, 22.0 and 23.0 samples respectively. The solid grey lines show the optimised galaxy population dividers.

Table 6.2: The distribution of known galaxy populations on the optimised BzK diagram. Columns 2, 3 and 4 show how the known passive, star-forming and low-redshift targets are distributed.

	Passive	Star-forming	Low-redshift
$K < 21.0$(totals)	28	12	92
p-BzK	23	2	16
sf-BzK	3	10	0
low-z-BzK	2	0	76
$K < 22.0$(totals)	43	45	203
p-BzK	33	4	29
sf-BzK	9	39	13
low-z-BzK	2	1	161
$K < 23.0$(totals)	44	85	287
p-BzK	33	4	29
sf-BzK	10	76	20
low-z-BzK	1	5	238

for the $K < 21.0$, 22.0 and 23.0 sample respectively are actually passive. Of all the galaxies selected to be high-redshift star-forming galaxies $10/13(\sim 77\%)$, $40/66(\sim 61\%)$, $76/106(\sim 72\%)$ are actually star-forming galaxies

Even though the contamination levels of passive galaxies in the allocating star-forming region have inevitably increased, the fractions of correctly selected passive galaxies has drastically increased. All of this is summarised in Table 6.2 where each column shows how the population of galaxies is distributed on the optimised BzK diagram. The optimised selection techniques for the three K-band magnitude limited samples are very similar. Using $BzK < -0.09$ and $z - K > 2.13$ for the $K < 21.0$ just slightly increases the contamination of low-redshift galaxies in the high-redshift passive selection region.

From the analysis above and the results in Table 6.2 the passive fraction at high-redshift is calculated as described in Table 6.3 which takes into account the known levels of contamination between the regions. The numerator of each fraction is the total

Table 6.3: The formulae for calculating the passive fraction for each of the optimised BzK diagrams. P is the total number of galaxies selected to be passive, S is the total number of galaxies selected as star-forming and the L is the total number of galaxies selected as low-redshift objects.

K-band cut	Passive Fraction
$K < 21.0$	$\frac{P\frac{23}{41}+S\frac{3}{13}+L\frac{2}{78}}{P\frac{25}{41}+S\frac{13}{13}+L\frac{2}{78}}$
$K < 22.0$	$\frac{P\frac{33}{66}+S\frac{9}{61}+L\frac{2}{164}}{P\frac{37}{66}+S\frac{48}{61}+L\frac{3}{164}}$
$K < 23.0$	$\frac{P\frac{33}{66}+S\frac{10}{106}+L\frac{1}{244}}{P\frac{37}{66}+S\frac{86}{106}+L\frac{6}{244}}$

number of believed passive galaxies and the denominator in each fraction is the total number of high-redshift galaxies.

6.1.2 The $(J-K)$ vs $(i-K)$ Diagram

The $(J-K)$ vs $(i-K)$ technique introduced by Pozzetti and Mannucci [2000] is used to separate the ERO ($i-K > 2.6$) population at $1 < z < 2$ into passively evolving and dusty star-forming galaxies. It uses the fact that old galaxies have a strong 4000Å break, which lies shortward of the J band ($1.2\mu m$) for galaxies at $1 < z < 2$, while dusty star-forming galaxies have a smoother drop off in the flux at bluer wavelengths (see Figure 1.17). Using a combination of spectra of local galaxies redshifted out to $z = 1-2$ and spectral synthesis models, Pozzetti and Mannucci [2000] divided the $J-K$ vs $i-K$ plane into regions where passively evolving and dusty star-forming galaxies are expected to be located. This can be seen in Figure 1.18 and is defined by $(J-K)_{AB} = 0.36(I-K)_{AB}+0.02$ and $(I-K)_{AB} > 2.6$ with passive galaxies defined as objects with $(J-K)_{AB} > 0.36(I-K)_{AB}+0.02$. Similar to the BzK method, Pozzetti and Mannucci [2000] calibrated this method for the $K < 20$(Vega) galaxies.

Figure 6.4 shows the original division made by Pozzetti and Mannucci [2000] and our sample of EROs ($i-K > 2.6$) in the redshift range $1 < z < 2$, with the three K-band limits used before. The top, middle and bottom panels are for the $K < 21.0$, 22.0 and 23.0 sample respectively. The red circles and blue triangles are known passive and star-forming galaxies respectively.

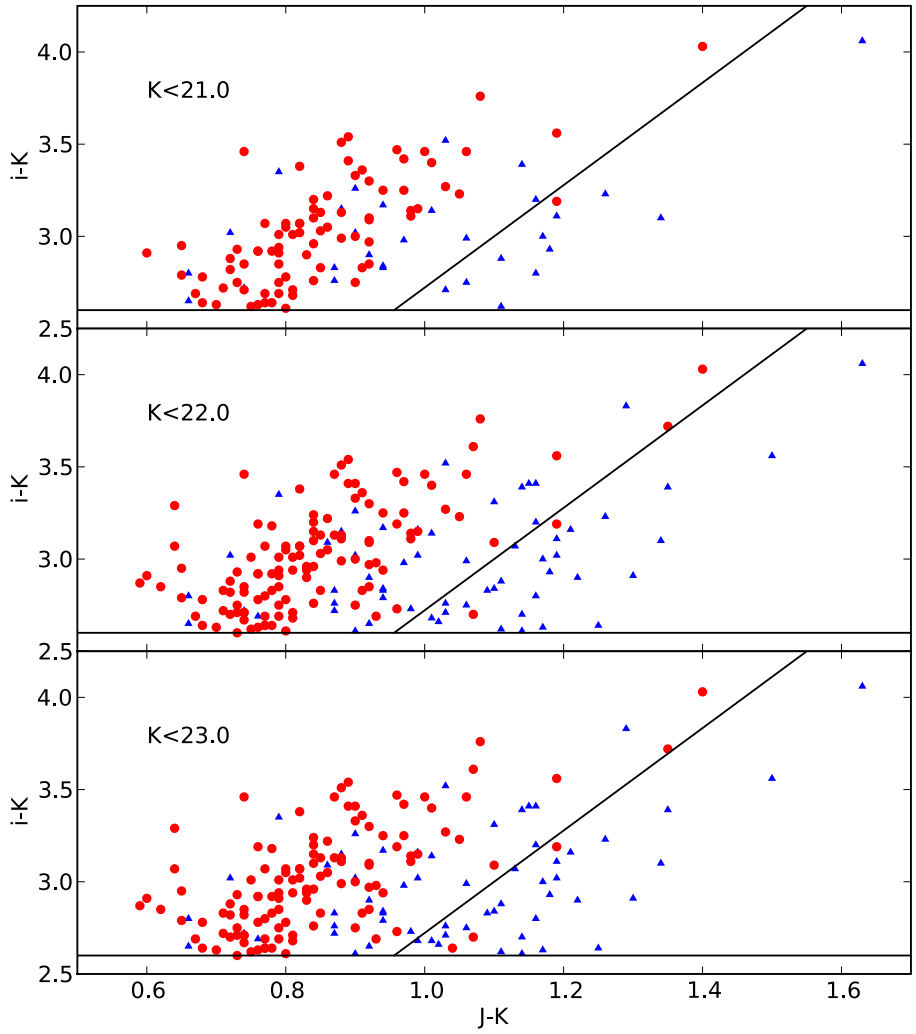

Figure 6.4: The $(J-K)$ vs $(i-K)$ plot for the EROs $(i-K>2.6)$ in the sample at redshift $1<z<2$. The line dividing the passive and dusty star-forming regions is defined as $(J-K)_{AB}=0.36(i-K)_{AB}+0.02$ from Pozzetti and Mannucci [2000]. The top, middle and bottom panels are for the $K<21.0$, 22.0 and 23.0 samples respectively. The red circles and blue triangles are known passive and star-forming galaxies respectively.

Table 6.4: The distribution of known galaxy populations on the $(J-K)$ vs $(i-K)$ diagram. Columns 2 and 3 show how the known passive and star-forming targets are distributed.

	Passive	Star-forming
$K < 21.0$(totals)	83	31
$(J-K)$ vs $(i-K)$ Passive	82	20
$(J-K)$ vs $(i-K)$ Star-forming	1	11
$K < 22.0$(totals)	119	61
$(J-K)$ vs $(i-K)$ Passive	117	34
$(J-K)$ vs $(i-K)$ Star-forming	2	27
$K < 23.0$(totals)	120	63
$(J-K)$ vs $(i-K)$ Passive	117	35
$(J-K)$ vs $(i-K)$ Star-forming	3	28

Assessment of the $(J-K)$ vs $(i-K)$ Diagram

The $(J-K)$ vs $(i-K)$ diagram was assessed using the same procedure as for the BzK diagram. The results are summarised in Table 6.4. The $(J-K)$ vs $(i-K)$ technique is successful at selecting passively evolving EROs at high-redshift but it is susceptible to high levels of contamination from dusty star-forming galaxies.

Optimising the $(J-K)$ vs $(i-K)$ Diagram

From the results presented above it is clear that the $(J-K)$ vs $(i-K)$ technique can be optimised. This was done using the same method as for the BzK diagram.

This method has been applied to the three samples studied above and the resulting optimal population dividers can be seen in Figure 6.5 as solid black lines. The symbols are as in Figure 6.4, the top, middle and bottom panels are for the $K < 21.0$, 22.0 and 23.0 samples respectively.

The optimal ERO population division lines are defined in Equation 6.4, 6.5 and 6.6 and the effectiveness of the optimised $(J-K)$ vs $(i-K)$ technique is summarised in Table 6.5.

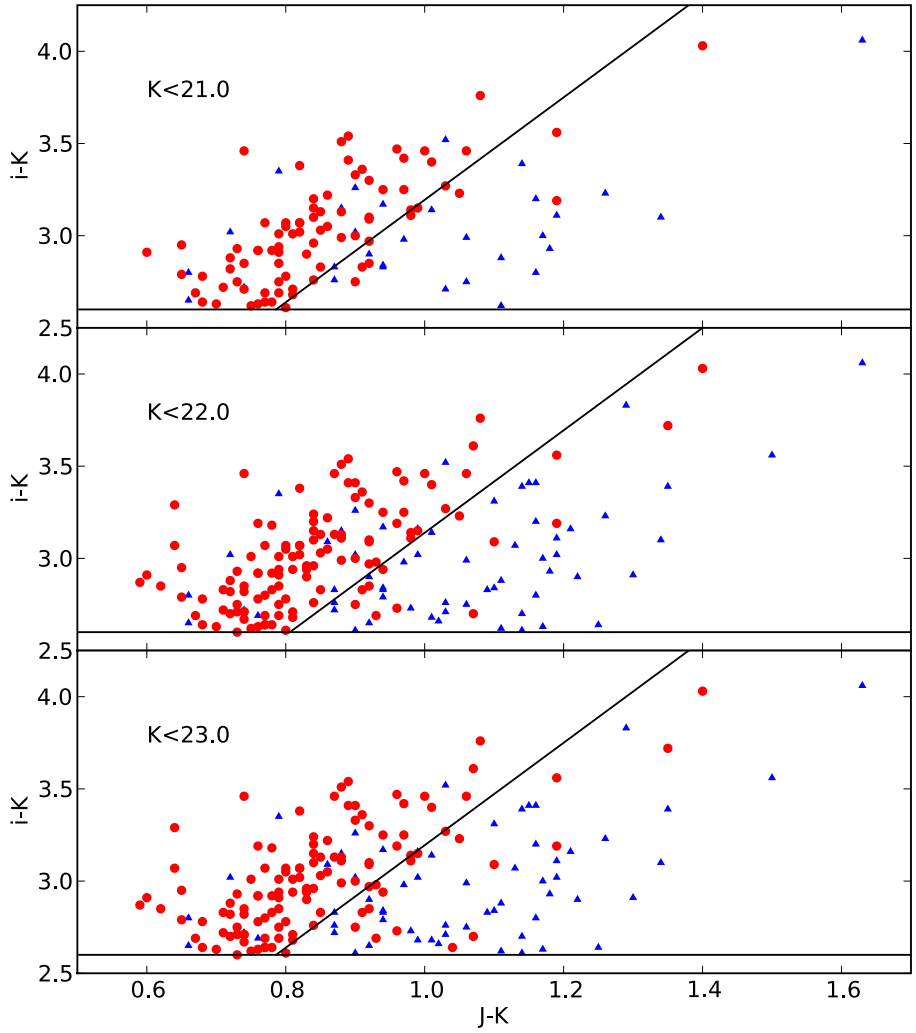

Figure 6.5: The $(J-K)$ vs $(i-K)$ plot for the EROs $(i-K > 2.6)$ in the sample at $1 < z < 2$. The black lines are the optimised population dividers, discussed in the text. The top, middle and bottom panels are for the $K < 21.0$, 22.0 and 23.0 samples respectively. The red circles and blue triangles are known passive and star-forming galaxies respectively.

Table 6.5: The distribution of known galaxy populations on the optimised $(J-K)$ vs $(i-K)$ diagram. Columns 2 and 3 show how the known passive and star-forming targets are distributed on the $(J-K)$ vs $(i-K)$ diagram.

	Passive	Star-forming
$K < 21.0$(totals)	83	31
$(J-K)$ vs $(i-K)$ Passive	71	10
$(J-K)$ vs $(i-K)$ Star-forming	12	21
$K < 22.0$(totals)	119	61
$(J-K)$ vs $(i-K)$ Passive	106	15
$(J-K)$ vs $(i-K)$ Star-forming	13	46
$K < 23.0$(totals)	120	63
$(J-K)$ vs $(i-K)$ Passive	100	13
$(J-K)$ vs $(i-K)$ Star-forming	20	50

$$(J-K) = 0.36(i-K) - 0.15 \quad \text{for} \quad K < 21.0 \tag{6.4}$$

$$(J-K) = 0.36(i-K) - 0.13 \quad \text{for} \quad K < 22.0 \tag{6.5}$$

$$(J-K) = 0.36(i-K) - 0.15 \quad \text{for} \quad K < 23.0 \tag{6.6}$$

Allowing for a small reduction in the selecting efficiency of passive galaxies the contamination from dusty star-forming galaxies has been heavily reduced. The optimised selection technique is essentially the same across the three samples.

From the analysis above, and the results shown in Table 6.5, the passive fraction of EROs at $1 < z < 2$ is calculated as described in Table 6.6 which takes into account the known levels of contamination between the regions. The numerator of each fraction is the total number of believed passive galaxies and the denominator in each fraction is the total number of EROs at $1 < z < 2$.

Table 6.6: The formulae for calculating the passive fraction for each of the optimised $(J-K)$ vs $(i-K)$ diagrams. P is the total number of galaxies selected to be passive, S is the total number of galaxies selected as star-forming and the T is the total number of EROs in the redshift range $1 < z < 2$.

K-band cut	Passive Fraction
$K < 21.0$	$\frac{P\frac{71}{81}+S\frac{12}{33}}{T}$
$K < 22.0$	$\frac{P\frac{106}{121}+S\frac{13}{59}}{T}$
$K < 23.0$	$\frac{P\frac{100}{113}+S\frac{20}{70}}{T}$

6.1.3 The $(V-J)$ vs $(U-V)_{\text{Rest-frame}}$ Technique

Using specific star-formation rates of galaxies, Williams et al. [2009] have recently published a technique to divide passive and star-forming galaxies out to $z = 2$ using the $(V-J)$ and $(U-V)$ rest-frame colours of galaxies. Here, using our spectra and the rest-frame U, V and J magnitudes acquired from the model SED fits, the passive galaxy selection criteria from Williams et al. [2009] for $1 < z < 2$ galaxies is examined. For this redshift range Williams et al. [2009] defines a passive galaxy to be one such that $(U-V) > 0.88(V-J) + 0.4$, $U-V > 1.3$ and $V-J < 1.6$. Figure 6.6 shows how our $1 < z < 2$ galaxies sit on the $(V-J)$ vs $(U-V)_{\text{Rest-frame}}$ plot, compared with the population division suggested by Williams et al. [2009]. The red circles and blue triangles are known passive and star-forming galaxies respectively and the solid black lines define the regions $(U-V) > 0.88(V-J) + 0.49$, $U-V > 1.3$ and $V-J < 1.6$. Williams et al. [2009] originally devised this method using the UDS DR1 down to a K-band limit of $K < 22.4$.

As with the previous two techniques this one is examined as a function of limiting K-band magnitude. Figure 6.6 shows the original division made by Williams et al. [2009] and the galaxies in the spectroscopic sample with $1 < z < 2$, at three different K-band limits.

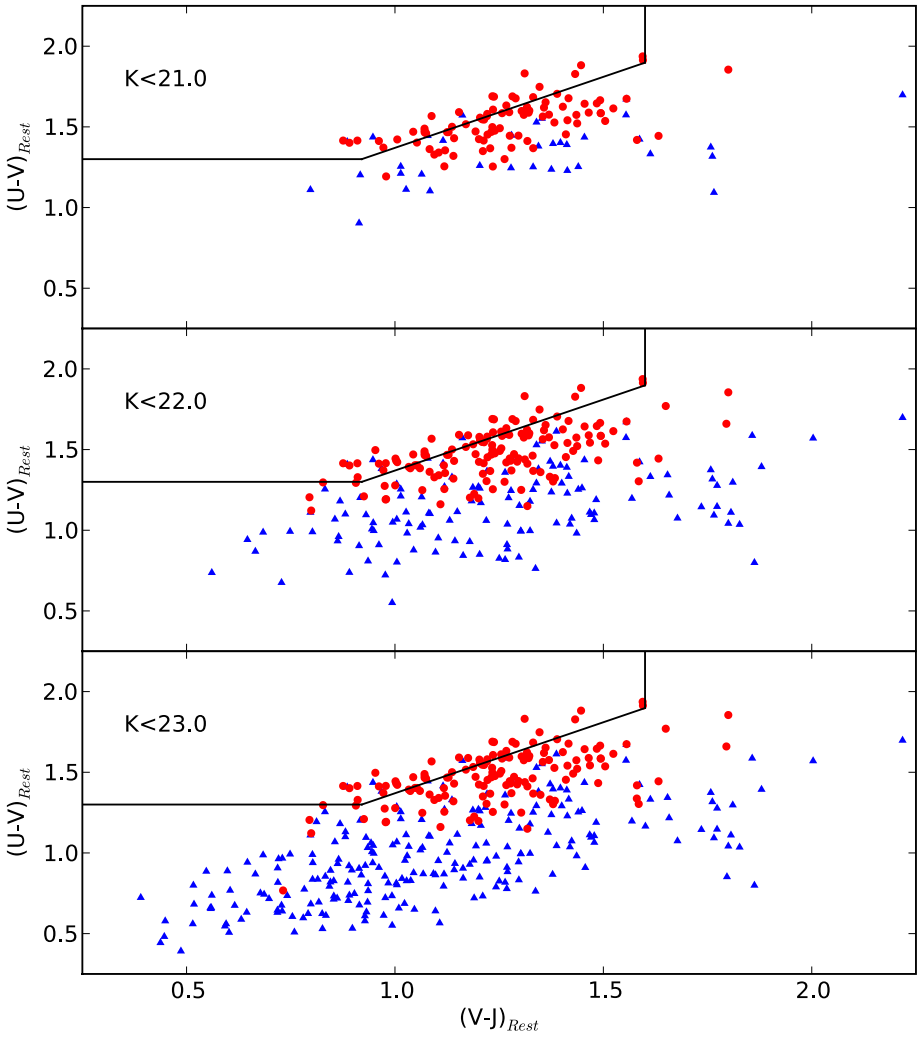

Figure 6.6: The $(V-J)$ vs $(U-V)_{\text{Rest-frame}}$ plot for the $1 < z < 2$ galaxies in our sample. The red circles and blue triangles are known passive and star-forming galaxies respectively, and the solid black lines define the region supposed to select passive galaxies, $(U-V) > 0.88(V-J) + 0.49$, $U-V > 1.3$ and $V-J < 1.6$. The top, middle and bottom panels are for the $K < 21.0$, 22.0 and 23.0 samples respectively.

Table 6.7: The distribution of known galaxy populations on the $(V-J)$ vs $(U-V)_{\text{Rest-frame}}$ diagram. Columns 2 and 3 show how the known passive and star-forming targets are distributed on the $(V-J)$ vs $(U-V)_{\text{Rest-frame}}$ diagram.

	Passive	Star-forming
$K < 21.0$(totals)	92	35
$(V-J)$ vs $(U-V)_{\text{Rest-frame}}$ Passive	30	4
$(V-J)$ vs $(U-V)_{\text{Rest-frame}}$ Star-forming	62	31
$K < 22.0$(totals)	140	130
$(V-J)$ vs $(U-V)_{\text{Rest-frame}}$ Passive	38	5
$(V-J)$ vs $(U-V)_{\text{Rest-frame}}$ Star-forming	102	125
$K < 23.0$(totals)	142	238
$(V-J)$ vs $(U-V)_{\text{Rest-frame}}$ Passive	38	5
$(V-J)$ vs $(U-V)_{\text{Rest-frame}}$ Star-forming	104	233

Assessment of the $(V-J)$ vs $(U-V)_{\text{Rest-frame}}$ Diagram

This technique was assessed in the same way as the BzK and $(J-K)$ vs $(i-K)$ diagrams. The assessment of the selection techniques for the spectroscopic sample is shown in Table 6.7.

It is clear from these results that this technique selects a passive sample with low levels of contamination from star-forming galaxies, but at the expense of missing a large fraction of genuinely passive galaxies. Conversely it selects a very high fraction of the star-forming galaxies at the expense of high levels of contamination from the passive population.

Optimising the $(V-J)$ vs $(U-V)_{\text{Rest-frame}}$ Technique

Similar to the previous selection techniques, the $(V-J)$ vs $(U-V)_{\text{Rest-frame}}$ technique can be subject to optimisation. This was done using the same method as for the previous two techniques.

The optimised $(V-J)$ vs $(U-V)_{\text{Rest-frame}}$ divider for the three samples can be seen in Figure 6.7. The red circles and blue triangles are known passive and star-forming

Table 6.8: The distribution of known galaxy populations on the optimised $(V-J)$ vs $(U-V)_{\text{Rest-frame}}$ diagram. Columns 2 and 3 show how the known passive and star-forming targets are distributed on the $(V-J)$ vs $(U-V)_{\text{Rest-frame}}$ diagram.

	Passive	Star-forming
$K < 21.0$(totals)	92	35
$(V-J)$ vs $(U-V)_{\text{Rest-frame}}$ Passive	85	9
$(V-J)$ vs $(U-V)_{\text{Rest-frame}}$ Star-forming	7	26
$K < 22.0$(totals)	140	130
$(V-J)$ vs $(U-V)_{\text{Rest-frame}}$ Passive	113	16
$(V-J)$ vs $(U-V)_{\text{Rest-frame}}$ Star-forming	27	114
$K < 23.0$(totals)	142	238
$(V-J)$ vs $(U-V)_{\text{Rest-frame}}$ Passive	136	42
$(V-J)$ vs $(U-V)_{\text{Rest-frame}}$ Star-forming	6	196

galaxies respectively. The optimal galaxy population dividers for the samples $K < 21.0$, 22.0 and 23.0 are given in Equations 6.7, 6.8 and 6.9 respectively and the success of these optimised selection techniques is summarised in Table 6.8.

$$(U-V) > 0.88(V-J) + 0.21, U-V > 1.26, V-J < 1.8 \quad \text{for} \quad K < 21.0 \quad (6.7)$$

$$(U-V) > 0.88(V-J) + 0.21, U-V > 1.29, V-J < 1.8 \quad \text{for} \quad K < 22.0 \quad (6.8)$$

$$(U-V) > 0.88(V-J) - 0.01, U-V > 1.19, V-J < 1.8 \quad \text{for} \quad K < 23.0 \quad (6.9)$$

The optimised method has heavily increased the number of passive galaxies selected, and has reduced the contamination levels in the star-forming selection region while only slightly reducing the selection efficiency of star-forming galaxies. The cut of $V-J < 1.8$ maybe a bit large as this is only anchored by two passive galaxies with extreme colours.

From the analysis above, and the results in Table 6.8, the passive fraction of galaxies at $1 < z < 2$ is calculated as described in Table 6.9 which takes into account the known levels of contamination between the regions. The numerator of each fraction is the total

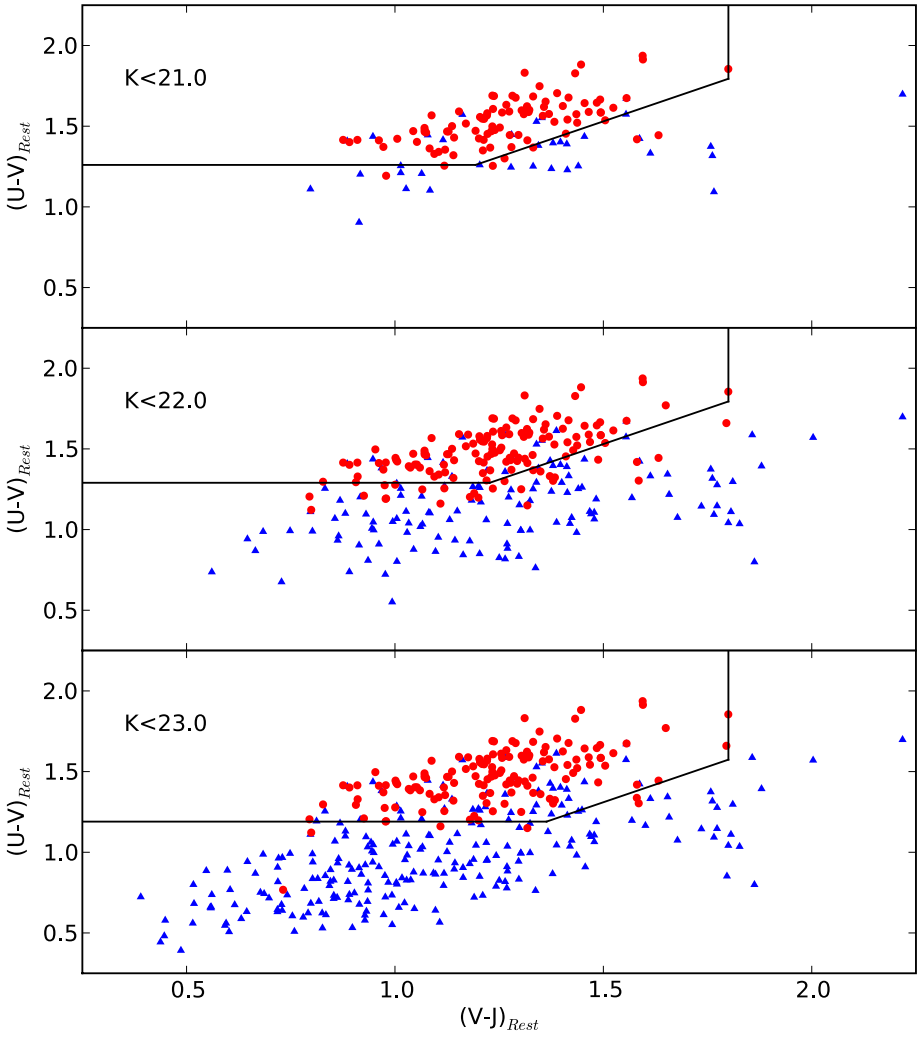

Figure 6.7: The $(V-J)$ vs $(U-V)_{\text{Rest-frame}}$ plot for the $1 < z < 2$ galaxies in our sample. The red circles and blue triangles are known passive and star-forming galaxies respectively and the solid black lines are the optimised galaxy population dividers discussed in the text. The top, middle and bottom panels are for the $K < 21.0$, 22.0 and 23.0 samples respectively.

Table 6.9: The formulae for calculating the passive fraction for each of the optimised $(V - J)$ vs $(U - V)_{\text{Rest-frame}}$ diagram. P is the total number of galaxies selected to be passive, S is the total number of galaxies selected as star-forming, and T is the total number of galaxies in the redshift range $1 < z < 2$.

K-band cut	Passive Fraction
$K < 21.0$	$\frac{P\frac{85}{94}+S\frac{7}{33}}{T}$
$K < 22.0$	$\frac{P\frac{113}{129}+S\frac{27}{141}}{T}$
$K < 23.0$	$\frac{P\frac{136}{178}+S\frac{6}{202}}{T}$

number of believed passive galaxies and the denominator in each fraction is the total number of galaxies at $1 < z < 2$.

6.2 Further Optimisation of the BzK Diagram with Photometric Redshifts

Optimising the BzK diagram with a sample of galaxies with spectroscopic redshifts has the benefit that it is known exactly which galaxies should be located in each region. However this technique has the obvious disadvantage that the spectroscopic sample is small. Therefore the further optimisation of the BzK diagram was investigated using the available high quality photometric redshifts in the UDS (courtesy of Dr. Michele Cirasuolo).

Similar to before a C_{spec} and I_{spec} index were calculated for each combination of parameters defining the galaxy population division but only based on whether the galaxies are above or below $z = 1.4$. A C_{photo} and I_{photo} were also calculated from how well the combination of parameters divided the low- and high-redshift photometric sample. The C index for each combination of parameters was now equal to, $C = C_{spec} \times C_{photo}$ and similarly for the I index, $I = I_{spec} \times I_{photo}$

Reassuringly, including the photometric redshift data did not change the optimal galaxy population dividers which were calculated from the spectroscopic data. The location of the photometric redshift catalog on the optimised (using only spectroscopic

targets) BzK diagram can be seen in Figures 6.8, 6.9 and 6.10 for the $K < 21.0$, 22.0 and 23.0 samples respectively. The solid black lines plotted in the top and bottom panels are the optimised galaxy population divider calculated with just the spectroscopic sample, defined in Section 6.1.1. The red circles, blue triangles and black crosses are for spectroscopic passive, star-forming and low redshift targets respectively. The grey dots in the upper panels are targets from the photometric redshift catalog with $z_{photo} < 1.4$ and the green dots in the lower panels are targets from the photometric redshift catalog with $1.4 < z_{photo} < 2.5$. The two populations have been plotted separately for clarity. It is clear from the figures that the optimised population dividers did not require movement.

6.3 Estimating the Passive Fraction at High-Redshift with Photometric Methods

It is of an interest to calculate the high-redshift passive fraction simply from a complete K-band selected sample as the spectroscopic sample has additional criteria in place. Using the optimised galaxy population dividers defined above from the spectroscopic data it is possible to estimate the passive fraction of various samples at high-redshift.

6.3.1 Using the BzK Diagram

Figure 6.11 shows the evolution of the optimised BzK diagram with increasingly deeper cuts in the K-band magnitude for the full 0.8 deg^2 area of the UDS. The top, middle and bottom panels are for the $K < 21.0$, 22.0 and 23.0 samples respectively. The red, blue and black dots are for galaxies selected to be $1.4 < z < 2.5$ and passive, $1.4 < z < 2.5$ and star-forming, and $z < 1.4$ respectively, and the grey dotted lines represent the optimal population dividers. The distinct trail of black dots in the low-redshift region is the stellar locus containing all the stars with BzK measurements.

In the $K < 21.0$ sample there are 10902 objects with 447 selected to be passively evolving at $1.4 < z < 2.5$ and 609 selected to be star-forming at $1.4 < z < 2.5$ and 9846 expected to be at $z < 1.4$. This gives a passive fraction for the $K < 21.0$, $1.4 < z < 2.5$ Universe of 447/1056 ($\sim 42\%$).

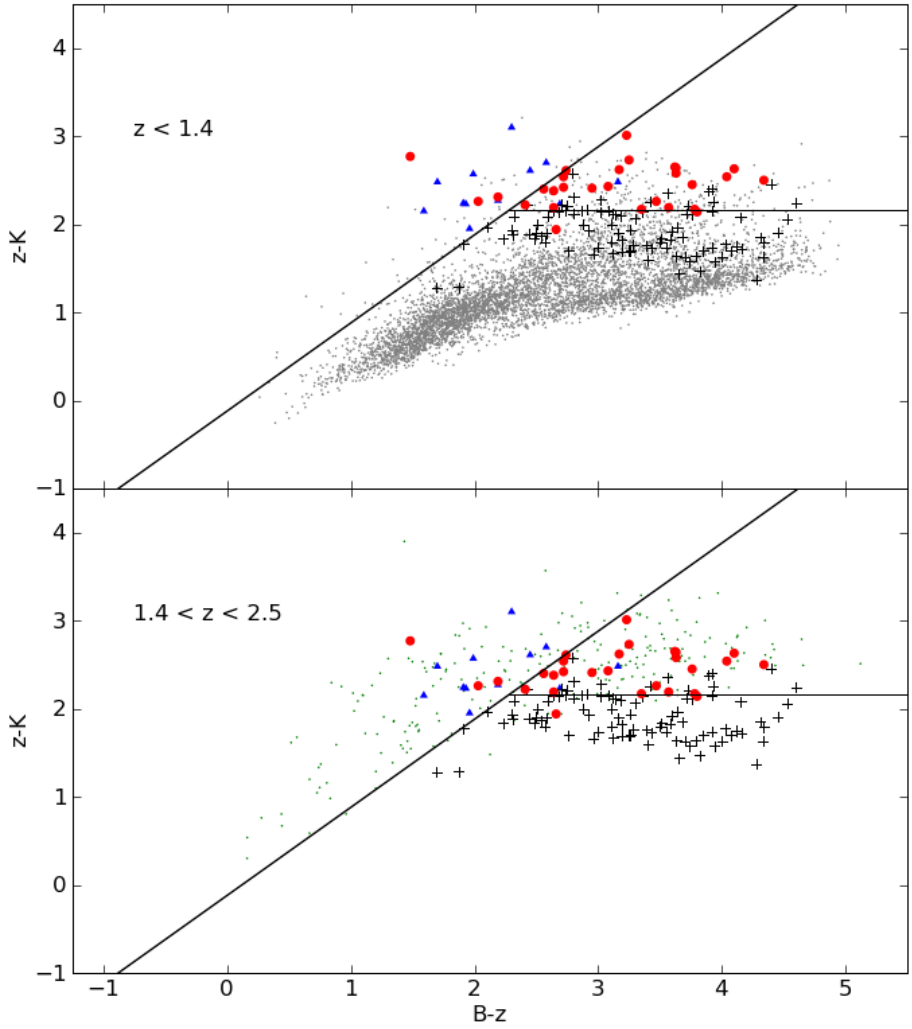

Figure 6.8: The optimised BzK diagram for the $K < 21.0$ sample. The solid black lines plotted in the top and bottom panels are the optimised galaxy population dividers calculated with just the spectroscopic sample, as defined in Section 6.1.1. The red circles, blue triangles and black crosses are for spectroscopic passive, star-forming and low redshift targets respectively. The grey dots in the upper panel are targets from the photometric catalog with $z_{photo} < 1.4$ and the green dots in the lower panel are targets from the photometric catalog with $1.4 < z_{photo} < 2.5$.

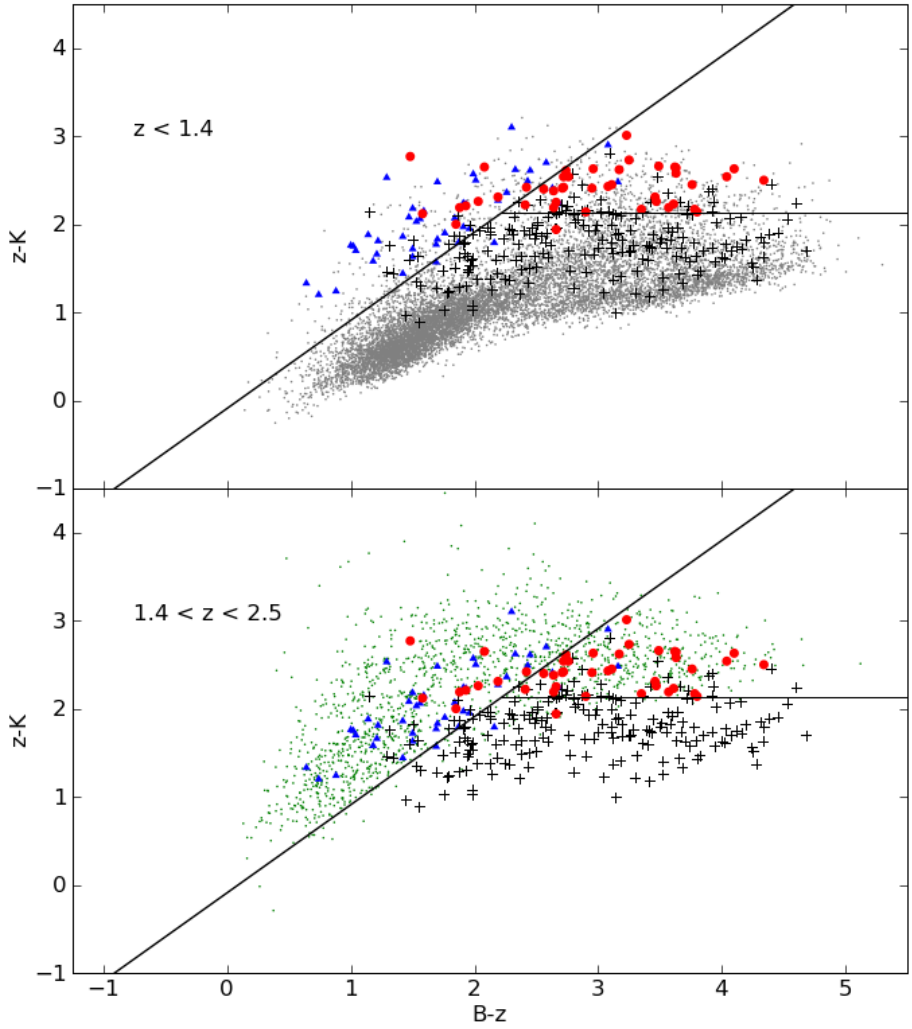

Figure 6.9: The optimised BzK diagram for the $K < 22.0$ sample. The solid black lines plotted in the top and bottom panels are the optimised galaxy population dividers calculated with just the spectroscopic sample, as defined in Section 6.1.1. The red circles, blue triangles and black crosses are for spectroscopic passive, star-forming and low redshift targets respectively. The grey dots in the upper panel are targets from the photometric catalog with $z_{photo} < 1.4$ and the green dots in the lower panel are targets from the photometric catalog with $1.4 < z_{photo} < 2.5$.

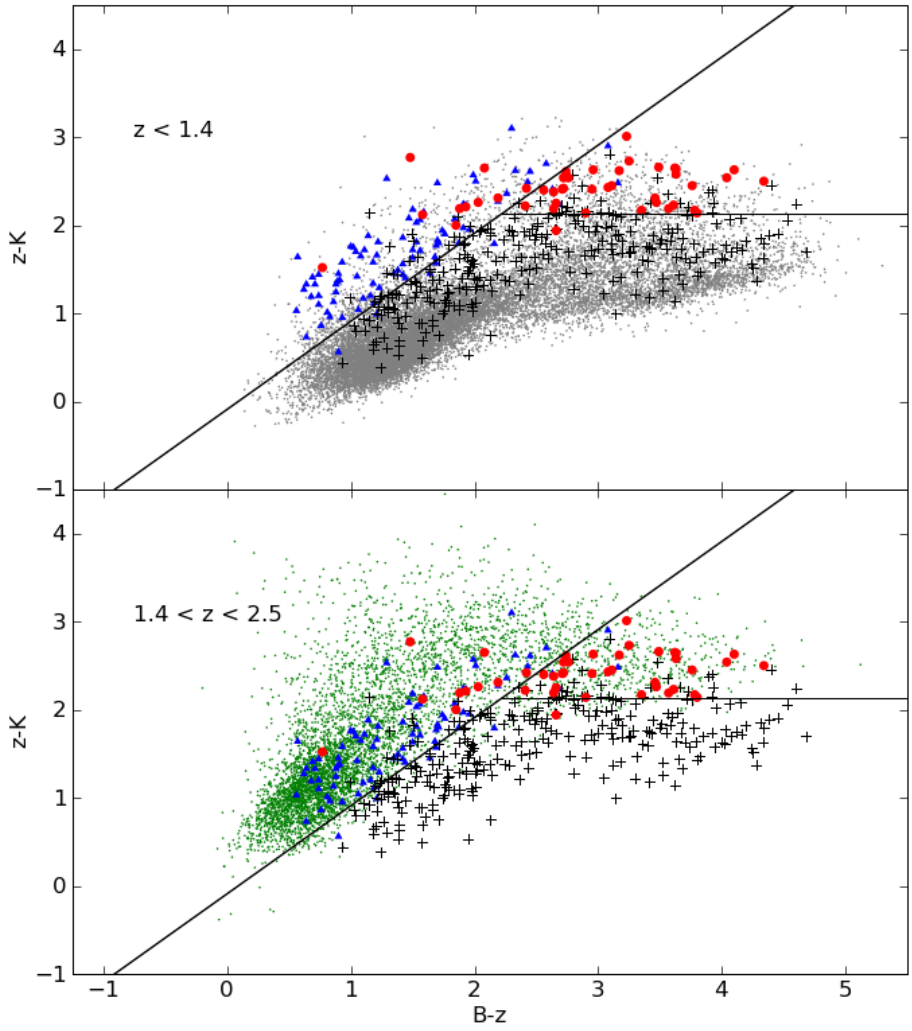

Figure 6.10: The optimised BzK diagram for the $K < 23.0$ sample. The solid black lines plotted in the top and bottom panels are the optimised galaxy population dividers calculated with just the spectroscopic sample, as defined in Section 6.1.1. The red circles, blue triangles and black crosses are for spectroscopic passive, star-forming and low redshift targets respectively. The grey dots in the upper panel are targets from the photometric catalog with $z_{photo} < 1.4$ and the green dots in the lower panel are targets from the photometric catalog with $1.4 < z_{photo} < 2.5$.

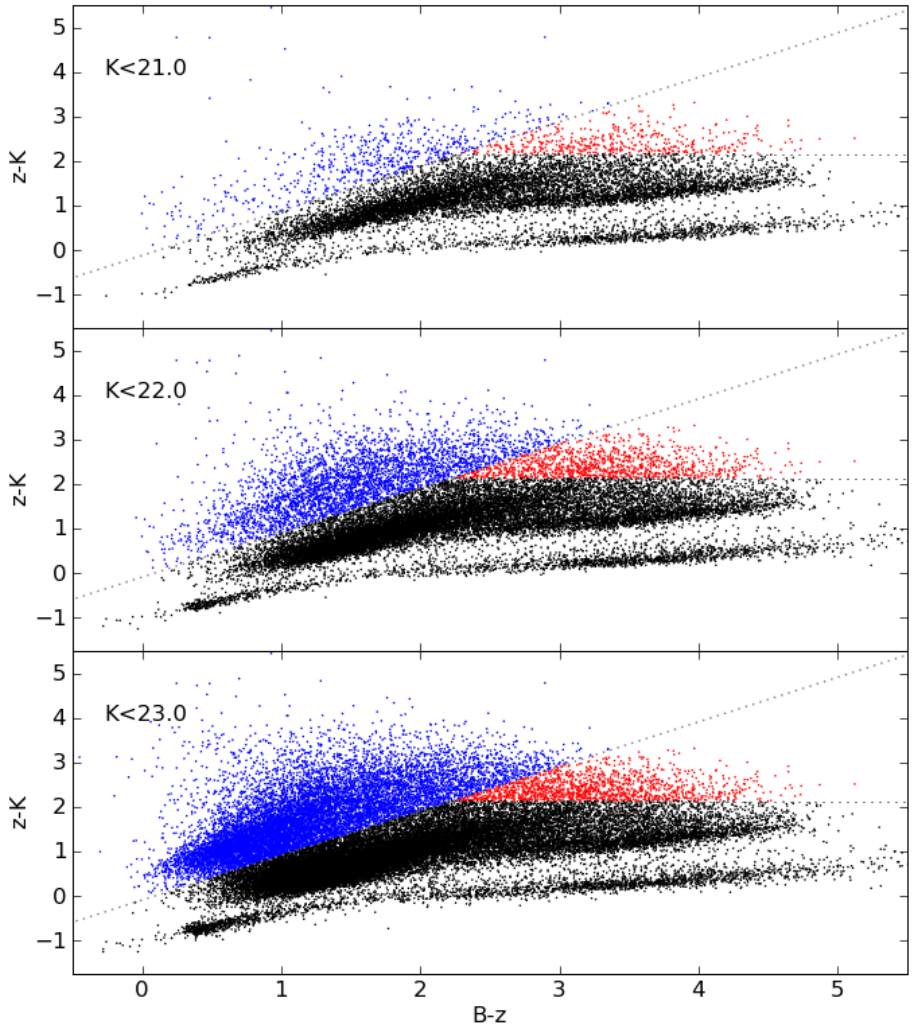

Figure 6.11: The optimised BzK diagram applied to the full UDS DR8 photometric sample. The top, middle and bottom panels are for the $K < 21.0$, 22.0 and 23.0 samples respectively. The red, blue and black dots are for galaxies selected to be $1.4 < z < 2.5$ and passive, $1.4 < z < 2.5$ and star-forming, and $z < 1.4$ respectively, and the grey dotted lines represent the optimal population dividers.

In the $K < 22.0$ sample there are 22425 objects with 1176 selected to be passively evolving at $1.4 < z < 2.5$ and 3510 selected to be star-forming at $1.4 < z < 2.5$ and 17739 expected to be at $z < 1.4$. This gives a passive fraction for the $K < 22.0$, $1.4 < z < 2.5$ Universe of 1176/4686 ($\sim 25\%$).

In the $K < 23.0$ sample there are 42315 objects with 1434 selected to be passively evolving at $1.4 < z < 2.5$ and 11419 selected to be star-forming at $1.4 < z < 2.5$ and 29462 expected to be at $z < 1.4$. This gives a passive fraction for the $K < 23.0$, $1.4 < z < 2.5$ Universe of 1434/12853 ($\sim 11\%$).

From cuts of $K = 21 - 23$ the passive fraction appears to approximately half with every increased magnitude of depth in the K-band. These raw values can be corrected for the known contamination levels and the known fraction of passive objects missed by the optimised selection process using the equation in Table 6.3.

For the $K < 21.0$ sample the estimated total number of passively evolving galaxies is $447 \times (23/41) + 609 \times (3/13) + 9846 \times (2/78) \approx 644$ and the estimated total number of galaxies at $1.4 < z < 2.5$ is $447 \times (25/41) + 609 \times (13/13) + 9846 \times (2/78) \approx 1134$. Therefore the corrected passive fraction is $\approx 644/1134 \approx 57\%$.

Using the same approach the corrected passive fractions for the $K < 22.0$ and $K < 23.0$ samples are $\sim 1322/3745 \approx 35\%$ and $\sim 1915/10793 \approx 18\%$ respectively. These corrected values have increased the passive fraction by approximately 35%, 40% and 65% respectively for the sample limited by $K < 21.0$, $K < 22.0$ and $K < 23.0$.

The passive fraction for the $K < 21$ sample is in agreement with that estimated from the $K < 21.5$ spectroscopic sample in Section 5.8. Even though there was a V, i and z cut involved in the spectroscopic sample that stopped bluer objects making it in to the sample at a K cut of $K < 21.5$, the majority of the objects are massive systems so there will be low contamination from blue systems.

If one was to use the original BzK diagram (with filter corrections from Hartley et al. 2008) the respective passive fractions would be $54/469 \approx 12\%$, $163/2977 \approx 5\%$ and $190/9805 \approx 2\%$ for the $K < 21.0$, $K < 22.0$ and $K < 23.0$ samples. These estimates range from a factor 5 to 10 below the estimates made with the optimised system (see Figure 6.12). This issue can be highlighted in the Hartley et al. [2008] paper itself where Hartley et al. [2008] finds 702 passive BzK galaxies for 11551 star-forming BzK

galaxies for the $K < 23$ sample of the UDS data release 1 (DR1). This gives a passive fraction of the of $702/16213 \approx 0.5\%$ which is a factor of ~ 20 below what was found from study here using UDS DR8. How this misclassification of galaxies effects the clustering analysis in Hartley et al. [2008] is beyond the scope of the work here.

6.3.2 Using the $(J-K)$ vs $(i-K)$ Diagram

In Figure 6.13 the division between passively-evolving and dusty star-forming EROs, as estimated by the $(J-K)$ vs $(i-K)$ technique, can be seen as a function of limiting K-band magnitude. The top, middle and bottom panels are for the $K < 21.0$, 22.0 and 23.0 samples respectively. The red and blue dots are for $1 < z < 2$ passive and star-forming galaxies respectively, and the grey dotted line depicts the optimal divider.

In the $K < 21.0$ sample there are 521 EROs in the redshift range $1 < z < 2$. Of these, 280 of them are selected to passive while 241 are selected to be dusty star-formings. Therefore the passive fraction of EROs at $1 < z < 2$ with $K < 21.0$ is $280/521$ ($\sim 54\%$). This is essentially unchanged for the $K < 22.0$ sample at $954/1765$ ($\sim 54\%$) and falls off to $1208/2925$ ($\sim 41\%$) for the $K < 23.0$ sample.

These values can be corrected for contamination and estimated fraction of missed targets (see Table 6.6). For the $K < 21.0$ sample the estimate of the total number of passive EROs at $1 < z < 2$, taking into account contamination, is $280 \times (71/81)$ and the estimated number of missed targets is $241 \times (12/33)$. Therefore, the passive fraction is $\sim 333/521 \approx 64\%$. The corrected value for the $K < 22.0$ sample is $\sim 1014/1765 \approx 57\%$ and for the $K < 23.0$ sample is $\sim 1560/2925 \approx 53\%$. The passive fraction of EROs, therefore is reasonably consistent with respect to the K-band magnitude down to $K = 23$.

The passive fraction found with the optimised BzK technique for the $K < 21.0$ is in good agreement with the estimations found here for bright EROs. This result can be understood when the K vs. $i-K$ colur-magnitude diagram is investigated. For all galaxies in the UDS DR8 sample with a redshift in the range $1 < z < 2.5$ the K vs. $i-K$ colour-magnitude diagram is shown in Figure 6.14. The horizontal black dashed line highlights the colour threshold for an ERO, $i-K = 2.6$, and the vertical black dashed lines represent the three K-band cuts invoked in the above analysis, $K = 21.0$,

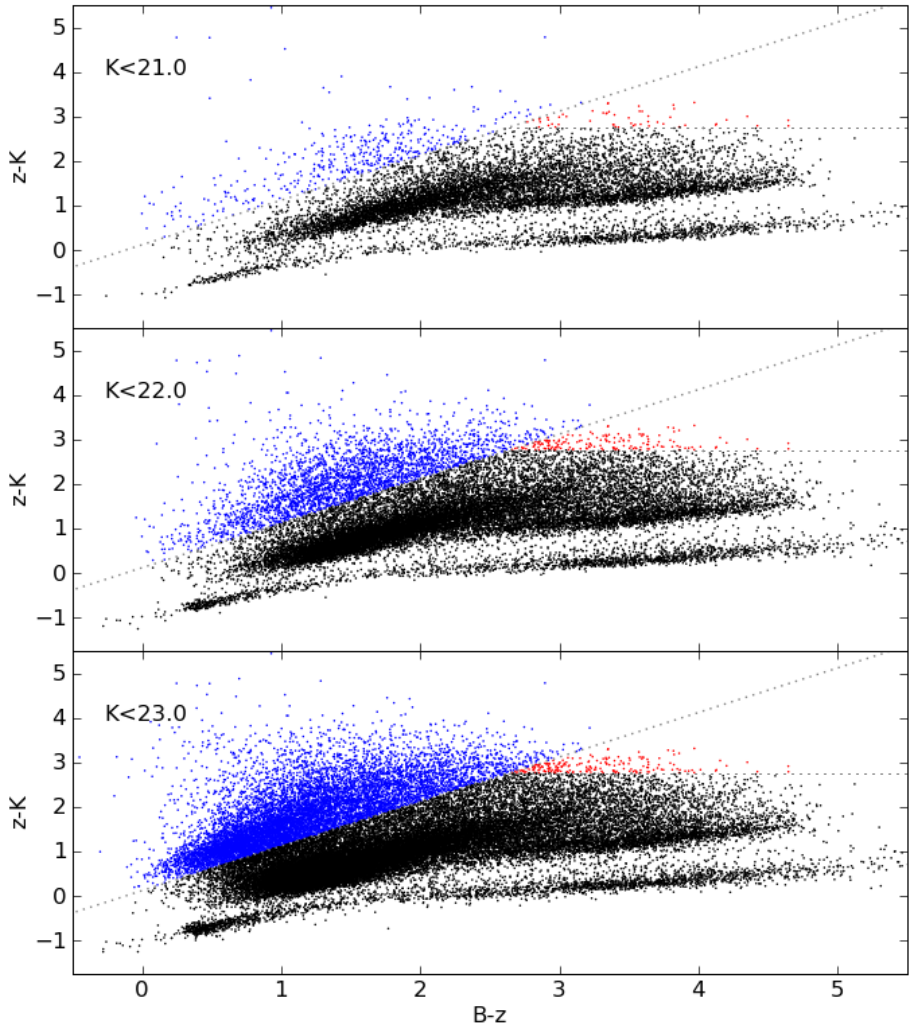

Figure 6.12: The original BzK diagram applied to the full UDS DR8 photometric sample. The top, middle and bottom panels are for the $K < 21.0$, 22.0 and 23.0 samples respectively. The red, blue and black dots are for galaxies selected to be $1.4 < z < 2.5$ and passive, $1.4 < z < 2.5$ and star-forming, and $z < 1.4$ respectively and the grey dotted lines represent the original population dividers.

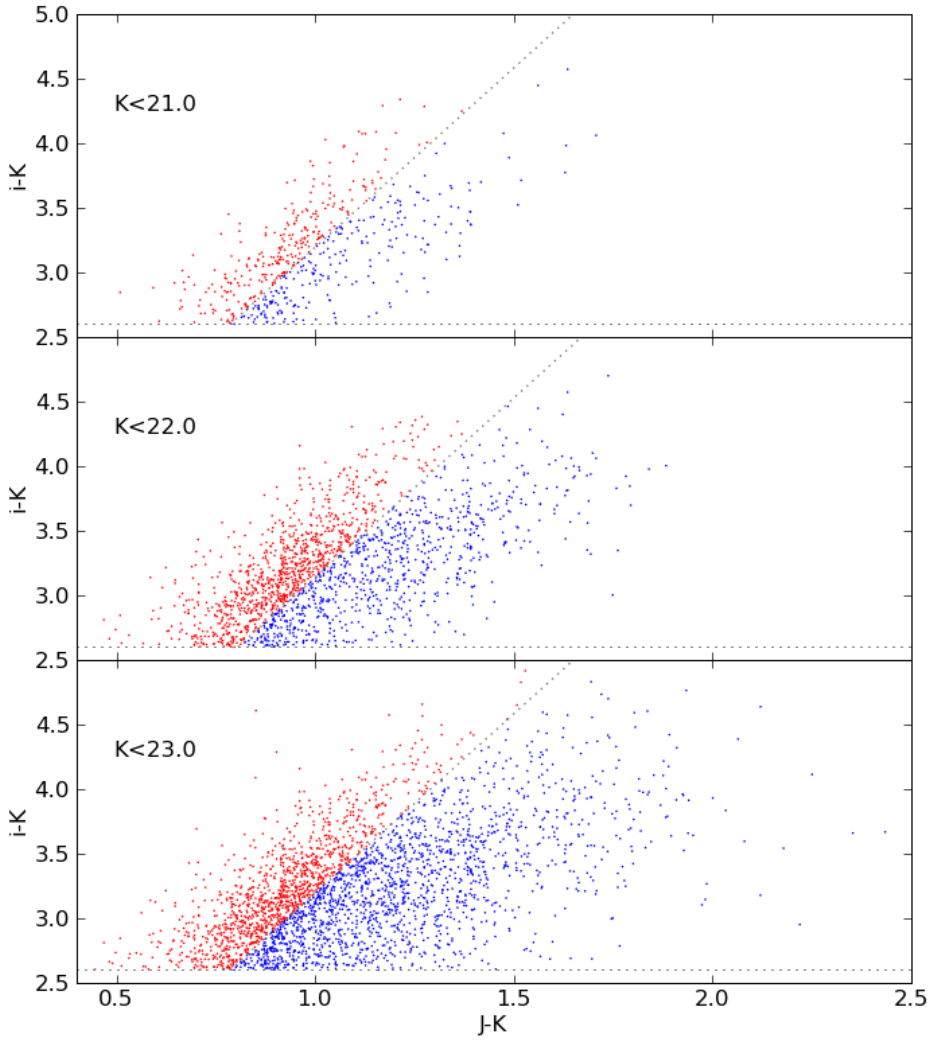

Figure 6.13: The optimised $(J-K)$ vs $(i-K)$ technique applied to the full UDS DR8 photometric sample. The top, middle and bottom panels are for the $K < 21.0$, 22.0 and 23.0 samples respectively. The red and blue dots are for $1 < z < 2$ passive and star-forming galaxies respectively. The grey dotted line depicts the optimal divider.

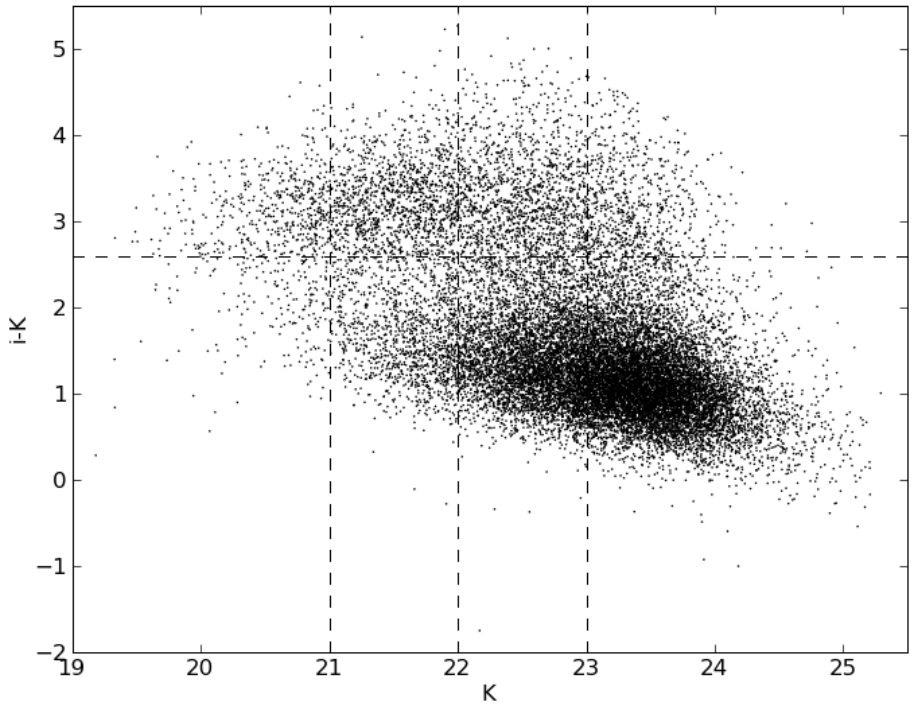

Figure 6.14: The K vs. $i-K$ colour-magnitude diagram for all galaxies in the UDS DR8 sample such that $1 < z_{photo} < 2.5$. The horizontal black dashed line highlights the colour for for an ERO, $i-K = 2.6$, and the vertical black dashed lines represent the three K-band cuts invoked in the above analysis, $K = 21.0$, 22.0 and 23.0.

22.0 and 23.0.

The $K < 21.0$ sample is made up of $\sim$ 70% EROs therefore the bright samples studied in the analysis of the BzK diagram and the $(J-K)$ vs $(i-K)$ technique have a very large overlap. The ERO fraction within the K-band limited samples drops to $\sim 54\%$ and $\sim 31\%$ for the $K < 22$ and $K < 23$ samples respectively. This supports the results that the passive fraction of simply K-band selected galaxies drops off as opposed to the ERO population which stay consistent with increasing K-band depth.

If one was to use the original $(J-K)$ vs $(i-K)$ diagram the respective passive fractions would be $460/521 \approx 88\%$, $1390/1765 \approx 79\%$ and $2048/2925 \approx 70\%$ for the $K < 21.0$, $K < 22.0$ and $K < 23.0$ samples (see Figure 6.15). These estimates are overpredicting the passive fraction by approximately 30-40% in all samples compared

to the optimised diagram.

6.3.3 Using the $(V-J)$ vs $(U-V)_{\mathbf{Rest\text{-}frame}}$ Diagram

In Figure 6.16 the division between passively-evolving and star-forming galaxies at $1 < z < 2$, as estimated by the $(V-J)$ vs $(U-V)_{\text{Rest-frame}}$ technique, can be seen as a function of limiting K-band magnitudes. The top, middle and bottom panels are for the $K < 21.0$, 22.0 and 23.0 samples respectively. The red and blue dots are for $1 < z < 2$ passive and star-forming galaxies respectively and the grey dotted lines depict the optimal dividers.

In the $K < 21.0$ sample there are 1190 galaxies in the redshift range $1 < z < 2$. Of these, 283 of them are selected as passive while 907 are selected to be dusty star-forming galaxies. Therefore the passive fraction at $1 < z < 2$ with $K < 21.0$ is 283/1190 ($\sim 24\%$). This then falls off to 507/4453 ($\sim 11\%$) for the $K < 22.0$ sample 1755/10607 ($\sim 17\%$) for the $K < 23.0$.

As before, these values can be corrected for contamination and the estimated fraction of missed targets using the formulae in Table 6.9. Therefore for the $K < 21.0$ sample the estimate of the total number of passive galaxies at $1 < z < 2$, taking into account contamination, is $283 \times (85/94)$ and the estimated number of missed targets is $907 \times (7/33)$, therefore the passive fraction is $\sim 448/1190 \approx 38\%$. The corrected value for the $K < 22.0$ sample is $\sim 1200/4453 \approx 27\%$ and for the $K < 23.0$ sample is $\sim 1604/10607 \approx 15\%$. This method predicts a passive fraction which is typically a factor of 1.5-3.5 below that produced by other techniques. This fraction is going to be model dependent and an SED estimate is required to estimate the rest-frame magnitudes this could be a cause of the disagreement.

Using the original $(V-J)$ vs $(U-V)_{\text{Rest-frame}}$ diagram the passive are even lower at $70/1190 \approx 6\%$, $153/4453 \approx 3\%$ and $191/10607 \approx 2\%$ for the $K < 21.0$, 22.0 and 23.0 samples respectively (see Figure 6.17).

The Poisson errors on all of the above passive fraction are in the range $\pm 10 - 20\%$.

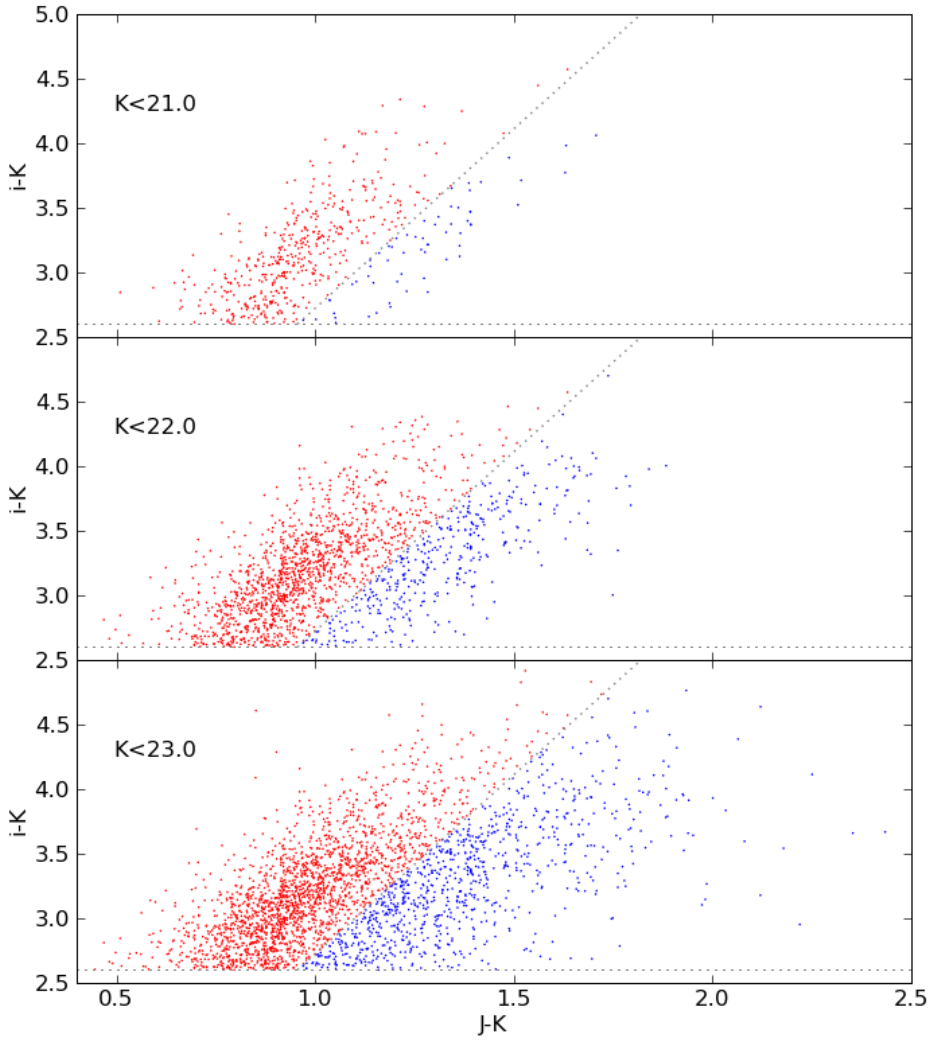

Figure 6.15: The original $(J-K)$ vs $(i-K)$ technique applied to the full UDS DR8 photometric sample. The top, middle and bottom panels are for the $K < 21.0$, 22.0 and 23.0 samples respectively. The red and blue dots are for $1 < z < 2$ passive and star-forming galaxies respectively. The grey dotted line depicts the original divider.

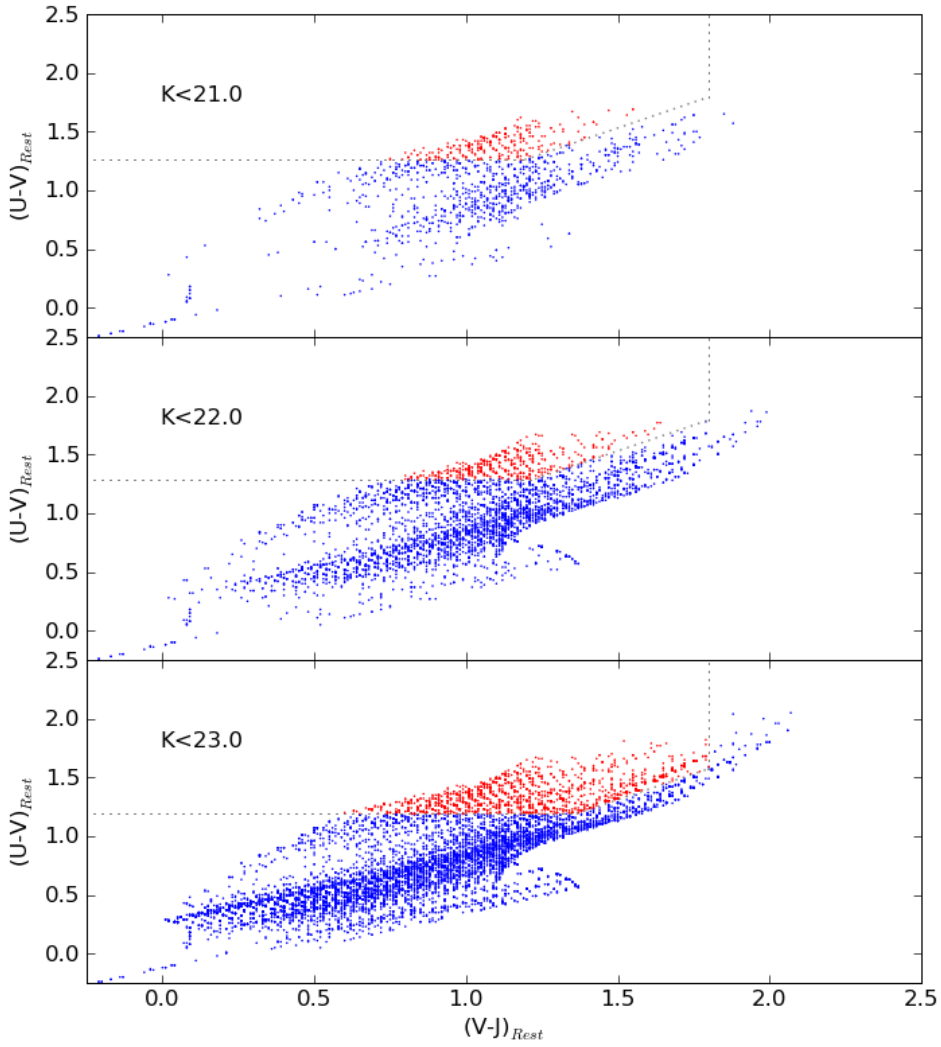

Figure 6.16: The optimised $(V-J)$ vs $(U-V)_{\text{Rest-frame}}$ technique applied to the full UDS DR8 photometric sample. The top, middle and bottom panels are for the $K < 21.0$, 22.0 and 23.0 samples respectively. The red and blue dots are for $1 < z < 2$ passive and star-forming galaxies respectively. The grey dotted line depicts the optimal dividers.

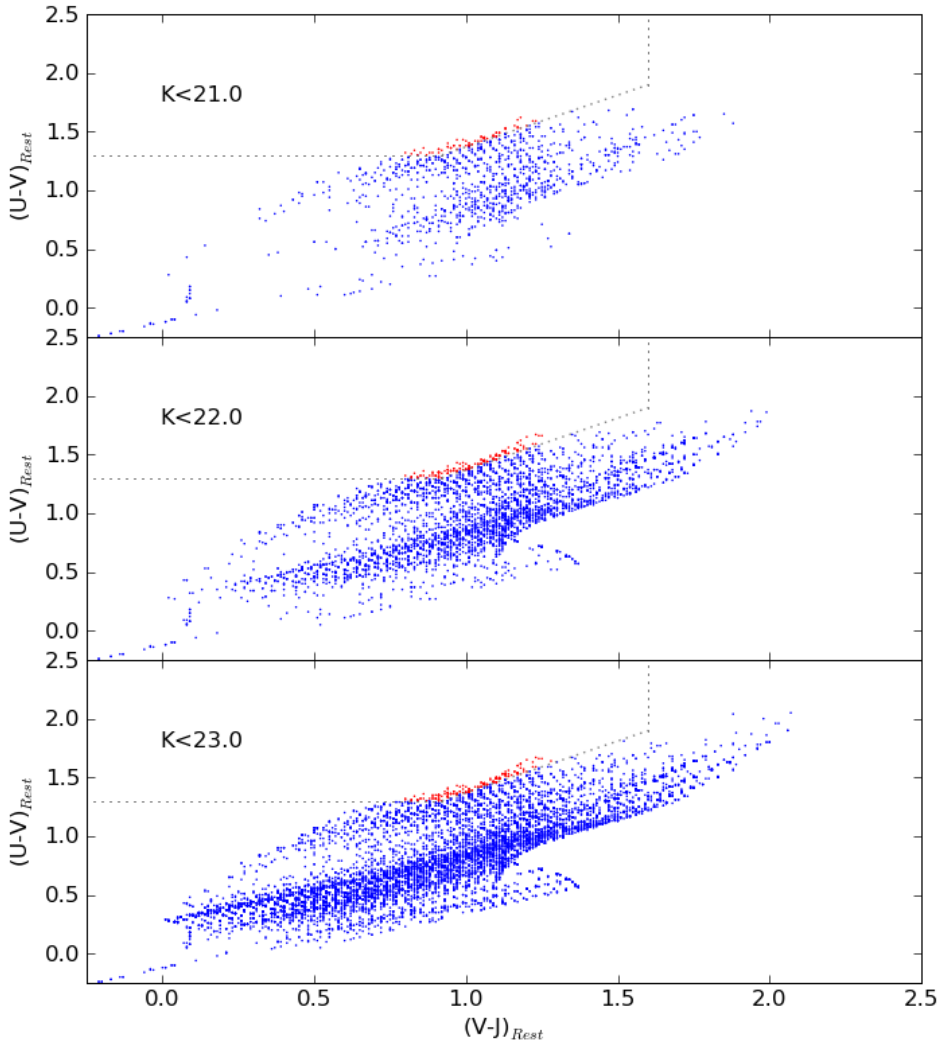

Figure 6.17: The original $(V-J)$ vs $(U-V)_{\text{Rest-frame}}$ technique applied to the full UDS DR8 photometric sample. The top, middle and bottom panels are for the $K < 21.0$, 22.0 and 23.0 samples respectively. The red and blue dots are for $1 < z < 2$ passive and star-forming galaxies respectively. The grey dotted line depicts the original dividers.

6.4 Separating Galaxy Populations with the Next Generation of Optical-NearIR Surveys

The Visible and Infrared Survey Telescope for Astronomy (VISTA) is the first of the new generation of NIR wide-field survey telescopes. Therefore it would be interesting to see how the above selection techniques work with the filters from the VISTA telescope. Using the best-fitting spectral energy distribution models found using the method described in Chapter 4 for the spectroscopic targets and the filters from the VISTA telescope the expected magnitudes in each band for each of the galaxies in the spectroscopic sample were estimated.

6.4.1 The BzK Diagram

A large public survey which is currently underway on VISTA is the VISTA Deep Extragalactic Observations (VIDEO) Survey (PI. Dr Matt Jarvis), and an optimised VISTA filter BzK diagram could be of great use to this survey. The K band can be replaced with the VISTA K_s filter and in addition, the VIDEO survey has accompanying Canada France Hawaii Telescope (CFHT) data; g-band, which is similar to the B-band, and z-band. Therefore an adapted gzK_s diagram can be constructed to select star-forming and passive galaxies at high-redshift.

For the spectroscopic sample of galaxies used above to optimise the BzK diagram the expected magnitudes in the VISTA and CHFT telescope bands were determined by integrating the best-fitting stellar population models over the filter profiles.

Figure 6.18 shows the gzK_s diagram for the galaxies in the sample with the original BzK galaxy population dividers (i.e. $gzK_s < -0.2$ and $z - K_s > 2.5$ where $gzK_s = (z - K_s) - (g - z)$) overplotted (grey lines). As done previously, the sample has been studied in increasing depths in the K_s-band magnitude. The top, middle and bottom panels are for the $K_s < 21.0$, 22.0 and 23.0 sample respectively. The red circles and blue triangles are known passive and star-forming galaxies respectively and the black crosses are galaxies with $z_{spec} < 1.4$.

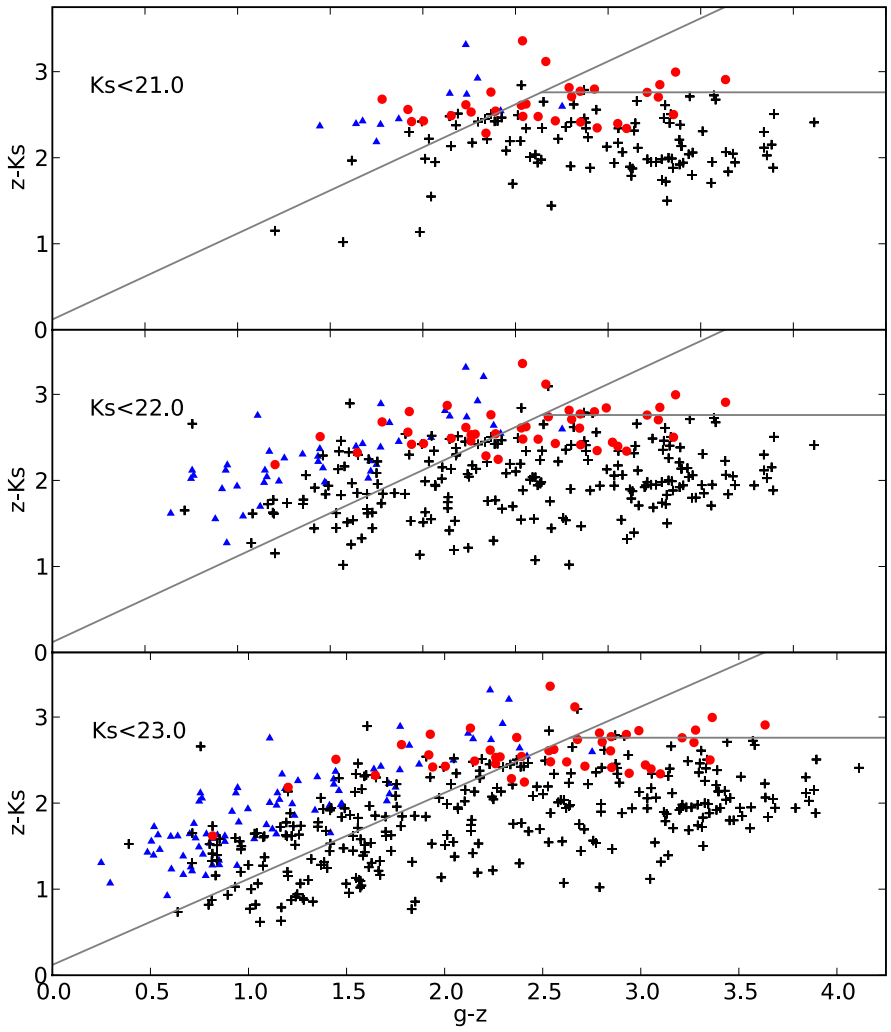

Figure 6.18: The gzK_s diagram for galaxies in the spectroscopic sample. The top, middle and bottom panels are for the $K_s < 21.0$, 22.0 and 23.0 sample respectively. The red circles and blue triangles are known passive and star-forming galaxies respectively based of the definition in Section 5.8 and the black crosses and galaxies with $z_{spec} < 1.4$. The grey solid lines are defined by $gZK_s < -0.2$ and $z - K_s > 2.5$ where $gzK_s = (z - K_s) - (g - z)$)

Table 6.10: The distribution of known galaxy populations on the gzK_s diagram. Columns 2, 3 and 4 shows how the known passive, star-forming and low-redshift targets are distributed.

	Passive	Star-forming	Low-redshift
$K_s < 21.0$(totals)	31	12	100
p-gzK_s	6	0	8
sf-gzK_s	20	12	24
low-z-gzK_s	5	0	68
$K_s < 22.0$(totals)	43	46	205
p-gzK_s	7	0	8
sf-gzK_s	30	46	79
low-z-gzK_s	6	0	118
$K_s < 23.0$(totals)	44	85	285
p-BzK	7	0	8
sf-BzK	31	85	132
low-z-BzK	6	0	145

Assessment of the Original BzK Dividers on the gzK_s Diagram

The gzK_s diagram has been assessed in exactly the same way as the original BzK diagram. The results can be seen in Table 6.10 and, as expected, the population dividers defined originally in BzK space are not appropriate.

Optimising the gzK_s Diagram

From Figure 6.18 it is clear that the dividers require optimisation to improve galaxy population selection. This was done with the same method used for the original BzK diagram and the optimised gzK_s diagram can be seen in Figure 6.19 and the calculated optimal population dividers are as follows:

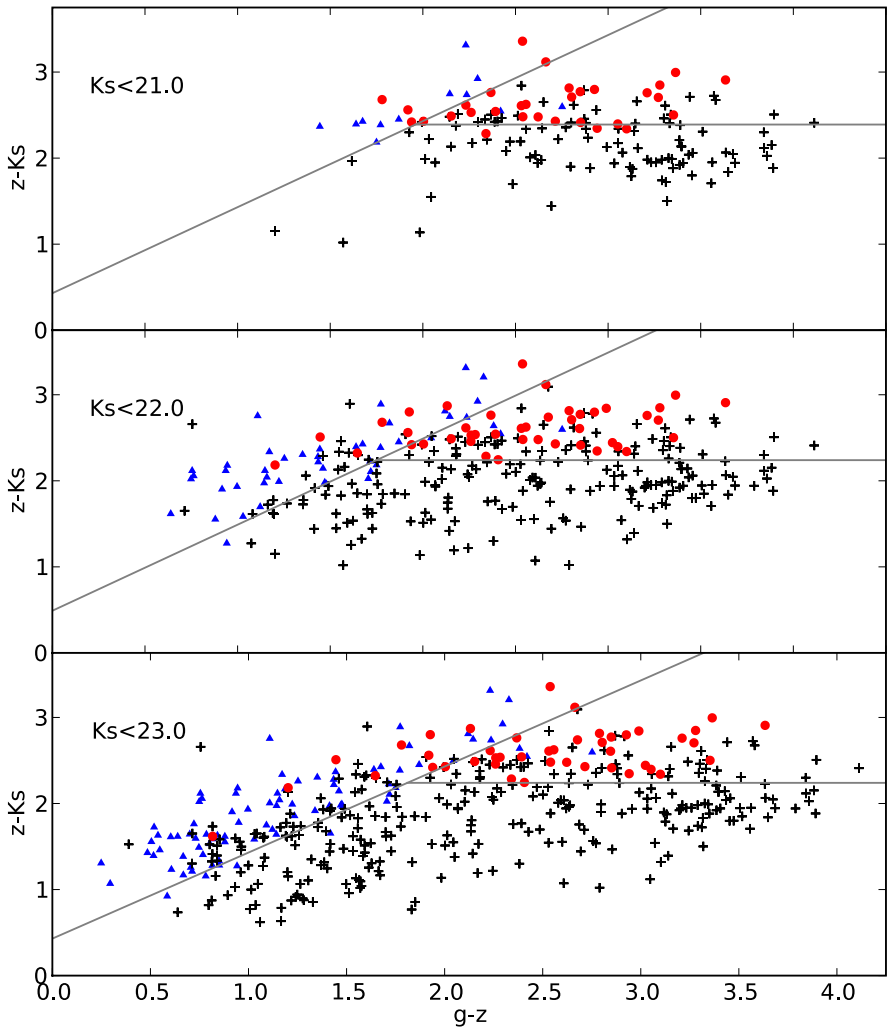

Figure 6.19: Optimised gZK_s diagram. The symbols are as in Figure 6.18, the top, middle and bottom panels are for the $K_s < 21.0$, 22.0 and 23.0 samples respectively. The solid grey lines show the optimised galaxy population dividers.

Table 6.11: The distribution of known galaxy populations in the optimised gZK_s diagram. Columns 2, 3 and 4 shows how the known passive, star-forming and low-redshift targets are distributed.

	Passive	Star-forming	Low-redshift
$K_s < 21.0$(totals)	31	12	100
p-gzK_s	23	2	29
sf-gzK_s	5	10	0
low-z-gzK_s	3	0	71
$K_s < 22.0$(totals)	43	46	205
p-gzK_s	35	4	50
sf-gzK_s	8	37	17
low-z-gzK_s	0	5	138
$K_s < 23.0$(totals)	44	85	285
p-gzK_s	33	3	49
sf-gzK_s	11	73	45
low-z-gzK_s	0	6	191

$$gzK_s < 0.43, z - K_s > 2.39 \quad \text{for} \quad K_s < 21.0 \tag{6.10}$$

$$gzK_s < 0.49, z - K_s > 2.24 \quad \text{for} \quad K_s < 22.0 \tag{6.11}$$

$$gzK_s < 0.43, z - K_s > 2.24 \quad \text{for} \quad K_s < 23.0, \tag{6.12}$$

where $gzK_s = (z - K_s) - (g - z)$. The results of this optimisation and effectiveness of this method are summarised in Table 6.11. With the exception of the $z - K_s$ cut found for the $K < 21.0$ sample the optimised diagrams are very similar for all samples.

These results are similar to what was achieved by optimising the BzK diagram. As before the formulae for calculating the passive fraction, taking into account the known levels of contamination and missed selection, is presented in Table 6.12. Again, the numerator of each fraction is the total number of believed passive galaxies and the denominator in each fraction is the total number of high-redshift galaxies.

Table 6.12: The formulae for calculating the passive fraction for each of the optimised gzK_s diagram. P is the total number of galaxies selected to be passive, S is the total number of galaxies to be selected as star-forming, and the L is the total number of galaxies selected as low-redshift objects.

K-band cut	Passive Fraction
$K < 21.0$	$\frac{P\frac{23}{54}+S\frac{5}{15}+L\frac{3}{74}}{P\frac{25}{54}+S\frac{15}{15}+L\frac{3}{74}}$
$K < 22.0$	$\frac{P\frac{35}{89}+S\frac{8}{62}}{P\frac{39}{89}+S\frac{45}{62}+L\frac{5}{143}}$
$K < 23.0$	$\frac{P\frac{33}{85}+S\frac{84}{129}}{P\frac{36}{85}+S\frac{84}{129}+L\frac{6}{197}}$

6.4.2 The $(J-K)$ vs $(i-K)$ Diagram

To go along with the K_s-band mentioned above the VISTA telescope has a J-band and the VIDEO survey has accompanying i-band data. Therefore as was done with the BzK diagram, a $(J-K_s)$ vs $(i-K_s)$ diagram can be constructed for the spectroscopic targets. As before the i-, J- and K_s-band magnitudes were estimated for our targets by integrating the best-fitting stellar population models for each across the VISTA and CHFT filters.

Figure 6.20 shows the $(J-K_s)$ vs $(i-K_s)$ plot for the ERO $(i-K > 2.6)$ $1 < z < 2$ galaxy sample. The sample is divided by cuts in the K-band magnitude. The top, middle and bottom panels are for the $K_s < 21.0$, 22.0 and 23.0 samples respectively. The red circles and blue triangles are known passive and star-forming galaxies respectively.

Assessment of the Original $(J-K)$ vs $(i-K)$ Dividers on the $(J-K_s)$ vs $(i-K_s)$ Diagram

The assessment of the original $(J-K)$ vs $(i-K)$ population division on the $(J-K_s)$ vs $(i-K_s)$ diagram is presented in Table 6.13. As with the original $(J-K)$ vs $(i-K)$ technique, passive EROs are well selected but there is very high contamination from the star-forming objects.

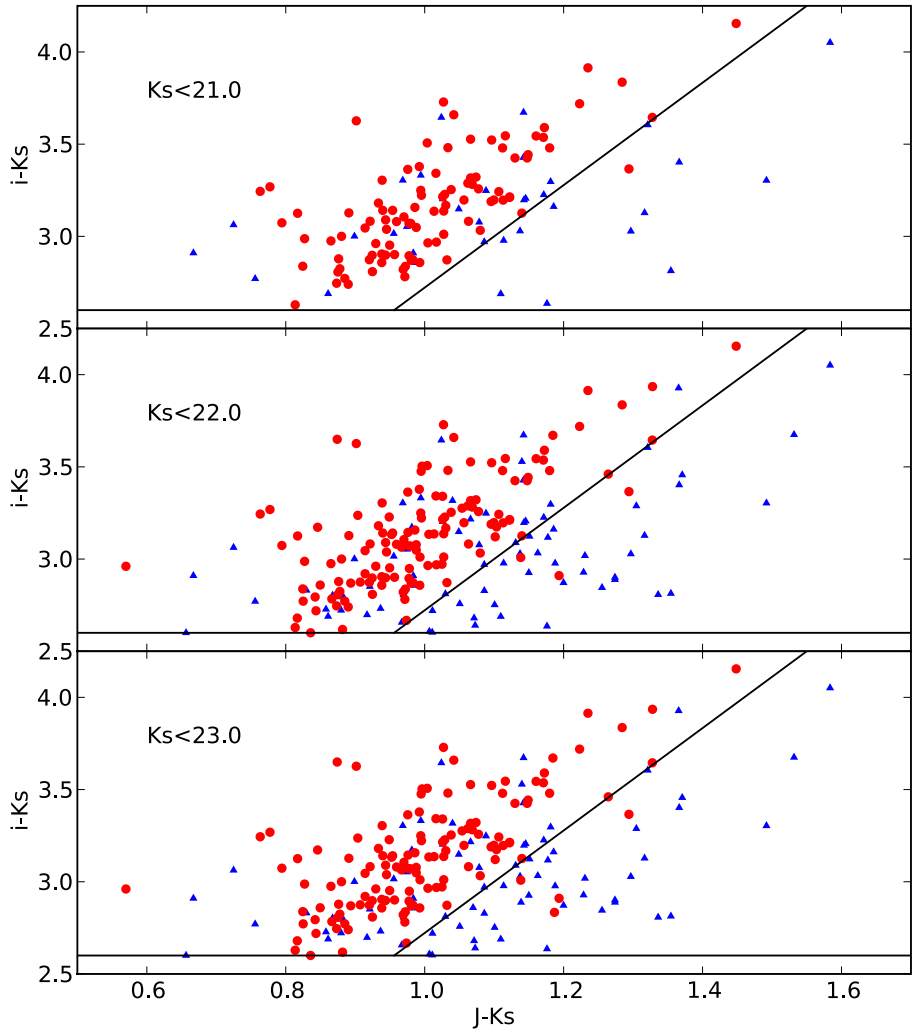

Figure 6.20: The $(J - K_s)$ vs $(i - K_s)$ plot for the ERO $(i - K_s > 2.6)$ $1 < z < 2$ galaxy sample. The black lines are the population dividers from Pozzetti and Mannucci [2000] to separate passively evolving and dusty star-forming galaxies. The top, middle and bottom panels are for the $K < 21.0$, 22.0 and 23.0 samples respectively. The red circles and blue triangles are known passive and star-forming galaxies respectively.

Table 6.13: Table presenting the distribution of known galaxy populations on the original $(J-K_s)$ vs $(i-K_s)$ diagram. Columns 2 and 3 show how the known passive and star-forming targets are distributed.

	Passive	Star-forming
$K < 21.0$(totals)	98	35
$(J-K)$ vs $(i-K)$ Passive	97	23
$(J-K)$ vs $(i-K)$ Star-forming	1	12
$K < 22.0$(totals)	134	76
$(J-K)$ vs $(i-K)$ Passive	131	41
$(J-K)$ vs $(i-K)$ Star-forming	3	35
$K < 23.0$(totals)	135	78
$(J-K)$ vs $(i-K)$ Passive	131	41
$(J-K)$ vs $(i-K)$ Star-forming	4	37

Optimising the $(J-K_s)$ vs $(i-K_s)$ Diagram

Using the method adopted throughout this Chapter, the $(J-K_s)$ vs $(i-K_s)$ diagram has been optimised to separate passive and star-forming EROs at high-redshift. The optimised population divider can be seen in Figure 6.21, and is defined as follows:

$$(J-K_s) = 0.36(i-K_s) - 0.03 \quad \text{for} \quad K_s < 21.0 \tag{6.13}$$

$$(J-K_s) = 0.36(i-K_s) - 0.02 \quad \text{for} \quad K_s < 22.0 \tag{6.14}$$

$$(J-K_s) = 0.36(i-K_s) - 0.03 \quad \text{for} \quad K_s < 23.0, \tag{6.15}$$

The optimal dividing lines are nearly identical in definition and as with the original $(J-K)$ vs $(i-K)$ diagram, have sacrificed the selection of some passive EROs to lower the levels of contamination from the star-forming galaxies. The effectiveness of this technique is presented in Table 6.14

Even after optimisation there is still a significant amount of contamination of passive galaxy in the star-forming region indicating that there is no clear separation between the

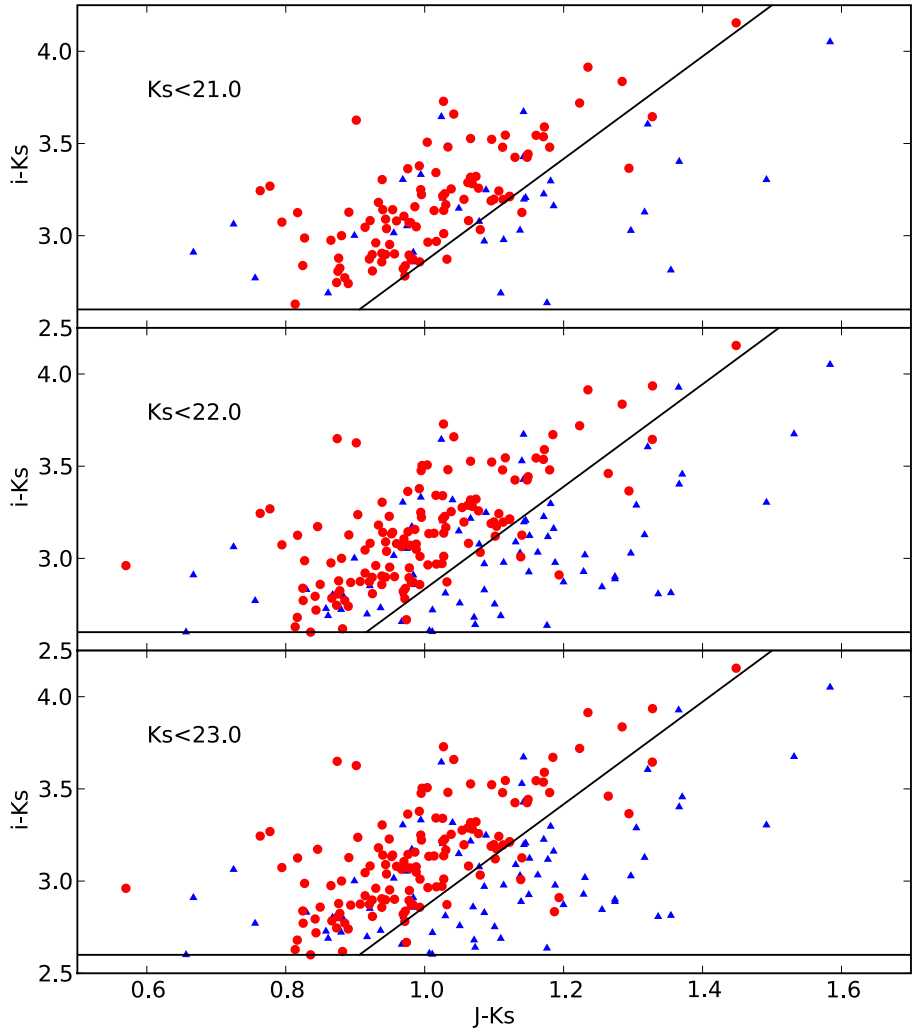

Figure 6.21: The $(J-K_s)$ vs $(i-K_s)$ plot for the ERO $(i-K_s > 2.6)$ $1 < z < 2$ galaxies in our sample. The black lines are the optimised population dividers, discussed in detail in the text. The top, middle and bottom panels are for the $K < 21.0$, 22.0 and 23.0 sample respectively. The red circles and blue triangles are known passive and star-forming galaxies respectively.

Table 6.14: The distribution of known galaxy populations on the optimal $(J-K_s)$ vs $(i-K_s)$ diagram. Columns 2 and 3 show how the known passive and star-forming targets are distributed.

	Passive	Star-forming
$K_s < 21.0$(totals)	98	35
$(J-K_s)$ vs $(i-K_s)$ Passive	92	17
$(J-K_s)$ vs $(i-K_s)$ Star-forming	6	18
$K_s < 22.0$(totals)	134	76
$(J-K_s)$ vs $(i-K_s)$ Passive	125	33
$(J-K_s)$ vs $(i-K_s)$ Star-forming	9	43
$K_s < 23.0$(totals)	135	78
$(J-K_s)$ vs $(i-K_s)$ Passive	123	32
$(J-K_s)$ vs $(i-K_s)$ Star-forming	12	46

Table 6.15: The formulae for calculating the passive fraction for each of the optimised $(J-K_s)$ vs $(i-K_s)$ diagrams. P is the total number of galaxies selected to be passive, S is the total number of galaxies selected as star-forming, and the T is the total number of galaxies.

K_s-band cut	Passive Fraction
$K_s < 21.0$	$\frac{P\frac{92}{109}+S\frac{6}{24}}{T}$
$K_s < 22.0$	$\frac{P\frac{125}{158}+S\frac{9}{52}}{T}$
$K_s < 23.0$	$\frac{P\frac{123}{155}+S\frac{12}{58}}{T}$

galaxy populations using these filters. As before the formulae for calculating the passive fraction taking into account the known levels of contamination and missed selection is presented in Table 6.15. Again, the numerator of each fraction is the total number of believed passive EROs and the denominator in each fraction is the total number of EROs at $1 < z < 2$.

Table 6.16: The distribution of known galaxy populations on the original gZK_s diagram. Columns 2, 3 and 4 shows how the known passive, star-forming and low-redshift targets are distributed.

	Passive	Star-forming	Low-redshift
$K_s < 21.0$(totals)	31	12	100
p-BzK	6	0	7
sf-BzK	21	12	26
low-redshift-BzK	4	0	67
$K_s < 22.0$(totals)	43	46	205
p-BzK	7	0	8
sf-BzK	32	46	82
low-redshift-BzK	4	0	115
$K_s < 23.0$(totals)	44	85	285
p-BzK	7	0	8
sf-BzK	33	85	132
low-redshift-BzK	4	0	145

6.4.3 Another BzK Diagram

The VIDEO survey will soon receive imaging data from the VISTA Z-band so, following on from the gzK_s diagram above, a gZK_s diagram has been developed, using VISTA Z and K_s filters and the g-band from CFHT.

Figure 6.22 shows the gZK_s diagram for the galaxies in the sample with the original BzK galaxy population dividers (i.e. $gZK_s < -0.2$ and $Z - K_s > 2.5$ where $gZK_s = (Z - K_s) - (g - Z)$) overplotted (grey lines). The figure structure and colour-coding is as in Figure 6.18.

Assessment of the Original BzK Dividers on the gZK_s Diagram

The results from comparing the spectroscopic sample on the gZK_s with the original BzK dividers can be seen in Table 6.16

As with the gzK_s diagram the population dividers defined originally in BzK space

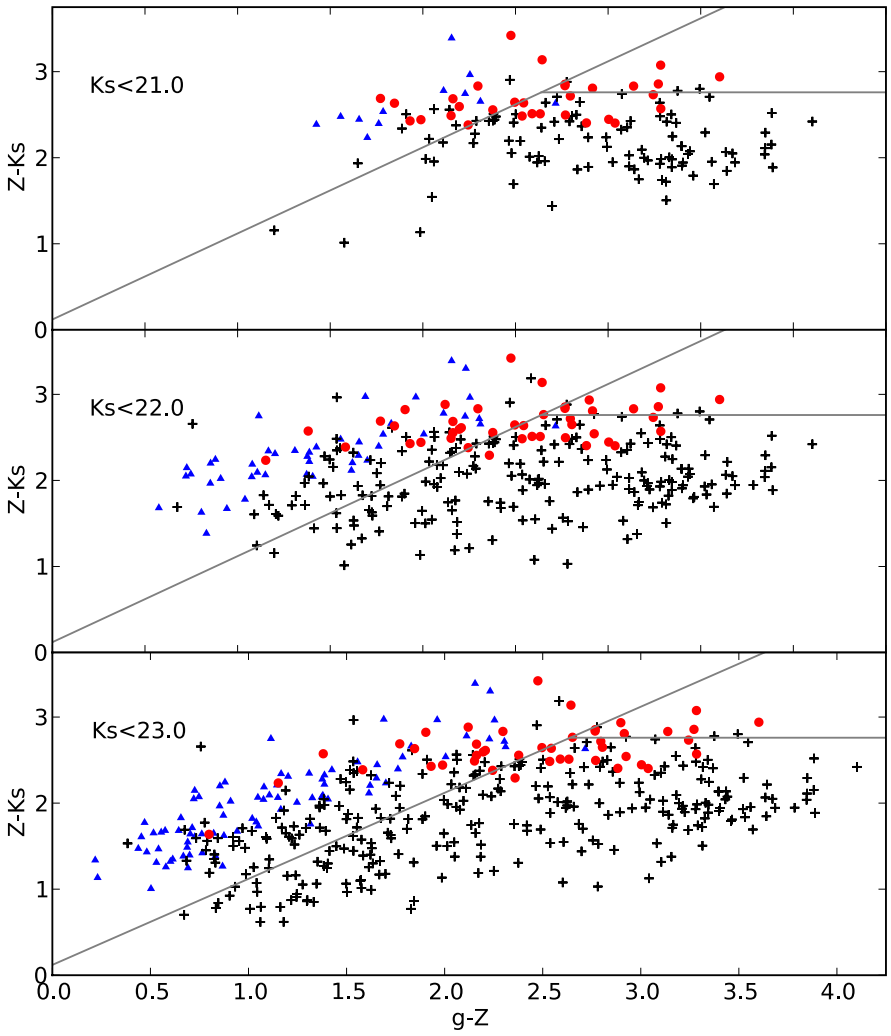

Figure 6.22: The gZK_s diagram for galaxies in the spectroscopic sample. The top, middle and bottom panels are for the $K_s < 21.0$, 22.0 and 23.0 sample respectively. The red circles and blue triangles are known passive and star-forming galaxies respectively based of the definition in Section 5.8 and the black crosses and galaxies with $z_{spec} < 1.4$. The grey dotted lines are defined by $gZK_s < -0.2$ and $Z - K_s > 2.5$ where $gZK_s = (Z - K_s) - (g - Z)$)

are not appropriate.

Optimising the gZK_s Diagram

Using the same method as throughout the gZK_s diagram has been optimised and is shown in Figure 6.23 and the calculated optimal dividers are given in Equation 6.16, 6.17 and 6.18 for the $K < 21.0$, 22.0 and 23.0 samples respectively.

$$gZK_s < 0.5, z - K_s > 2.38 \quad \text{for} \quad K_s < 21.0 \tag{6.16}$$

$$gZK_s < 0.53, z - K_s > 2.38 \quad \text{for} \quad K_s < 22.0 \tag{6.17}$$

$$gZK_s < 0.55, z - K_s > 2.38 \quad \text{for} \quad K_s < 23.0, \tag{6.18}$$

where $gZK_s = (z - K_s) - (g - Z)$.

The success of the optimised method is summarised in Table 6.17 and the formulae for calculating the passive fraction at high-redshift are given in Table 6.18.

6.5 Initial Estimation of the Passive Fraction from the VIDEO Catalog

The VIDEO survey provides the opportunity to compare the passive fraction of high-redshift K-band selected galaxies and EROs calculated above for the UDS field with the fractions in an independent field, the VIMOS-VLT Deep Survey (VVDS) field. Using the gzK_s and $(J - K_s)$ vs $(i - K_s)$ methods developed previously the passive fractions from the VIDEO D1 catalog have been estimated.

6.5.1 Using the gzK_s Diagram

The buildup of the gzK_s diagram as a function of K_s-band magnitude can be seen in Figure 6.24 for the first data release from the VIDEO survey.

Using the formulae in Table 6.12 the fraction of passive to star-forming galaxies as a function of K_s-band magnitude is $321/454 \approx 71\%$, $795/2532 \approx 31\%$ and $1763/8994 \approx 20\%$ for $K < 21$, 22 and 23 samples respectively. The results for the $K_s < 22.0$ and 23.0

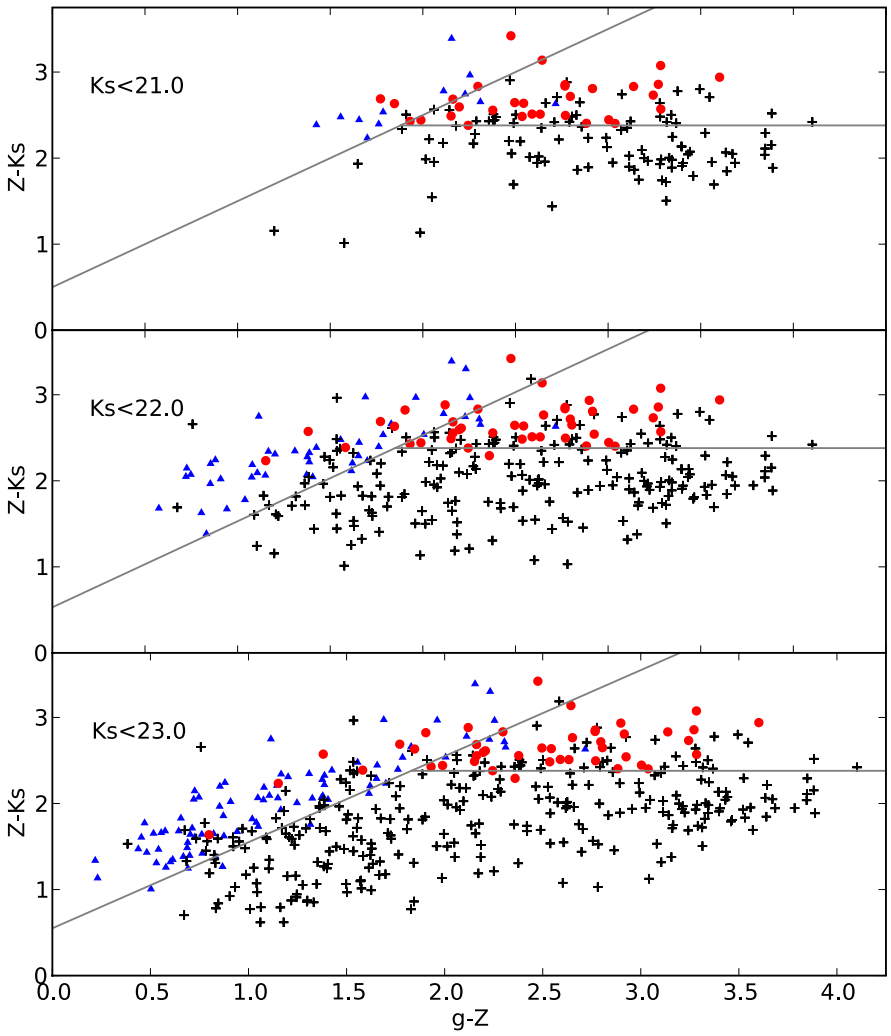

Figure 6.23: The optimised gZK_s diagram. The symbols are as in Figure 6.22, the top, middle and bottom panels are for the $K_s < 21.0$, 22.0 and 23.0 samples respectively. The solid grey lines show the optimised galaxy population dividers.

Table 6.17: The distribution of known galaxy populations on the optimised gZK_s diagram. Columns 2, 3 and 4 shows how the known passive, star-forming and low-redshift targets are distributed.

	Passive	Star-forming	Low-redshift
$K_s < 21.0$(totals)	31	12	100
p-gZK_s	26	2	30
sf-gZK_s	5	10	2
low-redshift-gZK_s	0	0	68
$K_s < 22.0$(totals)	43	46	205
p-gZK_s	33	4	36
sf-gZK_s	9	41	17
low-redshift-gZK_s	1	1	152
$K_s < 23.0$(totals)	44	85	285
p-gZK_s	34	5	36
sf-gZK_s	9	75	34
low-redshift-gZK_s	8	2	215

Table 6.18: The formulae for calculating the passive fraction for each of the optimised $gzKz$ diagram. P is the total number of galaxies selected to be passive, S is the total number of galaxies to be selected as star-forming and the L is the total number of galaxies selected as low-redshift objects.

K-band cut	Passive Fraction
$K_s < 21.0$	$\frac{P\frac{26}{58}+S\frac{5}{17}}{P\frac{28}{58}+S\frac{15}{17}}$
$K_<22.0$	$\frac{P\frac{33}{73}+S\frac{9}{67}+L\frac{1}{154}}{P\frac{37}{73}+S\frac{50}{67}+L\frac{2}{154}}$
$K_s < 23.0$	$\frac{P\frac{34}{75}+S\frac{9}{118}+L\frac{8}{225}}{P\frac{39}{75}+S\frac{84}{118}+L\frac{10}{225}}$

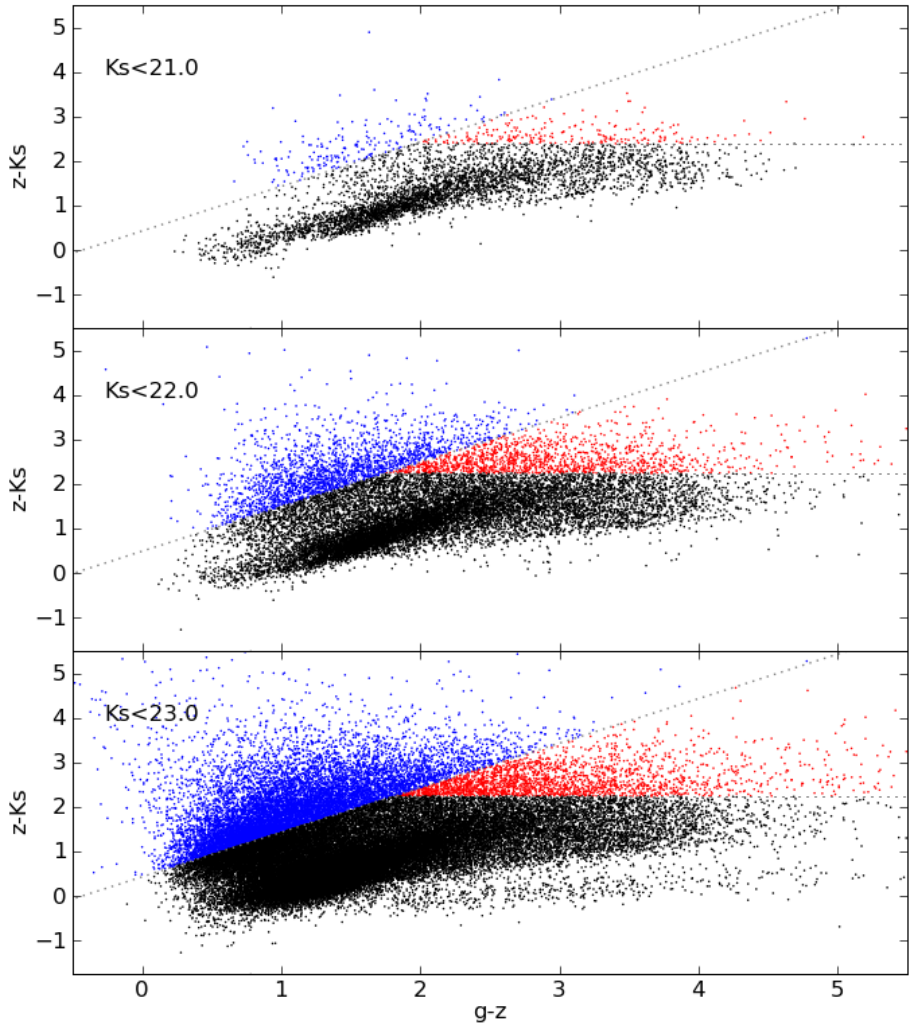

Figure 6.24: The optimised BzK diagram applied to the VIDEO D1 sample. The top, middle and bottom panels are for the $K_s < 21.0$, 22.0 and 23.0 samples respectively. The red, blue and black dots are for galaxies selected to be $1.4 < z < 2.5$ and passive, $1.4 < z < 2.5$ and star-forming and $z < 1.4$ respectively and the grey dotted lines represent the optimal population dividers.

samples are consistent with the fraction found with the optimised BzK diagram. But the fraction for the bright K-band sample is approximately 25% larger but this agrees within in the errors as all these fraction have Poisson errors of $\pm 10 - 20\%$.

6.6 Summary and Conclusions

Regularly used photometric techniques for dividing galaxy populations at high redshift have been assessed with the knowledge of the passivity of the sample of UDSz galaxies used throughout this thesis. It was found that the standard BzK, $(J-K)$ vs $(i-K)$ and $(V-J)$ vs $(U-V)_{\text{Rest-frame}}$ diagrams are far from optimal at selecting complete samples with minimum contamination.

Therefore the spectroscopic sample was used to optimise these techniques for $K <$ 21, 22 and 23 samples. From these optimised dividers, along with the known levels of contamination across the different selection regions, optimised formulae for passive galaxy selection have been presented in Equations 6.1, 6.2 and 6.3 for the BzK diagram, Equations 6.4, 6.5 and 6.6 for the $(J-K)$ vs $(i-K)$ diagram and Equations 6.7, 6.8 and 6.9 for the $(V-J)$ vs $(U-V)_{\text{Rest-frame}}$ diagram.

Using the devised optimal selection techniques, passive galaxy fractions in the high-redshift Universe have been estimated for K-band selected and ERO selected samples. From the BzK the passive fraction of K-band selected targets was estimated at 54%, 35% and 18% for $K < 21$, 22 and 23 samples. The passive fraction for the $K < 21$ sample is consistent with our results from Section 5.8 for the $K < 21.5$, $1.3 < z < 1.5$ Universe. Even though there was also criteria on V, i and z for the spectroscopic sample this is expected since $K < 21.5$ galaxies are bright and therefore will tend to be old red objects so would not be effected by this additional criterion.

The passive fractions of K-band selected objects estimated from the $(V-J)$ vs $(U-V)_{\text{Rest-frame}}$ diagram are consistent with that found with the BzK at 27% and 15% for the $K < 22$ and 23 samples. For the $K < 21$ sample the passive fraction is approximately a factor of 1.5 below that found with the BzK at 38%. But this value is within the range of values found by Cimatti et al. [2002a] and Smail et al. [2002] and is consistent with the theoretical prediction from Fontanot and Monaco [2010].

The ratio of passive to star-forming EROs was found with the optimised $(J-$

K) vs $(i - K)$ diagram to be 64%, 57% and 53% for the $K < 21$, 22 and 23 samples respectively. The passive fraction found with the optimised BzK technique for the $K < 21.0$ is in good agreement with the estimations found here for bright EROs. This is expected as $\sim 70\%$ of the $K < 21$ galaxies are EROs (see Figure 6.14). The results for the $K < 22$ and 23 samples are consistent with all the observational results mention in Section 5.8.1.

In preparation for the arrival of new data from VISTA, the first of a new generation of wide-field survey telescopes, and an ongoing state of the art survey, VIDEO, BzK and $(J-K)$ vs $(i-K)$ diagrams have been developed. A gzK_s and gZK_s diagram have been developed based on the g- and z-bands from CHFT and Z- and K_s-bands from VISTA since the VIDEO survey has deep accompanying CHFT data. A $(J - K_s)$ vs $(i - K_s)$ has also been developed with the i-band from CFHT and J- and K_s-bands from the VISTA telescope.

As a test for the passive fraction of a purely K-band selected sample the passive fraction have been estimated for the VIDEO D1 catalog. This gives an independent test for the fraction determined above. The passive fractions found with the gzK_s diagram and VIDEO D1 catalog are 71%, 31% and 20% for the $K_s < 21$, 22 and 23 samples respectively. Which, within the errors, are in agreement with the results from the optimised BzK diagram.

C

Chapter 7

Galaxy Population Studies with Composite Spectra

Galaxies come in a variety of forms and it is interesting to observe how their spectral characteristics such as continuum breaks, emission and absorption features and spectral slope change as function of physical characteristics such as stellar-mass, age and star-formation rate. Composite spectra offer a good way to do this as they provide high signal-to-noise spectral representations of a sub-sample of galaxies which share a common physical characteristic. In this Chapter, composite galaxy spectra are produced and compared to composite spectra constructed from previous surveys. Based on these composite spectra the redshift evolution of spectral characteristics as a function of various physical characteristics is investigated. Age estimates for the composite spectra are made by doing spectrophotometric fits with stellar synthesis models as was done previously for the individual galaxy spectra.

7.1 Composite Construction

Composite spectra constructed with the UDSz data in this Chapter were produced using the method laid out in Section 4.5. In addition to being constructed across a redshift grid, composite spectra were constructed across grids of various other galaxy characteristics. Specifically, composite spectra were constructed by dividing the galaxies into three bins of stellar-mass, absolute K-band magnitude, specific star-formation rate

Table 7.1: A summary of bins of stellar-mass, absolute K-band magnitude, specific star-formation rate and spectral type used in the construction of the composite spectra.

Characteristic	Bin 1	Bin 2	Bin 3
Stellar-mass	$M_\star < 7.5 \times 10^9 M_\odot$	$7.5 \times 10^9 \leq M_\star < 5 \times 10^{10} M_\odot$	$M_\star \geq 5 \times 10^{10} M_\odot$
M_K	< -24.25	$-24.25 \leq M_K < -23.25$	$M_K \geq -23.25$
SSFR	$< 2.5 \times 10^{-10}\mathrm{yr}^{-1}$	$2.5 \times 10^{-9} - 2.5 \times 10^{-10}\mathrm{yr}^{-1}$	$> 2.5 \times 10^{-9}\mathrm{yr}^{-1}$
Spectral Type	Early	Intermediate	Late

and spectral type (see Table 7.1 for details).

Finally, composite spectra were also constructed by splitting the sample into passive and star-forming galaxies (based on the definition from Section 5.8) and a bin containing the rare, most massive galaxies ($M_\star > 10^{11} M_\odot$). This bin contains the most massive 15% of the sample. Details of the classification scheme of early-, intermediate- and late-type galaxies are described in the following subsection.

7.1.1 Composite Spectra by Galaxy Spectral Type

To decide how to divide the spectroscopic galaxy sample studied here by spectral type, the approaches taken in previous studies were investigated.

Composite Spectra from the K20 Survey

The classification system invoked by the K20 survey [Mignoli et al., 2005] was based on assigning each galaxy a four digit code. Each digit could take a value 0, 1 or 2, where 0 was assigned if the spectral feature fell outside of the galaxy spectrum wavelength coverage. The 4 digits corresponded to four different spectral features; EW[OII], EW(Hα+[NII]), D4000 and C(28-39), see Table 7.2 for the criteria. The first two digits corresponded to $EW[OII]$ and $EW(H\alpha + [NII])$ respectively (where the equivalent widths were calculated by using the *splot* package in IRAF). The third digit relates to the strength of the 4000Å break (D4000) which was calculated using the definition from Bruzual [1983]. The fourth digit corresponds to the UV colour index

Table 7.2: Classification criteria for galaxy spectral types from the K20 survey [Mignoli et al., 2005].

Digit	Criteria
1	1 if $EW[OII] < 6$Å
	2 if $EW[OII] \geq 6$Å
2	1 if $EW(H\alpha + [NII]) < 8$Å
	2 if $EW(H\alpha + [NII]) \geq 8$Å
3	1 if $D4000 > 1.6$
	2 if $D4000 \leq 1.6$
4	1 if $C(28-39) \geq 1.5$
	2 if $C(28-39) < 1.5$

C(28-39) defined as,

$$CI = -2.5 \log \frac{f_\nu(2800)}{f_\nu(3900)} \tag{7.1}$$

where $f_\nu(2800)$ and $f_\nu(3900)$ are the mean flux densities in the regions 2550-3050Å and 3750-3950Å respectively.

An early-type galaxy was classified as a galaxy whose all non-zero digits are 1. A late-type galaxy had all its non-zero digits equal to 2. An intermediate-type galaxy has the first two digits equal to 2 and the last two equal to 1. For each spectral type of galaxy a composite spectra was constructed (see Figure 7.1). The K20 early-, intermediate- and late-type galaxy composite spectra are plotted in red, green and blue respectively. The flux units are arbitrary and the spectra are offset from each for clarity.

Composite Spectra from the GDDS Survey

In the GDDS survey [Abraham et al., 2004] the galaxies were classified in a slightly more subjective manner. The GDDS team initially recorded the lack (0) or presence (1) of a selection of spectral features, with a (2) if the feature does not fall in the spectral range. The emission features used were; [OII], [OIII] and Balmer lines blueward of Hβ. The absorption features used were; Fe2375, Fe2600, Mg2800, Mg2852, Ca H & K, Balmer break and 4000Å break. A visual classification of each galaxy was then made based on

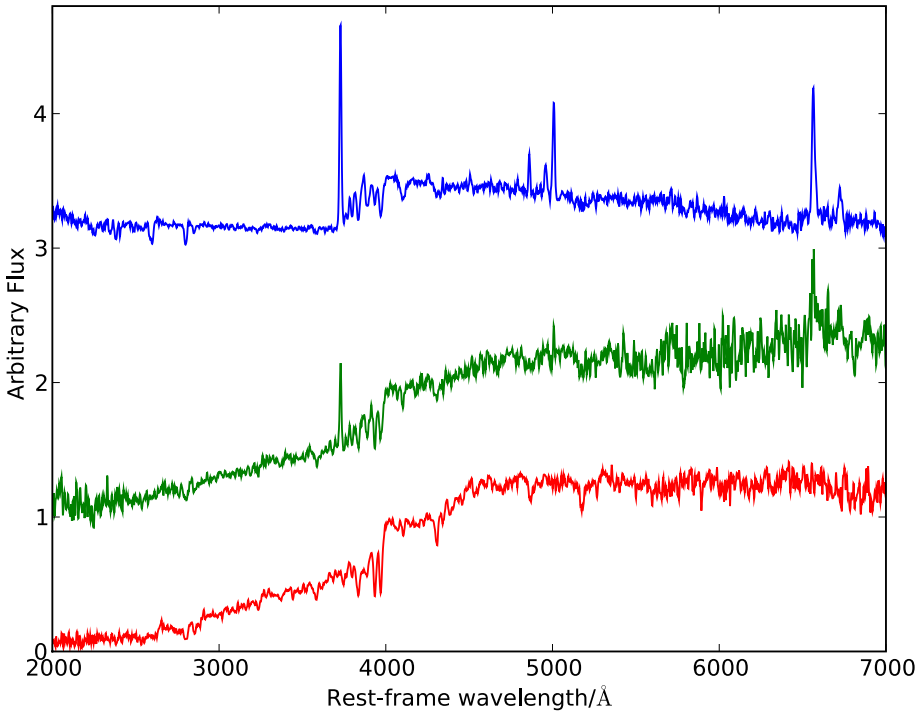

Figure 7.1: The early-, intermediate- and late-type galaxy composite spectra from the K20 survey [Mignoli et al., 2005] plotted in red, green and blue respectively.

these features. The GDDS early-, intermediate- and late-type galaxy composite spectra are plotted in red, green and blue respectively in Figure 7.2. The flux units are arbitrary and the spectra are offset from each for clarity.

Devising a Classification Scheme for the UDSz Sample

To establish an initial estimate of the galaxy spectral type for the objects in the UDSz sample each object was fitted with the composite spectra from the K20 and GDDS surveys (see Figures 7.1 and 7.2). The 4000Å break (D4000; Bruzual 1983), the equivalent width of the [OII] emission line (EW[OII]), the UV spectral slope index (CI) and the Balmer break [Kriek et al., 2006] (all defined in Section 4.3) were measured for each galaxy. Then using the initial estimate of galaxy spectral type from the fitting of the spectra to the K20 and GDDS composites, the evolution of the strength of these features

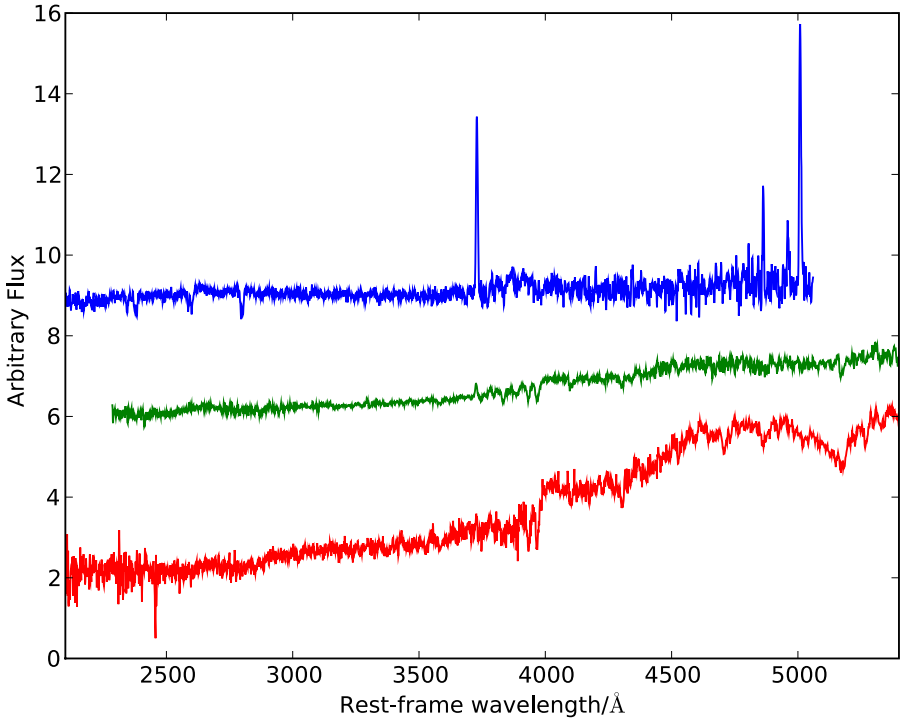

Figure 7.2: The early-, intermediate- and late-type galaxy composite spectra from the GDDS survey [Abraham et al., 2004] plotted in red, green and blue respectively.

Table 7.3: Classification criteria for galaxy spectral types.

Type	D4000	EW[OII]	CI
Early	>1.5	<10Å	>0.7
Late	<1.5	>10Å	<0.6

as function a of "proto"-type was investigated. The final scheme is laid out in Table 7.3 with intermediate-type galaxies defined as any galaxy that did not hold all the criteria for either a early- or late-type galaxy or galaxy with a Balmer break larger than 1.9. This scheme gave 95 early-types, 180 intermediate types and 144 late-types.

The early-, intermediate- and late-type composite spectra produced here are compared with their counterparts from the K20 and GDDS surveys in Figures 7.3, 7.4 and 7.5 respectively. In each figure the bottom black line is the composite spectrum pro-

duced with the UDSz data and the middle and top grey lines are the composite spectra from the K20 and GDDS surveys respectively. The composite spectra are offset from each other arbitrarily for presentation purposes. The early-type composite spectra produced here and the one from the GDDS survey have similar colours whereas the K20 early-type composite is bluer. This is expected as the K20 survey simply imposed a K-band cut whereas the GDDS and UDSz surveys invoked a colour cut in target selection, producing on average redder target. The intermediate-type composite spectra produced by the K20 and GDDS surveys are very similar whereas the one produced with the UDSz data has a significantly stronger [OII] emission line. The late-type composite spectra for all surveys show similar rest-frame continuum colours with the GDDS and UDSz composite spectra having [OII] emission lines with much larger equivalent widths. The composite spectra for the K20 are all of higher signal-to-noise. This is expected as they targeted brighter, lower-redshift sources.

7.2 Spectrophotometric Fitting of Composite Spectra

The composite spectra and photometry were subjected to the same spectrophotometric fitting process as the individual galaxy spectra (see Section 4.1), over the same parameter space (see Table 5.2). Only regions in the composite spectra made by the combination of 10 or more spectra were selected for the fitting process to avoid spectral regions being influences by the features in only a few objects in the sample. Only the spectra from the middle three redshift bins from Table 4.1 are used as this is where the bulk of the objects in the sample lie. The main aim of this process was to acquire an accurate age estimate for the composite spectra. The age estimate used throughout this section in the mass-weighted age defined by,

$$A_M = (A_O \times (1 - f_Y)) + (A_Y \times f_Y), \tag{7.2}$$

where A_M is the mass-weighted age, A_O is the age of old stellar population, A_Y is the age of young stellar population and f_Y is the mass fraction of the young stellar population. Fits to some example spectra are shown in Figure 7.6. The plot show the central redshift bin for the three M_K composite ranges, with the absolute K-band

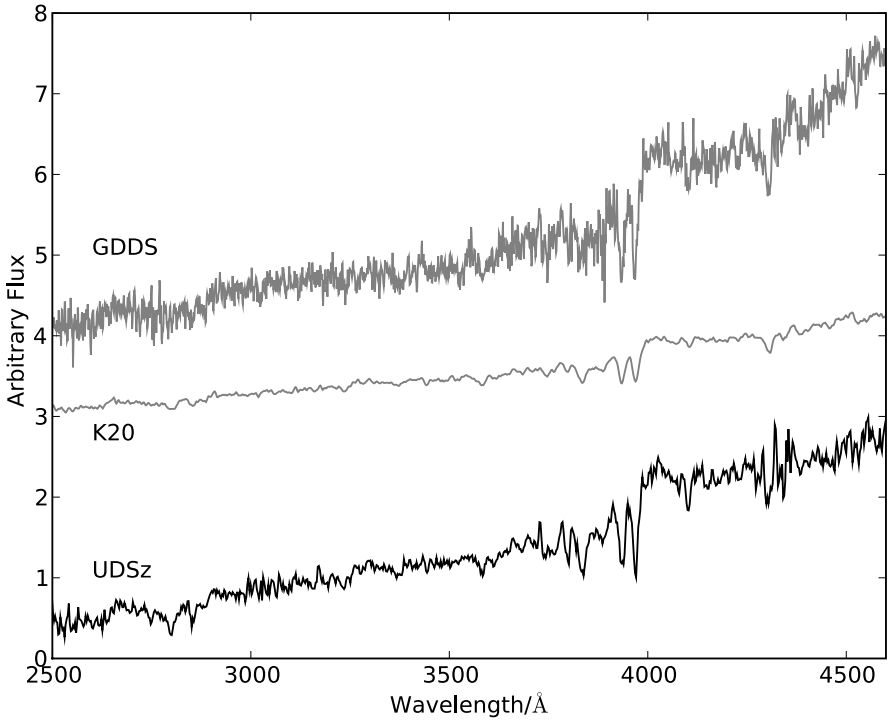

Figure 7.3: Early-type composite spectra from the UDSz, K20 and GDDS surveys. The bottom black line is the spectra produced with the UDSz data and the middle and top grey lines are the composite spectra from the K20 and GDDS surveys respectively. The composite spectra are offset from each other arbitrarily for presentation purposes.

magnitude increasing down the row. The black line is the composite spectra, the red is the composite photometry and the grey is the best-fitting model.

7.2.1 The Age of Galaxy Populations as a Function of Redshift

In this sub-section the ages of composite spectra are investigated as a function of redshift and various physical characteristics of the input galaxies.

The Ages of composite spectra Based on Stellar-mass

The ages of the stellar-mass based composite spectra can be seen as a function of redshift in Figure 7.7 with the blue, green and red lines corresponding to the $< 7.5 \times 10^9 M_\odot$, $7.5 \times 10^9 - 5 \times 10^{10} M_\odot$ and $> 5 \times 10^{10} M_\odot$ stellar-mass bins. The solid grey line depicts

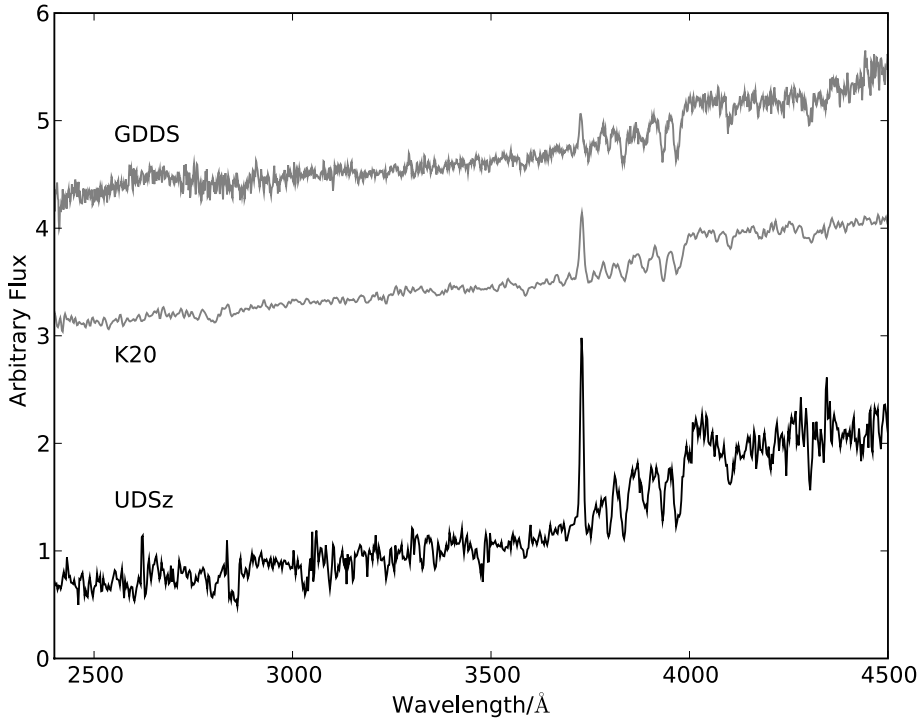

Figure 7.4: Intermediate-type composite spectra from the UDSz, K20 and GDDS surveys. The bottom black line is the spectra produced with the UDSz data and the middle and top grey lines are the composite spectra from the K20 and GDDS surveys respectively. The composite spectra are offset from each other arbitrarily for presentation purposes.

the age of the Universe as a function of redshift and the region above it is forbidden in the fitting process. The dashed grey lines correspond to 25%, 50% and 75% of the age of the Universe at a given redshift. In the plots throughout this section all the redshifts plotted are the median redshift of the objects that lay within the bin.

Generally the most massive bin contains the oldest galaxies. In the middle redshift range the intermediate mass bin has the same fractional age as the upper mass bin. This is possible as the intermediate mass bin can be dominated by galaxies with masses close to the upper limit. The lowest mass is consistently made up of younger galaxies than the other two bins.

Investigating the age of the most massive galaxies ($> 10^{11} M_{\odot}$) as a function of redshift shows, as expected from the above, they make the oldest systems in the Universe

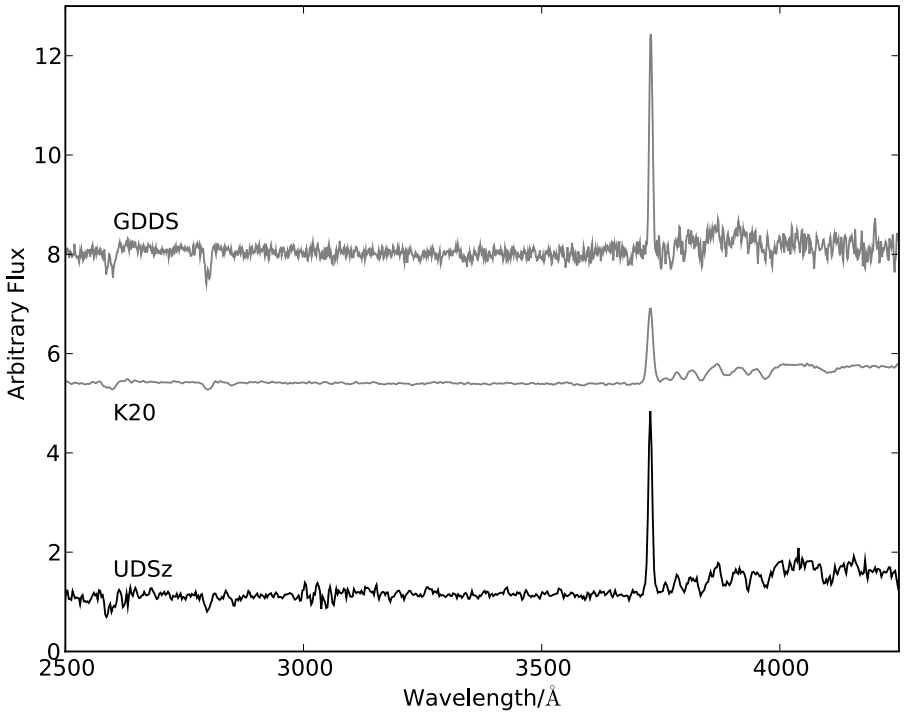

Figure 7.5: Late-type composite spectra form the UDSz, K20 and GDDS surveys. The bottom black line is the spectra produced with the UDSz data and the middle and top grey lines are the composite spectra from the K20 and GDDS surveys respectively. The composite spectra are offset from each other arbitrarily for presentation purposes.

at any redshift (see Figure 7.8).

The Ages of composite spectra Based on Absolute K-band Magnitude

The ages of the composite spectra based on absolute K-band magnitude can be seen as a function of redshift in Figure 7.9 with the blue, green and red lines corresponding to the $M_K < -24.25$, $-24.25 \leq M_K < -23.25$, $M_K \geq -23.25$ bins. The grey lines are as in Figure 7.7. For the redshift range covered by the composite bins ($z \sim 1 - 1.5$), the objects that are bright in rest-frame K-band are the oldest with the faintest being the youngest. This trend is expected given the results in Figure 7.7 and the fact that M_K should be a reasonable proxy for stellar-mass.

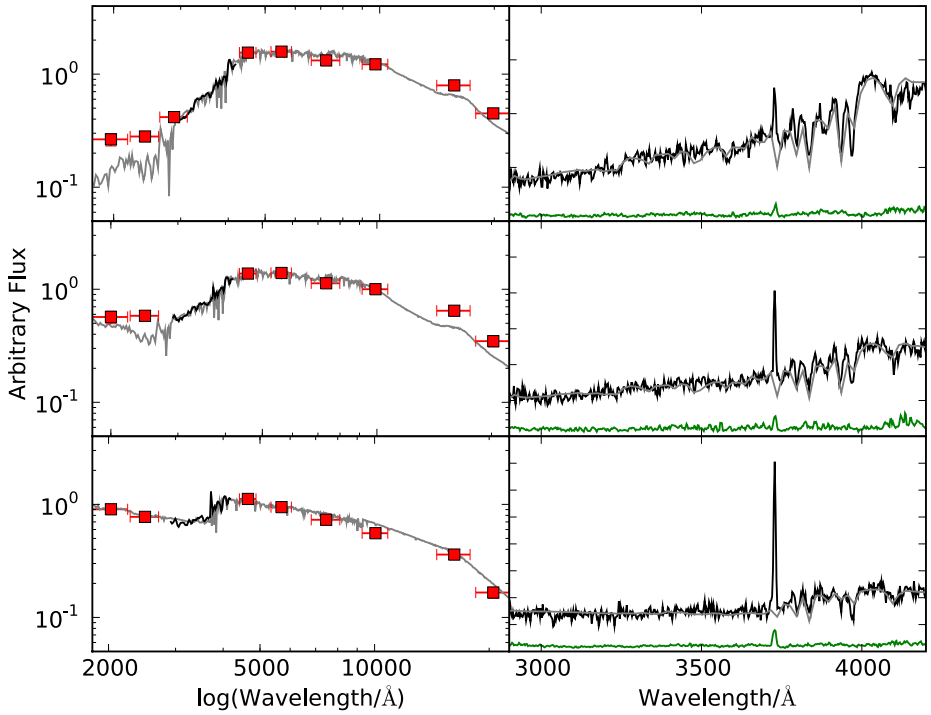

Figure 7.6: Spectrophotometric fits to the central redshift bin for the three M_K composite ranges. Absolute K-band magnitude increasing down the rows. The black line is the composite spectra, the red is the composite photometry and the grey is the best-fitting model.

The Ages of composite spectra Based on Specific Star-formation Rate

The ages of the SSFR based composite spectra can be seen as a function of redshift in Figure 7.10 with the blue, green and red lines corresponding to the $> 2.5 \times 10^{-9}\mathrm{yr}^{-1}$, $2.5 \times 10^{-9} - 2.5 \times 10^{-10}\mathrm{yr}^{-1}$ and $< 2.5 \times 10^{-10}\mathrm{yr}^{-1}$ SSFR bins. The galaxies with a SSFR $< 2.5 \times 10^{-10}\mathrm{yr}^{-1}$ are tracing the age of the Universe. This low SSFR bin will contain the most passive galaxies at these redshifts. The highest SSFR bin always recovers age less than 25% the age of the Universe whereas the middle bin covers a wide range of ages.

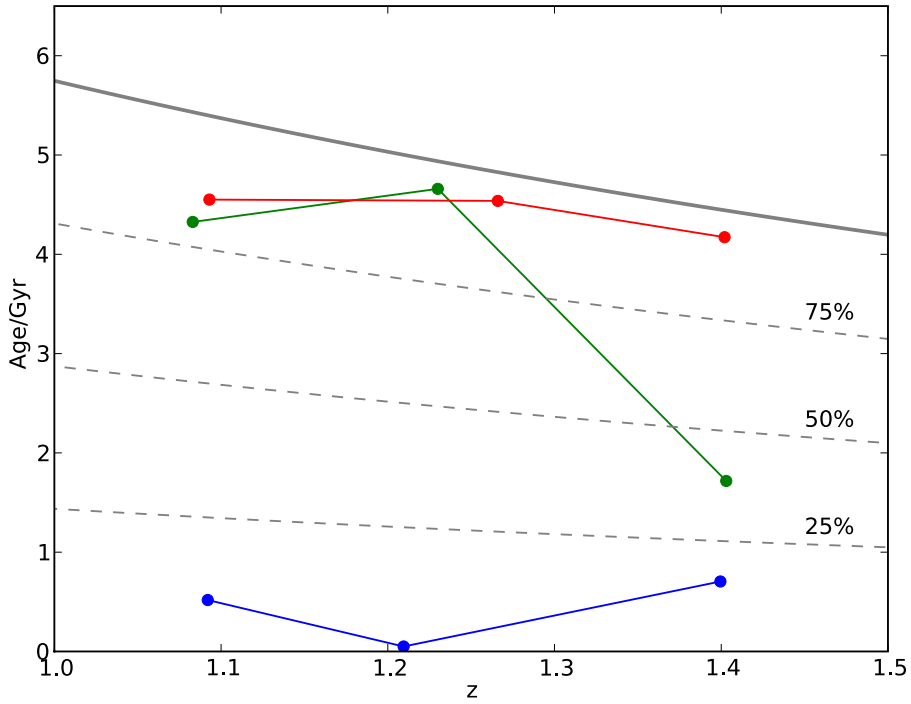

Figure 7.7: Mass-weighted age as a function of redshift for the composite spectra split by stellar-mass with the blue, green and red lines corresponding to the $< 7.5 \times 10^9 M_\odot$, $7.5 \times 10^9 - 5 \times 10^{10} M_\odot$ and $> 5 \times 10^{10} M_\odot$ stellar-mass bins. The solid grey line depicts the age of the Universe and the region above it as forbidden in the fitting process. The dashed grey lines correspond to 25%, 50% and 75% of the age of the Universe.

Ages of composite spectra Based on Galaxy Spectral Type

The ages of the composite spectra constructed by spectral type can be seen as a function of redshift in Figure 7.11 with the blue, green and red lines corresponding to the early-, intermediate- and late-type galaxy. The early-type galaxies are nearly tracing the age of the Universe across the full redshift range. The late-type galaxies recover consistently young ages. The intermediate galaxies are of intermediate age in the high redshift bin and then sit along side early-type galaxies at $z \sim 1.2 - 1.4$ before dropping below 50% the age of the Universe at $z < 1.1$.

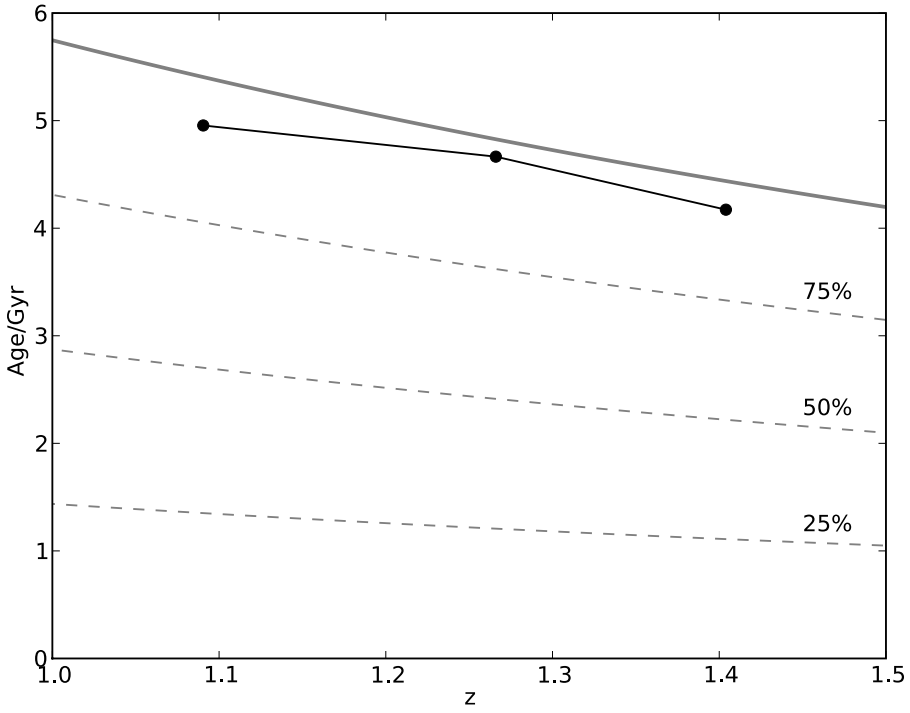

Figure 7.8: Mass-weighted age as a function of redshift for the composite spectra comprising of the most massive ($> 10^{11} M_{\odot}$) systems. The grey lines are as in Figure 7.7.

7.2.2 Summary of Ages Estimates Based on the Composite Spectra

Whether you split by mass, M_K or SSFR or spectral type the same clear result emerges that the oldest galaxies are the most massive, passive ETGs, with an age close to that of the Universe. Conversely the younger star-forming systems appear to be lower mass late-type galaxies. This is consistent with the picture of downsizing that the most massive systems finish their mass assembly at early times while the lower mass systems continue to be actively star-forming through to low redshift. The intermediate bins for each characteristic show odd behaviour but this may be due to the fact that this bin can easily basis towards either extreme.

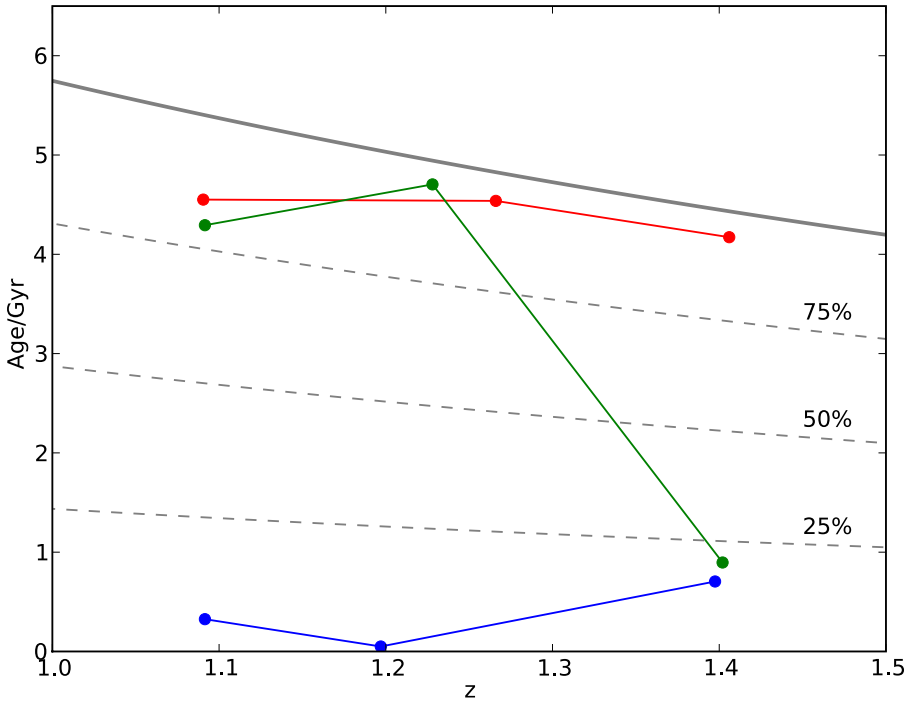

Figure 7.9: Mass-weighted age as a function of redshift for the composite spectra split by absolute K-band magnitude with the blue, green and red lines corresponding to the $M_K < -24.25$, $-24.25 \leq M_K < -23.25$, $M_K \geq -23.25$ bins. The grey lines are as in Figure 7.7.

7.3 The Evolution of Spectral Features

Here it is investigated how spectral features evolve as a function of age, stellar-mass, M_K, SSFR and spectral type. For the redshift range spanned by the FORS2 spectrograph the most common features to occur in the optical spectra, and which will be investigated here, are the 4000Å break (D4000; Bruzual 1983), the equivalent width of the [OII] emission line (EW[OII]), a UV spectral slope index and the Balmer break [Kriek et al., 2006]. The definition of these features was described in Section 4.3 and the parameter bins used to construct the composite spectra are listed in Table 7.1. Note that the EW[OII] rather than the $L_{[OII]}$ has been used for consistency with the other spectral features considered here all of which are measures of the spectral shape and hence independent of distance and luminosity of the source.

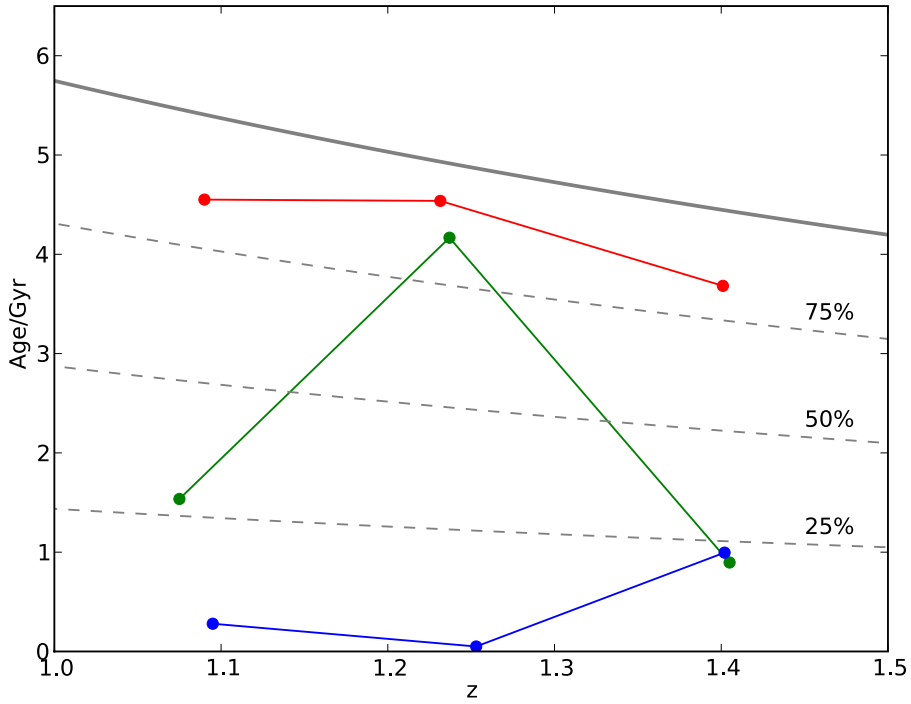

Figure 7.10: Mass-weighted age as a function of redshift for the composite spectra split by SSFR with the blue, green and red lines corresponding to the $> 2.5 \times 10^{-9}\mathrm{yr}^{-1}$, $2.5 \times 10^{-9} - 2.5 \times 10^{-10}\mathrm{yr}^{-1}$ and $< 2.5 \times 10^{-10}\mathrm{yr}^{-1}$ SSFR bins. The grey lines are as in Figure 7.7.

7.3.1 Feature Evolution as a Function of Stellar-mass

Figure 7.12 plots the evolution of these features as a function of redshift in the left-hand panels, and and as a function of age in the right-hand panels. From top to bottom the row of panels show the evolution of D4000, the Balmer break, the UV colour index and the equivalent width of the [OII] emission line respectively. The colour coding is as in Figure 7.7 and the additional black points are for the most massive ($> 10^{11} M_{\odot}$) galaxies.

It is clear from Figure 7.12 that the largest standard stellar-mass bin, and the extra bin containing the most massive galaxies, have the largest D4000 break. Given that D4000 is a strong age indicator, this results is consistent with the result shown in Figure 7.7. Moreover, this result is re-enforced by the D4000 as a function of age plot

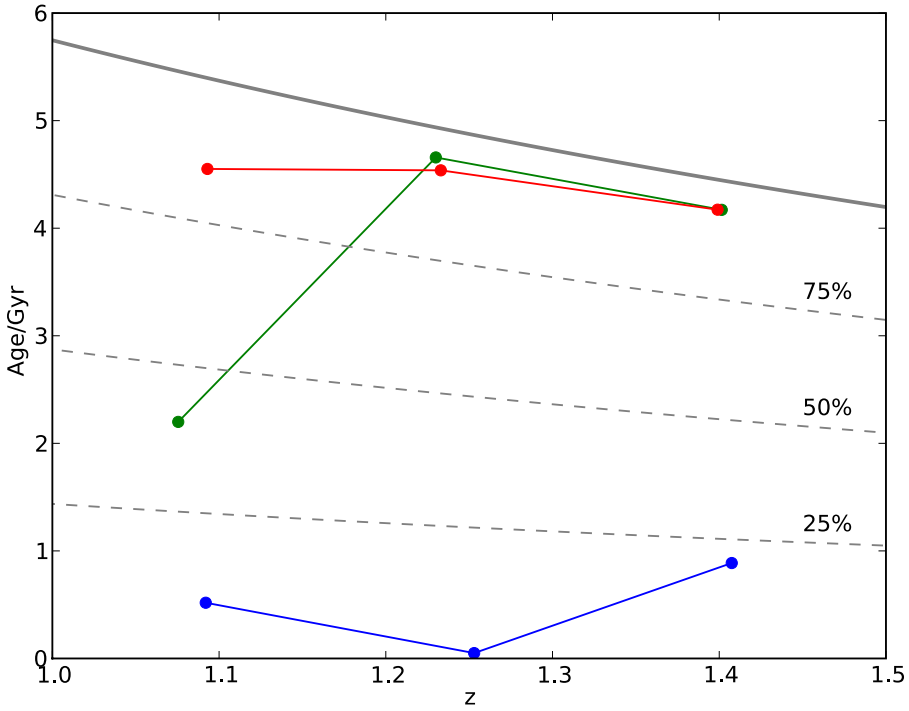

Figure 7.11: Mass-weighted age as a function of redshift for the composite spectra split by galaxy spectral type with the blue, green and red lines corresponding to early-, intermediate- and late-type galaxies. The grey lines are as in Figure 7.7.

in the top right-hand panel in which the red and black symbols populating the top right corner and the low mass (blue symbols) galaxies are located towards the lower left corner.

The Balmer break is believed to be at its strongest in galaxies for which the stellar population is dominated by intermediate aged stars. If mass can be considered as a proxy for age this effect is observed here with the middle mass bin containing the galaxies with the strongest Balmer breaks. As the lower mass bin contains galaxies with a range of ages, the Balmer break is stronger than the most massive bins.

The UV colour index plot is as expected, with the more massive, older, bins having redder colours and the lower-mass bins having bluer colours. Moreover, there tends to be a general increase in the redness of the colour index with lowering redshift and increasing age. The [OII] emission line is at its strongest for the low mass bins and

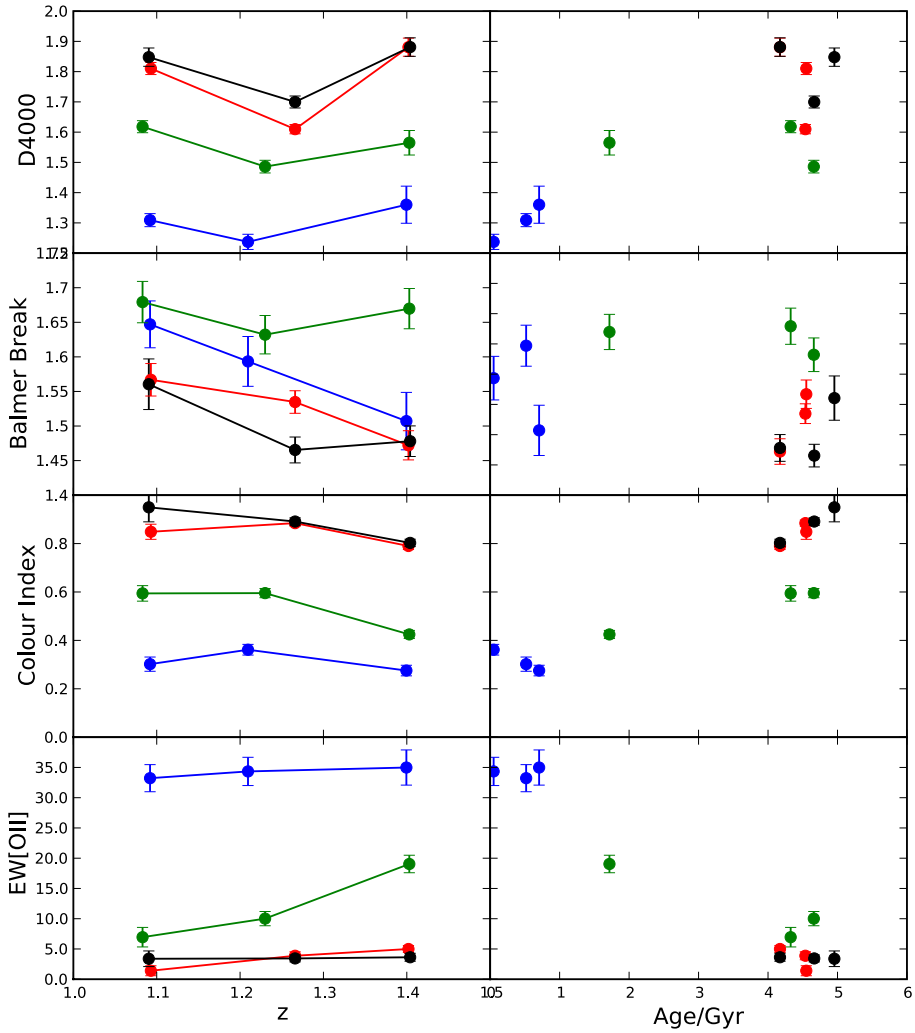

Figure 7.12: The evolution of spectral features as a function of redshift in the left-hand panels and as a function of age in the right-hand panels. From top to bottom the rows are for D4000, the Balmer break, the UV colour index and the equivalent width of the [OII] emission line. The colour coding is as in Figure 7.7 and the additional black points are for the most massive ($> 10^{11} M_{\odot}$) galaxies

decreases with increasing mass. All mass bins show a general decrease in the EW[OII] with increasing age and lowering redshift, indicating star-formation in decreasing in all mass bins with time.

7.3.2 Feature Evolution as a Function of Absolute K-band Magnitude

Figure 7.13 plots the evolution of spectral features as a function of redshift and age with the same layout as in Figure 7.12 and the colour coding of Figure 7.9. The results are nearly identical to those based on stellar-mass with the largest standard stellar-mass bin analogous to the brightest bin in absolute K-band magnitude. The only major difference appears to be in the evolution of the Balmer break which appears to be similar for all the M_K bins.

7.3.3 Feature Evolution as a Function of Specific Star-formation Rate

The evolution of spectral features with respect to SSFR as function of redshift and age can be seen in Figure 7.14. The figure has the same layout as Figure 7.10.

The objects with the lowest SSFR have the largest D4000 breaks, smallest Balmer breaks, highest colour index and smallest [OII] equivalent widths. This is the opposite with the exception in the Balmer break which peaks (by definition) for the middle bin, of the galaxies with the highest SSFR.

The results from the studies of the spectral feature evolution with respect to stellar-mass, M_K and SSFR are consistent with the idea of downsizing. The most massive systems (bright absolute K-band magnitude) are already established and are passively evolving systems at high redshift while the lower mass systems are still forming stars.

7.3.4 Feature Evolution as a Function of Galaxy Spectral Type

The evolution of spectral features as a function of galaxy spectral type can seen in Figure 7.15. Again the layout is as in Figure 7.12 and the colour coding is as in Figure 7.11.

Since these composites were constructed on criteria based on these features the plot is as expected. The early-type galaxies show strong D4000 breaks, a red rest-frame UV

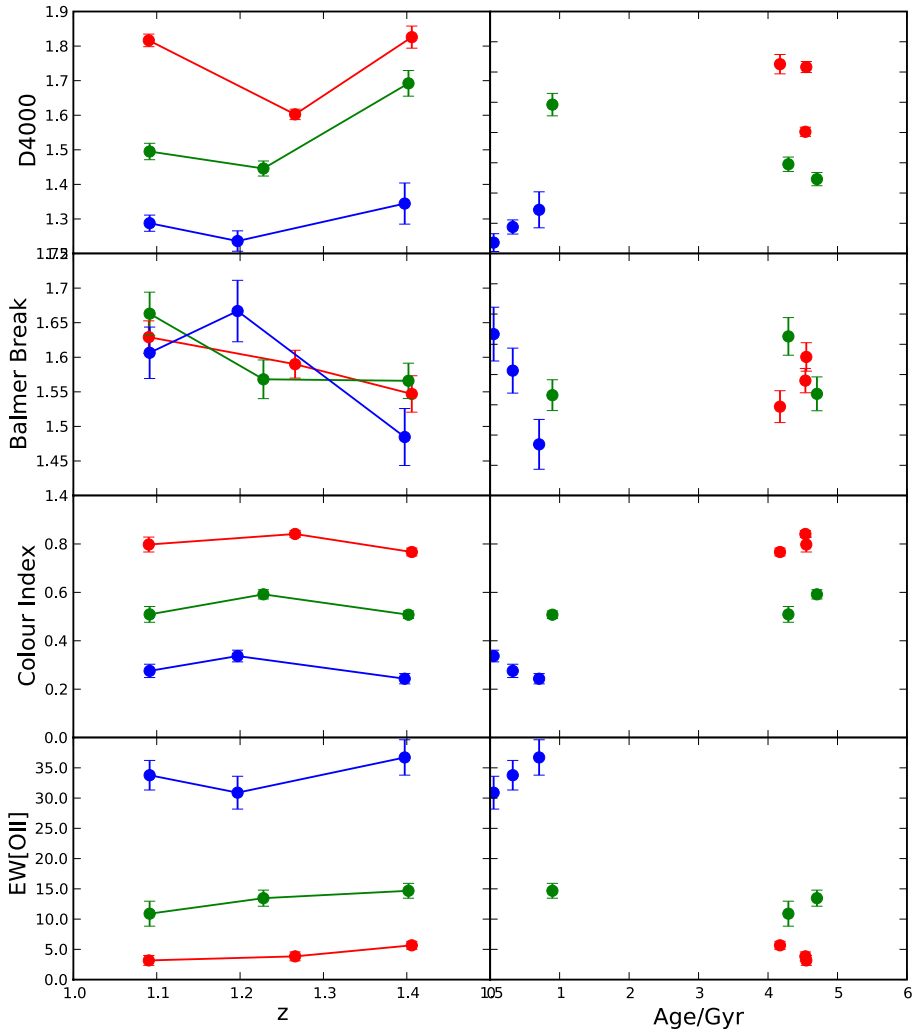

Figure 7.13: The evolution of spectral features as a function of redshift and age with respect to absolute K-band magnitude. The layout is as in Figure 7.12 and the colour coding is as in Figure 7.9.

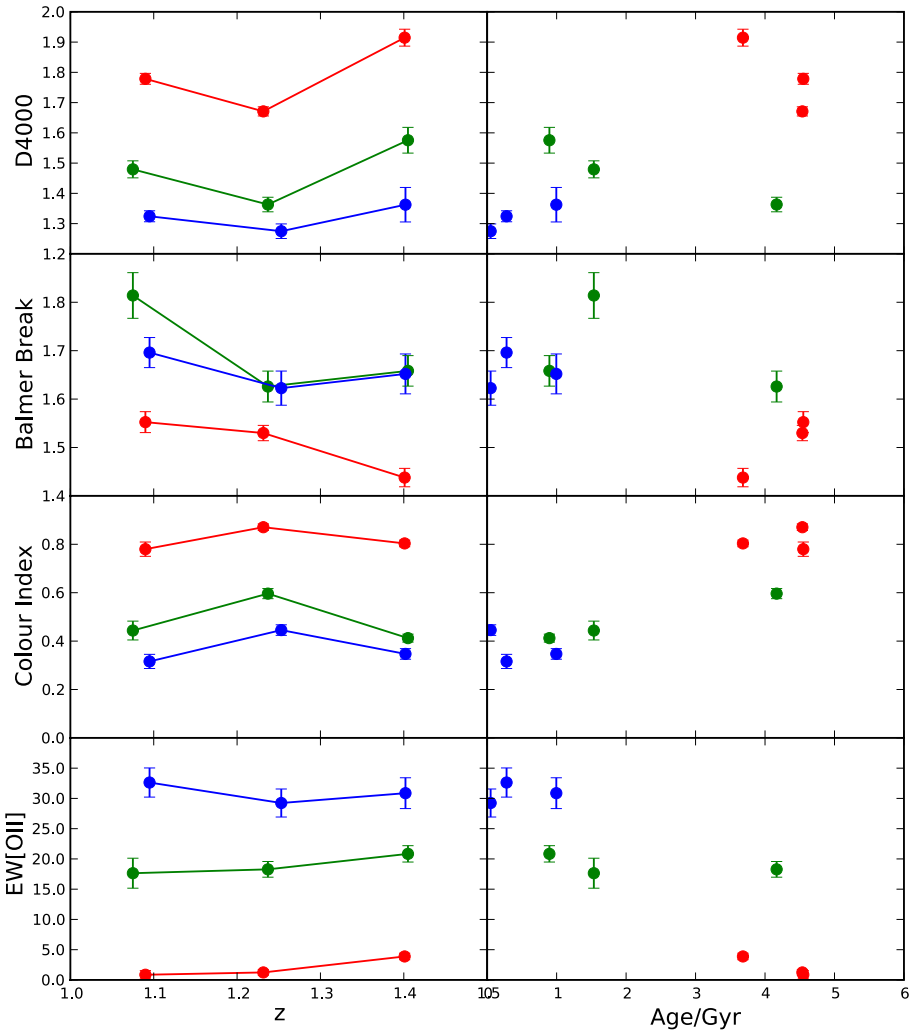

Figure 7.14: The evolution of spectral features as a function of redshift and age with respect to SSFR. The layout is as in Figure 7.12 The colour coding is as in Figure 7.10.

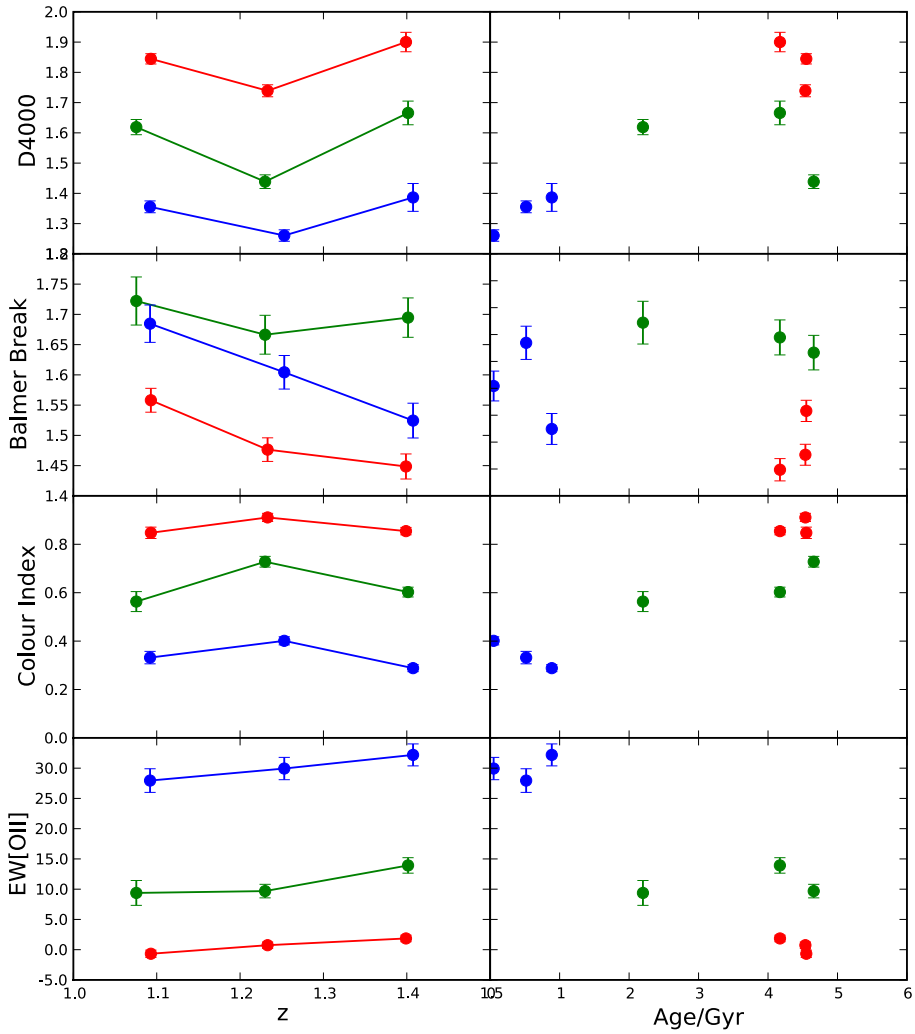

Figure 7.15: The evolution of spectral features as a function of redshift and age with respect to galaxy spectral type. The layout is as in Figure 7.12 The colour coding is as in Figure 7.11.

spectrum and low [OII] equivalent width. While the opposite is true for the late-type and high balmer break galaxies are dominated by intermediate-types.

Comparing these plots to those with respect to stellar-mass, M_K and SSFR early-type galaxies tend to be massive, bright in rest-frame K-band and in general passively evolving. Late-type galaxies appear to be still be undergoing significant star-formation and mass assembly.

7.4 Passive vs. Star-forming Galaxies

Based on the definition described in Section 5.8 the entire spectroscopic galaxy sample was split into passive and star-forming galaxies. The composite spectra for the star-forming and passive sub-samples averaged over the entire redshift space can be seen in the top and bottom panels of Figure 7.16 respectively. It can be noticed that the passive composite spectrum contains [OII] 3727 in emission which indicates that if galaxies contain enough mass they can still be classified as passive even with on-going star-formation. The presence of a small equivalent width MgII feature could indicate the presence of AGN.

7.4.1 The Ages of Composite Spectra based on Specific Star-formation Rate

The ages of the the passive and star-forming composite spectra as a function of redshift can be seen in Figure 7.17, with the blue and red lines representing the star-forming and passive composite spectra respectively. As expected, the passive systems are older than the star-forming at all redshifts. The star-forming systems have ages $\lesssim 25\%$ the age of the Universe at all redshifts whereas the quiescent systems have ages $> 75\%$ the age of the Universe for all redshifts.

7.4.2 Feature Evolution as a Function of Passivity

The evolution of spectral features for the passive (red lines) and star-forming (blue lines) composite spectra can be seen in Figure 7.18. The passive composite spectra are old systems with large D4000 breaks, red UV spectra and weak [OII] emission whereas the

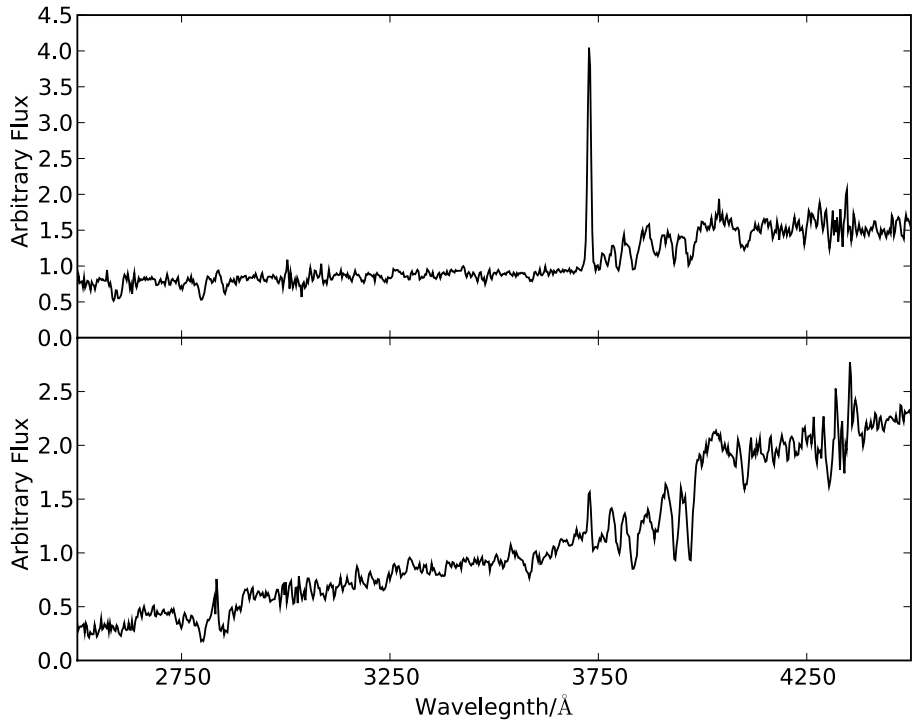

Figure 7.16: The composite spectra for the star-forming (top panel) and passive (bottom panel) composite spectra averaged over the entire redshift space.

star-forming composite spectra have strong [OII] emission, a weak D4000 break and a bluer rest-frame UV slope. The Balmer break is substantially stronger in star-forming galaxies than passive galaxies at every redshift. This is explained by the median age of the star-forming galaxies being ~ 1 Gyr compared to ~ 4.75 Gyrs fior the much older passive systems.

7.4.3 High-redshift Passive Galaxies

The passive stack from the high redshift bin covers a similar redshift range to that of the GMASS passive galaxy stack from Cimatti et al. [2008]. The GMASS passive stack was made of 13 passive objects in the redshift range $1.39 < z < 1.99$ with an average redshift of $z = 1.6$. The high-redshift passive composite from the UDSz contains 19 galaxies in the redshift range $1.477 < z < 1.830$ with an average redshift of 1.59 ± 0.1.

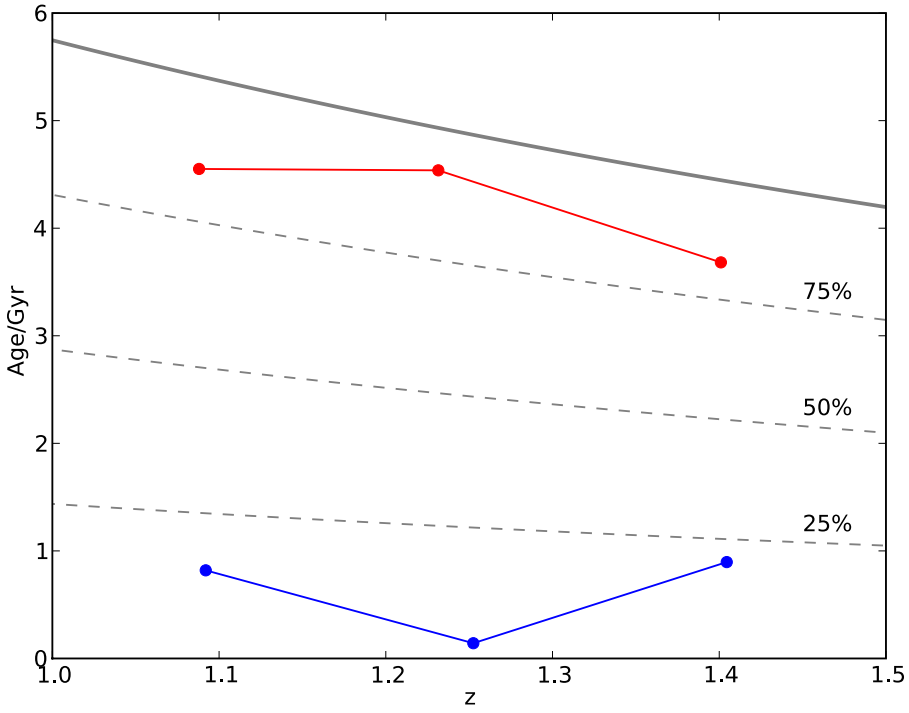

Figure 7.17: The ages of the the passive and star-forming composite spectra as a function of redshift with the blue and red lines representing the star-forming and passive composite spectra respectively The grey lines are as in Figure 7.7.

The rest-frame UV spectra of the GMASS spectrum along with the composite created here can be seen in Figure 7.19. The upper spectrum (black) is the high-redshift passive stack from the sample studies here and the lower spectrum (grey) is the GMASS passive stack (the spectra are offset for presentation purposes). Having 50% more objects has given the UDSz high-z passive composite higher signal-to-noise particularly at the red end of the UV spectrum with the H10 Balmer line and CN absorption visible as the red end. The two spectra have very similar feature measurements. For a full comparison of the spectral feature measurements for these two interesting composite spectra see Table 7.4. The Mg_{UV} [Daddi et al., 2005b] is designed to measure the extent of absorption due to Mg and Fe in the region $\sim 2600 - 2900$Åand is defined as,

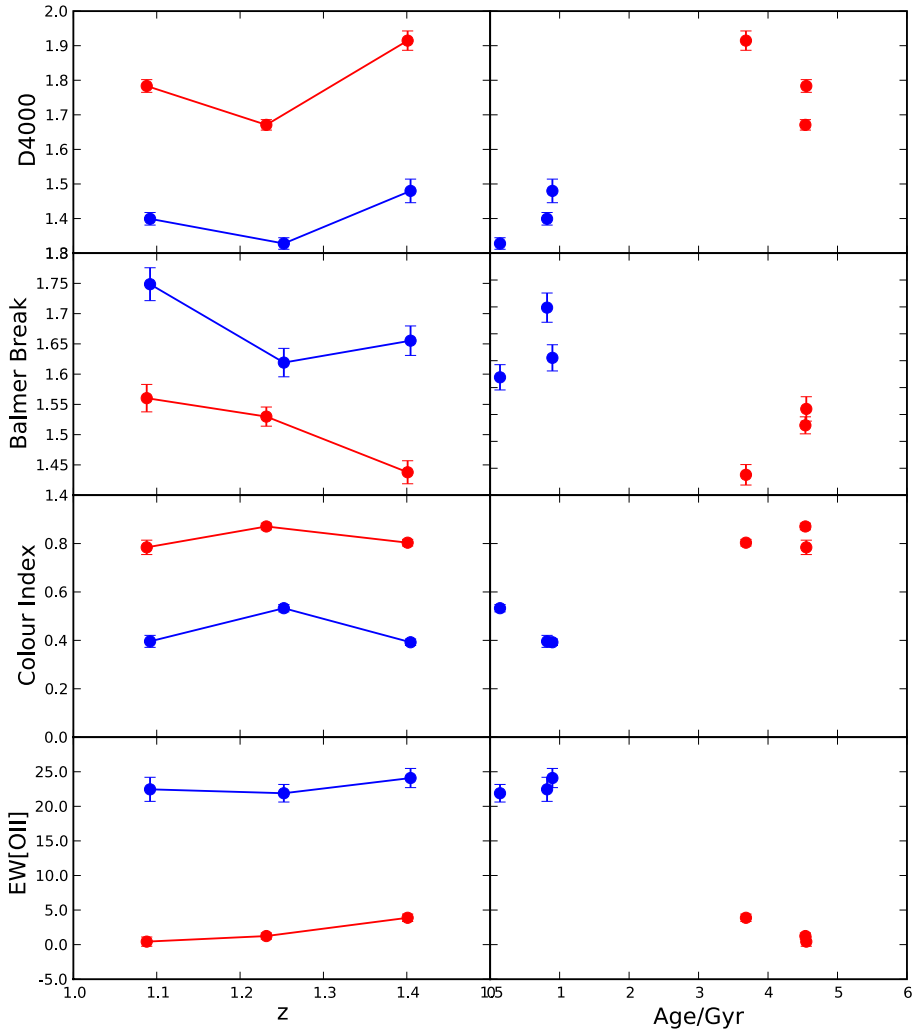

Figure 7.18: The evolution of spectral features for the passive (red lines) and star-forming (blue lines) composite spectra. The layout is as in Figure 7.12.

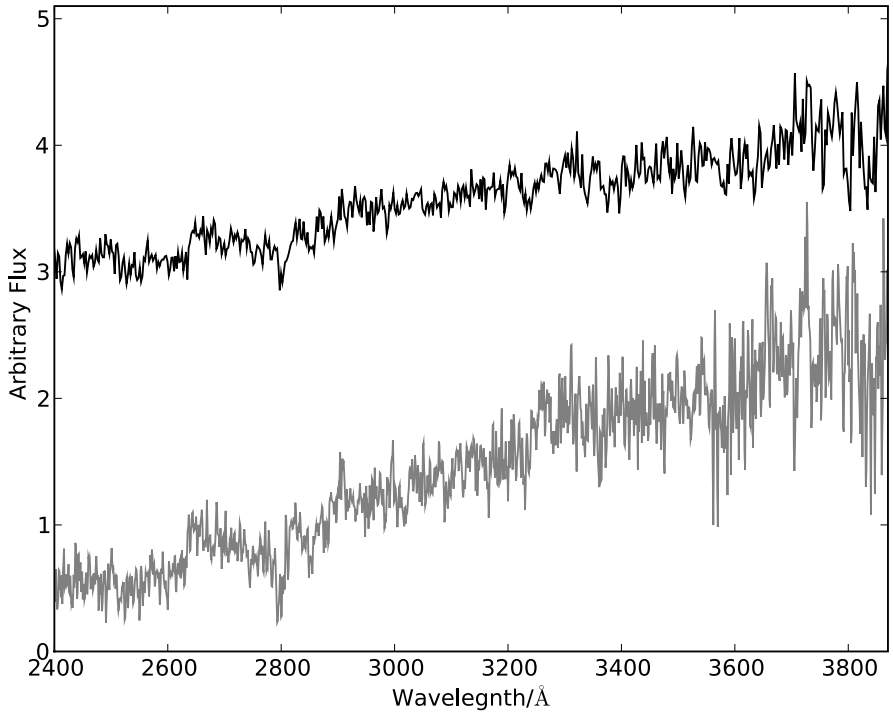

Figure 7.19: The lower spectrum (black) is the high-redshift passive stack from the sample studies here and the upper spectrum (grey) is the GMASS passive stack from Cimatti et al. [2008]. The spectra are offset for presentation purposes.

$$\mathrm{Mg}_{UV} = \frac{2\int_{2725}^{2625} f_\lambda d\lambda}{\int_{2625}^{2525} f_\lambda d\lambda + \int_{2725}^{2625} f_\lambda d\lambda}, \tag{7.3}$$

and the B(2640) and B(2900) [Spinrad et al., 1997] are breaks in the rest-frame continuum in the same region as the Mg_{UV} feature. These breaks are defined as,

$$B(2640) = \frac{F_\lambda(2645-2675)}{F_\lambda(2600-2630)} B(2900) = \frac{F_\lambda(2915-2945)}{F_\lambda(2855-2885)} \tag{7.4}$$

Through fitting stellar population models to the spectra alone the GMASS team recovered an age of ~ 1 Gyrs with an average reddening of $A_v = 0.3$. The UDSz high redshift passive stack was fitted to the TCM models with and without the inclusion of

Table 7.4: Comparison of the Spectral Features in the high redshift passive composite spectra from the GMASS and UDSz surveys.

Feature	UDSz	GMASS
Mg_{UV}	1.28 ± 0.04	1.40
Balmer Break	1.62 ± 0.05	-
UV Colour Index	0.60 ± 0.02	0.81
EW[OII]	2.15 ± 1.75	2.61
B(2640)	1.62 ± 0.17	1.53
B(2900)	1.35 ± 0.09	1.27

the composite photometry. The fit to the composite spectra alone recovered a mass-weighted age of 0.55 Gyrs reddening by an $A_v = 0.8$. These results are similar but the UDSz stack chose a slightly younger and more heavily reddened model. The UDSz composite was also fitted with the models with the inclusion of the composite photometry. This recovers a mass-weighted age of 1 Gyr with a reddening $A_v = 0.1$. These fits can be seen on Figure 7.20. The top panel shows the fits to just the composite spectra (orange) and composite plus composite photometry (grey). The black lines are the composite spectra and red points are the composite photometry. The middle panel shows the model fit through the spectra for the model fit to the composite spectra plus composite photometry and the lower panel shows the model fit just to the composite spectra.

It can be seen that the fit to the spectra alone misses all the composite photometry indicating that photometry shortward and longward of the optical spectra is very important when making age estimates of stellar populations

7.5 Summary and Conclusions

Composite spectra have been produced as a function of redshift as well as a stellar-mass, absolute K-band magnitude, SSFR and spectral type. Investigating the composite as a function of age has produced an incredibly clean results that massive, bright in K-band, passively evolving ETGs are always the oldest population and nearly always trace the

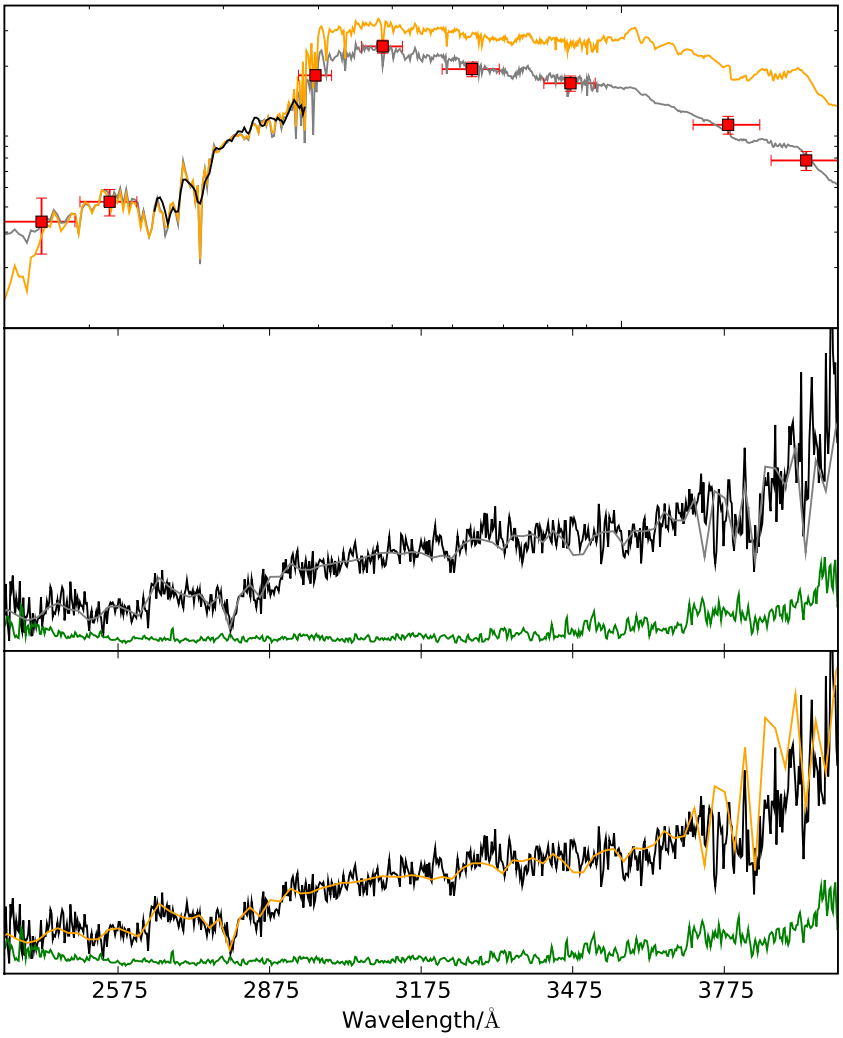

Figure 7.20: Model fits to the high-redshift passive composite spectra. The top panel shows the fits to just the composite spectra (orange) and composite plus composite photometry (grey). The black lines are the composite spectra and red points are the composite photometry. The middle panel shows the model fit through the spectra for the model fit to the composite spectra plus composite photometry and the lower panel shows the model fit just to the composite spectra.

age of the Universe. The late-type, low-mass, star-forming galaxies are always found to be much younger system. This is strong evidence for downsizing.

The evolution of spectral features was investigated as a function of age and redshift. These were as expected with the massive, passive ETGs containing strong 4000Å breaks, a red UV continuum and weak [OII] and the opposite was observed for late-type low-mass star-forming galaxies.

Fitting the high-redshift passive composite to models with just the composite spectra and the composite spectra plus the composite photometry has highlighted the importance of photometry short and longward of the optical spectra when acquiring accurate age estimates.

Chapter 8

Summary and Conclusions

The work in this thesis in based on the data from part of a ESO Large Programme (UDSz) to perform spectroscopic follow up of K-band selected galaxies in the UDS field. The primary motivation for the project was to study stellar-mass assembly as a function of lookback time and investigate the relation between environment and galaxy properties at $z > 1$. Target selection was made from a K-band limited ($K < 23$) and photometric redshift constrained ($z_{photo} > 1$) sample. The targets were split between VIMOS and FORS2, with the FORS2 sample observing the redder (V>24.5) objects due to its increased red sensitivity. The work throughout this thesis was solely based on the FORS2 sample.

Due to the faintness of the objects targeted by FORS2 the reduction achieved with the VLT's own pipeline was far below an acceptable standard for scientific analysis to be performed on the spectra. The optimisation of the pipeline for the reduction of the sources in the FORS2 sample of the UDSz project was a large part of the work done throughout this thesis. A thorough explanation of the issues encountered and the resolutions are presented in Chapter 3.

Here the initial goals laid out in the introduction will be addressed along with highlighting the important results discovered throughout the analysis of the FORS2 spectra.

8.1 The Size-Mass Relation at High Redshift

Using the deep spectra obtained from the VLT and the multi-wavelength data available within the UDS of a sample of K-band bright ($K < 21.5$) and high redshift ($1.3 \lesssim< z <\lesssim 1.5$) galaxies, spectrophotometric fits were performed with stellar synthesis models from CB07, which include the affects of TP-AGB stars, with a wide range of star-formation histories. The fits provided accurate stellar-mass estimates which, along with radii estimated from the deep K-band data available in the UDS, allowed a detailed investigation of the size-mass relation at $1.3 < z < 1.5$. Comparing the results to local size-mass relation found a differential trend with stellar-mass (Figure 5.9). The lower mass systems sit on the local relation whereas the systems with large mass tend to sit below the relation that is seen locally.

This result is reasonably robust since the mass estimate have been made using a Chabrier IMF and the use of a Salpeter IMF would increase the stellar masses by a factor of ~ 2. The models here account for the possible effects of TP-AGB stars which when removed would also increase the stellar-mass. Since the radii have been estimated from low resolution ground based imaging if anything they could be overestimates. All these potential sources of errors do therefore not change the results that it appears high-redshift massive systems sit below the local size-mass relation.

Following the work of Saracco et al. [2009] the sample was split into young and old galaxies in relation to whether they were older or younger than 50% of the age of the Universe. The young systems span the local size-mass relation as opposed to the older systems which sit, on average, a factor ~ 1.5 below the relation (Figure 5.11). A very similar result was found when the sample was split by passivity, with the more passive objects sitting below the relation, and spectral type, with ETGs also consistently sitting below the relation (Figure 5.12).

Velocity dispersions were estimated for the largest single sample of ETGs at $z > 1.3$. The method used to calculate the velocity dispersion used the controversial Ca H & K features but through thorough tests using a large sample of SDSS spectra it was shown that the method could reproduce the estimates made by the SDSS team. The velocity dispersions estimated here were used to calculate the dynamical masses as these are model independent mass estimates and therefore a solid test for the high-redshift size-

mass relation. Comparing the resulting dynamical masses to ones acquired from velocity dispersions estimates from the SDSS it is shown (Figure 5.15) that all 13 objects sit towards or below the lower edge of the local size-dynamical mass relation indicating that these objects really are compact.

The results from the dynamical masses along with the potential errors in the stellar-mass size relation discussed above indicate that at high redshift, massive, passive galaxies do sit below the local size-mass relation. This is in agreement with many other authors [e.g. Trujillo et al. 2006a, Trujillo et al. 2006b, Trujillo et al. 2007, Longhetti et al. 2007, McGrath et al. 2008, Buitrago et al. 2008] and leads to two potential scenarios.

One option is that size evolution of the massive systems at high-redshift is required to join the local size-mass relation. There are several theories to explain this evolution which include the redistribution of stellar-mass due to mass ejection from quasar feedback [Fan et al., 2008], the dry merger hypothesis where dense cores are created at high-redshift through a gas rich merger and then dry mergers between then and the present increase the effective radii [Khochfar and Silk, 2006] and also size-evolution has been considered as a result of the accretion of mass via minor mergers [Naab et al., 2009].

Another option is that compact galaxies are present in the local Universe and that normal sized galaxies are present at high-redshift but, due to selection effects, both populations have been missed. Recently Taylor et al. [2010] went is search of compact galaxies in the local Universe. It was shown, especially at low redshift $z \leq 0.05$, that SDSS selection effects would miss bright and compact objects to avoid saturation and cross-talk in the spectrograph. Taylor et al. [2010] found 63 galaxies to sit a factor of 2 or more below the local relation from Shen et al. [2003] and have higher than average velocity dispersions. Moreover, Mancini et al. [2010] found that 9 of the K-band brightest and most massive objects from the COSMOS field at $z \geq 1.4$ sat on the local size-mass relation. This idea proposes that no size evolution is required between high-redshift and the present day and that complete samples at low- and high-redshift have not yet been acquired.

8.2 The Passive Fraction of the High-Redshift K Bright Universe

Using the same sample for which the size-mass relation was studied ($K < 21.5$ and $1.3 \lesssim z <\lesssim 1.5$) specific star-formation rates were measured using the rest-frame UV, the [OII] emission line and $24\mu m$ data. With these SSFRs the passive fraction for the K-band bright Universe was estimated at $58 \pm 10\%$. This is consistent with several other studies in the literature such as Cimatti et al. [2002a] and Miyazaki et al. [2003]. Most of the studies in the literature have been of a purely ERO sample as opposed to simply a cut in K-band magnitude. The consistency of the result here is unsurprising as $\sim 75\%$ of the sample are EROs. When cutting the sample at $K < 20.65$ to get a pure ERO sample the passive galaxy fraction is very high ($75 \pm 19\%$) even though it is a pure ERO sample the K-band cut is brighter than in the literature. Therefore it only contains the brightest and most massive galaxies and it is therefore showing more evidence of downsizing, with the more massive sub-sample containing a higher passive fraction.

Passive fractions were estimated for a fainter ERO sample ($K < 21.5$, $R-K < 3.38$) and high mass sample ($M_\star > 7 \times 10^{10} M_\odot$). The passive fraction for these sample were estimated at $78 \pm 33\%$ and $80 \pm 19\%$ respectively. The large errors put the ERO passive fraction in agreement with other studies. Compared to Fontana et al. [2009] the passive fraction of the high-mass sample is large but the $K < 21.5$ sample is only mass complete down to $\sim 1 \times 10^{11}$ which could be a source for the difference and cosmic variance could also play a role in the difference of these results.

8.3 Optimisation of Photometric Galaxy Population Selection Techniques

The BzK [Daddi et al., 2004a], $(J-K)$ v $(i-K)$ [Pozzetti and Mannucci, 2000] and $(V-J)$ vs $(U-V)_{\text{Rest-frame}}$ [Williams et al., 2009] diagrams for selecting passive galaxies at high redshift were analysed with the UDSz FORS2 spectroscopic sample, all of which had known passivity. All of these techniques were found to be far from optimal. Using

the UDSz FORS2 sample the population dividers within these diagram were optimised for $K < 21$, 22 and 23 samples. The formulae for these can be found in Equations 6.1, 6.2 and 6.3 for the BzK diagram, Equations 6.4, 6.5 and 6.6 for the $(J-K)$ vs $(i-K)$ diagram and Equations 6.7, 6.8 and 6.9 for the $(V-J)$ vs $(U-V)_{\text{Rest-frame}}$ diagram.

Using the devised optimal selection techniques, passive galaxy fractions in the high-redshift Universe have been estimated for K-band selected and ERO selected samples. From the BzK diagram the passive fraction of K-band selected targets was estimated at 54%, 35% and 18% for $K < 21$, 22 and 23 samples. The passive fraction for the $K < 21$ sample is consistent with our results from Section 5.8 for the $K < 21.5$, $1.3 < z < 1.5$ Universe. Even though there was also criteria on V, i and z for the spectroscopic sample, this is expected since $K < 21.5$ galaxies are bright and therefore will tend to be old red objects so would not be effected by this additional criterion.

The passive fractions of K-band selected objects estimated from the $(V-J)$ vs $(U-V)_{\text{Rest-frame}}$ diagram are consistent with that found with the BzK at 27% and 15% for the $K < 22$ and 23 samples. For the $K < 21$ sample the passive fraction is approximately a factor of 1.5 below that found with the BzK at 38%. However this value is within the range of values found by Cimatti et al. [2002a] and Smail et al. [2002] and is consistent with the theoretical prediction from Fontanot and Monaco [2010].

The ratio of passive to star-forming EROs was found with the optimised $(J-K)$ vs $(i-K)$ diagram to be 64%, 57% and 53% for the $K < 21$, 22 and 23 samples respectively. The passive fraction found with the optimised BzK technique for the $K < 21.0$ is in good agreement with the estimations found here for bright EROs. This is expected as $\sim 70\%$ of the $K < 21$ galaxies are EROs (see Figure 6.14). The results for the $K < 22$ and 23 samples are consistent with all the observational results mention in Section 5.8.1.

8.4 Galaxy Population Division with New Telescopes

Visible and Infrared Survey Telescope for Astronomy (VISTA) is the next generation of NIR wide-field survey telescope. Therefore it would be beneficial to see how the above selection techniques worked with the filters from the VISTA telescope. The best-fitting spectral energy distribution models found using the method described in Chapter 4 for

the spectroscopic targets were used, along with the filters from the VISTA telescope, to calculate expected magnitudes.

A new generation of NIR survey to use the VISTA telescope which is currently ongoing is the VISTA Deep Extragalactic Observations (VIDEO) survey. This survey so far has NIR data from VISTA and optical data from the CFHT. BzK and $(J - K)$ vs $(i - K)$ diagrams have been developed for the filters used in this survey.

A gzK_s and gZK_s diagram have been developed based on the g- and z-bands from CFHT and the Z- and K_s-bands from VISTA and a $(J - K_s)$ vs $(i - K_s)$ diagram has also been developed with the i-band from CFHT and J- and K_s-bands from the VISTA telescope.

As a test for the passive fraction of a purely K-band selected sample the passive fraction have been estimated for the VIDEO D1 catalog. This gives an independent test for the fractions determined with the standard BzK, $(J - K)$ v $(i - K)$ and $(V - J)$ vs $(U - V)_{\text{Rest-frame}}$ diagrams in the UDS. The passive fractions found with the gzK_s diagram and VIDEO D1 catalog are 71%, 31% and 20% for the $K_s < 21$, 22 and 23 samples respectively. Which, within the errors, are in agreement with the results from the optimised BzK diagram.

8.5 Investigating Galaxy Population with Composite Spectra

Composite spectra have been produced as a function of redshift as well as stellar-mass, absolute K-band magnitude, SSFR and spectral type. Investigating these composite spectra as a function of age has produced an incredibly clean result that massive, bright in K-band, passively evolving ETGs are always the oldest population and nearly always trace the age of the Universe. The late-type, low-mass, star-forming galaxies are always found to be much younger systems. This is strong evidence for downsizing, with the most massive systems finishing their mass assembly before their lower mass counterparts

The evolution of spectral features was investigated as a function of age and redshift. These were as expected with the massive, passive ETGs containing strong 4000Å breaks, a red UV continuum and weak [OII] and the opposite being true for late-type low-mass

star-forming galaxies.

The results throughout this thesis reiterate the conclusion that massive ETGs finish their buildup of stellar-mass before their lower mass counterparts i.e. the idea of downsizing. Evidence for this is shown through the study of massive galaxies in the redshift range $1.3 < z < 1.5$ (Chapter 5) where the most massive ($> 10^{11}\mathrm{M}_{\odot}$) systems are the oldest and passively evolving systems which are tracing the age of the Universe at all redshifts. It is found that approximately half of these massive systems have already entered a stage of passive evolution by $z \sim 1.5$, only ~ 4 Gyrs after the Big Bang. The study of high redshift galaxy populations in Chapter 6 also provides evidence for this concept with the passive fraction of galaxies increasing with K-band brightness, which can be seen as a proxy for stellar-mass. Mass-assembly downsizing if seen throughout study of high-redshift composite spectra (Chapter 7) with the massive (bright in absolute K-band magnitude) systems having the lowest SSFRs and being the oldest populations at all redshifts. Due to the idea of downsizing being found in all the studies done here and consistent cleanliness of the result found through the study of the composites all contribute towards the robustness of the result.

With the understanding of the galaxy size-mass evolution from high redshift to the present day being a current hot topic in observational and theoretical astronomy solid evidence is provided here to help with this current field of interest. Due to the potential errors in the stellar mass estimates a method was developed to determine the stellar velocity dispersion of a galaxy from its Ca H & K absorption features to then be used in conjunction with the radius to provide a model independent estimate of the mass within a galaxy. Providing the largest single sample of velocity dispersions of high-redshift targets we confirm that massive ETGs at high redshift are more compact than their local mass counterparts. But, as described above, until more complete samples of the low- and high-redshift Universe are available the need for size evolution in these systems still remains uncertain. The latest semi-analytical studies are now finding agreement with the results indicating that of size evolution from high redshift to the present Universe is required. Using a simple merger model that includes gas dissipation and star formation Covington et al. [2011] finds a steeping of the size-mass relation as a function of redshift with the low mass systems sitting on the local relation at all

redshifts but the more massive being sat below the relation at high redshift and moving on to it with decreasing redshift.

Appendix A

Reduction Input Files

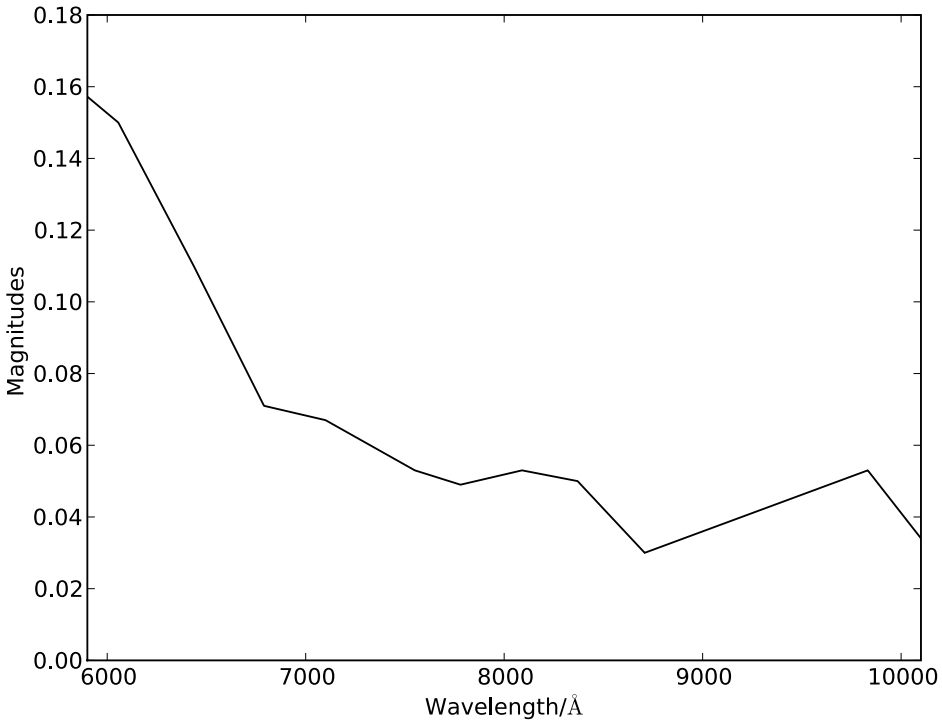

Figure A.1: The atmosphere extinction file used in the extraction of 1D spectra.

Table A.1: Example of standard star calibration table used by the *standard* package in IRAF.

Wavelength	Magnitude(AB)	Band Width
5556.0	11.48	80.0
5700.0	11.44	80.0
5840.0	11.41	80.0
5950.0	11.41	80.0
6056.0	11.38	80.0
6180.0	11.35	80.0
6310.0	11.34	80.0
6436.0	11.3	80.0
6640.0	11.26	80.0
6790.0	11.26	80.0
7100.0	11.23	80.0
7250.0	11.23	80.0
7400.0	11.22	80.0
7550.0	11.2	80.0
7780.0	11.16	80.0
7890.0	11.16	80.0
7990.0	11.15	80.0
8090.0	11.13	80.0
8370.0	11.13	80.0
8708.0	11.08	80.0
9832.0	11.05	80.0
10256.0	11.08	80.0
10400.0	11.13	80.0

Table A.2: Example of output file from the *standard* package in IRAF.

[std.fits] 1 1717 1.00 1.029 5501.600 10992.800			
5556.0	9.1442e-14	80.0	35.412
5700.0	9.014e-14	80.0	34.945
5840.0	8.8276e-14	80.0	1039.2
5950.0	8.5042e-14	80.0	42878.0
6056.0	8.4391e-14	80.0	114556.0
6180.0	8.3309e-14	80.0	154156.0
6310.0	8.0651e-14	80.0	172370.0
6436.0	8.0433e-14	80.0	187546.0
6640.0	7.8403e-14	80.0	205753.0
6790.0	7.4977e-14	80.0	217585.0
7100.0	7.0494e-14	80.0	231778.0
7400.0	6.5495e-14	80.0	232953.0
7550.0	6.4088e-14	80.0	230261.0
7780.0	6.2619e-14	80.0	224985.0
7890.0	6.0886e-14	80.0	218779.0
7990.0	5.992e-14	80.0	211547.0
8370.0	5.5618e-14	80.0	190261.0
8708.0	5.3806e-14	80.0	169602.0
9832.0	4.339e-14	80.0	51525.0
10256.0	3.8789e-14	80.0	11575.0
10400.0	3.6025e-14	80.0	4468.6

References

R. G. Abraham, K. Glazebrook, P. J. McCarthy, D. Crampton, R. Murowinski, I. Jørgensen, K. Roth, I. M. Hook, and et al. The Gemini Deep Deep Survey. I. Introduction to the Survey, Catalogs, and Composite Spectra. *AJ*, 127:2455–2483, May 2004.

R. G. Abraham, P. Nair, P. J. McCarthy, K. Glazebrook, E. Mentuch, H. Yan, S. Savaglio, D. Crampton, R. Murowinski, S. Juneau, D. Le Borgne, R. G. Carlberg, I. Jørgensen, K. Roth, H. Chen, and R. O. Marzke. The Gemini Deep Deep Survey. VIII. When Did Early-Type Galaxies Form? ApJ, 669:184–201, Nov. 2007.

D. M. Alexander, F. E. Bauer, W. N. Brandt, D. P. Schneider, A. E. Hornschemeier, C. Vignali, A. J. Barger, P. S. Broos, L. L. Cowie, G. P. Garmire, L. K. Townsley, M. W. Bautz, G. Chartas, and W. L. W. Sargent. The Chandra Deep Field North Survey. XIII. 2 Ms Point-Source Catalogs. AJ, 126:539–574, Aug. 2003.

C. M. Baugh. A primer on hierarchical galaxy formation: the semi-analytical approach. *Reports on Progress in Physics*, 69:3101–3156, Dec. 2006.

N. Bavouzet, H. Dole, E. Le Floc'h, K. I. Caputi, G. Lagache, and C. S. Kochanek. Estimating the total infrared luminosity of galaxies up to z $\sim$ 2 from mid- and far-infrared observations. A&A, 479:83–96, Feb. 2008.

M. Bernardi. The σ-L Correlation in Nearby Early-Type Galaxies. AJ, 133:1954–1961, May 2007.

E. Bertin and S. Arnouts. SExtractor: Software for source extraction. A&AS, 117: 393–404, June 1996.

P. Bizenberger, M. J. McCaughrean, C. Birk, D. Thompson, and C. Storz. Omega Prime: the wide-field near-infrared camera for the 3.5-m telescope of the Calar Alto Observatory. In A. M. Fowler, editor, *Society of Photo-Optical Instrumentation Engineers (SPIE) Conference Series*, volume 3354 of *Presented at the Society of Photo-Optical Instrumentation Engineers (SPIE) Conference*, pages 825–832, Aug. 1998.

A. W. Blain, I. Smail, R. J. Ivison, J. Kneib, and D. T. Frayer. Submillimeter galaxies. Phys. Rep., 369:111–176, Oct. 2002.

M. Bolzonella, J. Miralles, and R. Pelló. Photometric redshifts based on standard SED fitting procedures. A&A, 363:476–492, Nov. 2000.

R. G. Bower. The evolution of groups of galaxies in the Press-Schechter formalism. MNRAS, 248:332–352, Jan. 1991.

J. Brinchmann, S. Charlot, S. D. M. White, C. Tremonti, G. Kauffmann, T. Heckman, and J. Brinkmann. The physical properties of star-forming galaxies in the low-redshift Universe. *MNRAS*, 351:1151–1179, July 2004.

G. Bruzual. Spectral evolution of galaxies. I - Early-type systems. ApJ, 273:105–127, Oct. 1983.

G. Bruzual and S. Charlot. Spectral evolution of stellar populations using isochrone synthesis. ApJ, 405:538–553, Mar. 1993.

G. Bruzual and S. Charlot. Stellar population synthesis at the resolution of 2003. MNRAS, 344:1000–1028, Oct. 2003.

F. Buitrago, I. Trujillo, and C. J. Conselice. Extremely Compact Massive Galaxies at $1.7 < z < 3$. *ArXiv e-prints*, Nov. 2008.

D. Calzetti, L. Armus, R. C. Bohlin, A. L. Kinney, J. Koornneef, and T. Storchi-Bergmann. The Dust Content and Opacity of Actively Star-forming Galaxies. *ApJ*, 533:682–695, Apr. 2000.

M. Cappellari, S. di Serego Alighieri, A. Cimatti, E. Daddi, A. Renzini, J. D. Kurk, P. Cassata, M. Dickinson, and et al. Dynamical Masses of Early-Type Galaxies at z ˜ 2: Are they Truly Superdense? *ApJL*, 704:L34–L39, Oct. 2009.

K. I. Caputi, J. S. Dunlop, R. J. McLure, and N. D. Roche. A deeper view of extremely red galaxies: the redshift distribution in the GOODS/CDFS ISAAC field. MNRAS, 353:30–42, Sept. 2004.

D. Carter, D. J. B. Smith, S. M. Percival, I. K. Baldry, C. A. Collins, P. A. James, M. Salaris, C. Simpson, J. P. Stott, and B. Mobasher. Optical and near-infrared colours as a discriminant of the age and metallicity of stellar populations. MNRAS, 397:695–708, Aug. 2009.

M. Casali, A. Adamson, C. Alves de Oliveira, O. Almaini, K. Burch, T. Chuter, J. Elliot, M. Folger, and et al. The UKIRT wide-field camera. A&A, 467:777–784, May 2007.

P. Cassata, A. Cimatti, A. Franceschini, E. Daddi, E. Pignatelli, G. Fasano, G. Rodighiero, L. Pozzetti, M. Mignoli, and A. Renzini. The evolution of the galaxy B-band rest-frame morphology to z˜ 2: new clues from the K20/GOODS sample. MNRAS, 357:903–917, Mar. 2005.

P. Cassata, A. Cimatti, J. Kurk, G. Rodighiero, L. Pozzetti, M. Bolzonella, E. Daddi, M. Mignoli, S. Berta, M. Dickinson, A. Franceschini, C. Halliday, A. Renzini, P. Rosati, and G. Zamorani. GMASS ultradeep spectroscopy of galaxies at $z \sim 2$. III. The emergence of the color bimodality at $z \sim 2$. A&A, 483:L39–L42, June 2008.

G. Chabrier. Galactic Stellar and Substellar Initial Mass Function. PASP, 115: 763–795, July 2003.

A. Cimatti, S. Bianchi, A. Ferrara, and C. Giovanardi. On the dust extinction in high-z galaxies and the case of extremely red objects. MNRAS, 290:L43–L49, Sept. 1997.

A. Cimatti, P. Andreani, H. Röttgering, and R. Tilanus. Vigorous star formation hidden by dust in a galaxy at a redshift of 1.4. Nature, 392:895–897, Apr. 1998.

A. Cimatti, E. Daddi, M. Mignoli, L. Pozzetti, A. Renzini, G. Zamorani, T. Broadhurst, A. Fontana, P. Saracco, F. Poli, S. Cristiani, S. D'Odorico, E. Giallongo, R. Gilmozzi, and N. Menci. The K20 survey. I. Disentangling old and dusty star-forming galaxies in the ERO population. A&A, 381:L68–L72, Jan. 2002a.

A. Cimatti, L. Pozzetti, M. Mignoli, E. Daddi, N. Menci, F. Poli, A. Fontana, A. Renzini, G. Zamorani, T. Broadhurst, S. Cristiani, S. D'Odorico, E. Giallongo, and R. Gilmozzi. The K20 survey. IV. The redshift distribution of $K_s < 20$ galaxies: A test of galaxy formation models. A&A, 391:L1–L5, Aug. 2002b.

A. Cimatti, E. Daddi, M. Mignoli, L. Pozzetti, A. Fontana, T. Broadhurst, F. Poli, P. Saracco, and et al. The K20 survey: new light on galaxy formation and evolution. *The Messenger*, 111:29–35, Mar. 2003.

A. Cimatti, E. Daddi, A. Renzini, P. Cassata, E. Vanzella, L. Pozzetti, S. Cristiani, A. Fontana, and et al. Old galaxies in the young Universe. *Nat*, 430:184–187, July 2004.

A. Cimatti, P. Cassata, L. Pozzetti, J. Kurk, M. Mignoli, A. Renzini, E. Daddi, M. Bolzonella, and et al. GMASS ultradeep spectroscopy of galaxies at z 2. II. Superdense passive galaxies: how did they form and evolve? *AAP*, 482:21–42, Apr. 2008.

M. Cirasuolo, R. J. McLure, J. S. Dunlop, O. Almaini, S. Foucaud, and C. Simpson. A new measurement of the evolving near-infrared galaxy luminosity function out to z ˜= 4: a continuing challenge to theoretical models of galaxy formation. MNRAS, 401:1166–1176, Jan. 2010.

J. G. Cohen, R. Blandford, D. W. Hogg, M. A. Pahre, and P. L. Shopbell. Caltech Faint Galaxy Redshift Survey. VIII. Analysis of the Field J0053+1234. ApJ, 512: 30–47, Feb. 1999a.

J. G. Cohen, D. W. Hogg, M. A. Pahre, R. Blandford, P. L. Shopbell, and K. Richberg. Caltech Faint Galaxy Redshift Survey. VII. Data Analysis Techniques and Redshifts in the Field J0053+1234. ApJS, 120:171–178, Feb. 1999b.

S. Cole, A. Aragon-Salamanca, C. S. Frenk, J. F. Navarro, and S. E. Zepf. A Recipe for Galaxy Formation. MNRAS, 271:781–+, Dec. 1994.

S. Cole, C. G. Lacey, C. M. Baugh, and C. S. Frenk. Hierarchical galaxy formation. MNRAS, 319:168–204, Nov. 2000.

S. Cole, P. Norberg, C. M. Baugh, C. S. Frenk, J. Bland-Hawthorn, T. Bridges, R. Cannon, M. Colless, C. Collins, W. Couch, N. Cross, G. Dalton, R. De Propris,

S. P. Driver, G. Efstathiou, R. S. Ellis, K. Glazebrook, C. Jackson, O. Lahav, I. Lewis, S. Lumsden, S. Maddox, D. Madgwick, J. A. Peacock, B. A. Peterson, W. Sutherland, and K. Taylor. The 2dF galaxy redshift survey: near-infrared galaxy luminosity functions. MNRAS, 326:255–273, Sept. 2001.

S. Cole, W. J. Percival, J. A. Peacock, P. Norberg, C. M. Baugh, C. S. Frenk, I. Baldry, J. Bland-Hawthorn, T. Bridges, R. Cannon, M. Colless, C. Collins, W. Couch, N. J. G. Cross, G. Dalton, V. R. Eke, R. De Propris, S. P. Driver, G. Efstathiou, R. S. Ellis, K. Glazebrook, C. Jackson, A. Jenkins, O. Lahav, I. Lewis, S. Lumsden, S. Maddox, D. Madgwick, B. A. Peterson, W. Sutherland, and K. Taylor. The 2dF Galaxy Redshift Survey: power-spectrum analysis of the final data set and cosmological implications. MNRAS, 362:505–534, Sept. 2005.

A. J. Connolly, A. S. Szalay, M. Dickinson, M. U. Subbarao, and R. J. Brunner. The Evolution of the Global Star Formation History as Measured from the Hubble Deep Field. ApJ, 486:L11+, Sept. 1997.

K. Coppin, E. L. Chapin, A. M. J. Mortier, S. E. Scott, C. Borys, J. S. Dunlop, M. Halpern, D. H. Hughes, A. Pope, D. Scott, S. Serjeant, J. Wagg, D. M. Alexander, O. Almaini, I. Aretxaga, T. Babbedge, P. N. Best, A. Blain, S. Chapman, D. L. Clements, M. Crawford, L. Dunne, S. A. Eales, A. C. Edge, D. Farrah, E. Gaztañaga, W. K. Gear, G. L. Granato, T. R. Greve, M. Fox, R. J. Ivison, M. J. Jarvis, T. Jenness, C. Lacey, K. Lepage, R. G. Mann, G. Marsden, A. Martinez-Sansigre, S. Oliver, M. J. Page, J. A. Peacock, C. P. Pearson, W. J. Percival, R. S. Priddey, S. Rawlings, M. Rowan-Robinson, R. S. Savage, M. Seigar, K. Sekiguchi, L. Silva, C. Simpson, I. Smail, J. A. Stevens, T. Takagi, M. Vaccari, E. van Kampen, and C. J. Willott. The SCUBA Half-Degree Extragalactic Survey - II. Submillimetre maps, catalogue and number counts. MNRAS, 372:1621–1652, Nov. 2006.

M. D. Covington, J. R. Primack, L. A. Porter, D. J. Croton, R. S. Somerville, and A. Dekel. The role of dissipation in the scaling relations of cosmological merger remnants. MNRAS, pages 1029–+, July 2011.

L. L. Cowie, J. P. Gardner, S. J. Lilly, and I. McLean. A K band deep galaxy survey. ApJ, 360:L1–L5, Sept. 1990.

L. L. Cowie, E. M. Hu, and A. Songaila. Detection of massive forming galaxies at redshifts z>1. Nature, 377:603–605, Oct. 1995.

L. L. Cowie, A. Songaila, E. M. Hu, and J. G. Cohen. New Insight on Galaxy Formation and Evolution From Keck Spectroscopy of the Hawaii Deep Fields. AJ, 112:839–+, Sept. 1996.

E. Daddi, A. Cimatti, L. Pozzetti, H. Hoekstra, H. J. A. Röttgering, A. Renzini, G. Zamorani, and F. Mannucci. Detection of strong clustering of extremely red objects: implications for the density of $z > 1$ ellipticals. A&A, 361:535–549, Sept. 2000a.

E. Daddi, A. Cimatti, and A. Renzini. EROs and the formation epoch of field ellipticals. A&A, 362:L45–L48, Oct. 2000b.

E. Daddi, A. Cimatti, A. Renzini, A. Fontana, M. Mignoli, L. Pozzetti, P. Tozzi, and G. Zamorani. A New Photometric Technique for the Joint Selection of Star-forming and Passive Galaxies at $1.4 < z < 2.5$. *ApJ*, 617:746–764, Dec. 2004a.

E. Daddi, A. Cimatti, A. Renzini, J. Vernet, C. Conselice, L. Pozzetti, M. Mignoli, P. Tozzi, T. Broadhurst, S. di Serego Alighieri, A. Fontana, M. Nonino, P. Rosati, and G. Zamorani. Near-Infrared Bright Galaxies at z˜=2. Entering the Spheroid Formation Epoch? ApJ, 600:L127–L130, Jan. 2004b.

E. Daddi, M. Dickinson, R. Chary, A. Pope, G. Morrison, D. M. Alexander, F. E. Bauer, W. N. Brandt, M. Giavalisco, H. Ferguson, K. Lee, B. D. Lehmer, C. Papovich, and A. Renzini. The Population of BzK-selected ULIRGs at z ˜ 2. ApJ, 631:L13–L16, Sept. 2005a.

E. Daddi, A. Renzini, N. Pirzkal, A. Cimatti, S. Malhotra, M. Stiavelli, C. Xu, A. Pasquali, and et al. Passively Evolving Early-Type Galaxies at $1.4 < z < 2.5$ in the Hubble Ultra Deep Field. *ApJ*, 626:680–697, June 2005b.

G. B. Dalton, M. Caldwell, A. K. Ward, M. S. Whalley, G. Woodhouse, R. L. Edeson, P. Clark, S. M. Beard, A. M. Gallie, S. P. Todd, J. M. D. Strachan, N. N. Bezawada, W. J. Sutherland, and J. P. Emerson. The VISTA infrared camera. In *Society of Photo-Optical Instrumentation Engineers (SPIE) Conference Series*, volume 6269 of *Presented at the Society of Photo-Optical Instrumentation Engineers (SPIE) Conference*, July 2006.

R. A. Daly and S. G. Djorgovski. A Model-Independent Determination of the Expansion and Acceleration Rates of the Universe as a Function of Redshift and Constraints on Dark Energy. ApJ, 597:9–20, Nov. 2003.

S. di Serego Alighieri, J. Vernet, A. Cimatti, B. Lanzoni, P. Cassata, L. Ciotti, E. Daddi, M. Mignoli, and et al. The evolution of early-type galaxies at $z \sim 1$ from the K20 survey. A&A, 442:125–136, Oct. 2005.

M. Dickinson, M. Giavalisco, and GOODS Team. The Great Observatories Origins Deep Survey. In R. Bender & A. Renzini, editor, *The Mass of Galaxies at Low and High Redshift*, pages 324–+, 2003.

S. Djorgovski, B. T. Soifer, M. A. Pahre, J. E. Larkin, J. D. Smith, G. Neugebauer, I. Smail, K. Matthews, D. W. Hogg, R. D. Blandford, J. Cohen, W. Harrison, and J. Nelson. Deep galaxy counts in the K band with the Keck telescope. ApJ, 438: L13–L16, Jan. 1995.

A. Dressler. The dynamics and structure of the cD galaxy in Abell 2029. ApJ, 231: 659–670, Aug. 1979.

A. Dressler. Studying the internal kinematics of galaxies using the calcium infrared triplet. ApJ, 286:97–105, Nov. 1984.

N. Drory, G. Feulner, R. Bender, C. S. Botzler, U. Hopp, C. Maraston, C. Mendes de Oliveira, and J. Snigula. The Munich Near-Infrared Cluster Survey - I. Field selection, object extraction and photometry. MNRAS, 325:550–562, Aug. 2001.

N. Drory, R. Bender, G. Feulner, U. Hopp, C. Maraston, J. Snigula, and G. J. Hill. The Munich Near-Infrared Cluster Survey (MUNICS). VI. The Stellar Masses of K-Band-selected Field Galaxies to z˜1.2. ApJ, 608:742–751, June 2004.

J. Dunlop, J. Peacock, H. Spinrad, A. Dey, R. Jimenez, D. Stern, and R. Windhorst. A 3.5-Gyr-old galaxy at redshift 1.55. Nature, 381:581–584, June 1996.

J. S. Dunlop. Cosmic Star-Formation and Radio Source Evolution. In M. N. Bremer, N. Jackson, & I. Perez-Fournon, editor, *Observational Cosmology with the New Radio Surveys*, volume 226 of *Astrophysics and Space Science Library*, pages 157–+, 1998.

G. Efstathiou, C. S. Frenk, S. D. M. White, and M. Davis. Gravitational clustering from scale-free initial conditions. MNRAS, 235:715–748, Dec. 1988.

D. Elbaz, H. S. Hwang, B. Magnelli, E. Daddi, H. Aussel, B. Altieri, A. Amblard, P. Andreani, V. Arumugam, R. Auld, T. Babbedge, S. Berta, A. Blain, J. Bock, A. Bongiovanni, A. Boselli, V. Buat, D. Burgarella, N. Castro-Rodriguez, A. Cava, J. Cepa, P. Chanial, R.-R. Chary, A. Cimatti, D. L. Clements, A. Conley, L. Conversi, A. Cooray, M. Dickinson, H. Dominguez, C. D. Dowell, J. S. Dunlop, E. Dwek, S. Eales, D. Farrah, N. Förster Schreiber, M. Fox, A. Franceschini, W. Gear, R. Genzel, J. Glenn, M. Griffin, C. Gruppioni, M. Halpern, E. Hatziminaoglou, E. Ibar, K. Isaak, R. J. Ivison, G. Lagache, D. Le Borgne, E. Le Floc'h, L. Levenson, N. Lu, D. Lutz, S. Madden, B. Maffei, G. Magdis, G. Mainetti, R. Maiolino, L. Marchetti, A. M. J. Mortier, H. T. Nguyen, R. Nordon, B. O'Halloran, K. Okumura, S. J. Oliver, A. Omont, M. J. Page, P. Panuzzo, A. Papageorgiou, C. P. Pearson, I. Perez Fournon, A. M. Pérez García, A. Poglitsch, M. Pohlen, P. Popesso, F. Pozzi, J. I. Rawlings, D. Rigopoulou, L. Riguccini, D. Rizzo, G. Rodighiero, I. G. Roseboom, M. Rowan-Robinson, A. Saintonge, M. Sanchez Portal, P. Santini, M. Sauvage, B. Schulz, D. Scott, N. Seymour, L. Shao, D. L. Shupe, A. J. Smith, J. A. Stevens, E. Sturm, M. Symeonidis, L. Tacconi, M. Trichas, K. E. Tugwell, M. Vaccari, I. Valtchanov, J. Vieira, L. Vigroux, L. Wang, R. Ward, G. Wright, C. K. Xu, and M. Zemcov. Herschel unveils a puzzling uniformity of distant dusty galaxies. A&A, 518:L29+, July 2010.

R. Elston, G. H. Rieke, and M. J. Rieke. Deep 2 micron imaging of the sky - Evidence for a new extragalactic population. ApJ, 331:L77–L80, Aug. 1988.

R. Elston, M. J. Rieke, and G. H. Rieke. Observations of deep 2 micron survey galaxies - Primeval galaxy candidates. ApJ, 341:80–88, June 1989.

L. Fan, A. Lapi, G. De Zotti, and L. Danese. The Dramatic Size Evolution of Elliptical Galaxies and the Quasar Feedback. *ApJl*, 689:L101–L104, Dec. 2008.

G. Fasano, C. Marmo, J. Varela, M. D'Onofrio, B. M. Poggianti, M. Moles, E. Pignatelli, D. Bettoni, P. Kjærgaard, L. Rizzi, W. J. Couch, and A. Dressler. WINGS: a WIde-field Nearby Galaxy-cluster Survey. I. Optical imaging. A&A, 445:805–817, Jan. 2006.

A. E. Firth, R. S. Somerville, R. G. McMahon, O. Lahav, R. S. Ellis, C. N. Sabbey, P. J. McCarthy, H. Chen, R. O. Marzke, J. Wilson, R. G. Abraham, M. G. Beckett,

R. G. Carlberg, J. R. Lewis, C. D. Mackay, D. C. Murphy, A. E. Oemler, and S. E. Persson. The Las Campanas Infrared Survey - II. Photometric redshifts, comparison with models and clustering evolution. MNRAS, 332:617–646, May 2002.

A. Fontana, L. Pozzetti, I. Donnarumma, A. Renzini, A. Cimatti, G. Zamorani, N. Menci, E. Daddi, and et al. The K20 survey. VI. The distribution of the stellar masses in galaxies up to z $\sim$ 2. A&A, 424:23–42, Sept. 2004.

A. Fontana, S. Salimbeni, A. Grazian, E. Giallongo, L. Pentericci, M. Nonino, F. Fontanot, N. Menci, P. Monaco, S. Cristiani, E. Vanzella, C. de Santis, and S. Gallozzi. The Galaxy mass function up to z =4 in the GOODS-MUSIC sample: into the epoch of formation of massive galaxies. A&A, 459:745–757, Dec. 2006.

A. Fontana, P. Santini, A. Grazian, L. Pentericci, F. Fiore, M. Castellano, E. Giallongo, N. Menci, and et al. The fraction of quiescent massive galaxies in the early Universe. *AAP*, 501:15–20, July 2009.

F. Fontanot and P. Monaco. The active and passive populations of extremely red objects. MNRAS, 405:705–717, June 2010.

R. Fosbury, J. Bergeron, C. Cesarsky, S. Cristiani, R. Hook, A. Renzini, and P. Rosati. The Great Observatories Origins Deep Survey (GOODS). *The Messenger*, 105:40–41, Sept. 2001.

M. Franx, A. Moorwood, H. Rix, K. Kuijken, H. Röttgering, P. van der Werf, P. van Dokkum, I. Labbe, and G. Rudnick. FIRES at the VLT: the Faint InfraRed Extragalactic Survey. *The Messenger*, 99:20–22, Mar. 2000.

J. S. Gallagher, D. A. Hunter, and H. Bushouse. Star-formation rates and forbidden O II emission in blue galaxies. AJ, 97:700–707, Mar. 1989.

J. Gallego, J. Zamorano, A. Aragon-Salamanca, and M. Rego. The Current Star Formation Rate of the Local Universe. ApJ, 455:L1+, Dec. 1995.

R. Giacconi, A. Zirm, J. Wang, P. Rosati, M. Nonino, P. Tozzi, R. Gilli, V. Mainieri, G. Hasinger, L. Kewley, J. Bergeron, S. Borgani, R. Gilmozzi, N. Grogin, A. Koekemoer, E. Schreier, W. Zheng, and C. Norman. Chandra Deep Field South: The 1 Ms Catalog. ApJS, 139:369–410, Apr. 2002.

J. R. Graham and A. Dey. The Redshift of an Extremely Red Object and the Nature of the Very Red Galaxy Population. ApJ, 471:720–+, Nov. 1996.

G. L. Granato, G. De Zotti, L. Silva, A. Bressan, and L. Danese. A Physical Model for the Coevolution of QSOs and Their Spheroidal Hosts. ApJ, 600:580–594, Jan. 2004.

W. G. Hartley, K. P. Lane, O. Almaini, M. Cirasuolo, S. Foucaud, C. Simpson, S. Maddox, I. Smail, and et al. The clustering and abundance of star-forming and passive galaxies at $z \sim 2$. *MNRAS*, 391:1301–1307, Dec. 2008.

B. P. Holden, A. van der Wel, M. Franx, G. D. Illingworth, J. P. Blakeslee, P. van Dokkum, H. Ford, D. Magee, and et al. The Fundamental Plane of Cluster Elliptical Galaxies at z=1.25. ApJ, 620:L83–L86, Feb. 2005.

P. F. Hopkins, K. Bundy, N. Murray, E. Quataert, T. R. Lauer, and C. Ma. Compact high-redshift galaxies are the cores of the most massive present-day spheroids. MNRAS, 398:898–910, Sept. 2009.

D. A. Howell, M. Sullivan, K. Perrett, T. J. Bronder, I. M. Hook, P. Astier, E. Aubourg, D. Balam, S. Basa, R. G. Carlberg, S. Fabbro, D. Fouchez, J. Guy, H. Lafoux, J. D. Neill, R. Pain, N. Palanque-Delabrouille, C. J. Pritchet, N. Regnault, J. Rich, R. Taillet, R. Knop, R. G. McMahon, S. Perlmutter, and N. A. Walton. Gemini Spectroscopy of Supernovae from the Supernova Legacy Survey: Improving High-Redshift Supernova Selection and Classification. ApJ, 634:1190–1201, Dec. 2005.

E. M. Hu and S. E. Ridgway. Two extremely red galaxies. AJ, 107:1303–1306, Apr. 1994.

D. H. Hughes, S. Serjeant, J. Dunlop, M. Rowan-Robinson, A. Blain, R. G. Mann, R. Ivison, J. Peacock, A. Efstathiou, W. Gear, S. Oliver, A. Lawrence, M. Longair, P. Goldschmidt, and T. Jenness. High-redshift star formation in the Hubble Deep Field revealed by a submillimetre-wavelength survey. Nature, 394:241–247, July 1998.

M. E. Jones, R. Saunders, J. C. Baker, G. Cotter, A. Edge, K. Grainge, T. Haynes, A. Lasenby, G. Pooley, and H. Rottgering. Detection of a Cosmic Microwave Background Decrement toward the ital Z = 3.8 Quasar Pair PC 1643+4631A,B. ApJ, 479:L1+, Apr. 1997.

I. Jorgensen, M. Franx, and P. Kjaergaard. Spectroscopy for E and S0 galaxies in nine clusters. MNRAS, 276:1341–1364, Oct. 1995.

I. Jorgensen, M. Franx, and P. Kjaergaard. The Fundamental Plane for cluster E and S0 galaxies. *MNRAS*, 280:167–185, May 1996.

A. Karim, E. Schinnerer, A. Martínez-Sansigre, M. T. Sargent, A. van der Wel, H. Rix, O. Ilbert, V. Smolčić, C. Carilli, M. Pannella, A. M. Koekemoer, E. F. Bell, and M. Salvato. The Star Formation History of Mass-selected Galaxies in the COSMOS Field. ApJ, 730:61–+, Apr. 2011.

N. Kashikawa, T. Takata, Y. Ohyama, M. Yoshida, T. Maihara, F. Iwamuro, K. Motohara, T. Totani, M. Nagashima, K. Shimasaku, H. Furusawa, M. Ouchi, M. Yagi, S. Okamura, M. Iye, T. Sasaki, G. Kosugi, K. Aoki, and F. Nakata. Subaru Deep Survey. III. Evolution of Rest-Frame Luminosity Functions Based on the Photometric Redshifts for a K'-Band-Selected Galaxy Sample. AJ, 125:53–65, Jan. 2003.

G. Kauffmann and S. D. M. White. The merging history of dark matter haloes in a hierarchical universe. MNRAS, 261:921–928, Apr. 1993.

G. Kauffmann, S. D. M. White, and B. Guiderdoni. The Formation and Evolution of Galaxies Within Merging Dark Matter Haloes. MNRAS, 264:201–+, Sept. 1993.

R. C. Kennicutt, Jr. The rate of star formation in normal disk galaxies. ApJ, 272: 54–67, Sept. 1983.

R. C. Kennicutt, Jr. Star Formation in Galaxies Along the Hubble Sequence. *ARAA*, 36:189–232, 1998.

S. Khochfar and J. Silk. A Simple Model for the Size Evolution of Elliptical Galaxies. ApJ, 648:L21–L24, Sept. 2006.

R. A. Knop, G. Aldering, R. Amanullah, P. Astier, G. Blanc, M. S. Burns, A. Conley, S. E. Deustua, M. Doi, R. Ellis, S. Fabbro, G. Folatelli, A. S. Fruchter, G. Garavini, S. Garmond, K. Garton, R. Gibbons, G. Goldhaber, A. Goobar, D. E. Groom, D. Hardin, I. Hook, D. A. Howell, A. G. Kim, B. C. Lee, C. Lidman, J. Mendez, S. Nobili, P. E. Nugent, R. Pain, N. Panagia, C. R. Pennypacker, S. Perlmutter, R. Quimby, J. Raux, N. Regnault, P. Ruiz-Lapuente, G. Sainton, B. Schaefer, K. Schahmaneche, E. Smith, A. L. Spadafora, V. Stanishev, M. Sullivan, N. A. Walton, L. Wang, W. M. Wood-Vasey, and N. Yasuda. New Constraints on Ω_M, Ω_Λ, and w from an Independent Set of 11 High-Redshift Supernovae Observed with the Hubble Space Telescope. ApJ, 598:102–137, Nov. 2003.

C. S. Kochanek, M. A. Pahre, E. E. Falco, J. P. Huchra, J. Mader, T. H. Jarrett, T. Chester, R. Cutri, and S. E. Schneider. The K-Band Galaxy Luminosity Function. ApJ, 560:566–579, Oct. 2001.

J. Kormendy and D. B. Sanders. Ultraluminous IRAS galaxies - Formation of elliptical galaxies by merger-induced dissipative collapse. ApJ, 390:L53–L56, May 1992.

M. Kowalski, D. Rubin, G. Aldering, R. J. Agostinho, A. Amadon, R. Amanullah, C. Balland, K. Barbary, G. Blanc, P. J. Challis, A. Conley, N. V. Connolly, R. Covarrubias, K. S. Dawson, S. E. Deustua, R. Ellis, S. Fabbro, V. Fadeyev, X. Fan, B. Farris, G. Folatelli, B. L. Frye, G. Garavini, E. L. Gates, L. Germany, G. Goldhaber, B. Goldman, A. Goobar, D. E. Groom, J. Haissinski, D. Hardin, I. Hook, S. Kent, A. G. Kim, R. A. Knop, C. Lidman, E. V. Linder, J. Mendez, J. Meyers, G. J. Miller, M. Moniez, A. M. Mourão, H. Newberg, S. Nobili, P. E. Nugent, R. Pain, O. Perdereau, S. Perlmutter, M. M. Phillips, V. Prasad, R. Quimby, N. Regnault, J. Rich, E. P. Rubenstein, P. Ruiz-Lapuente, F. D. Santos, B. E. Schaefer, R. A. Schommer, R. C. Smith, A. M. Soderberg, A. L. Spadafora, L. Strolger, M. Strovink, N. B. Suntzeff, N. Suzuki, R. C. Thomas, N. A. Walton, L. Wang, W. M. Wood-Vasey, and J. L. Yun. Improved Cosmological Constraints from New, Old, and Combined Supernova Data Sets. ApJ, 686:749–778, Oct. 2008.

M. Kriek, P. G. van Dokkum, M. Franx, N. M. Förster Schreiber, E. Gawiser, G. D. Illingworth, I. Labbé, D. Marchesini, R. Quadri, H. Rix, G. Rudnick, S. Toft, P. van der Werf, and S. Wuyts. Direct Measurements of the Stellar Continua and Balmer/4000 Å Breaks of Red z $>$ 2 Galaxies: Redshifts and Improved Constraints on Stellar Populations1,. ApJ, 645:44–54, July 2006.

J. Kurk, A. Cimatti, E. Daddi, M. Mignoli, M. Bolzonella, L. Pozzetti, P. Cassata, C. Halliday, and et al. A VLT Large Programme to Study Galaxies at z ˜ 2: GMASS - the Galaxy Mass Assembly Ultra-deep Spectroscopic Survey. *The Messenger*, 135: 40–44, Mar. 2009.

R. L. Kurucz. Model Atmospheres for Population Synthesis. In B. Barbuy & A. Renzini, editor, *The Stellar Populations of Galaxies*, volume 149 of *IAU Symposium*, pages 225–+, 1992.

G. Lagache, H. Dole, and J. Puget. Modelling infrared galaxy evolution using a phenomenological approach. MNRAS, 338:555–571, Jan. 2003.

D. Larson, J. Dunkley, G. Hinshaw, E. Komatsu, M. R. Nolta, C. L. Bennett, B. Gold, M. Halpern, R. S. Hill, N. Jarosik, A. Kogut, M. Limon, S. S. Meyer, N. Odegard, L. Page, K. M. Smith, D. N. Spergel, G. S. Tucker, J. L. Weiland, E. Wollack, and E. L. Wright. Seven-year Wilkinson Microwave Anisotropy Probe (WMAP) Observations: Power Spectra and WMAP-derived Parameters. ApJS, 192: 16–+, Feb. 2011.

A. Lawrence, S. J. Warren, O. Almaini, A. C. Edge, N. C. Hambly, R. F. Jameson, P. Lucas, M. Casali, A. Adamson, S. Dye, J. P. Emerson, S. Foucaud, P. Hewett, P. Hirst, S. T. Hodgkin, M. J. Irwin, N. Lodieu, R. G. McMahon, C. Simpson, I. Smail, D. Mortlock, and M. Folger. The UKIRT Infrared Deep Sky Survey (UKIDSS). MNRAS, 379:1599–1617, Aug. 2007.

D. Le Borgne, R. Abraham, K. Daniel, P. J. McCarthy, K. Glazebrook, S. Savaglio, D. Crampton, S. Juneau, R. G. Carlberg, H. Chen, R. O. Marzke, K. Roth, I. Jørgensen, and R. Murowinski. Gemini Deep Deep Survey. VI. Massive Hδ-strong Galaxies at z ˜= 1. ApJ, 642:48–62, May 2006.

J. Le Borgne, G. Bruzual, R. Pelló, A. Lançon, B. Rocca-Volmerange, B. Sanahuja, D. Schaerer, C. Soubiran, and et al. STELIB: A library of stellar spectra at R ˜ 2000. *AAP*, 402:433–442, May 2003.

S. J. Lilly, M. S. Longair, and J. R. Allington-Smith. Infrared Observations of 1-JANSKY Radio Source Identifications and Empty Fields. MNRAS, 215:37–+, July 1985.

S. J. Lilly, L. Tresse, F. Hammer, D. Crampton, and O. Le Fevre. The Canada-France Redshift Survey. VI. Evolution of the Galaxy Luminosity Function to Z approximately 1. ApJ, 455:108–+, Dec. 1995.

S. J. Lilly, O. Le Fevre, F. Hammer, and D. Crampton. The Canada-France Redshift Survey: The Luminosity Density and Star Formation History of the Universe to Z approximately 1. ApJ, 460:L1+, Mar. 1996.

M. Longhetti, P. Saracco, P. Severgnini, R. Della Ceca, V. Braito, F. Mannucci, R. Bender, N. Drory, and et al. Dating the stellar population in massive early-type galaxies at z˜ 1.5. *MNRAS*, 361:897–906, Aug. 2005.

M. Longhetti, P. Saracco, P. Severgnini, R. Della Ceca, F. Mannucci, R. Bender, N. Drory, G. Feulner, and et al. The Kormendy relation of massive elliptical galaxies at z ˜ 1.5: evidence for size evolution. *MNRAS*, 374:614–626, Jan. 2007.

P. Madau, H. C. Ferguson, M. E. Dickinson, M. Giavalisco, C. C. Steidel, and A. Fruchter. High-redshift galaxies in the Hubble Deep Field: colour selection and star formation history to z˜4. MNRAS, 283:1388–1404, Dec. 1996.

P. Madau, L. Pozzetti, and M. Dickinson. The Star Formation History of Field Galaxies. ApJ, 498:106–+, May 1998.

C. Mancini, E. Daddi, A. Renzini, F. Salmi, H. J. McCracken, A. Cimatti, M. Onodera, M. Salvato, and et al. High-redshift elliptical galaxies: are they (all) really compact? MNRAS, 401:933–940, Jan. 2010.

F. Mannucci, L. Pozzetti, D. Thompson, E. Oliva, C. Baffa, G. Comoretto, S. Gennari, and F. Lisi. The relative abundances of ellipticals and starbursts among the extremely red galaxies. MNRAS, 329:L57–L61, Feb. 2002.

C. Maraston. Evolutionary population synthesis: models, analysis of the ingredients and application to high-z galaxies. MNRAS, 362:799–825, Sept. 2005a.

C. Maraston. Evolutionary population synthesis: models, analysis of the ingredients and application to high-z galaxies. MNRAS, 362:799–825, Sept. 2005b.

J. C. Mather, D. J. Fixsen, and R. A. Shafer. Design for the COBE far-infrared absolute spectrophotometer (FIRAS). In M. S. Scholl, editor, *Society of Photo-Optical Instrumentation Engineers (SPIE) Conference Series*, volume 2019 of *Presented at the Society of Photo-Optical Instrumentation Engineers (SPIE) Conference*, pages 168–179, Oct. 1993.

J. C. Mather, E. S. Cheng, D. A. Cottingham, R. E. Eplee, Jr., D. J. Fixsen, T. Hewagama, R. B. Isaacman, K. A. Jensen, S. S. Meyer, P. D. Noerdlinger, S. M. Read, L. P. Rosen, R. A. Shafer, E. L. Wright, C. L. Bennett, N. W. Boggess, M. G. Hauser, T. Kelsall, S. H. Moseley, Jr., R. F. Silverberg, G. F. Smoot, R. Weiss, and D. T. Wilkinson. Measurement of the cosmic microwave background spectrum by the COBE FIRAS instrument. ApJ, 420:439–444, Jan. 1994.

J. C. Mather, D. J. Fixsen, R. A. Shafer, C. Mosier, and D. T. Wilkinson. Calibrator Design for the COBE Far-Infrared Absolute Spectrophotometer (FIRAS). ApJ, 512: 511–520, Feb. 1999.

P. J. McCarthy, D. Le Borgne, D. Crampton, H. Chen, R. G. Abraham, K. Glazebrook, S. Savaglio, R. G. Carlberg, R. O. Marzke, K. Roth, I. Jørgensen, I. Hook, R. Murowinski, and S. Juneau. Evolved Galaxies at $z > 1.5$ from the Gemini Deep Deep Survey: The Formation Epoch of Massive Stellar Systems. ApJ, 614:L9–L12, Oct. 2004.

H. J. McCracken, P. Capak, M. Salvato, H. Aussel, D. Thompson, E. Daddi, D. B. Sanders, J. Kneib, C. J. Willott, C. Mancini, A. Renzini, R. Cook, O. Le Fèvre,

O. Ilbert, J. Kartaltepe, A. M. Koekemoer, Y. Mellier, T. Murayama, N. Z. Scoville, Y. Shioya, and Y. Tanaguchi. The COSMOS-WIRCam Near-Infrared Imaging Survey. I. BzK-Selected Passive and Star-Forming Galaxy Candidates at z gsim 1.4. ApJ, 708:202–217, Jan. 2010.

E. J. McGrath, A. Stockton, G. Canalizo, M. Iye, and T. Maihara. Morphologies and Color Gradients of Luminous Evolved Galaxies at z ˜ 1.5. *ApJ*, 682:303–318, July 2008.

M. Mignoli, A. Cimatti, G. Zamorani, L. Pozzetti, E. Daddi, A. Renzini, T. Broadhurst, S. Cristiani, S. D'Odorico, A. Fontana, E. Giallongo, R. Gilmozzi, N. Menci, and P. Saracco. The K20 survey. VII. The spectroscopic catalogue: Spectral properties and evolution of the galaxy population. A&A, 437:883–897, July 2005.

M. Miyazaki, K. Shimasaku, T. Kodama, S. Okamura, H. Furusawa, M. Ouchi, F. Nakata, M. Doi, M. Hamabe, M. Kimura, Y. Komiyama, S. Miyazaki, C. Nagashima, T. Nagata, T. Nagayama, Y. Nakajima, H. Nakaya, A. J. Pickles, S. Sato, K. Sekiguchi, M. Sekiguchi, K. Sugitani, T. Takata, M. Tamura, M. Yagi, and N. Yasuda. Evolution of Elliptical Galaxies at z gtrsim 1 Revealed from a Large, Multicolor Sample of Extremely Red Objects. PASJ, 55:1079–1103, Dec. 2003.

S. Miyazaki, Y. Komiyama, M. Sekiguchi, S. Okamura, M. Doi, H. Furusawa, M. Hamabe, K. Imi, M. Kimura, F. Nakata, N. Okada, M. Ouchi, K. Shimasaku, M. Yagi, and N. Yasuda. Subaru Prime Focus Camera – Suprime-Cam. PASJ, 54: 833–853, Dec. 2002.

P. Monaco, F. Fontanot, and G. Taffoni. The MORGANA model for the rise of galaxies and active nuclei. MNRAS, 375:1189–1219, Mar. 2007.

A. Moorwood, J. Cuby, P. Biereichel, J. Brynnel, B. Delabre, N. Devillard, A. van Dijsseldonk, G. Finger, H. Gemperlein, R. Gilmozzi, T. Herlin, G. Huster, J. Knudstrup, C. Lidman, J. Lizon, H. Mehrgan, M. Meyer, G. Nicolini, M. Petr, J. Spyromilio, and J. Stegmeier. ISAAC sees first light at the VLT. *The Messenger*, 94: 7–9, Dec. 1998.

A. M. J. Mortier, S. Serjeant, J. S. Dunlop, S. E. Scott, P. Ade, D. Alexander, O. Almaini, I. Aretxaga, C. Baugh, A. J. Benson, P. N. Best, A. Blain, J. Bock, C. Borys, A. Bressan, C. Carilli, E. L. Chapin, S. Chapman, D. L. Clements, K. Coppin, M. Crawford, M. Devlin, S. Dicker, L. Dunne, S. A. Eales, A. C. Edge, D. Farrah, M. Fox, C. Frenk, E. Gaztañaga, W. K. Gear, E. Gonzales-Solares, G. L. Granato, T. R. Greve, J. A. Grimes, J. Gundersen, M. Halpern, P. Hargrave, D. H. Hughes, R. J. Ivison, M. J. Jarvis, T. Jenness, R. Jimenez, E. van Kampen, A. King, C. Lacey, A. Lawrence, K. Lepage, R. G. Mann, G. Marsden, P. Mauskopf, B. Netterfield, S. Oliver, L. Olmi, M. J. Page, J. A. Peacock, C. P. Pearson, W. J. Percival, A. Pope, R. S. Priddey, S. Rawlings, N. Roche, M. Rowan-Robinson, D. Scott, K. Sekiguchi, M. Seigar, L. Silva, C. Simpson, I. Smail, J. A. Stevens, T. Takagi, G. Tucker, C. Vlahakis, I. Waddington, J. Wagg, M. Watson, C. Willott, and M. Vaccari. The SCUBA Half-Degree Extragalactic Survey - I. Survey motivation, design and data processing. MNRAS, 363:563–580, Oct. 2005.

L. A. Moustakas, S. Casertano, C. J. Conselice, M. E. Dickinson, P. Eisenhardt, H. C. Ferguson, M. Giavalisco, N. A. Grogin, A. M. Koekemoer, R. A. Lucas, B. Mobasher, C. Papovich, A. Renzini, R. S. Somerville, and D. Stern. Morphologies and Spectral Energy Distributions of Extremely Red Galaxies in the GOODS-South Field. ApJ, 600:L131–L134, Jan. 2004.

T. Naab, P. H. Johansson, and J. P. Ostriker. Minor Mergers and the Size Evolution of Elliptical Galaxies. *ApJl*, 699:L178–L182, July 2009.

A. B. Newman, R. S. Ellis, T. Treu, and K. Bundy. Keck Spectroscopy of z $\geq$ 1 Field Spheroidals: Dynamical Constraints on the Growth Rate of Red "Nuggets". ApJ, 717:L103–L107, July 2010.

S. Niklas, U. Klein, and R. Wielebinski. A radio continuum survey of Shapley-Ames galaxies at λ 2.8cm. II. Separation of thermal and non-thermal radio emission. A&A, 322:19–28, June 1997.

C. Nipoti, T. Treu, M. W. Auger, and A. S. Bolton. Can Dry Merging Explain the Size Evolution of Early-Type Galaxies? ApJ, 706:L86–L90, Nov. 2009.

R. B. Partridge and P. J. E. Peebles. Are Young Galaxies Visible? ApJ, 147:868–+, Mar. 1967.

P. J. E. Peebles. The Black-Body Radiation Content of the Universe and the Formation of Galaxies. ApJ, 142:1317–+, Nov. 1965.

Y. C. Pei and S. M. Fall. Cosmic Chemical Evolution. ApJ, 454:69–+, Nov. 1995.

C. Y. Peng, L. C. Ho, C. D. Impey, and H. Rix. Detailed Structural Decomposition of Galaxy Images. AJ, 124:266–293, July 2002.

A. A. Penzias and R. W. Wilson. A Measurement of Excess Antenna Temperature at 4080 Mc/s. ApJ, 142:419–421, July 1965.

W. J. Percival, C. M. Baugh, J. Bland-Hawthorn, T. Bridges, R. Cannon, S. Cole, M. Colless, C. Collins, W. Couch, G. Dalton, R. De Propris, S. P. Driver, G. Efstathiou, R. S. Ellis, C. S. Frenk, K. Glazebrook, C. Jackson, O. Lahav, I. Lewis, S. Lumsden, S. Maddox, S. Moody, P. Norberg, J. A. Peacock, B. A. Peterson, W. Sutherland, and K. Taylor. The 2dF Galaxy Redshift Survey: the power spectrum and the matter content of the Universe. MNRAS, 327:1297–1306, Nov. 2001.

S. Perlmutter, C. R. Pennypacker, G. Goldhaber, A. Goobar, R. A. Muller, H. J. M. Newberg, J. Desai, A. G. Kim, M. Y. Kim, I. A. Small, B. J. Boyle, C. S. Crawford, R. G. McMahon, P. S. Bunclark, D. Carter, M. J. Irwin, R. J. Terlevich, R. S. Ellis, K. Glazebrook, W. J. Couch, J. R. Mould, T. A. Small, and R. G. Abraham. A supernova at Z = 0.458 and implications for measuring the cosmological deceleration. ApJ, 440:L41–L44, Feb. 1995.

V. Petrosian. Surface brightness and evolution of galaxies. ApJ, 209:L1–L5, Oct. 1976.

L. Pozzetti and F. Mannucci. Extremely red galaxies: age and dust degeneracy solved? *MNRAS*, 317:L17–L21, Sept. 2000.

L. Pozzetti, A. Cimatti, G. Zamorani, E. Daddi, N. Menci, A. Fontana, A. Renzini, M. Mignoli, F. Poli, P. Saracco, T. Broadhurst, S. Cristiani, S. D'Odorico, E. Giallongo, and R. Gilmozzi. The K20 survey. V. The evolution of the near-IR Luminosity Function. A&A, 402:837–848, May 2003.

W. H. Press and P. Schechter. Formation of Galaxies and Clusters of Galaxies by Self-Similar Gravitational Condensation. ApJ, 187:425–438, Feb. 1974.

P. Puget, E. Stadler, R. Doyon, P. Gigan, S. Thibault, G. Luppino, G. Barrick, T. Benedict, T. Forveille, W. Rambold, J. Thomas, T. Vermeulen, J. Ward, J. Beuzit, P. Feautrier, Y. Magnard, G. Mella, O. Preis, P. Vallee, S. Wang, C. Lin, D. N. Hall, and K. W. Hodapp. WIRCam: the infrared wide-field camera for the Canada-France-Hawaii Telescope. In A. F. M. Moorwood & M. Iye, editor, *Society of Photo-Optical Instrumentation Engineers (SPIE) Conference Series*, volume 5492 of *Presented at the Society of Photo-Optical Instrumentation Engineers (SPIE) Conference*, pages 978–987, Sept. 2004.

A. Rettura, P. Rosati, V. Strazzullo, M. Dickinson, R. A. E. Fosbury, B. Rocca-Volmerange, A. Cimatti, S. di Serego Alighieri, and et al. Comparing dynamical and photometric-stellar masses of early-type galaxies at z ˜ 1. *AAP*, 458:717–726, Nov. 2006.

J. Retzlaff, P. Rosati, M. Dickinson, B. Vandame, C. Rité, M. Nonino, C. Cesarsky, and GOODS Team. The Great Observatories Origins Deep Survey. VLT/ISAAC near-infrared imaging of the GOODS-South field. A&A, 511:A50+, Feb. 2010.

A. G. Riess, A. V. Filippenko, D. C. Leonard, B. P. Schmidt, N. Suntzeff, M. M. Phillips, R. Schommer, A. Clocchiatti, R. P. Kirshner, P. Garnavich, P. Challis, B. Leibundgut, J. Spyromilio, and R. C. Smith. Time Dilation from Spectral Feature Age Measurements of Type IA Supernovae. AJ, 114:722–729, Aug. 1997.

N. D. Roche, O. Almaini, J. Dunlop, R. J. Ivison, and C. J. Willott. The clustering, number counts and morphology of extremely red ($R - K > 5$) galaxies to $K \leq 21$. MNRAS, 337:1282–1298, Dec. 2002.

N. D. Roche, J. Dunlop, and O. Almaini. The nature, evolution, clustering and X-ray properties of extremely red galaxies in the Chandra Deep Field South/Great Observatories Origins Deep Survey field. MNRAS, 346:803–817, Dec. 2003a.

P. F. Roche, P. W. Lucas, C. D. Mackay, E. Ettedgui-Atad, P. R. Hastings, A. Bridger, N. P. Rees, S. K. Leggett, C. Davis, A. R. Holmes, and T. Handford. UFTI: the 0.8 - 2.5 μm fast track imager for the UK infrared telescope. In M. Iye & A. F. M. Moorwood, editor, *Society of Photo-Optical Instrumentation Engineers (SPIE) Conference Series*, volume 4841 of *Presented at the Society of Photo-Optical Instrumentation Engineers (SPIE) Conference*, pages 901–912, Mar. 2003b.

R. K. Sachs and A. M. Wolfe. Perturbations of a Cosmological Model and Angular Variations of the Microwave Background. ApJ, 147:73–+, Jan. 1967.

P. Saracco, M. Longhetti, and S. Andreon. The population of early-type galaxies at $1 \leq z \leq 2$ - new clues on their formation and evolution. MNRAS, 392:718–732, Jan. 2009.

P. Saracco, M. Longhetti, and A. Gargiulo. The number density of superdense early-type galaxies at $1 \leq z \leq 2$ and the local cluster galaxies. MNRAS, 408:L21–L25, Oct. 2010.

P. Saracco, M. Longhetti, and A. Gargiulo. Constraining the star formation and the assembly histories of normal and compact early-type galaxies at $1 < z < 2$. MNRAS, 412:2707–2716, Apr. 2011.

W. L. W. Sargent, P. L. Schechter, A. Boksenberg, and K. Shortridge. Velocity dispersions for 13 galaxies. ApJ, 212:326–334, Mar. 1977.

S. Savaglio, K. Glazebrook, D. Le Borgne, S. Juneau, R. G. Abraham, H. Chen, D. Crampton, P. J. McCarthy, R. G. Carlberg, R. O. Marzke, K. Roth, I. Jørgensen, and R. Murowinski. The Gemini Deep Deep Survey. VII. The Redshift Evolution of the Mass-Metallicity Relation. ApJ, 635:260–279, Dec. 2005.

M. Schmidt. The Rate of Star Formation. II. The Rate of Formation of Stars of Different Mass. ApJ, 137:758–+, Apr. 1963.

S. E. Scott, M. J. Fox, J. S. Dunlop, S. Serjeant, J. A. Peacock, R. J. Ivison, S. Oliver, R. G. Mann, A. Lawrence, A. Efstathiou, M. Rowan-Robinson, D. H. Hughes, E. N. Archibald, A. Blain, and M. Longair. The SCUBA 8-mJy survey - I. Submillimetre maps, sources and number counts. MNRAS, 331:817–838, Apr. 2002.

S. Shen, H. J. Mo, S. D. M. White, M. R. Blanton, G. Kauffmann, W. Voges, J. Brinkmann, and I. Csabai. The size distribution of galaxies in the Sloan Digital Sky Survey. *MNRAS*, 343:978–994, Aug. 2003.

J. D. Silge and K. Gebhardt. Dust and the Infrared Kinematic Properties of Early-Type Galaxies. AJ, 125:2809–2823, June 2003.

C. Simpson, A. Martínez-Sansigre, S. Rawlings, R. Ivison, M. Akiyama, K. Sekiguchi, T. Takata, Y. Ueda, and M. Watson. Radio imaging of the Subaru/XMM-Newton Deep Field - I. The 100-μJy catalogue, optical identifications, and the nature of the faint radio source population. MNRAS, 372:741–757, Oct. 2006.

I. Smail, F. N. Owen, G. E. Morrison, W. C. Keel, R. J. Ivison, and M. J. Ledlow. The Diversity of Extremely Red Objects. ApJ, 581:844–864, Dec. 2002.

G. P. Smith, T. Treu, R. Ellis, I. Smail, J. Kneib, and B. L. Frye. Near-Infrared Spectroscopy and Hubble Space Telescope Imaging of a Dusty Starburst Extremely Red Object. ApJ, 562:635–640, Dec. 2001.

G. Smoot, C. Bennett, R. Weber, J. Maruschak, R. Ratliff, M. Janssen, J. Chitwood, L. Hilliard, M. Lecha, R. Mills, R. Patschke, C. Richards, C. Backus, J. Mather, M. Hauser, R. Weiss, D. Wilkinson, S. Gulkis, N. Boggess, E. Cheng, T. Kelsall,

P. Lubin, S. Meyer, H. Moseley, T. Murdock, R. Shafer, R. Silverberg, and E. Wright. COBE Differential Microwave Radiometers - Instrument design and implementation. ApJ, 360:685–695, Sept. 1990.

G. F. Smoot, C. L. Bennett, A. Kogut, E. L. Wright, J. Aymon, N. W. Boggess, E. S. Cheng, G. de Amici, S. Gulkis, M. G. Hauser, G. Hinshaw, P. D. Jackson, M. Janssen, E. Kaita, T. Kelsall, P. Keegstra, C. Lineweaver, K. Loewenstein, P. Lubin, J. Mather, S. S. Meyer, S. H. Moseley, T. Murdock, L. Rokke, R. F. Silverberg, L. Tenorio, R. Weiss, and D. T. Wilkinson. Structure in the COBE differential microwave radiometer first-year maps. ApJ, 396:L1–L5, Sept. 1992.

R. S. Somerville and J. R. Primack. Semi-analytic modelling of galaxy formation: the local Universe. MNRAS, 310:1087–1110, Dec. 1999.

R. S. Somerville, J. R. Primack, and S. M. Faber. The nature of high-redshift galaxies. MNRAS, 320:504–528, Feb. 2001.

D. N. Spergel, L. Verde, H. V. Peiris, E. Komatsu, M. R. Nolta, C. L. Bennett, M. Halpern, G. Hinshaw, N. Jarosik, A. Kogut, M. Limon, S. S. Meyer, L. Page, G. S. Tucker, J. L. Weiland, E. Wollack, and E. L. Wright. First-Year Wilkinson Microwave Anisotropy Probe (WMAP) Observations: Determination of Cosmological Parameters. ApJS, 148:175–194, Sept. 2003.

H. Spinrad, A. Dey, D. Stern, J. Dunlop, J. Peacock, R. Jimenez, and R. Windhorst. LBDS 53W091: an Old, Red Galaxy at z=1.552. ApJ, 484:581–+, July 1997.

C. C. Steidel, K. L. Adelberger, M. Giavalisco, M. Dickinson, and M. Pettini. Lyman-Break Galaxies at z≥˜4 and the Evolution of the Ultraviolet Luminosity Density at High Redshift. ApJ, 519:1–17, July 1999.

D. Stern, R.-R. Chary, P. R. M. Eisenhardt, and L. A. Moustakas. Spitzer Observations of the Prototypical Extremely Red Objects HR 10 and LBDS 53W091: Separating Dusty Starbursts from Old Elliptical Galaxies. *AJ*, 132:1405–1414, Sept. 2006.

T. Takagi, Y. Ono, K. Shimasaku, and H. Hanami. A close relationship at z ˜ 2: submillimetre galaxies and BzK-selected galaxies. MNRAS, 389:775–786, Sept. 2008.

E. N. Taylor, M. Franx, K. Glazebrook, J. Brinchmann, A. van der Wel, and P. G. van Dokkum. On the Dearth of Compact, Massive, Red Sequence Galaxies in the Local Universe. ApJ, 720:723–741, Sept. 2010.

S. Toft, P. van Dokkum, M. Franx, I. Labbe, N. M. Förster Schreiber, S. Wuyts, T. Webb, G. Rudnick, A. Zirm, M. Kriek, P. van der Werf, J. P. Blakeslee, G. Illingworth, H. Rix, C. Papovich, and A. Moorwood. Hubble Space Telescope and Spitzer Imaging of Red and Blue Galaxies at $z \sim 2.5$: A Correlation between Size and Star Formation Activity from Compact Quiescent Galaxies to Extended Star-forming Galaxies. ApJ, 671:285–302, Dec. 2007.

R. Tojeiro, W. J. Percival, A. F. Heavens, and R. Jimenez. The stellar evolution of Luminous Red Galaxies, and its dependence on colour, redshift, luminosity and modelling. *ArXiv e-prints*, Nov. 2010.

C. Tonini, C. Maraston, D. Thomas, J. Devriendt, and J. Silk. Hierarchical models of high-redshift galaxies with thermally pulsing asymptotic giant branch stars: comparison with observations. MNRAS, 403:1749–1758, Apr. 2010.

C. A. Tremonti, T. M. Heckman, G. Kauffmann, J. Brinchmann, S. Charlot, S. D. M. White, M. Seibert, E. W. Peng, D. J. Schlegel, A. Uomoto, M. Fukugita, and J. Brinkmann. The Origin of the Mass-Metallicity Relation: Insights from 53,000 Star-forming Galaxies in the Sloan Digital Sky Survey. ApJ, 613:898–913, Oct. 2004.

I. Trujillo, G. Feulner, Y. Goranova, U. Hopp, M. Longhetti, P. Saracco, R. Bender, V. Braito, and et al. Extremely compact massive galaxies at z $\sim$ 1.4. *MNRAS*, 373: L36–L40, Nov. 2006a.

I. Trujillo, N. M. Förster Schreiber, G. Rudnick, M. Barden, M. Franx, H. Rix, J. A. R. Caldwell, D. H. McIntosh, S. Toft, B. Häussler, A. Zirm, P. G. van Dokkum, I. Labbé, A. Moorwood, H. Röttgering, A. van der Wel, P. van der Werf, and L. van Starkenburg. The Size Evolution of Galaxies since z˜3: Combining SDSS, GEMS, and FIRES. ApJ, 650:18–41, Oct. 2006b.

I. Trujillo, C. J. Conselice, K. Bundy, M. C. Cooper, P. Eisenhardt, and R. S. Ellis. Strong size evolution of the most massive galaxies since z ˜ 2. *MNRAS*, 382:109–120, Nov. 2007.

T. Valentinuzzi, J. Fritz, B. M. Poggianti, A. Cava, D. Bettoni, G. Fasano, M. D'Onofrio, W. J. Couch, A. Dressler, M. Moles, A. Moretti, A. Omizzolo, P. Kjærgaard, E. Vanzella, and J. Varela. Superdense Massive Galaxies in Wings Local Clusters. ApJ, 712:226–237, Mar. 2010a.

T. Valentinuzzi, B. M. Poggianti, R. P. Saglia, A. Aragón-Salamanca, L. Simard, P. Sánchez-Blázquez, M. D'onofrio, A. Cava, W. J. Couch, J. Fritz, A. Moretti, and B. Vulcani. Superdense Massive Galaxies in the ESO Distant Cluster Survey (EDisCS). ApJ, 721:L19–L23, Sept. 2010b.

A. van der Wel, M. Franx, P. G. van Dokkum, H. Rix, G. D. Illingworth, and P. Rosati. Mass-to-Light Ratios of Field Early-Type Galaxies at z ˜ 1 from Ultradeep Spectroscopy: Evidence for Mass-dependent Evolution. ApJ, 631:145–162, Sept. 2005.

P. G. van Dokkum and S. A. Stanford. The Fundamental Plane at z=1.27: First Calibration of the Mass Scale of Red Galaxies at Redshifts z $>$ 1. *ApJ*, 585:78–89, Mar. 2003.

P. G. van Dokkum, M. Franx, M. Kriek, B. Holden, G. D. Illingworth, D. Magee, R. Bouwens, D. Marchesini, R. Quadri, G. Rudnick, E. N. Taylor, and S. Toft. Confirmation of the Remarkable Compactness of Massive Quiescent Galaxies at z ˜ 2.3: Early-Type Galaxies Did not Form in a Simple Monolithic Collapse. ApJ, 677: L5–L8, Apr. 2008.

S. D. M. White and C. S. Frenk. Galaxy formation through hierarchical clustering. ApJ, 379:52–79, Sept. 1991.

S. D. M. White and M. J. Rees. Core condensation in heavy halos - A two-stage theory for galaxy formation and clustering. MNRAS, 183:341–358, May 1978.

R. J. Williams, R. F. Quadri, M. Franx, P. van Dokkum, and I. Labbé. Detection of Quiescent Galaxies in a Bicolor Sequence from Z = 0-2. ApJ, 691:1879–1895, Feb. 2009.

R. A. Windhorst, G. M. van Heerde, and P. Katgert. A deep Westerbork survey of areas with multicolor Mayall 4 M plates. I - The 1412 MHz catalogue, source counts and angular size statistics. A&AS, 58:1–37, Oct. 1984.

M. J. Wolf and A. I. Sheinis. Host Galaxies of Luminous Quasars: Structural Properties and the Fundamental Plane. AJ, 136:1587–1606, Oct. 2008.

C. G. Wynn-Williams and E. E. Becklin, editors. *Infrared astronomy with arrays*, 1987.

L. Yan, P. I. Choi, D. Fadda, F. R. Marleau, B. T. Soifer, M. Im, L. Armus, D. T. Frayer, L. J. Storrie-Lombardi, D. J. Thompson, H. I. Teplitz, G. Helou, P. N. Appleton, S. Chapman, F. Fan, I. Heinrichsen, M. Lacy, D. L. Shupe, G. K. Squires, J. Surace, and G. Wilson. Spitzer 24 Micron Observations of Optical/Near-Infrared-Selected Extremely Red Galaxies: Evidence for Assembly of Massive Galaxies at z˜1-2? ApJS, 154:75–79, Sept. 2004.

A. W. Zirm, A. van der Wel, M. Franx, I. Labbé, I. Trujillo, P. van Dokkum, S. Toft, E. Daddi, G. Rudnick, H. Rix, H. J. A. Röttgering, and P. van der Werf. NICMOS Imaging of DRGs in the HDF-S: A Relation between Star Formation and Size at z $\sim$ 2.5. ApJ, 656:66–72, Feb. 2007.